Background Reduction for XFI with Human-Sized Phantoms

Dissertation
zur Erlangung des Doktorgrades
an der Fakultät für Mathematik, Informatik und Naturwissenschaften
Fachbereich Physik
Universität Hamburg

vorgelegt von
Florian Blumendorf

Hamburg
2019

Gutachter der Dissertation	Prof. Dr. Florian Grüner Prof. Dr. Wolfgang Hillert
Zusammensetzung der Prüfungskommission	Prof. Dr. Robin Santra Prof. Dr. Florian Grüner Prof. Dr. Wolfgang Hillert Prof. Dr. Erika Garutti Prof. Dr. Wolfgang Parak
Vorsitzender der Prüfungskommission	Prof. Dr. Robin Santra
Datum der Disputation	20.01.2020
Vorsitzender Fach-Promotionsausschusses PHYSIK	Prof. Dr. Michael Potthoff
Leiter des Fachbereichs PHYSIK	Prof. Dr. Wolfgang Hansen
Dekan der Fakultät MIN	Prof. Dr. Heinrich Graener

Abstract

X-ray Fluorescence Imaging (XFI) is a functional medical imaging modality that can be used for, e.g., cancer diagnostics or pharmacokinetic tracking studies. This is achieved by the detection of fluorescence photons emitted from metabolized tracers with a high atomic number that are excited by an external X-ray source. While the concept of XFI has been known for almost a century, it has not made its way to daily clinical practice. This is due to the high intrinsic background in large phantoms caused by multiple Compton scattering. This thesis tries to overcome the sensitivity limit for a spatial resolution of 1 mm without any a priori knowledge about the location of the tracer inside the phantom. Only the combined use of two filtering mechanisms enables the detection of tracer amounts as reported in small animal studies. First, a dedicated leaf-based collimator makes use of the inhomogeneity of the scattering positions inside the phantom to reduce the higher Compton scattering orders. After that, a pixel selection algorithm exploits the anisotropy of the remaining lower scattering orders and that of the fluorescence photons (if also anisotropic) to reduce the detector solid angle until an optimum sensitivity is reached. In fact, simulations show that it is not optimal to use all detectable data for the signal analysis even if that means discarding fluorescence photons.

After the introduction of these spatial filtering concepts on the example of a 30 cm sphere, variations of the detector layout and experimental parameters, such as energy, bandwidth, phantom size or target position inside the phantom, are studied. To validate these simulations, experiments performed at the P07 beamline at PETRA III at DESY are then compared yielding good agreements. As more realistic phantoms, the background filtering methods are applied to human voxel models with realistic anatomical structure for different target positions. Since the necessary large solid angle detectors are not available yet, two small scale experiments for a human finger and a rat model are prepared using small detectors and compared to using large solid angle detectors with the same filtering mechanisms as for the large phantoms. As an outlook two further filtering concepts using the additional detection of the photon arrival time in the detector and the polarization of the detected photons are discussed.

Zusammenfassung

X-ray Fluorescence Imaging (XFI) ist eine Methode zur funktionalen medizinischen Bildgebung, die u.a. zur Krebsdiagnose oder für pharmakokinetische Studien angewandt werden kann. Hierfür wird ein verstoffwechselter Tracer mit hoher elementarer Ordnungszahl durch eine externe Röntgenquelle zur Fluoreszenz angeregt, welche anschließend detektiert wird. Obwohl dieses Konzept seit knapp einem Jahrhundert bekannt ist, hat es den Einzug in die regelmäßige klinische Anwendung bisher nicht geschafft. Dies liegt maßgeblich an dem hohen intrinsischen Signaluntergrund durch multiple Comptonstreuung in großen Objekten, welcher die Sensitivität limitiert. In dieser Arbeit wird der Versuch unternommen, diese Beschränkung unter Verwendung einer räumlichen Auflösung von 1 mm ohne vorherige Kenntnis der räumlichen Verteilung des Tracers zu überwinden. Hierfür wird zunächst der mehrfach gestreute Comptonuntergrund durch einen geeigneten Fächerkollimator reduziert. Dieses wird durch die unterschiedlichen räumlichen Verteilungen der Streuorte im Phantom ermöglicht. Anschließend nutzt eine datenbasierte Pixelauswahl die Anisotropie der verbliebenen niedrigen Streuordnungen und der Fluoreszenzverteilung, sofern diese auch anisotrop ist, um eine optimale Teilmenge der auszuwertenden Detektorelemente zu ermitteln. Es stellt sich heraus, das es nicht optimal ist, einen möglichst großen Detektor für die Datenauswertung zu verwenden, selbst wenn man dadurch Fluoreszenzphotonen verliert. Nur durch die kombinierte Anwendung beider Filterungsmechanismen, wird die Detektion von biologisch relevanten Tracerkonzentrationen aus Kleintierstudien erst möglich.

Nach der Einführung dieser Filterungsmechanismen am Beispiel einer 30 cm Kugel, werden Parametervariation bezüglich des Detektoraufbaus und der experimentellen Größen, wie Strahlenergie, Energiebandbreite, Phantomgröße oder verschiedene Tracerpositionen im Phantom untersucht. Zur Validierung der verwendeten Computersimulationen werden einige Experimente an der P07 Beamline am PETRA III Synchrotron bei DESY durchgeführt und eine gute Übereinstimmung gezeigt. Als Schritt zu realitätsnäheren Phantomen werden die Filterungsmechanismen auf menschliche Voxelmodelle mit verschiedenen Tracerpositionen im Körper angewandt. Da die simulierten Detektoren zur Abdeckung des vollen Raumwinkel

bisher nicht verfügbar sind, werden zwei Experimente im kleineren Maßstab mit einem Rattenmodell und einem menschlichen Finger vorbereitet und als Ausblick mit den Filterungsmethoden für große Objekte verglichen. Abschließend werden zwei weitere Methoden zur Untergrundsreduktion diskutiert, wobei einmal der Detektionszeitpunkt und einmal die Polarisation der detektierten Photonen zusätzlich zur Energie verwendet wird.

Contents

Abstract **I**

Zusammenfassung **II**

1 Introduction **1**

2 Theory **5**
2.1 Physics Processes 5
2.1.1 General Photon Attenuation 5
2.1.2 Fluorescence Process 6
2.1.3 Compton Scattering 8
2.2 Radiation Dose 10
2.3 Data Analysis 12
2.4 Methods 16
2.4.1 Used Software 16
2.4.2 Amptek XR-100CdTe Detector 16
2.4.3 Hexitec Detector 21
2.4.4 Ideal Detectors 22

3 Background Reduction Methods **23**
3.1 XFI with 30 cm Spherical Phantom 23
3.2 Reduction of Higher Scattering Orders with a Collimator 26
3.3 Reduction of Lower Scattering Orders with Pixel Selection 34
3.3.1 Operating Principle of the Pixel Selection 34
3.3.2 Parameter Choices 39
3.4 Reconstruction of Tracer Positions 45

4 Variation of Collimator Parameters **47**
4.1 Overview of Collimator Geometries 47
4.2 Phi Collimator 49
4.2.1 Variation of Detector Size 49
4.2.2 Variation of Number of Collimator Leaves 51
4.2.3 Variation of Collimator Leaf Thickness 52
4.3 Parallel Collimator 54
4.4 Theta Collimator 55

5 Simple Phantoms **57**
5.1 Variation of Phantom Size 57
5.2 Variation of Target Elements 59
5.3 Variation of Incident Energy 61
5.4 Variation of Energy Bandwidth 63
5.5 Variation of Target Position 65
5.6 Impact of Phantom Inhomogeneity 67
5.7 Comparison with Transmission Imaging 68

6 Experimental Validation **71**
6.1 Angular Scans of PMMA Cylinder Phantoms 72
6.2 Molybdenum Collimator 76

7 Human Voxel Model **85**
7.1 Gold Target Located in the Kidneys and the Brain 87
7.2 Gold Target Located in the Lungs 92
7.3 Gold Target Located in the Thyroid 94
7.4 Gold Target Located in the Liver 96
7.5 Gold Targets Located in the Abdomen 97

8 Gadolinium Retention from MRI Contrast Agents **101**
8.1 Human Finger 102

9 Rat Voxel Model **109**
9.1 XFI with Full Solid Angle Detectors 110
9.2 XFI with Small Detectors 113
9.2.1 Assessment of Collimators for Small Detectors 115

9.3 Medium-Z Target Elements for Rats 119

10 Additional Filtering Possibilities **123**
10.1 Time Filters 123
10.2 Polarization Filters 129

11 Conclusion **139**

List of Abbreviations **VII**

Bibliography **VIII**

List of Figures **XXIII**

List of Tables **XXIV**

Acknowledgements **XXV**

Declaration **XXVI**

1 Introduction

Wilhelm Conrad Röntgen did not only revolutionize the world of physics but also of medicine with his discovery of X-rays in 1895 for which he was awarded the first nobel prize [1]. Together with Computed Tomography (CT) [2], Magnetic Resonance Imaging (MRI) [3] and ultrasound imaging [4], the classical two dimensional transmission X-rays form the category of structural or anatomical imaging used to image, such as bones, non-invasively. A different category of medical imaging is called functional or molecular imaging. Functional imaging is used to image biological functions, such as metabolism, blood flow or regional molecular abnormalities, such as senile plaque in the brain of Alzheimer's patients [5]. Its most common modalities used today are scintigraphy, Single Photon Emission Computed Tomography (SPECT) [6] and Positron Emission Tomography (PET) [7]. A new method currently under development since its invention in 2005 is called Magnetic Particle Imaging (MPI) [8]. It should be mentioned that the transition between those two broad imaging categories is fluid due to the possible use of contrast agents [9], dual or multi energy CTs [10], functional MRI [11] or the use of multimodal devices, such as PET/CT [7] or even PET/MRI [12].

X-ray Fluorescence Imaging (XFI) offers a different approach for functional imaging without the need for nuclear tracers. Instead, non-radioactive metabolizable Functionalized Diagnostic Agents (FDAs), such as gold, are brought into the body. After its excitation with an X-ray source, the detection of fluorescence photons allows for the location and quantification of the tracer inside the body. Gold is a suitable element, because it is naturally not present, non-toxic and its high fluorescence energy caused by its high atomic number is less attenuated by the body itself. In addition, it is reported to enhance the dose deposition depending on the cancer concentration, which for cancer can be a desired effect. Furthermore, it can be built in form of nanoparticles of different shape and size, that can be functionalized with biological molecules [13–15].

Since 1928, when Glocker and Schreiber [16] proposed to use the excitation of inner shell electrons by primary radiation and the subsequent detection of the characteristic fluorescence lines,

XFI has been established in various field besides medical imaging, for instance, assessing the authenticity of art and archaeological objects [17], material composition in geology [18] or studies of nutrient and contamination compositions in plants [19]. Its use in medical imaging with in vivo human was begun in 1968 by Paul Hoffer [20] with the scan of iodine in the thyroid. In the 1980s several papers were published by a Swedish group of Christoffersson and Jonson et al. [21–23] studying amongst other things the uptake and retention of cisplatin in kidneys, which is a drug used in cancer treatment. Although missing almost any spatial information, their setup was already quite sophisticated using a uranium filtered X-ray source, explicitly polarized radiation, a positioning of the detector at 90° and locating the region of interest via ultrasound [23]. The first in vivo XFI measurement of gold was published in 1993 individually by Börjesson et al. [24] and Shakeshaft et al. [25] studying the retention of gold salts for the treatment of rheumatoid arthritis, also known as chrysotherapy. This therapy, however, is not so common anymore due to the side effects [26]. Since then, XFI for humans has been used to assess the deposition of many trace elements in body parts that, unlike body fluids or hair, cannot be probed without damage. The patients are mainly exposed workers or patients undergoing therapy with drugs containing high-Z elements, including arsenic, iodine, platinum, lead, mercury and cadmium in, e.g., eyes, skin, prostate, bones, kidneys or liver. An overview about this is given by Börjesson et al. or Chettle [27, 28]. However, XFI has not yet made its way into clinical practice for the location of explicitly administered (functionalized) nanoparticles.

Compared to other functional imaging modalities, such as PET, XFI potentially offers some advantages. First, the spatial resolution intrinsically only depends on the size of the incident X-ray beam, whereas for clinical PET the current spatial resolution is approximately 5 mm and 1 cm for SPECT [6]. This is caused amongst other things by the size of the detector elements, the positron range and the acollinearity of the 511 keV photons created from the electron positron annihilation. Even with perfect technical devices, the resolution would be limited to approximately 2 mm [29, 30]. However, for preclinical PET devices, a resolution of 1 mm is possible using special collimators at the cost of sensitivity [31]. Moreover, for preclinical SPECT devices, even spatial resolutions of only 0.25 mm are reported [32] using pinhole collimators at the cost of sensitivity, but at the clinical level it lacks sensitivity and spatial resolution compared to PET. Second, for XFI, the time between the administration of the FDAs and the actual imaging is arbitrary, which allows for long-time and/or repeated measurements, such as pharmacokinetics. For PET, the radioactive decay of the administered drug creates a limit on that time. Typical half-life times range from 76 s for ^{82}Rb to 110 min

for ^{18}F. Longer half-life times, like 78 h as offered by ^{89}Zr, potentially allows for long time measurements [33, 34], however, at the cost of radiation dose. Third, for XFI, there is no radiation exposure for medical personal, other patients, visitors or even taxi drivers outside of the medical imaging time. Fourth, the production of FDAs for XFI should be easier and less expensive due to the lack of radioactivity.

To bring XFI into clinical practice, several well known problems have to be overcome as addressed for instance by Busch et al. [35]. Regarding the medical application with humans, the volume of the body and the depth of the target region results in a high attenuation of the fluorescence photons. The measurement time is limited, especially for ill patients. Incoherent scattering from low-Z elements in the body creates a large background occluding the signal. The optimization of a set of parameters, such as incident photon energy, polarization, collimators, detector positions, or the choice of fluorescence lines, is rather complex because they are interdependent. Besides, to get quantitative information careful calibration or Monte Carlo studies have to be performed [27, 36].

Besides the work on detector resolution, detector sizes, spatial reconstruction techniques and background filtering techniques, XFI would benefit greatly from a compact X-ray source with a high flux, small beamsize, low emittance and narrow spectrum, which is combined in the definition of high brilliance. Synchrotrons offer all of that apart from the compactness and although some authors suggest to build medical beamlines at synchrotron facilities, the access would be limited due to the costs and the space needed. Besides using synchrotrons, e.g. [37, 38], the XFI community mainly relies on filtered conventional polychromatic X-ray sources, e.g. [23, 36, 39], or the gamma radiation from radioactive isotopes, e.g. [20, 40, 41], which both lack in brilliance. A possible future solution might be obtained by the development of compact laser-driven all optimal Thomson X-ray sources [42, 43].

Under the current development of new sources and the availability of a synchrotron source for some basic validation experiments, in this thesis the potential and sensitivity limits of XFI for humans shall be assessed based on Monte Carlo simulations with large detector areas, collimators and optimal X-ray beam properties. The aim in this thesis is to use a spatial resolution of 1 mm without a priori knowledge of the tracer distribution along the beam and a radiation dose comparable to common CT or PET scans. In order to maximize the sensitivity a combined method of using a leaf-based collimator and a selection of detector pixels for the data analysis is presented for the example of a soft tissue sphere with a diameter of 30 cm, which has been published by our group [44, 45]. Only the combined use of both filtering

methods allows for the detection of gold masses in the order of 1 µg. After the description of the applied background reduction strategies in section 3, the detector layout is optimized in section 4 and applied for parameter studies with simple spherical phantoms in section 5. These simulations are then verified with experiments in section 6 and afterwards applied to a more realistic setup with human voxel models in section 7. After the preparation of two future small scale experiments in section 8 and 9, the thesis finishes with an outlook on other background filtering possibilities in section 10 using additional timing information, which until today is not technically feasible with the necessary resolution.

2 Theory

2.1 Physics Processes

In the X-ray energy regime there are three relevant processes for photons when passing through matter:

- photoelectric absorption
- inelastic or Compton scattering
- elastic or Rayleigh scattering

Pair production is not discussed in this work, since the photon energies used in medical imaging are in the order of 100 keV, which is way below 1.022 MeV needed for pair production.

2.1.1 General Photon Attenuation

Unlike electrons, photons have no electric charge. Therefore, they do not lose energy continuously when passing through matter and the photon beam does not widen gradually. Instead, the intensity of the beam is degraded exponentially following the Lambert-Beer formula [46]. For homogeneous materials, the number of photons transmitted without interaction through a specific length L is calculated using

$$N(L) = \exp\left(-\frac{\mu}{\rho}\rho L\right) \tag{2.1}$$

with the energy- and material dependent mass attenuation coefficient μ/ρ and the density of the material ρ. The yield of photons $Y(L) = 1 - N(L)$, that undergo a certain process, is just the inverse of the transmitted photons calculated for that specific process. The mass attenuation

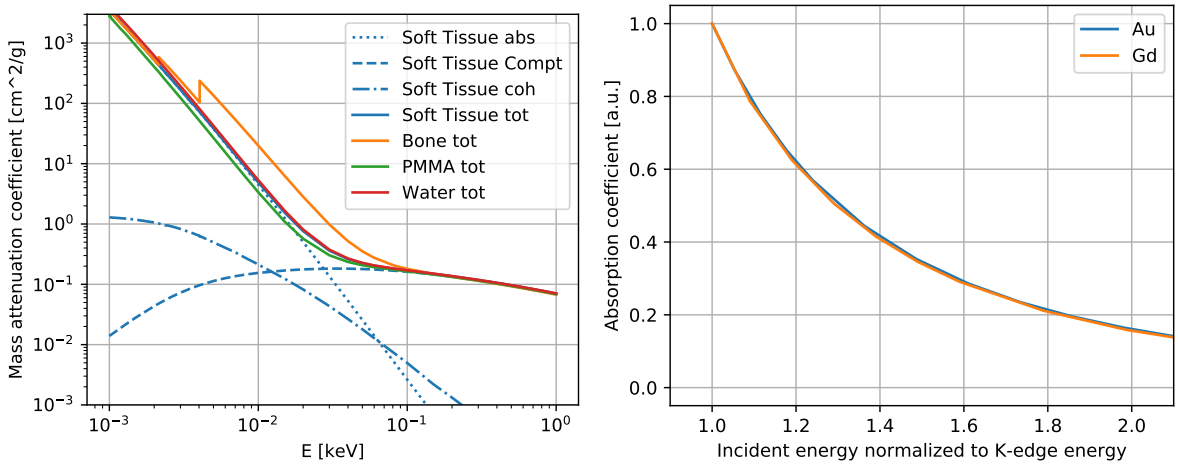

(a) (b)

Figure 2.1 – In (a) the mass attenuation coefficient for various materials are plotted in the X-ray regime. For soft tissue the absolute value is explicitly split up into its components: absorption, Compton and elastic scattering. (b) shows the absorption coefficients normalized to K-edge energy for gold and gadolinium.

coefficients are tabulated for many different materials [47] and directly proportional to the cross section σ [48] via

$$\frac{\mu}{\rho}\rho = \sigma n \tag{2.2}$$

with the particle density n. In figure 2.1(a) there is an overview over the most used materials in this thesis. It is shown, that the values for soft tissue, water and the PMMA substitute are all very similar and that Compton scattering is the relevant process for energies above 30 keV. For bones, the high calcium content increases the absorption. At 4 keV its K-edge is visible as an increase in absorption. In (b) the absorption cross sections, which are relevant for the amount of created fluorescence photons, are plotted for gold and gadolinium normalized to the K-edge energy.

2.1.2 Fluorescence Process

The spontaneous emission of a secondary photon after an atom has been excited by a primary photon or other charged particle is called fluorescence. During the excitation process an elec-

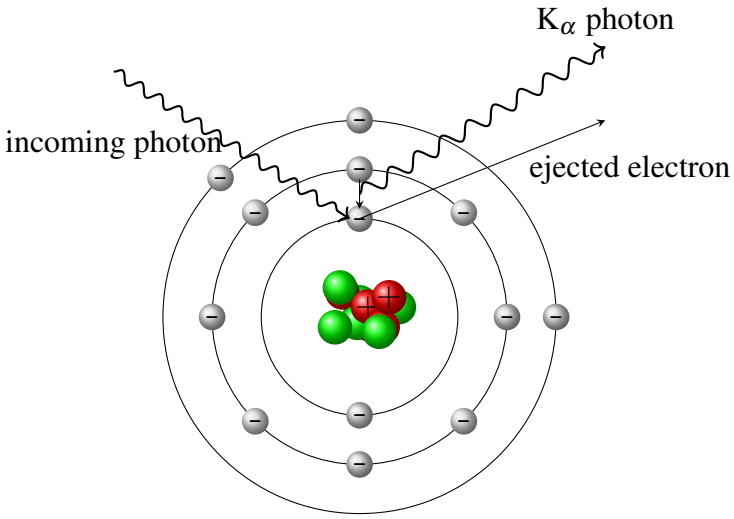

Figure 2.2 – Simplified illustration of a fluorescence process caused by photoabsorption inside an atom [49].

tron from an inner shell leaves the atom. This hole is filled by a less tightly bound electron from an outer shell. The difference in binding energy is then released in form of a photon (or non-radiative Auger effect at which the energy is transferred to another electron which then also leaves the atom). In figure 2.2 that process is illustrated. Since the binding energies are element specific, the so called characteristic fluorescence lines can be assigned to their corresponding element, if their energy is measured precisely.

Although the International Union of Pure and Applied Chemistry (IUPAC) proposed a new kind of notation in 1991 [51], the older Siegbahn notation [52] is still commonly used in X-ray spectroscopy and XFI and will be used throughout this thesis. The Siegbahn notation consists of a capital Letter for the shell which hole is going to be filled during this process starting with K for the innermost shell. It is then followed by a Greek letter which roughly corresponds to the shell the moving electron originates from and a number referring to the relative intensity of the line. Since the different energy lines were grouped according to their energy, there are inconsistencies and even a few missing notations, which were the reason for the IUPAC to

Table 2.1 – Values for fluorescence energies and the K-edges in units of [keV] used in this thesis for gold and gadolinium. [50]

	K-edge	K$_{\alpha 1}$	K$_{\alpha 2}$	K$_{\beta 1}$
Gd	50.2391	42.9963	42.3088	48.6951
Au	80.7249	68.8062	66.9913	77.9819

propose the new notation, in which the exact two electron orbitals are named, that are involved in the process. If the energy of the incident particle is higher than the K-absorption-edge, the most dominant fluorescence line is therefore called $K_{\alpha 1}$ in Siegbahn notation or K-L_3 in the IUPAC notation. Table 2.1 shows the most relevant fluorescence energies used in this work. The lower energetic L-fluorescence lines will not be treated here because their attenuation coefficients are too high to be relevant for large phantoms.

The over 100 year old Moseley's law [53] gives an estimation for the fluorescence energies of the $K_{\alpha 1}$-fluorescence energy

$$E_{K_\alpha} = \frac{3}{8} m_e c^2 \alpha^2 (Z-1)^2 \tag{2.3}$$

with the fine structure constant α, the electron mass m_e and the atomic number Z. This simple equation already makes it apparent, why gold with an atomic number of 79 is such a suitable candidate for medical XFI. Although for heavy elements relativistic corrections need to be applied [54] because the K-electron is bound with an energy corresponding to a kinetic energy moving with half the speed of light, Moseley's law yielding $E_{K_\alpha} = 62.1\,\mathrm{keV}$ already comes close to the actual value of 68.8 keV. Relativistic correction then yields 68.4 keV agreeing with the tabulated values in the xraylib [50] within 1%.

2.1.3 Compton Scattering

The inelastic scattering process of a photon in the X-ray regime with an electron, where a part of the energy from the photon is transferred to the electron, is called Compton scattering. For unpolarized photons and free electrons at rest, the angular dependence can be calculated using the Klein-Nishina differential cross section [55, 56]

$$\left(\frac{\mathrm{d}\sigma}{\mathrm{d}\Omega}\right)_{\mathrm{KN}} = \frac{1}{2} r_e^2 \left(\frac{E'}{E}\right)^2 \left(\frac{E'}{E} + \frac{E}{E'} - \sin^2\theta\right) \tag{2.4}$$

where E is the incident photon energy, E' is the photon energy after the scattering process and θ is the scattering angle. The classical electron radius [57] is calculated as

$$r_e = \frac{e^2}{4\pi\varepsilon_0 m_e c^2} \approx 2.82\,\mathrm{fm} \tag{2.5}$$

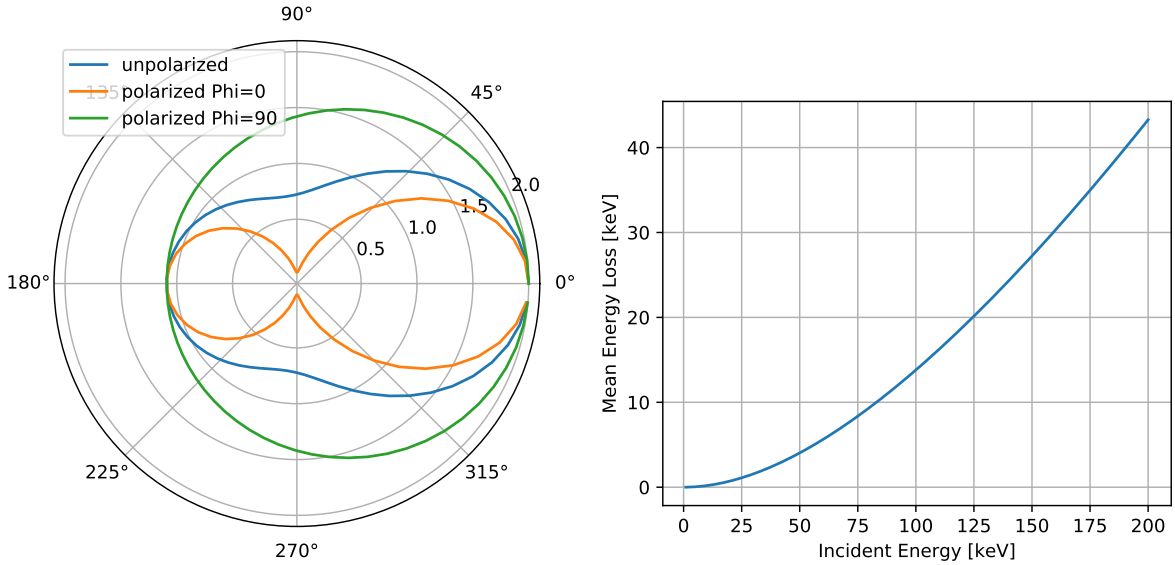

(a) (b)

Figure 2.3 – In (a) the differential Klein-Nishina cross section for 100 keV is plotted for unpolarized photons in blue, for polarized photons scattering in the plane of polarization in orange and perpendicular to that in green. The cross section is plotted in units of $\frac{1}{2}r_e^2$. (b) shows the mean energy loss of a photon after Compton scattering using eq. (2.8).

with the elementary charge e, the electron mass m_e, the speed of light c and the permittivity of free space ε_0. The energy after the scattering process $E'(E,\theta)$ can be calculated using

$$E'(E,\theta) = \frac{1}{1+\frac{E}{m_e c^2}(1-\cos\theta)} \cdot E\,. \tag{2.6}$$

For polarized incident radiation, the differential cross section (2.4) is no longer independent of the azimuthal angle Φ between the plane of scattering and the incident polarization vector. The cross section is then written as [58]

$$\left(\frac{\mathrm{d}\sigma}{\mathrm{d}\Omega}\right)_{\mathrm{KN,pol}} = \frac{1}{2}r_e^2\left(\frac{E'}{E}\right)^2\left(\frac{E'}{E} + \frac{E}{E'} - 2\sin^2\theta\sin^2\Phi\right). \tag{2.7}$$

By averaging over Φ, the polarized cross section turns into the unpolarized cross section again because the scattering angle θ does not depend on the polarization. This effect of polarization is shown in figure 2.3 for the two extreme cases of Φ.

For the estimation of applied energy dose to an object, it is helpful to consider the mean

deposited energy for one event of Compton scattering using

$$\overline{\Delta E} = \frac{\int \left(\frac{\mathrm{d}\sigma}{\mathrm{d}\Omega}\right)_{\mathrm{KN}} (E - E')\mathrm{d}\Omega}{\int \left(\frac{\mathrm{d}\sigma}{\mathrm{d}\Omega}\right)_{\mathrm{KN}} \mathrm{d}\Omega}\,. \tag{2.8}$$

The values for the mean energy loss are plotted in figure 2.3(b).

To take into account the binding energy of the electron, it is possible to multiply the Klein-Nishina cross section with an incoherent scattering factor $S(E,\theta,Z)$, which was tabulated by Hubbel et al. [59]. Regarding low photon energies or low scattering angles, the scattering cross section would thus be lowered. However, since for photon energies relevant for the K-fluorescence of gold and relevant materials existing in a human body S hardly differs from the atomic number Z, it will be approximated with Z throughout this work. Furthermore, the assumption of an electron at rest bound in an atomic orbital does not hold true. Hence, the energy transfer can be larger or smaller than expected depending on the electron's momentum. This effect is called Doppler broadening [60]. It is included in the simulations, but not in the analytic calculations used to check their plausibility [61].

2.2 Radiation Dose

Since the absorbed energy of X-rays is harmful to living organisms, it is the aim of medical imaging to reduce the absorbed dose as much as possible. Besides radiation sickness or even death for extremely high radiation exposures, the International Commission on Radiological Protection (ICRP) estimates an additional risk of 5% per 1 Sv to develop cancer [62], which is often underestimated, even by physicians [63]. Common dose values accepted for medical diagnostics today range from 10 µSv for a dental X-ray to 20 mSv for CT [64] or PET scans [65]. The absorbed dose within a volume element is defined as

$$D = \frac{\mathrm{d}E_{\mathrm{dep}}(x,y,z)}{\mathrm{d}\rho(x,y,z)} \tag{2.9}$$

with the deposited energy E_{dep} and the local density ρ. Unlike the equivalent dose, it does not take into account the effectiveness of the radiation, which is a factor of one for photons, or the individual harm to different organs. Since both are measured in the same basic SI units, joule per kilogram, specific names are recommended to avoid confusion [66]. The absorbed dose should be given in gray $[1\,\mathrm{Gy} = 1\,\mathrm{J/kg}]$, whereas the equivalent dose should be expressed in sievert $[1\,\mathrm{Sv} = 1\,\mathrm{J/kg}]$. If not explicitly mentioned otherwise, the dose values given in this

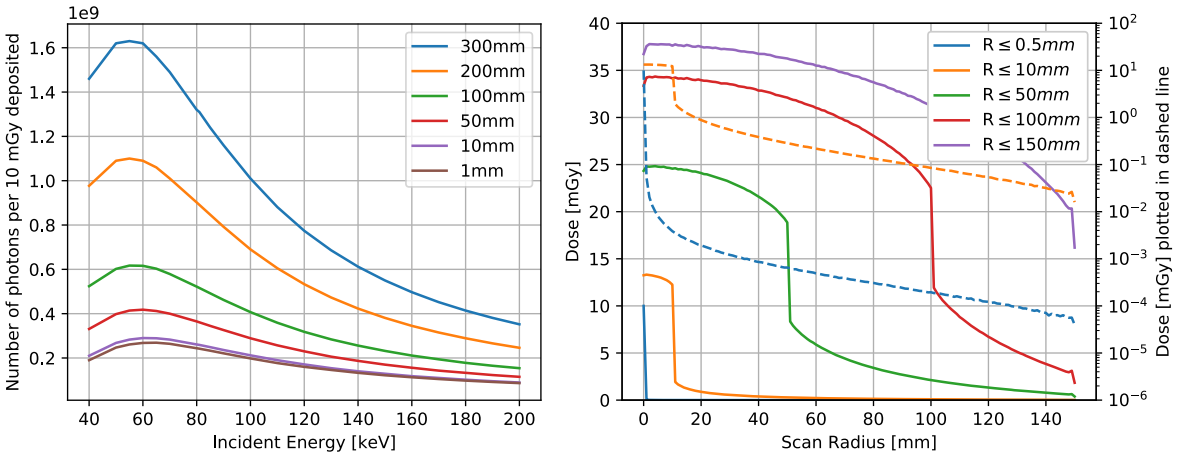

(a) Number of photons per 10 mGy

(b) Dose distribution for continuously scanned areas

Figure 2.4 – (a): The allowed numbers of incident photons for a dose of 10 mGy inside the beam volume is plotted against the incident energy for different phantom lengths in soft tissue with a 1 mm diameter circular beam. (b) shows the deposition of dose outside the beam for a continuously scanned area of different radii around the center within a 30 cm sphere with 85 keV. For each 1mm beam, the dose inside the beam volume was 10 mGy. The dashed lines show the same data plotted logarithmically with the axis on the right.

thesis are the integrated absorbed dose for the intersection volume of the phantom and the incident beam. For the sensitivity limits of XFI, a dose value of 10 mGy, similar to CT or PET, is assumed to be acceptable in this thesis. Depending on the desired sensitivity for a measurement, this value can then be increased or lowered accordingly.

In figure 2.4(a), the number of incident photons to reach the 10 mGy are plotted for a beam radius of 0.5 mm in soft tissue [67]. The maximum at 60 keV marks the point, at which the average energy deposited by Compton scattering becomes larger than the energy deposited by photoabsorption. When larger areas are scanned, the dose deposition in adjacent tissues, however, has to be taken into account. In figure 2.4(b), the dose depositions outside the beam for continuously scanned areas of different radii are plotted. The areas are scanned with adjacent 1 mm beams and although the dose deposition inside the beam volume for each scan point is only 10 mGy, the depositions outside add up for larger areas. For example, for a single beam plotted in blue, in a distance of 1 cm to the beam, the dose is 2600 times smaller than inside the beam. However, to scan an area with a radius of 1 cm, as shown in orange, 400 times more photons are necessary explaining the difference in both curves. This does not only increase the dose outside of the scanned area by a factor of 400, but also in the center from 10 to 13 mGy.

If the whole phantom is scanned, as shown in purple, the dose in the center even increases to 37 mGy with an average dose of 30 mGy throughout the phantom. Therefore, if larger volumes are to be scanned and local dose shall not overcome 10 mGy per beam volume, the total number of photons and thus the sensitivity have to be lowered accordingly. The conversion from the dose inside the beam to the total dose in the phantom is not trivial because the ratio depends on the incident energy, the length of the phantom, the position of a beam inside a phantom and the scanned area.

Since the significance of a signal scales with the square root of the photon statistics $Z \propto \sqrt{N}$, it is important to make sure, that these values are correct. Therefore, they are cross-checked using a very simple calculation. The probability p_X is calculated for a specific process within the length L inside a phantom with the mass attenuation coefficients μ/ρ_X for the specific process and the total attenuation coefficients with coherent scattering μ/ρ_{tot} [47] using

$$p_X = \lim_{N->\infty} \sum_{i=1}^{N} \left[1 - \exp\left(-\left(\frac{\mu}{\rho}\right)_X \rho \frac{L}{N}\right)\right] \cdot \left[\exp\left(-\left(\frac{\mu}{\rho}\right)_{\text{tot}} \rho \frac{L}{N}\right)\right]^{i-1}. \tag{2.10}$$

The deposited energy for photoabsorption, where the full photon energy is deposited and the deposited energy for Compton scattering is then calculated using

$$E_{\text{dep,photoabs}} = N_\gamma \cdot E_{\text{inc}} \cdot p_{\text{photoabs}} \tag{2.11}$$

$$E_{\text{dep,Com}} = N_\gamma \cdot E_{\text{Com,mean}} \cdot p_{\text{Com}} \tag{2.12}$$

with the number of incident photons N_γ, the incident photon energy E_{inc} and the mean energy deposited for a Compton scattering $E_{\text{Com,mean}}$ calculated using eq. (2.8). Then the deposited dose is calculated using

$$\bar{D}_V = \frac{E_{\text{dep,photoabs}} + E_{\text{dep,Com}}}{\pi r_{\text{beam}}^2 L}. \tag{2.13}$$

Although this is very simplified, the result agrees with the data plotted in figure 2.4(a) within 2%.

2.3 Data Analysis

To analyze the simulated or experimentally obtained data, the photon energies are sorted into a histogram. For ideal detector materials, the finite energy resolution of the detector is sampled

using a Gaussian function

$$f(x) = A \exp\left(-\frac{(x-\mu)^2}{2\sigma^2}\right) \tag{2.14}$$

with the mean μ and the standard deviation σ. The actual amount of fluorescence photons in the Gaussian peaks is then determined using

$$N_\gamma = \frac{\sqrt{2\pi} A \sigma}{b_{\text{bin}}} \tag{2.15}$$

with the histogram bin width b_{bin} and the parameters for the Gaussian function A and σ obtained from a fit. The background is estimated from fitting the energy below and above and interpolating the values for the signal range. If it possible to obtain a zero measurement without signal, for example by tuning the incident energy below and above the K-edge, simply removing the target (if possible) or moving the beam slightly besides the target, the background can be subtracted or a fit function can be obtained using a non-parametric kernel density estimation [68]. Since fits always are a potential source of error, for the simulations made in this thesis, the real information about fluorescence and background is always used at least in comparison. Of course, for a real experiment this is not possible.

Statistical Significance In this work the detectability of a signal over background is assessed using the statistical significance commonly used in particle physics [69, 70]. It is a common misconception, that the statistical significance proves *that there is high-Z material* in the XFI measurement or that it calculates the probability of high-Z material being in the experiment based on the data alone. Instead, a background hypothesis is assumed, in this case: *There is no high-Z fluorescence in the spectrum*. Then the probability is calculated that based on the estimated amount of photon counts, the measured data would be at least as extreme as observed based on statistical fluctuations alone. Using a preset threshold value, the background hypothesis can then be accepted or discarded. This probability is called p-value and it is calculated using a Poissonian distribution

$$p = \sum_{n \geq n_{\text{obs}}}^{\infty} \frac{\mu^n e^{-\mu}}{n!} \tag{2.16}$$

with the mean $\mu = n_{\text{exp}}$ and the observed number of photons n_{obs}. Since the p-value is very inconvenient to handle, it is usually converted into units of standard deviations from a Gaussian

normal distribution. For this purpose, the p-value is converted into a distance x from which a Gaussian normal distribution has to be integrated until infinity, so that the integral equals the p-value. Since the standard deviation of the Gaussian normal distribution is one, the unit of the significance is called σ (sigma). This is performed mathematically via

$$Z = \Phi^{-1}(1-p) \tag{2.17}$$

with the cumulative (integrated) standard normal distribution

$$\Phi(x) = \int_{-\infty}^{x} \frac{1}{\sqrt{2\pi}} \exp\left(\frac{-y^2}{2}\right) \mathrm{d}y\,. \tag{2.18}$$

Considering large numbers of photons, this calculation can be simplified to

$$Z = \frac{n_{\mathrm{obs}} - n_{\mathrm{exp}}}{\sqrt{n_{\mathrm{exp}}}} = \frac{s}{\sqrt{b}} \tag{2.19}$$

with the signal photons s and background photons b. This simplification is obtained by replacing the Poissonian distribution in the formula for the p-value in eq. (2.16) with a Gaussian distribution with the mean of b and a standard deviation of $\sqrt{b}$, inserting that into eq. (2.17) and performing a variable substitution with $y = (n-b)/\sqrt{b}$. Since typical numbers for signal and background photons are well above one thousand, the obtained error is negligible. It has to be stated, that here a one-sided test is performed. In the context of XFI it does not make sense to expect less photon counts with a fluorescent material than without. Similarly the Higgs-boson is also a one-sided test [71]. This has even been initially mixed up and later corrected in the Nature magazine [72]. In table 2.2 some exemplary p-values are calculated.

Although in many other fields than physics, such as clinical trials, a 95% threshold is used as a threshold for significance [73], in this work a limit of $Z = 3\sigma$ is assessed as a detectable amount of fluorescence photons in a spectrum. In particle physics this is usually called *evidence* of a particle whereas 5σ are necessary for a *discovery* [74]. If another limit, e.g. $Z = 5\sigma$ shall be employed, the minimum detectable concentrations of high-Z material can simply be scales using $\rho_{5\sigma} = 5/3 \cdot \rho_{3\sigma}$. This arises from eq. (2.19), where the significance is directly proportional to the amount of measured signal photons.

Definition of a Signal Region The energy interval to determine the amount of signal photons and background photons, that are needed to calculate the statistical significance, is chosen as $[E_{\text{fluo}} - 3\sigma, E_{\text{fluo}} + 3\sigma]$ with the fluorescence energy E_{fluo} and the detector resolution σ given as the Root Mean Square (RMS) at that energy. Regarding the perfect detector in the simulations, a constant detector resolution of 200 eV RMS is assumed yielding a signal interval of $6\sigma = 1.2\,\text{keV}$. For the K_α-fluorescence, a combined signal region for the $K_{\alpha 1}$ and $K_{\alpha 2}$ region is considered using

$$Z = \frac{s_{K\alpha 1} + s_{K\alpha 2}}{\sqrt{b_{K\alpha 1} \cup b_{K\alpha 2}}} \tag{2.20}$$

with the amount of signal photons s_i and background photons b_i. For a Gaussian detector resolution smaller than 300 eV RMS, both K_α background regions are disjoint and the union in the denominator turns into a simple plus sign. With the $K_{\alpha 2}$ line being 59% as intense as the $K_{\alpha 1}$ line [50], for two disjoint energy intervals, the significance increases by 12% if a constant background is assumed. Besides increasing the sensitivity, the stability of the fit to the spectrum is increased a lot, if not one Gaussian function is added to a background function, but two Gaussians with a known relative peak height and two known energies at which the signal is expected. Adding also the $K_{\beta 1}$ line decreases the significance because having only 22% of the $K_{\alpha 1}$ intensity it is too weak in comparison. Furthermore, the energy interval, in which the background has to be reduced to achieve a good signal, is a lot larger.

Reduced chi-square To assess the goodness of a fit, the reduced chi-square value [75] is calculated using

$$\chi^2_{\text{red}} = \frac{1}{\nu} \sum_{i=0}^{N} \left(\frac{y_i - f(x_i, a_j)}{\sigma_i} \right)^2 . \tag{2.21}$$

Table 2.2 – Corresponding one-sided and two-sided p-values for some exemplary significance values. For the context of XFI, the one-sided p-value is used. The difference is exactly a factor of two.

	1σ	2σ	3σ	4σ	5σ
one-sided probability	15.9%	2.3%	0.13%	0.0032%	0.000029%=1/ 3.5e6
two-sided probability	31.7%	4.6%	0.27%	0.0063%	0.000057%=1/1.75e6

For the application in XFI, N is the number of bins in the fitting range of the energy histogram, y_i is the bin content of the i-th bin, f is the fitting function with parameters a_j and the bin position x_i and σ_i is the error of the i-th bin. $\nu = N - N_{\text{fit}}$ is called number of degrees of freedom and calculated as the difference between the number of bins and the number of fitting parameters.

2.4 Methods

2.4.1 Used Software

The XFI simulations presented here have all been performed using Geant4, a toolkit for Monte Carlo simulations for the interactions of particles with matter [76]. For all simulations in this thesis, the G4EmLivermorePhysics [77] physics model was used. In contrast, the Penelope model [77], which was tested as a comparison, showed almost the same Compton background spectrum, but the amount of created fluorescence photons in mixed materials, e.g. 1 mg/ml of gold in water, did not behave as expected, especially for variations of the concentration of gold.

The simulated and experimental data used in this thesis were both evaluated and plotted with the data analysis framework ROOT [78]. It offers several very useful classes for histograms and fit functions used to distinguish between the fluorescence photons, which corresponds to the signal in XFI measurements, and other photons in the same energy range which usually had been scattered incoherently. The analytical calculations were performed using Python [79], which was also used as a plotting tool.

2.4.2 Amptek XR-100CdTe Detector

For the experiments described in section 6, an Amptek XR-100CdTe [80] detector was used. The small detector with a weight of only 125 g uses a Cadmium Telluride (CdTe) diode with an area of 5x5 mm^2 and a thickness of 1 mm to detect photon spectra in the X-ray range. Because of its high atomic number and a wide band gap, CdTe offers a high photon attenuation coefficient allowing for high efficiency in a small volume without the need for cryogenic cooling. This material with the given thickness of 1 mm offers a detection efficiency of almost 100%

between 10 and 50 keV and 90% at 70 keV, which corresponds to the gold K_α-fluorescence energy range. At 100 keV the efficiency then drops to 60%. The applied voltage was set to 500 V and the rise time discrimination[1] was turned off. In such a semiconductor detector ionizing radiation creates a signal by generating electron hole pairs, whose number is proportional to the amount of deposited energy $N_{\mathrm{eh}} = E_\gamma / E_{\mathrm{pair}}$ with $E_{\mathrm{pair}} = 4.43\,\mathrm{eV}$. Due to an applied electric field, the free charges move to the electrodes and produce a current, which is converted into a voltage step proportional to the deposited energy by an amplifier.

The detection process and detector effects are explained in detail by Redus et al. [81, 82]. Here only some information relevant to understand the detector effects are summarized. In figure 2.5 a measured spectrum of a monoenergetic beam of 82.84 keV taken at PETRA III is shown. A perfect detector would yield a delta-function-like peak at the photon energy. For a real detector, however, some effects need to be considered. First, there is Gaussian broadening due to the statistical nature of the electron hole creation process. Second, there is a process called hole tailing arising from holes trapped at crystal defect sites. The short lifetimes of the holes are the reason for the asymmetric peak shape with the characteristic edge, here visible at 75 keV. Third, there are escape peaks which can arise if the ionization in the detector material creates cadmium or tellurium fluorescence which leaves the detector. Then the detector detects the difference in energy between the original photon and the escaped fluorescence photon. The escape peaks are much more prominent compared to silicon detectors because in silicon the probability for a radiationless Auger effect is 95% and in CdTe only 15% [50], the higher fluorescence energies of CdTe have a longer mean free path than fluorescence photons in silicon, therefore a larger portion of the chip can create escape peaks, and in contrast to silicon, in CdTe there are four peaks visible: K_α and K_β for Cd and Te each. Fourth, a photon can perform Compton scattering in the detector chip once or several times. If the photon leaves the chip afterwards, only the deposited energy is measured. However, for CdTe in the considered energy intervals (usually below 100 keV), this effect is of minor importance because the absorption cross section is a lot higher than the Compton cross section. In the color-coded spectra in chapter 8 and 9 the photons, which only deposit a part of their energy, are sorted into two categories: incomplete counts and escape peaks. Only those photons are marked as an escape peak, whose energy can clearly be attributed to a monoenergetic peak, such as fluorescence or the Rayleigh peak for a monoenergetic X-ray source, minus a

[1] The rise time discrimination is a method by Amptek which discards photons based on the rise time of a voltage step in the detector amplifier. A slow rising voltage suggests a long travel path for the slower holes in the semiconductor which results in energy loss and thus asymmetric broadening of the peak. For quantitative analysis Amptek recommends not to use this method.

fluorescence energy from the chip's material. Everything else is summarized as incomplete counts.

For the calculation of the detector effects, the Hecht equation [83] is used to calculate the relative charge loss by hole tailing dependent on the position of the energy deposition in the chip

$$\frac{Q*}{Q} = \frac{\lambda_h}{L}\left(1-\exp\left(\frac{-x}{\lambda_h}\right)\right)+\frac{\lambda_e}{L}\left(1-\exp\left(\frac{x-L}{\lambda_e}\right)\right) \tag{2.22}$$

with the detector thickness L, the energy deposition depth x and the electron/hole trapping lengths $\lambda_{e/h}$. The values for calculating $\lambda_i = \mu_i \tau_i U/L$ are tabulated [82] except for the variable voltage. For 500 V and the 1 mm chip thickness, the electron trapping length is 16.5 cm, whereas for the holes it is only 1 cm, explaining significant higher charge losses of the holes. However, in this thesis the hole trapping length is reduced to 45% of the literature values because in the experimental spectra, the edge of the hole tailing is rather at 90% of the incident value than at 95% as suggested by the tabulated trapping lengths. After the depth dependent charge loss, there is a Gaussian broadening applied using

$$\sigma_E = \sqrt{F_{\mathrm{CdTe}} E_{\mathrm{eh}} E_\gamma} + c_{\mathrm{fit}} \tag{2.23}$$

with the Fano factor[2] for CdTe $F_{\mathrm{CdTe}} = 0.1$ [81], the energy necessary to produce an electron-hole pair $E_{\mathrm{eh}} = 4.43\,\mathrm{eV}$ and a fitting constant $c_{\mathrm{fit}} = 119\,\mathrm{eV}$ from own calibration measurements with gamma lines from radioactive source, monoenergetic beam spectra from PETRA III and fluorescence spectra obtained at PETRA III with pure metal foils.

To explain the detector effects visible in the spectra, the capital letters in figure 2.5(a) are used. A shows the full absorption of the incident beam, which is exponentially attenuated through the chip. At B there is the absorption of incident photons that lose some energy due to small angle scattering in air or the detector window. This is usually occluded by the hole tailing. At C there are backscattered photons from the ceramic substrate behind the chip. At D there are the four escape peaks of the incident beam, of which due to the limited resolution in the plot only three are visible. E are broadened escape events of the backscattered photons in C. F is supposedly silver fluorescence from the cooling element. Although Amptek published no information about this, it is included in the simulations because in almost all experimental

[2]The Fano factor is the ratio of the actual variance and the Poissonian variance based on the number of created electron hole pairs: $F = \sigma/\sqrt{N}$ [84]. It poses a fundamental limit on the energy resolution.

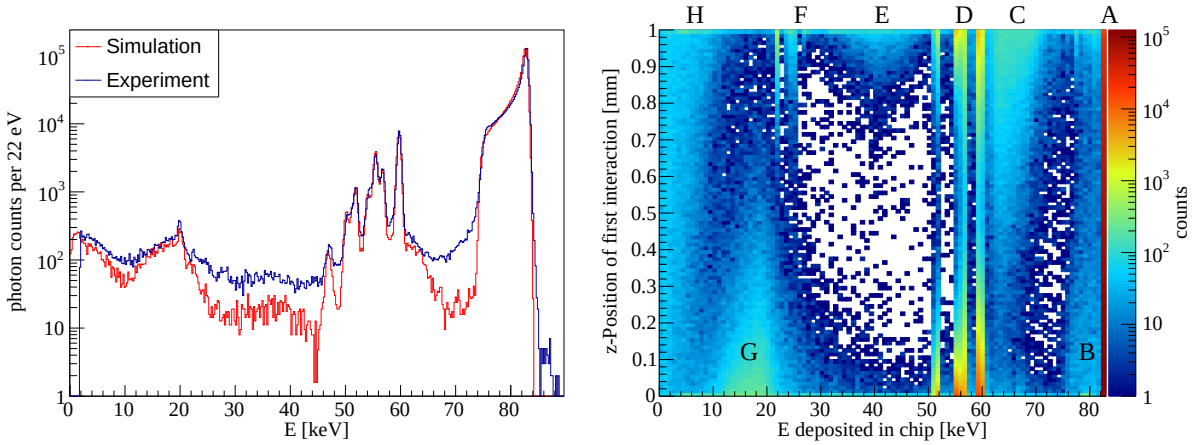

(a) log. spectrum of 82.8keV monoenergetic photons

(b) interaction regions in the detector chip

Figure 2.5 – (a): shown are a direct monoenergetic beam spectrum measured at the P07 beamline at PETRA III and simulations as comparison to show the detector response. In (b) the interaction positions for the simulated detections of photons are marked to help understanding the detector effects.

spectra a small peak is visible that fits the silver energy minus the hole tailing difference for entering the chip from the backside. G is the energy deposition caused by Compton backscattering at the surface of the chip. H is the deposition of energy loss by Compton forward scattering for small angles. Overall, the experiment can be well reproduced using simulations with the explained effects. Strictly speaking, at the bottom level of the spectrum the simulation does not produce as many photon counts as the experiment. Possible reasons for the deviations are electronic noise not considered in the simulations, actual scattering somewhere in the experimental hutch that is not fully rebuilt in the simulations, charge loss at impurities in the semiconductor or inhomogeneities in the electric field distribution. The latter is required to be homogeneous for the calculation of the hole tailing with the sharp edge at 90% of the actual photon energy and research showed, that homogeneity is not necessarily given [85, 86]. The discrepancy could be lowered by adding an additional constant to the resampling function for the detector response. On the other hand there is usually a broad Compton spectrum in the considered XFI simulations, as a result the gold K_α signal region around 70 keV are dominated by actual scattered photons anyway and not by detector effects from photons over 80 keV.

With regard to the fitting of fluorescence peaks, an adapted version of a Hypermet function is used, for which it is usually referred to the early work by Philips and Marlow [87]. The classic

Hypermet function for silicon or germanium detectors adds a plateau and an exponential tail to a Gaussian which reaches to zero. To account for the edge, Amptek suggests to add a step function $H(E)$. Instead, it is also possible to multiply the exponential term with an error function, terminating it at the lower edge of the tail. A Hypermet function

$$f(E) = G(E) + P(E) + D(E) + H(E) \tag{2.24}$$

can therefore be used as the sum of a Gaussian G, a box-like function H, an exponential tail D and an optional Plateau P accounting for electronic noise. These functions are defined as

$$G(E) = A \cdot \exp\left(-\frac{(E-\mu)^2}{2\sigma^2}\right) \tag{2.25}$$

$$P(E) = AB \cdot 0.5 \cdot \left(1 - \operatorname{erf}\left(\frac{E-\mu}{\sqrt{2}\sigma}\right)\right) \tag{2.26}$$

$$D(E) = AC \cdot 0.5 \cdot \exp\left(\frac{E-\mu}{\beta}\right) \cdot \left(1 - \operatorname{erf}\left(\frac{E-\mu}{\sqrt{2}\sigma} + \frac{\sigma}{\beta\sqrt{2}}\right)\right) \tag{2.27}$$

$$H(E) = AD \cdot \left(1 + \operatorname{erf}\left(\frac{x-\mu \cdot K_p}{K_w}\right)\right) \cdot \operatorname{erfc}\left(\frac{x-\mu}{\sqrt{2}\sigma}\right) \tag{2.28}$$

with the weights A, B, C, D, the energy incident energy μ, the detector resolution σ, a value scaling the exponential tail β and two parameters for the edge K_p, K_w. These fitting parameters are determined empirically by fitting experimental data.

Definition of the signal interval for the Amptek detector Because of the asymmetric peak shape in the Amptek measurements, the choice of the signal interval is reviewed. Possible choices for the definition of a signal interval are the Full Width at Half Maximum (FWHM), which is the easiest to determine if the detector has not been fully characterized, the RMS of

Table 2.3 – The relative significances for different signal interval definitions are given normalized to the optimum for each line. The gadolinium signal region at 42 keV and the gold region at 68 keV are compared to a normal Gaussian function without depth dependent detector effects.

	FWHM	3 Gaussian RMS	1 Full RMS	2 Full RMS	3 Full RMS
Pure Gaussian	99%	81%	96%	95%	81%
Amptek 42 keV	99%	84%	97%	92%	66%
Amptek 68 keV	99%	93%	82%	71%	65%

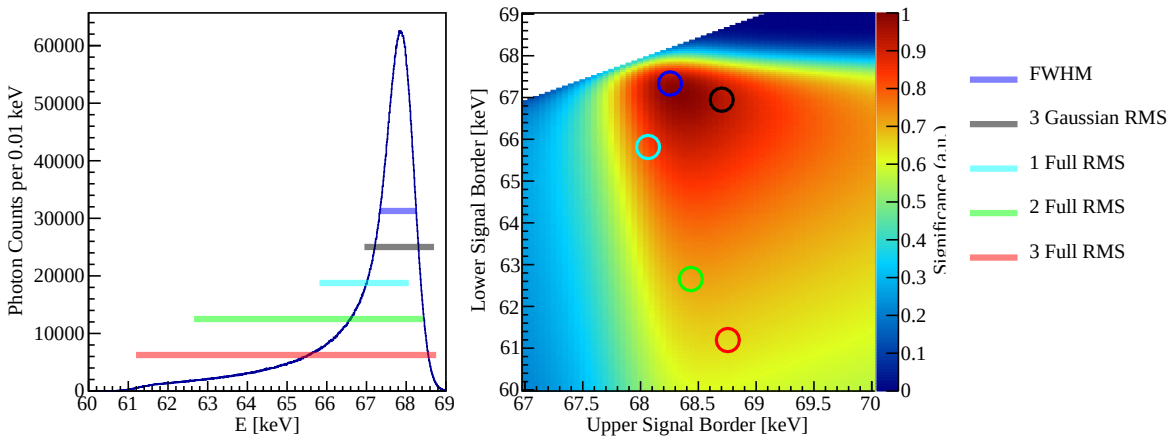

Figure 2.6 – A simulation of a monoenergetic beam of 68 keV including hole tailing detected by an Amptek is shown. The energy intervals for 5 different criteria explained in the text are marked. On the right the corresponding significances are shown for all kinds of possible signal interval combinations within the plot range.

the main Gaussian peak $G(E)$ and the RMS of the full peak broadened by the Hecht equation (2.22). Concerning the latter, the intervals are set such that the integrated counts below and above the interval limits are equal to the Gaussian values given in table 2.2. 1,2 and 3 RMS are listed here explicitly for this case. However, the enlarged signal interval accumulates more background reducing the significances. In figure 2.6 a spectrum of 68 keV simulated with the Amptek detector using the Hecht equation and Gaussian broadening is given. For this energy corresponding to the gold K_α, five different signal intervals are marked in the spectrum and their significances are calculated. The results for this energy together with a normal Gaussian and the molybdenum K_α energy region are listed in table 2.3. Although the FWHM limits yield the best significances, which are almost the optimum for all three cases, the signal interval will be defined in this work as $\pm 3\sigma$ by the main Gaussian peak calculated using eq. (2.23). This is done to be consistent with previous work in the group and the majority of XFI literature.

2.4.3 Hexitec Detector

A second detector used in this work is the Hexitec by Quantum Detectors [88]. The Hexitec detector is only used in chapter 9 and 8 as a simplified model. No experimental data is presented in this thesis, but it has already been used by our group and will be used for future beam

times. The Hexitec has a pixelated CdTe-Chip consisting of 80x80 pixels with a total size of 2x2 cm. Besides the advantage of a larger detector chip, the pixelation reduces the hole tailing, increases the data acquisition rate for slowly pulsed X-ray sources and the independent read out possibilities for the pixels offer the effective use of ,e.g., collimators with parallel sheets, such as presented in section 4.3. The disadvantages include a worse detector resolution compared to the Amptek detector and a smaller detection efficiency due to charge sharing between the pixels. Furthermore, there are more prominent escape peaks and additional Cd and Te fluorescence peaks. This can be caused by the creation of a fluorescence photon in pixel *A*, which then moves to pixel *B* to be reabsorbed. As a result, the detector detects an escape event in pixel *A* and a Cd/Te fluorescence photon in pixel *B*. Due to the missing pixels, this is impossible for the Amptek detector. Regarding future experiments, where dose plays an important role, the Hexitec is also interesting because it is already used in arrays of 5x5 CdTe chips resulting in an area of 10x10 cm [89]. Moved close to a small animal, such as a laboratory mouse, the covered solid angle can come close to 50%.

For the simulations, the Hexitec is built as a continuous CdTe chip taking into account transmission through the chip, Compton scattering and escape peaks. However, charge sharing and other pixel-related effects are not simulated. Due to a missing calibration, the energy resolution experimentally determined at 70 keV is simplified to have a constant RMS of $\sigma_E = 350\,\text{eV}$.

2.4.4 Ideal Detectors

The simulations with human-sized objects will be performed using detectors covering almost the whole solid angle, called 4π-detectors. Since these detectors are not commercially available yet, it is not clear which material they might consist of. Therefore, the quantum efficiency and the position of escape peaks in the spectrum is unknown. For each possible material, there are different incident X-ray energy intervals, which would cause escape peak events in the signal region. Since at this stage the material of such a detector is unknown, the material dependent effects will be ignored by assuming a perfect detector material that detects every photon with 100% efficiency. The detector response used will be a Gaussian peak shape with 200 eV RMS constant for all photon energies.

3 Background Reduction Methods

To maximize the sensitivity limits for XFI with large objects, which is necessary to bring XFI into clinical practice, the signal background consisting of multiple scattered Compton photons has to be reduced. In order to achieve this, a combination of two elements is used: a leaf-based collimator and a subsequent pixel selection using a large solid angle detector. The collimator is used to reduce the higher Compton scattering orders, that do not reach the detector straight from the beam axis. The pixel selection is then performed to find the composition of detector elements yielding the highest significance for the fluorescence signal in their combined data. This is made possible because the remaining lower scattering orders, that are less collimated, are highly anisotropic. Therefore, a higher signal significance is obtained, if parts of the measured data is discarded, although inevitably fluorescence photons are lost, too. Only the use of the combination of both manages to maximize the sensitivity. Without a collimator the spectrum would be too isotropic due to the higher Compton orders as to allow a pixel selection to be effective. Whereas without a pixel selection, at the low incident energies proposed here, there would be too much single Compton scattering left, so that the inevitable loss of fluorescence photons would outperform the background reduction. For higher incident energies, a collimator is more effective for the full solid angle, but the combination of both works best for energies close to 85 keV. After the description of the starting point with a 30 cm sphere in a collimated large solid angle detector, both the collimator itself and the pixel selection are discussed in detail.

3.1 XFI with 30 cm Spherical Phantom

The starting point of this thesis is an example case published by our group [44]. As a simplification for the XFI simulations with human models, a spherical phantom made of soft tissue with 30 cm diameter is used. In its center there is a target sphere with a diameter of 1 mm

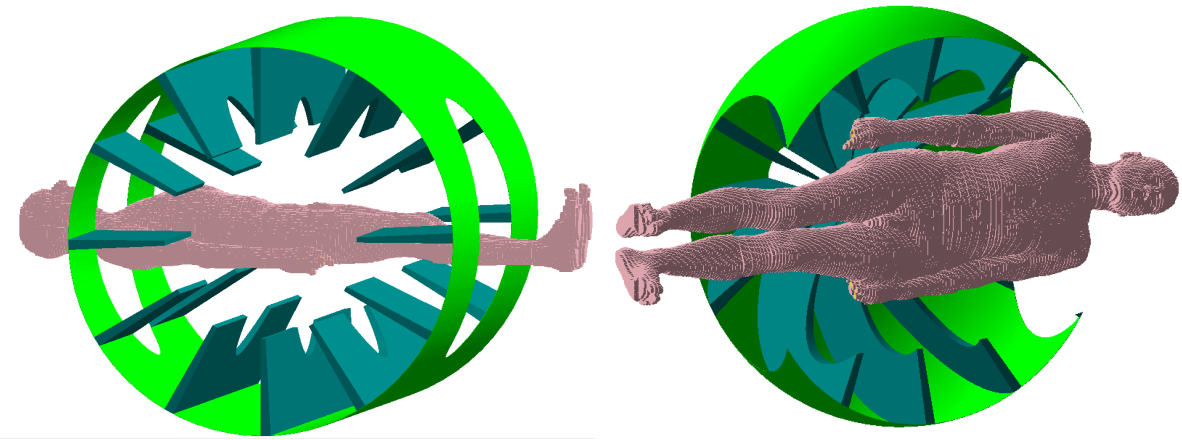

(a) Cylinder detector (b) Spherical detector

Figure 3.1 – Two versions of the detector layout with phi collimator. The human phantom from chapter 7 is placed perpendicular to the beam in an opening of the detector in which it could be moved relative to the detector. The collimator leaves are parallel to the beam axis, therefore in (a) the beam enters the phantom from the side and in (b) from the front if the hemisphere is placed in forward direction.

containing 10 mg/ml of gold. It is placed in the center of a cylinder detector with a radius of 600 mm and a length of 1600 mm with 3600 molybdenum collimator leaves extending radially outwards starting at a minimum radius of 300 mm and ending at the detector surface. The non-collimated part of the detector on the cylinder covers is not read out for the gold K_α fluorescence analysis here because it accumulates an unnecessary of background. The phantom is then irradiated centrally with a spherical beam of 1 mm diameter using $1.3 \cdot 10^9$ photons with 85 keV, so that a dose of 10 mGy is reached in the beam volume. In addition, the incident radiation is linearly polarized, which is usually the case for radiation sources using an undulator, such as synchrotrons. However, apart from the φ-asymmetry, which will be seen later on in the background pixel maps, e.g. in figure 3.9, the polarization is irrelevant for the sensitivity of the sphere if a large solid angle detector is used. The difference is smaller than the statistical error, therefore polarization is not required. A very similar detector design has already been published [36], although the Highly oriented pyrolytic graphite (HOPG) crystals used there are not used here. The proposed collimator design is used since for this general case there shall be no restriction upon the possible locations of fluorescence targets along the beam axis. If instead the aim is to only measure a possible signal from a previously known location inside a phantom, other collimator layouts may be more beneficial, see section 4. Since the expected amount of fluorescence photons in large objects is rather small due to the high

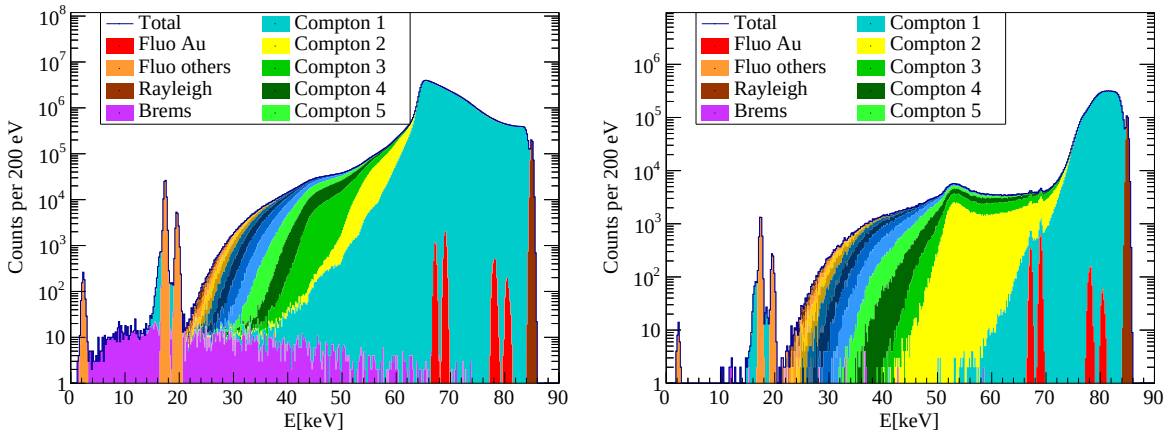

(a) spectrum of 4π detector

(b) spectrum of pixel selection

Figure 3.2 – Spectrum of a 30 cm sphere with a gold target in its center using a collimated 4π detector, similar data was published [44]. The multiple Compton background in the 4π spectrum in (a) is already reduced compared to the uncollimated spectrum in figure 3.3(a). In (b) the single Compton scattering is reduced using the pixel selection from figure 3.9(b) yielding a significance of $Z = 13$.

attenuation, the detector solid angle should, simply put, be as large as possible. Therefore, every detector element is able to detect fluorescence photons from anywhere along the beam axis. Using molybdenum as collimator material is an almost arbitrary choice and it can be replaced by other materials available. However, due to its high density ($\rho = 10.28\,\mathrm{mg/cm^3}$) and its medium position in the periodic table with an atomic number of $Z = 42$, its absorption coefficients are sufficiently high. Furthermore, it is mechanically processable, affordable and has no own fluorescence signal anywhere near gold, which could disturb the measurements. The choice of these values and the possibility to choose other detector shapes will be justified in the next section 4.

In figure 3.1, there is an illustration of the described detector layout with a human model inside and two additional holes for head and feet, that are not included for these simulations using only a spherical phantom. The resulting spectra of this setup are given in figure 3.2, where on the left the full detector is read out yielding an insignificant signal of $Z = 1.5$ and on the right an optimal pixel selection is used for the spectrum increasing the significance to $Z = 13$ with a statistical error of only 2%. This increase is made possible by a reduction of the background by a factor of 780 by discarding 70% of the detector pixels. The 96% share of Compton1 photons in the signal background is reduced to 20%, making Compton2 the most relevant remaining

background contribution with 45%. Note, that the actual amount of background reduction depends on the size of the remaining detector solid angle. For a remaining detector size of 40%, the background reduction is rather a factor of 500, but the resulting significance is almost the same. Therefore, the reduction ratio varies between different simulations. Moreover, it obviously depends on the detector layout used as a starting point, especially the minimum radius of the covers on the cylinder that are not shielded by a collimator. Considering a detection limit of $Z = 3$, this translates to a minimum detectable concentration of 2.3 mg/ml or a minimum mass of 1.2 µg. This concentration is below the reported 3.9 mg/ml, which Manohar et al. reported in a tumor bearing mouse [39]. Therefore, if similar concentrations can be obtained by human patients, millimeter-sized tumors could be detected using this detector setup.

The color codes used for the spectra throughout the thesis mark the signal fluorescence, other fluorescence lines, such as molybdenum from the collimator at 20 keV and the different Compton scattering orders. A photon marked with *Compton i*, has performed exactly *i* Compton scatterings between its creation and entering the detector. Additional elastic scatterings are not counted for this case. In order not to overload the legend box, not every Compton scattering order marked in the spectrum is explicitly listed, but they are added to the stack in increasing order, therefore a clear identification is still possible. The remaining color mark events, such as bremsstrahlung abbreviated with *Brems* or Rayleigh scattering, which implies photons originating from the X-ray source that did not perform any Compton scattering. Since only photons are used as incident particles in this thesis, bremsstrahlung is not an important process because it is only created from electrons created by ionization processes. Without color coding or looking at very low energies, for instance 10 keV, this process would not be visible at all.

3.2 Reduction of Higher Scattering Orders with a Collimator

The most significant restraint on the sensitivity, especially with large objects, is (multiple) Compton scattering. Single Compton scattering could simply be eliminated using an incident energy high enough to make it energetically impossible for the photons to lose enough energy to reach the gold K_α signal energy, if the Doppler effect is neglected. The filtering of higher

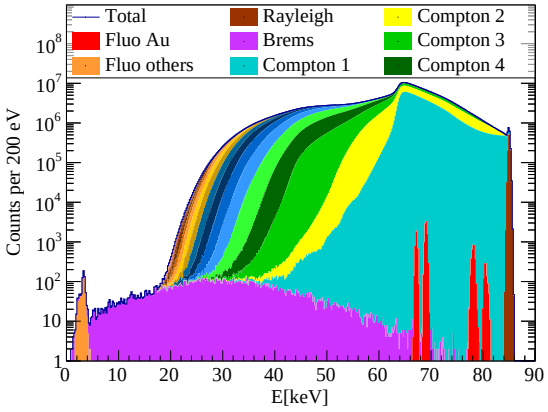

(a) 4π spectrum without collimator

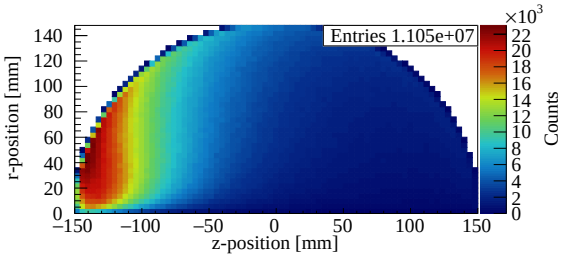

(b) Compton 3 distribution

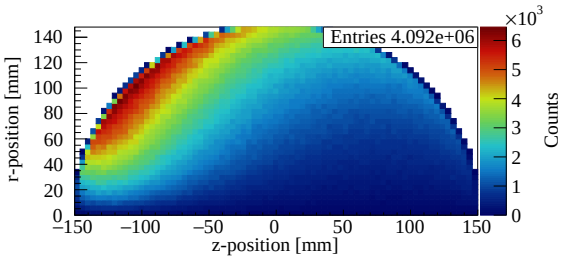

(c) Compton 4 distribution

Figure 3.3 – (a) shows a spectrum without a collimator. In (b) and (c) the last scattering event before reaching the detector within $68 \pm 2\,\text{keV}$ close to the K_α fluorescence of gold for triple and quadruple scattered photons is illustrated. The beam enters the phantom from the left at $r = 0$ and $z = -150$.

Compton scattering orders is made possible because the mean distance to the beam axis increases for each scattering, see for example table 3.1. The position of the last scattering event before reaching the detector is crucial to understanding the collimation effect quantitatively. Since the photon moves to the detector in a straight line from this point, the mean angular difference to radially orientated planes, such as the collimator leaves, are higher on average. In figure 3.3(a) there is a spectrum of an uncollimated detector showing a lot more multiple scattered photons than the collimated spectrum from figure 3.2. Likewise, the bremsstrahlung counts also decrease by a factor of 7 when using this collimator because they are created all over the phantom from ionized electrons. Nonetheless, their share of the total counts in the spectrum is negligible. In (b) and (c) positions of the last scattering event for triple and quadruple scattered photons is shown. There it is clearly visible that for the third scattering event, the positions move farther away from the beam axis. In table 3.1 the actual reduction is listed per scattering order together with the mean scattering distance to the beam axis.

The starting point of choosing 3600 collimator leaves is derived from calculating the Field of view (FOV) between two collimator leaves, as it has been done in previous work of this

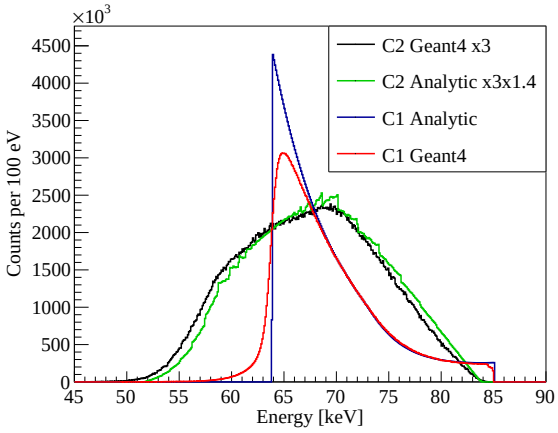

(a) Comparison of analytic spectra with analytic model

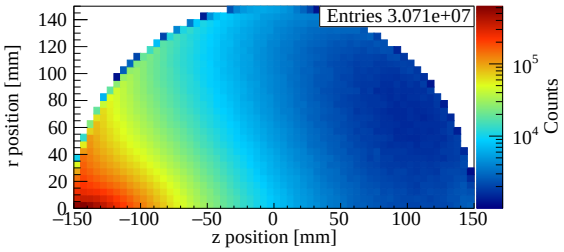

(b) sim. Compton 2 distribution

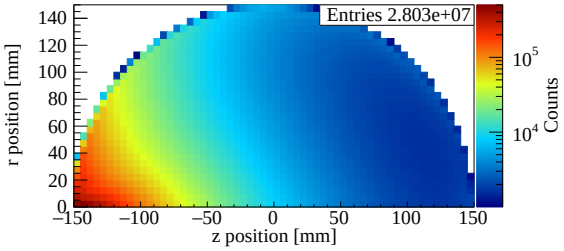

(c) ana. Compton 2 distribution

Figure 3.4 – For $1.3 \cdot 10^9$ photons with 85 keV the C1 and C2 part of the simulated spectrum without a collimator is compared to an analytic model. Note that the analytic C2 plot is scaled. In (b) and (c) the last scattering event for double scattered photons in 68 ± 2 keV is plotted once simulated and once calculated using eq. (3.3) as an analytic model.

group [90] using

$$r_{\mathrm{FOV}} = \frac{r_{\max} r_{\min} \sin\gamma}{r_{\max} - r_{\min}} \tag{3.1}$$

with the collimator's minimum and maximum distance from the beam axis $r_{\max}$ and $r_{\min}$ and the opening angle γ between two leaves. This opening angle is the product of the leaf separation angle β and the gap-to-segment ratio, which is set to 0.9 in order not to cover too much detector surface. The relevant values for this calculation are sketched in figure 3.5(a).

To validate the Compton scattering distributions, which is a key point for this thesis, in more detail, a simple analytic model is presented. Analytic in this sense means using no random numbers. After dividing the phantom into a grid of voxels, the amount of scattered photons can be calculated by multiplying the transmission values $T_{i \to j}$ between the X-ray source, the scattering positions and the detector with the integrated Klein-Nishina cross sections. For the integration, the limits are set so that the resulting photon energy reaches a previously defined interval based on the scattering angles. The product is then summed over all possible scattering

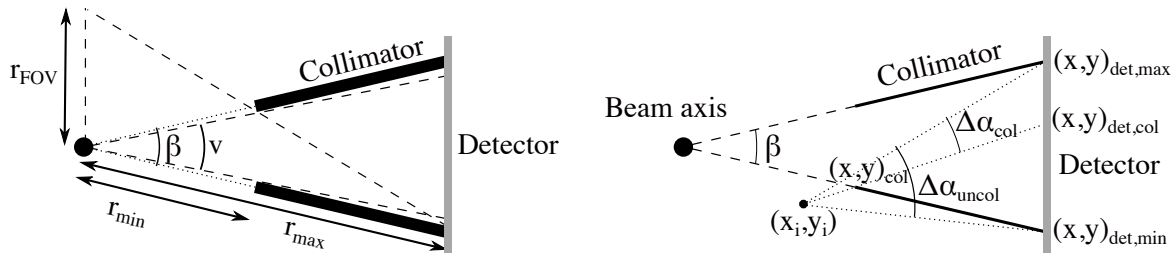

(a) Calculation of r_{FOV} in eq. (3.1)

(b) Calculation of $\xi_(x_i, y_i)$ in eq. (3.12)

Figure 3.5 – The sketches illustrate the relevant values for the analytical geometric calculations used for the collimator. Only two collimator leaves are plotted perpendicular to the drawing layer with a separation angle of β and the gap angle of γ in between. As a simplification, in (b) the leaf thickness is neglected and the possible detection angle α for an arbitrary scattering position (x_i, y_i) is illustrated.

positions:

$$N_{\mathrm{C1}}(r,z) = \sum_{z_1} \left(T_{0\to 1} \cdot C_1 \cdot T_{1\to \mathrm{Det}}\right) \tag{3.2}$$

$$N_{\mathrm{C2}}(r,z) = \sum_{z_1,z_2,r_2} \left(T_{0\to 1} \cdot C_1 \cdot T_{1\to 2} \cdot C_2 \cdot T_{2\to \mathrm{Det}}\right). \tag{3.3}$$

These models were discussed in my master's thesis up to scatter order 3 [49]. However, especially for higher scattering orders they lack speed and for more complicated geometries flexibility, which simulation tools like Geant4 offer. Therefore, these models are only used for isolated cases. In figure 3.4(a) the single and double scattered background in the spectrum, see fig. 3.3, are compared to these analytic calculations showing good agreement. The analytic spectra are specifically calculated with eq. (3.2) and (3.3) for different detected photon energies thus for different Compton scattering angles. Each bin in the spectrum represents one such energy interval for the calculations. Note that for single scattering the Doppler effect in the simulations blurs the otherwise sharp edges at the 180° scattering. For double scattering the analytic model is scaled by 1.36 to the simulated values, which is attributed to a lack of precision, i.e. too large voxels. Using smaller voxels will improves the result, but the calculation time scales with $t \propto L^{-}3$ with the voxel length L. For the spatial distribution of the scattering locations in figure 3.4(b) and (c) detected on the cylinder jacket, the absolute difference in counts in the gold signal energy region is only 10% and the mean difference per pixel is 7%. The estimation of the number of detected fluorescence photons in rather straightforward. By multiplying the transmission from the source to the target with the fluorescence

yield using NIST [47] values and the transmission to the detector, one obtains 14570 ± 121 K_α photons assuming Poissonian statistics. The spectrum in figure 3.3 shows 14704 photons in comparison. Therefore, both agree within their statistical errors.

A very simple mathematical model shall be employed to aid in the comprehension of the collimation effect starting with two leaves only. For this, nothing but simple trigonometry and linear equations are necessary. With the gap angle γ between the collimator leaves, the inner collimator radius r_{col} and the detector radius r_{det} which equals the outer collimator radius, the corresponding corner points of the collimator leaves can be calculated.

$$y_{\mathrm{det,min}} = -r_{\mathrm{det}} \sin(\gamma/2) \tag{3.4}$$

$$y_{\mathrm{det,max}} = r_{\mathrm{det}} \sin(\gamma/2) \tag{3.5}$$

$$x_{\mathrm{det}} = r_{\mathrm{det}} \cos(\gamma/2) \tag{3.6}$$

$$x_{\mathrm{col}} = r_{\mathrm{col}} \cos(\gamma/2) \tag{3.7}$$

$$y_{\mathrm{col}} = -r_{\mathrm{col}} \sin(\gamma/2) \tag{3.8}$$

The x coordinate is parallel to the normal of the detector chip and y is parallel to the chip surface. In figure 3.5(b), the geometry is sketched. Note that $y_{\mathrm{det,min/max}}$ are not the corner points of the detector chip but of the detector area in between the collimator leaves. Thus for each pixel (x_i, y_i), the minimum y-position on the detector chip accepted due to the lower collimator leaf can be calculated using the linear equation

$$y_{\mathrm{det,col}}(x_i, y_i) = \frac{y_{\mathrm{col}} - y_i}{x_{\mathrm{col}} - x_i} \cdot r_{\mathrm{det}} + \left(y - \frac{y_{\mathrm{col}} - y_i}{x_{\mathrm{col}} - x_i} \cdot x_i\right). \tag{3.9}$$

Using this, full uncollimated detector angle and the reduced detector angle due to the collimator leaf are calculated.

$$\Delta\alpha_{\mathrm{uncol}} = \arctan \frac{y_{\mathrm{det,max}} - y_i}{x_{\mathrm{det}} - x_i} - \arctan \frac{y_{\mathrm{det,min}} - y_i}{x_{\mathrm{det}} - x_i} \tag{3.10}$$

$$\Delta\alpha_{\mathrm{col}} = \arctan \frac{y_{\mathrm{det,max}} - y_i}{x_{\mathrm{det}} - x_i} - \arctan \frac{y_{\mathrm{det,col}}(x_i, y_i) - y_i}{x_{\mathrm{det}} - x_i} \tag{3.11}$$

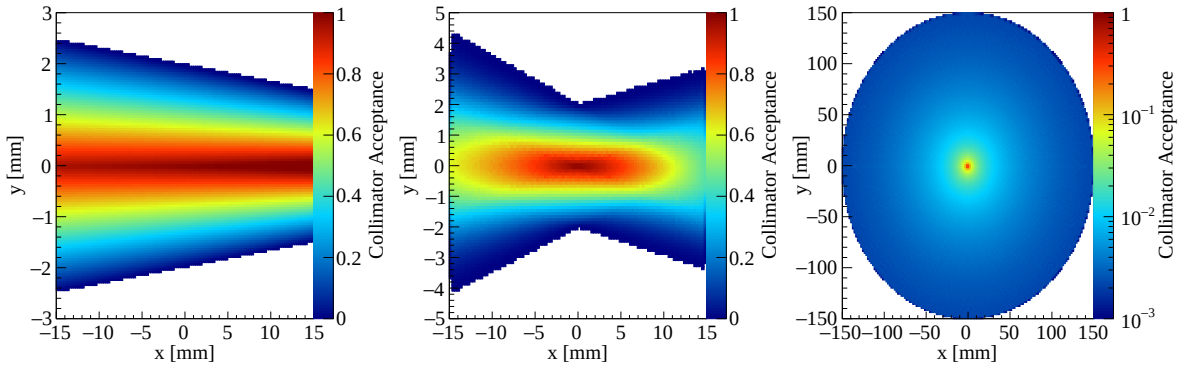

(a) Using 2 leaves (b) Using 21 leaves (c) Using 3600 leaves

Figure 3.6 – Analytic field of view of leaf based collimators using eq. 3.12, where the beam is supposed to be in the origin parallel to $\hat{z}$. (a) illustrates the FOV of only one detector element between two leaves, in (b) 21 leaves are combined for a Hexitec detector used in section 9.2.1 and in (c) the full solid angle is covered representing a 4π collimator.

The collimator acceptance value ξ is then obtained using

$$\xi(x_i, y_i) = \begin{cases} 0 & y_{\text{det,col}}(x_i, y_i) \geq y_{\text{det}} \\ 1 & y_{\text{det,col}}(x_i, y_i) \leq -y_{\text{det}} \\ \Delta\alpha_{\text{uncol}}/\Delta\alpha_{\text{col}} & \text{otherwise} \end{cases} \tag{3.12}$$

with $\xi = 0$ meaning that there is a complete collimator so that no photon reaches the chip and $\xi = 1$ meaning that there is no collimation effect at all.

Due to mirror symmetry there is $\xi(x_i, y_i) = \xi(x_i, -y_i)$. By looping over all pixels (x_i, y_i) the collimator acceptance map can be calculated. If more than two leaves are employed which usually is the case, the new map for n leaves can be obtained by adding n copies of the two-

Table 3.1 – Relative reduction of Compton scattering orders in the gold K_α-fluorescence region $E_{K\alpha} \pm 600\,\text{eV}$ using a collimator with 3600 leaves compared to an uncollimated detection. The second line gives the mean distance to the incident beam for the last scattering position, from which the photon moves to the detector in a straight path. In the last column the sum of all background photons is compared.

	C1	C2	C3	C4	C5	Total
relative reduction	1.5	25.6	104	171	198	2.4
Mean Scatter Distance[mm]	0.47	36	66	84	94	

leaves case rotated by the separation angle β and dividing the result by n. In order to avoid numeric artifacts due to the rotation in a Cartesian histogram it is helpful to use a high resolution for calculation and combine bins for smoothing the histogram later. The collimator acceptance ξ is shown in figure 3.6 for the simple case of just 2 leaves, for a small array of 21 leaves suitable for a small detector, such as a Hexitec, and for a 4π detector with the corresponding collimator and detector radii.

This model of course makes several simplifications. First, it assumes the collimator leaves to be perfect in a way that every photon touching them is absorbed and there is no scattering. Second, Rayleigh scattering is ignored because only Compton events are considered, which is not a dominant process in air or soft tissue for the photon energies involved. Third, scattering outside of the phantom in the experimental apparatuses is ignored which would allow a photon to come from the side and bypass the collimator. Fourth, isotropy for the possible photon paths from the last scattering event till the detector is assumed. The validity of this simplification depends on the size of the phantom.

When applying these simple geometric calculations to the scattering distributions obtained from Geant4 simulations, a very good match is obtained. This is done in figure 3.7 for the first three scattering orders. The drop of counts for C1 at $r = 0.5$ can simply be attributed to the beamsize. Without the possibility of additional elastic scattering, there would be no counts at all originating outside the beam volume. This is also the reason for the deviation of the collimation effect being slightly better for C1 in the simulations than in the analytic calculations. Photons that perform an additional elastic scattering afterwards also increase their collimation probability, which is not considered in the calculated curve. The analytic calculation starts at 1.1 at $r = 0$ due to the gap-to-segment ratio of 0.9. From here the slope increases until it becomes almost linear for radii larger than twice the beam radius. For larger radii around $r = 100$, the collimation effect in the simulations is smaller than calculated analytically. The reason here is the attenuation of the phantom. If in the simulations a point source is placed at the same position without a phantom, the calculated value matches the simulated counts. However, due to the large phantom size, the assumption of an isotropic emittance of scattered photons into the detector from this point is wrong. Even if an isotropic scattering is assumed, the probability of a photon taking the shortest path out of the phantom is higher than moving all the way back through the center and exit on the other side. Therefore, the photons scattering here, preferably leave the phantom on the shortest path. In addition, the collimation effect in this direction is smaller because starting at the scattering position the opening between the collimator leaves nearby is of course larger compared to collimator leaves farther away.

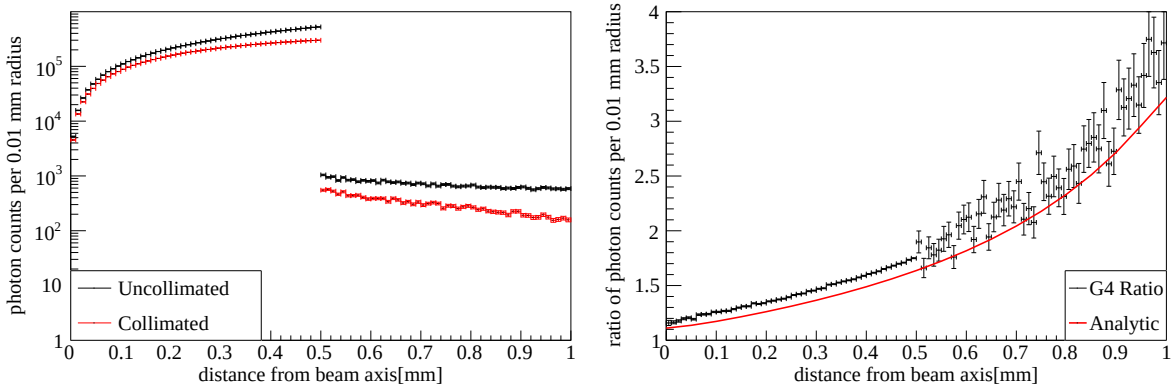

(a) C1 distribution of scattering points

(b) C1 collimation ratio

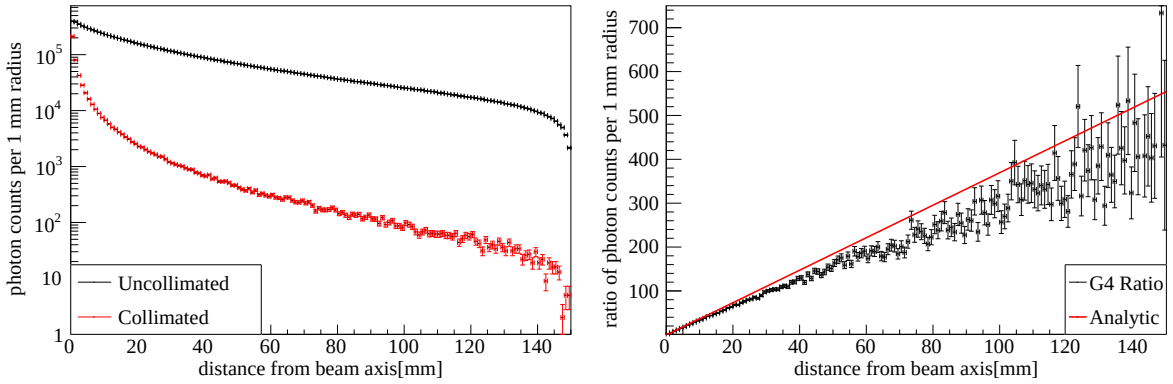

(c) C2 distribution of scattering points

(d) C2 collimation ratio

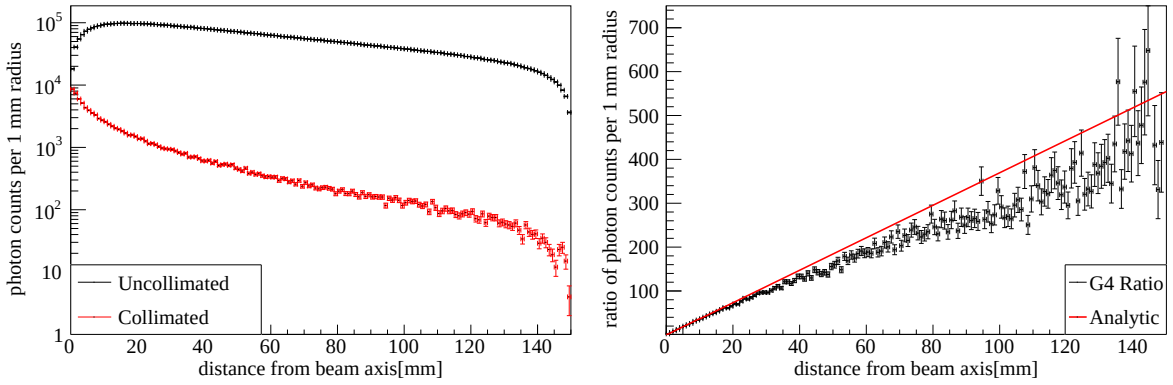

(e) C3 distribution of scattering points

(f) C3 collimation ratio

Figure 3.7 – For the first three Compton scattering orders, the absolute number of counts regardless of the energy for an uncollimated and a collimated 4π spectrum is shown on the left. On the right the relative reduction obtained by the ratio of the plots in the left column is plotted.

3.3 Reduction of Lower Scattering Orders with Pixel Selection

3.3.1 Operating Principle of the Pixel Selection

For XFI scans with large phantoms, large solid angle detectors are necessary to compensate for the high attenuation of fluorescence photons in the phantom. However, for a highly anisotropic background or signal distribution, it becomes helpful to not use the full detector information, even if it means losing signal photons. In figure 3.8(a) the anisotropy of the K_α background is plotted separately for different Compton scattering orders. There it can be seen that the amount of anisotropy depends strongly on the scatter order. Due to the amount possible of scatter angle combinations, the prominent shape of C1 becomes more and more blurred with each scattering until it approaches isotropy. For C1, the two local maxima can directly be assigned to the necessary scattering angles calculated with eq. 2.6 to lose enough energy from 85 keV to coincide with the $K_{\alpha 1/2}$ energies of gold. Besides scattering throughout the phantom length of 30 cm in the beam and less probable scattering in the air before and after the phantom, those peaks are also broadened by the Doppler effect due to the electrons Because of the Doppler effect due to the electron's momenta, they are broadened. This anisotropy makes it apparent, why a full solid angle detection is not the best case for these parameters since the background differs by over three orders of magnitude, which is due to the large share of single Compton scattering. Without a collimator, the almost isotropic higher orders, like the plotted third or fourth order, dominate the background, so that a pixel selection based on the background alone becomes pointless. Of course, one might propose to also reduce the first order scattering in order to use the full solid angle for detection, but this involves other drawbacks. A higher incident energy, for example, reduces the fluorescence cross section and increases the probability for higher scattering orders simply because more scatter angle combinations are energetically possible to enter the signal energy interval. Collimators could also reduce first order scattering, but they would then also exclude certain possible target positions along the beam by blocking the fluorescence photons.

This anisotropy arises from the Klein-Nishina cross section itself, but also from the attenuation inside large phantoms. Therefore, for large phantoms the forward direction is shielded by the phantom itself, which makes the detection there more effective compared to smaller phantoms, which is also shown in section 5.1. The changes in solid angle for the detector pixels for

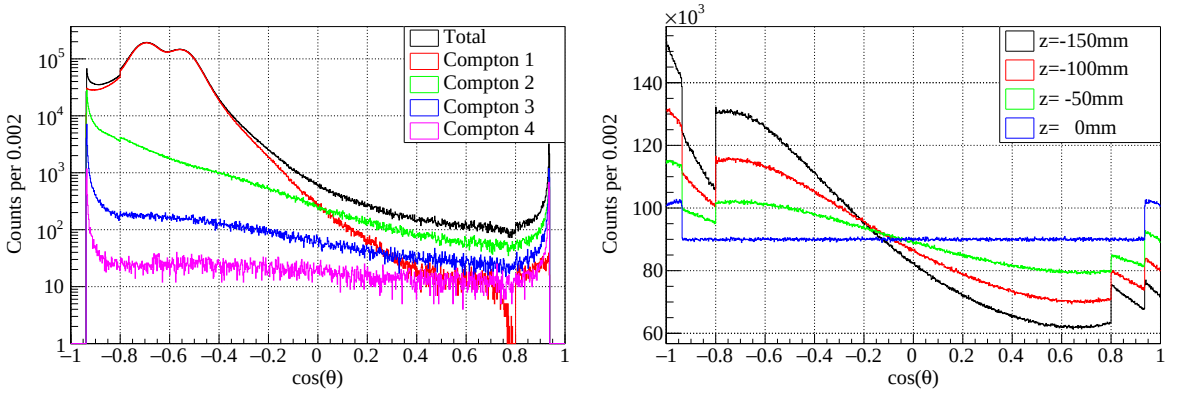

(a) Anisotropy for Compton background

(b) Solid angle effects for different scattering positions

Figure 3.8 – In (a) the Compton background anisotropy for the K_α background with a collimated detector and 85 keV is shown. In (b) the effective change in solid angle for a translation of the scattering origin from 0 to −150 mm is illustrated using a detector with collimator. Note, that this effect has only a small contribution for the anisotropy in (a).

scattering positions with an offset from the center of the detector is shown in figure 3.8(b). Since for every photon, the actual size ratio of the detector pixels depends on the scattering position, which are more likely to be in the first part of the phantom due to the attenuation, this also contributes to the background anisotropy. Nonetheless, even for the beginning of the phantom at $Z = -150\,\text{mm}$, this effect only yields a factor of 2 compared to the three orders of magnitude shown in (a). The steps in the plots can be attributed to the geometry of the detector. At $\cos(\theta) = \pm 0.8$, there is the transition from the cylinder jacket to the cylinder so that the orientation of the pixel elements changes by 90° and the collimator only covers the part between $\cos(\theta) = \pm 0.9$ resulting in a 10% step.

The determination of a solid angle that yields the highest possible sensitivity for all possible signal and background photon distributions is not trivial. For small phantoms, the idea of optimal detector positioning is frequently discussed. To name a few examples without claim of completeness, Busch et al. [35] investigated a 30 cm diameter phantom with different detection angles for gold K_α and K_β-fluorescence but failed to reduce the multiple Compton background. Sjölin et al. [91] discussed ideal detection angles using a 10 cm phantom for a collimated detector with gold K_α and K_β and even included other fluorescence elements. Ahmad et al. [92] proposed to use larger detection areas for optimization of the detector setup and and determined some θ ranges for a specific parameter combination. Even so, they did not develop a method to actually determine the optimal detection area for arbitrary parame-

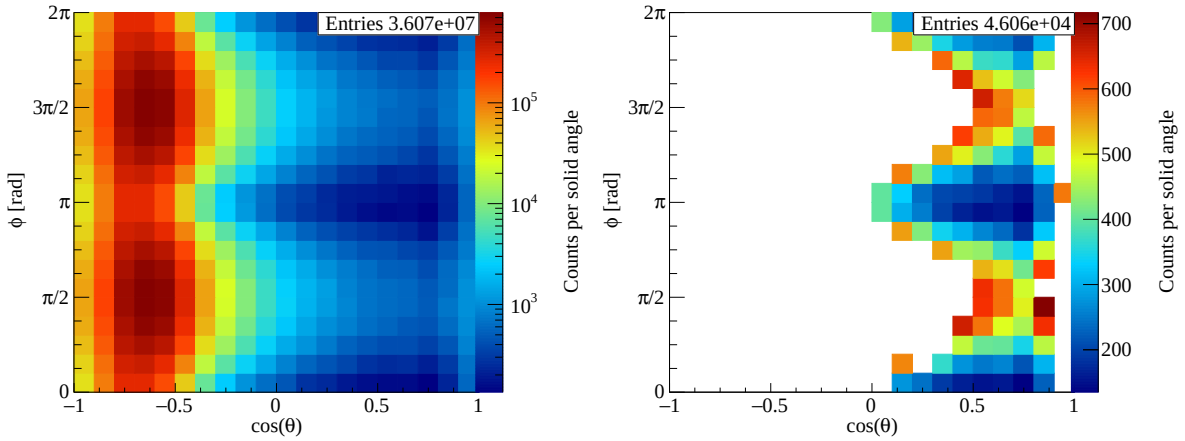

(a) Full solid angle K_α background

(b) K_α background for optimal pixel selection with 61% of the pixels discarded

Figure 3.9 – For the collimated spectrum in figure 3.2, the K_α background photon distribution is shown for the full solid angle in (a) and for the optimal selection in (b). Thus, the highest significance is already achieved for a detector covering less than half of the solid angle. The white pixels here are removed from the algorithm including all their detected photons. The asymmetry in φ results from a linear polarization of the incident beam. Similar data was published [44].

ters or to make sure how close their proposed area is to the actual optimum. Instead, *"These θ ranges were [...] tuned in a trial-and-error approach. [They] took this approach because strict optimization of θ is a difficult task"([92] p.1123).* In this thesis a simple method to achieve this without any previous knowledge based only on the data alone is proposed. To the best of my knowledge, similar methods have not been applied to XFI before. Instead, almost all available literature about medical XFI deals with small detectors with a size not larger than a few centimeters because these detectors have been commercially available for decades and proposed experiments can be performed today. Detectors covering the whole solid angle are usually just an outlook for optimization and not treated in detail.

For the example case of the 30 cm phantom shown in figure 3.2 with the corresponding signal background distribution figure 3.9, the full solid angle spectrum does not yield a significant signal. If the solid angle is segmented into, e.g., 16x16 pixels, no single pixel would yield a significant signal either. Therefore, it is not possible to determine the amount of fluorescence pixels in one pixel without large errors. To find the optimal combination of pixels it is not possible to check every possible combination by brute force, since for 16x16 pixels there are $\binom{256}{1} = 256$ possibilities to choose one pixel, $\binom{256}{2} = 32640$ to choose two and $\sum_k \binom{256}{k} = 10^{77}$

possibilities to choose an arbitrary subset.

The basic approach to solve that problem is to start with all available pixels. Next, the supposedly worst pixel is chosen and its data deleted. This is then repeated until an optimum is found. The whole process is illustrated in more detail in figure 3.10. As starting points, all pixels are numbered consecutively with i and a combined significance Z is determined together with the χ^2 of the fit. According to section 3.3.2, it is determined which pixel is allowed to be removed in this step. Then, starting with the first pixel allowed to be removed, its data is temporarily removed and a significance of the remaining pixels $Z_{\not\ni i}$ is calculated. If the fit seems trustworthy, depending on its χ^2 value, it is checked, if the significance has improved. If yes, the new value Z_{opt} and the bin number j is saved. Then the same is performed for all N pixels. After that the pixel, which deletion yields the highest increase of significance, is deleted together with its data. If no such pixel is found or if the fits do not work properly, the pixel containing the highest background value is deleted. As a anti-noise condition, it turned out to be useful to delete isolated left over pixels, if all adjacent pixels are already gone. This is most likely only caused by statistical fluctuations. This procedure is then repeated until no pixel is left or until an exit condition, such as only 10% of pixels left, is reached. It is not advisable to stop right when one step yields no improvement, since the fits are not perfect and not always the right choice is made. After the process is finished, a plot of the significance can be made against the deletion progress, see figure 3.11, which can be smoothed to find a possible combination yielding the maximum significance. The resulting spectrum is then shown in figure 3.2(b) and the corresponding background distribution in figure 3.9(b). Note, that photon distribution is always subject to statistical fluctuations and the fit-based decisions of the algorithm are not completely accurate. Therefore, for instance, the single pixel left in 3.9(b) at $\cos(\theta) = 0.9$ is just a coincidence, which is probably gone for a repeated measurement or simulation. However, its impact on the summed significance is rather small.

It is not claimed that the presented algorithm is the only or necessarily the best way to achieve an ideal pixel selection. However, it is a very simple and robust method not used in XFI publications so far. A variation would be to use Adaptive Mesh Refinement (AMR) [93], but the underlying method is more or less the same. AMR temporally combines small pixels into fewer larger pixels to start with a coarse grid, which during the process is then refined where deemed necessary. It would, for instance, be possible to start with a grid of 2x2 pixels for which all possible 15 combinations could be analyzed independently. Next, each pixel is divided into 2x2 smaller pixels, so that there are 4x4 in total. If a significant signal is already found, the corresponding pixel selection can now be used as a starting point and one

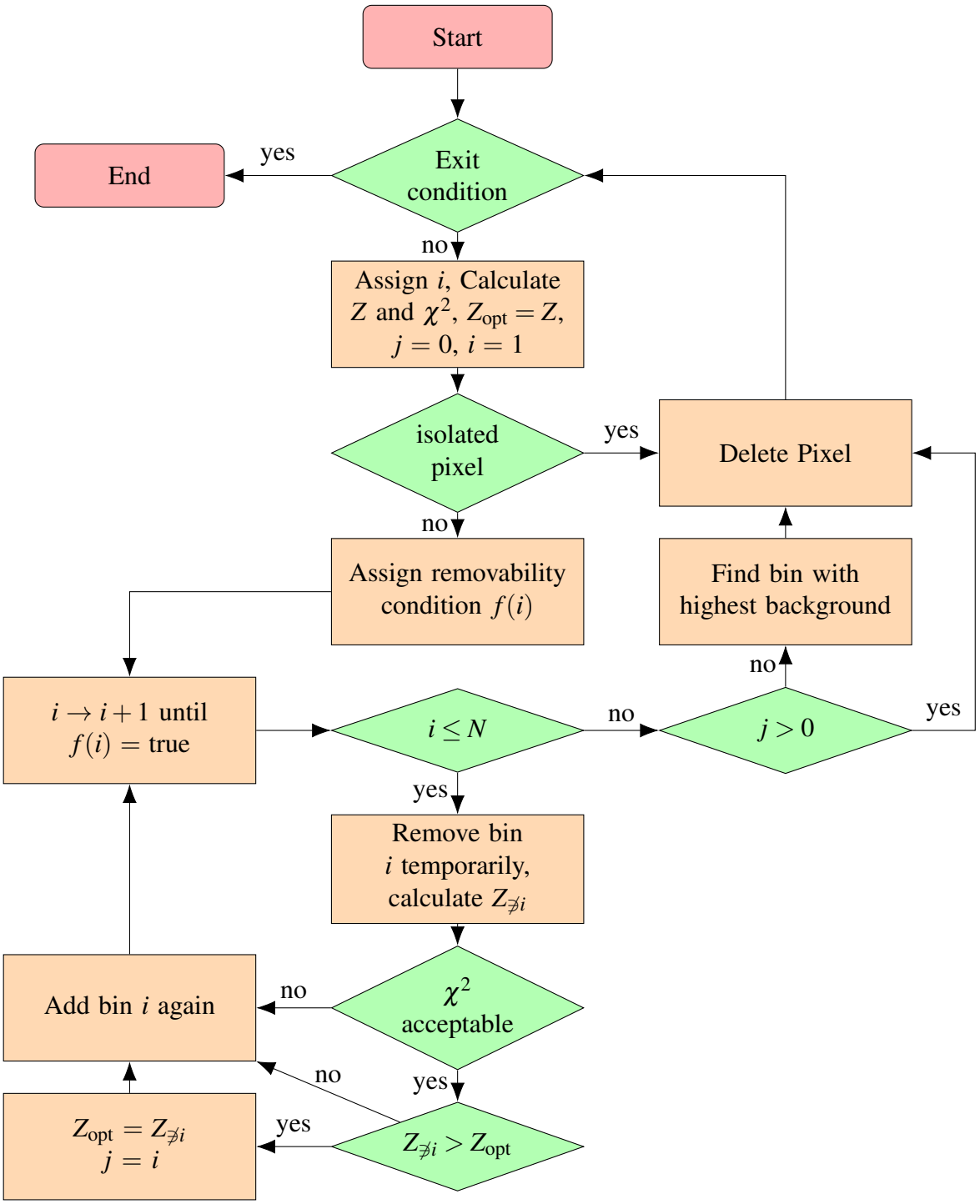

Figure 3.10 – This flow chart illustrates the pixel selection algorithm for large solid angle detectors. i is a running index for the N bins left, j is the index whose removal seems best and $Z_{\not\ni i}$ the significance of the remaining pixels without bin i.

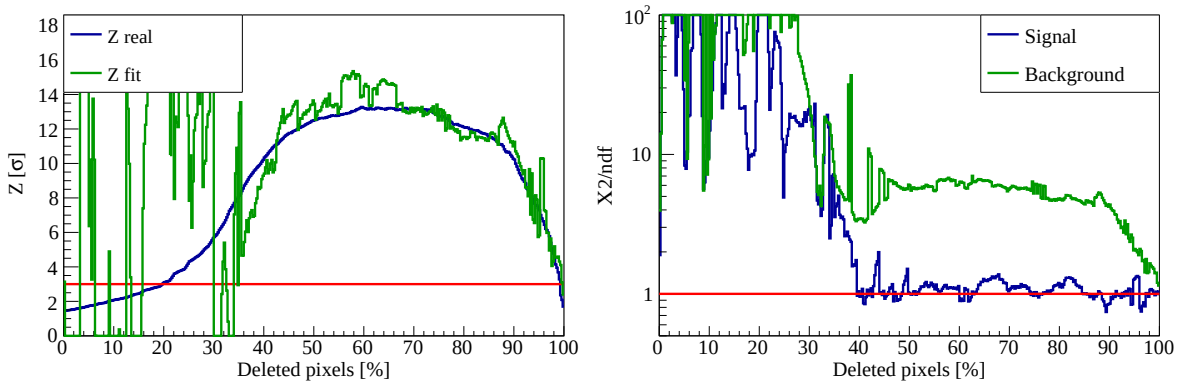

(a) Significance during the pixel selection process

(b) χ^2 during the pixel selection process

Figure 3.11 – Progress of the significances and χ^2 values for the pixel selection in figure 3.12. The significances from a fit are compared with the actual real values obtained from simulation. For the fits, two functions are tested: one containing a signal and one without. In (a) the horizontal red line marks the detection limit $Z = 3$ and in (b) the ideal value for the fit with $\chi^2 = 1$.

can concentrate on the border between the *good* and the *bad* pixels to add or remove pixels primarily there. The advantage of this method is, that the first result, if there is a signal at all, might be found very quickly. Then, the pixels are divided into smaller subpixels as often as it seems necessary. Once the errors, of the fitting parameters, are larger than the alleged improvement per step, it does not make sense to continue the division in smaller subpixels.

3.3.2 Parameter Choices

Fitting Finding a general fit function appropriate for any set of parameters is probably impossible because the shape of the spectrum largely depends on the incident energy, the detector layout, the collimator, the shape of the phantom and its rotation and translation towards the beam. Furthermore, removing pixels from the spectrum drastically changes its shape, too, as it is intended to remove as much background as possible. In figure 3.12, the differences in possible background shapes only due to different pixel selections can be seen. Therefore, if no zero measurement is available, a set of different fit functions is tried out until one reaches a previously set χ^2-limit, e.g. $\chi^2 < 2$. For this set, polynomials are used with the possible addition of an exponential function $f(x) = \exp(ax+b)$ starting with the lowest amount of fit parameters. Depending on the experimental setup and the set of parameters, these fit functions

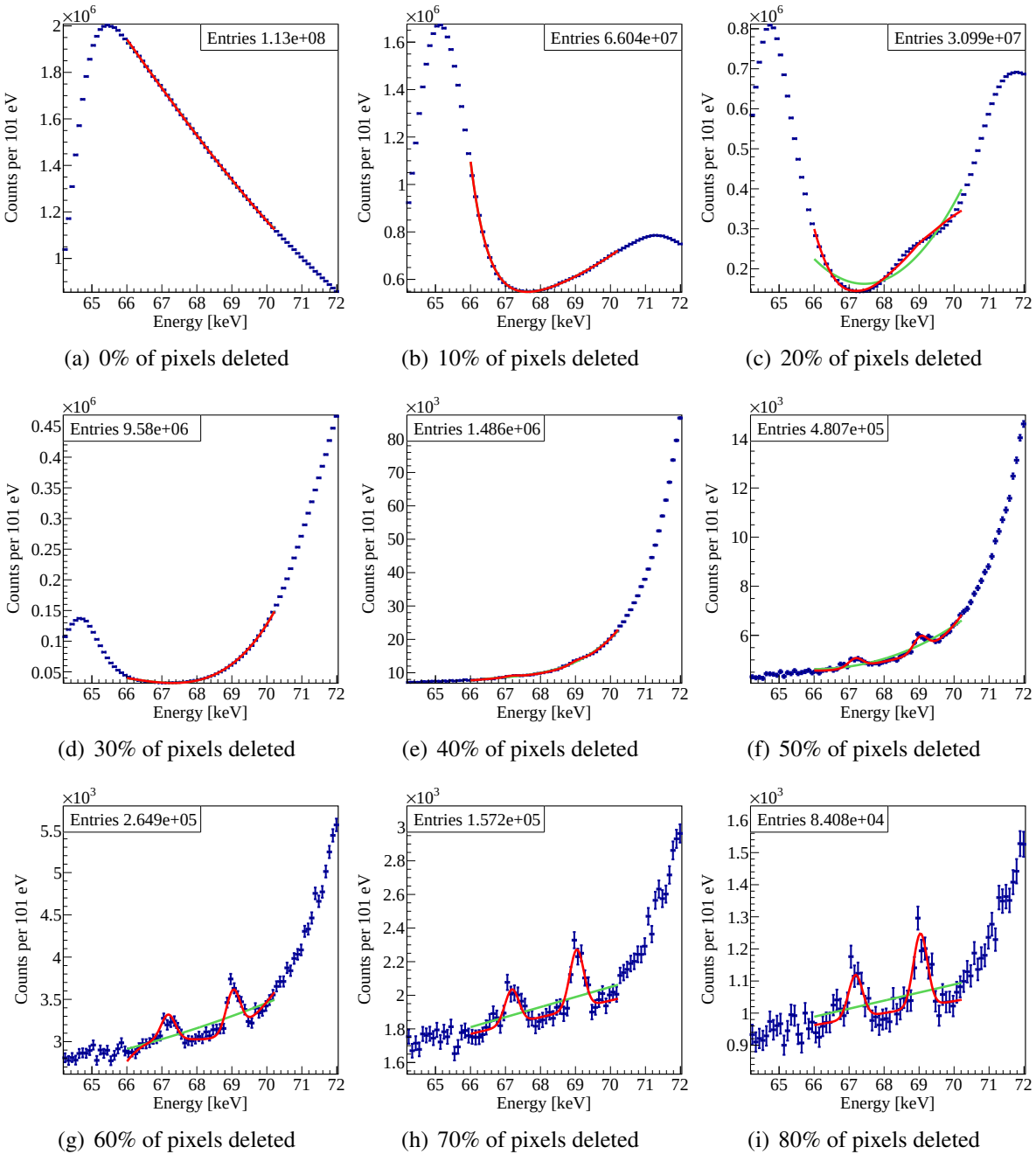

(a) 0% of pixels deleted (b) 10% of pixels deleted (c) 20% of pixels deleted

(d) 30% of pixels deleted (e) 40% of pixels deleted (f) 50% of pixels deleted

(g) 60% of pixels deleted (h) 70% of pixels deleted (i) 80% of pixels deleted

Figure 3.12 – Development of the summed spectrum for different stages of the pixel selection. In each histogram the corresponding fit function containing signal is plotted in red and the function without signal is plotted in green.

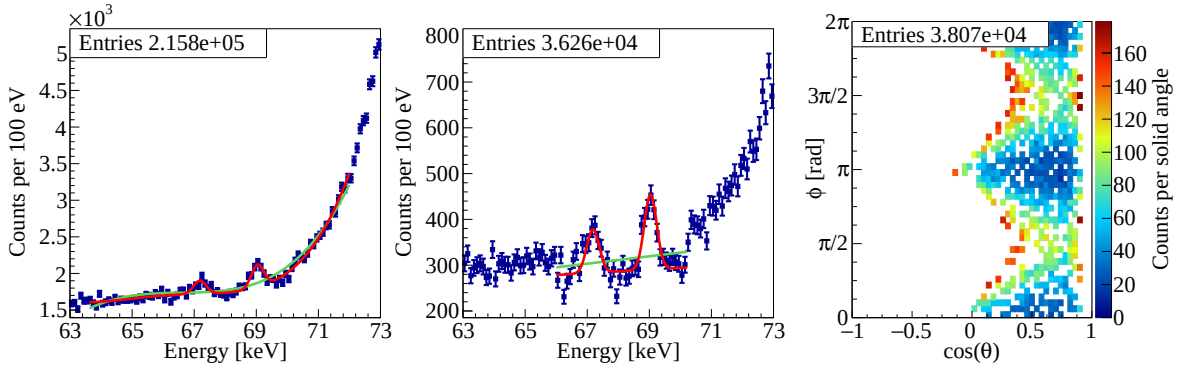

(a) Fit for 30% remaining pixels (b) Fit for 10% remaining pixels (c) Background for 26 % remaining pixels

Figure 3.13 – If no constraints are applied to which pixel may be removed, the algorithm yields maximum significance selection of pixels shown in (c). In reality there is no gold fluorescence present. The two peaks only arise from choosing background that looks like a signal. For (a) and (b) the alleged significances are $Z = 12$ and $Z = 15$ with $\chi^2_{\text{red}} = 1.2$ and 1.7 for the red curve.

have to be adjusted accordingly. If for example lead is used somewhere as a radiation shield, lead fluorescence peaks might have to be added to the background fit function. Although at first glance, the fit seems to describe the data well in figure 3.12(a)–(c), their χ^2 values in figure 3.11 show that the alleged number of fluorescence photons and thus the calculation of the significance, is not really reliable because of the high statistics. The resulting small statistical error bars cause even small relative deviations of the fit function resulting in a bad fit.

Avoiding False Signals There are several ways, this algorithm can lead to a wrong result. First, inappropriate fit functions can result in wrong assumptions of signal and background counts per pixel which could lead to missing a small signal completely. Moreover, it can also cause an overestimation of the signal, which can even be the wrong assumption of the existence of an actually non-present signal. Especially the latter is always a possibility since the algorithm can just choose pixels, in which there is a random accumulation of counts that looks like a signal, but it is actually not. Second, even if the true information obtained from the simulations is used or the fits work perfectly, random fluctuations due to low statistics of either signal or background photons can cause a non-physical increase of the signal. Such an example is shown in figure 3.13, where actually no gold is used in the simulations. The combination of pixels, that just seem to contain a signal, creates an illusion of a signal with a false significance of up to $Z = 15$. For the symmetric setup, it is obvious that the chosen

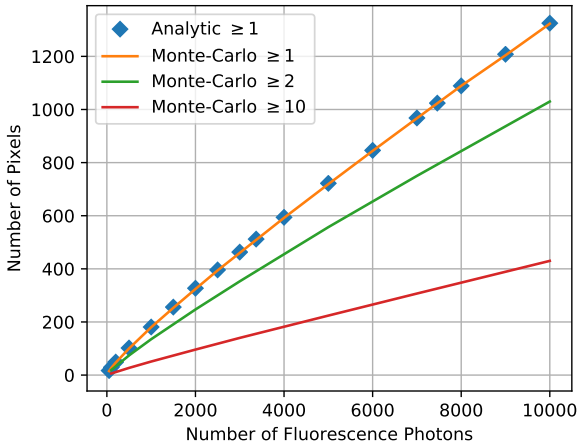

Figure 3.14 – For different numbers of randomly distributed fluorescence photons, the minimum number of pixels is calculated, so that each contains at least n photons in 50% of the cases. For $n = 1$, a Monte-Carlo calculation is compared to analytic calculations with eq. (3.14) showing full agreement. Besides, for 2 or 10 fluorescence photons, only the Monte-Carlo values are given.

combination of pixels for the data analysis in (c) has to be influenced by the statistics. The algorithm chose pixels that contain a disproportionate amount of photon counts exactly where the gold signal would be expected. In (b) for a smaller range of the fit function, the algorithm additionally lowers the background close to the false fluorescence lines. Especially at 70 keV, there is almost a step in the spectrum between the range considered for the pixel selection and the surrounding spectrum. To avoid wrong decisions based on errors in the fit or decisions lead by low statistics, it is, therefore, helpful to impose some constraints on the parameters of the pixel choice.

Upper Limit for Number of Pixels For the use of the pixel selection algorithm, it is not reasonable to use as many detector pixels as possible because the photon statistics is limited. Ideally the difference in the amounts of signal and background photons from one pixel to the next is larger than the statistical error and based on different attenuation or the angle-dependent Klein-Nishina cross section (2.4).

To make a very basic assessment of the choice of an upper limit for the number of detector pixels, the variation of the significance from one pixel to the next is considered. Since for an animal or human phantom, the amount of signal photons is expected to be a lot less than the

number of background photons, the statistical fluctuations of the signal photons are considered. For this, isotropy of the signal photons throughout the detector pixels is assumed. By generalizing the inclusion-exclusion principle [94]

$$p(A \cup B) = p(A) + p(B) - p(A \cap B) \tag{3.13}$$

for the addition of probabilities from two events to an arbitrary amount of events, the probability to get empty pixels (meaning no signal photon) is calculated using

$$p(\exists \geq 1 \text{ emptybin}) = \sum_{i=1}^{n-1} (-1)^{i-1} \binom{n}{i} \left(\frac{n-i}{n}\right)^k \tag{3.14}$$

for the number of pixels n and the number of photons k. In order to avoid empty pixels, p is set equal to 0.5 and eq. (3.14) is solved for the number of pixels. The result is shown in figure 3.14. To compare those values with the example of the 30 cm sphere with 2.3 mg/ml and 10 mGy with $Z = 3$, there are approximately 2200 fluorescence photons detected if using a collimator. Hence, the choice of more than 350 pixels would result in the existence of pixels without any fluorescence photons at all.

Constraints on the Removability of Pixels Besides the upper limit on the number of pixels, more conditions have proven useful to avoid false signals. First, for most cases it is not reasonable to keep single pixels containing data, when every surrounding pixel has already been deleted. Most likely, it would only be a statistical coincidence that it is kept because it a background fluctuation is misinterpreted as a signal. This argument can be expanded to a small number of connected pixels. If such a connected set below a preset size is found during the algorithm, these pixels shall be removed. Second, the opposite is usually not reasonable either, which means taking away single pixels when they are completely surrounded by pixels that are still used for the optimal pixel set. Even if a condition is applied, that at least one neighbor already has been removed, the shape of the remaining pixel can still look like there are tunnels drilled in from various sides. Although with inhomogeneous phantoms it might be possible to create cases, where this might be justifiable, it is usually not. In practice it has been useful to impose the conditions that at least two or three adjacent pixels, including those at the corners, are already removed. Besides stabilizing the algorithm and decreasing the chances of false signals, the performance speed increases if not every pixel left has to be tested for its effect on the significance in every round. As a starting condition all pixels can

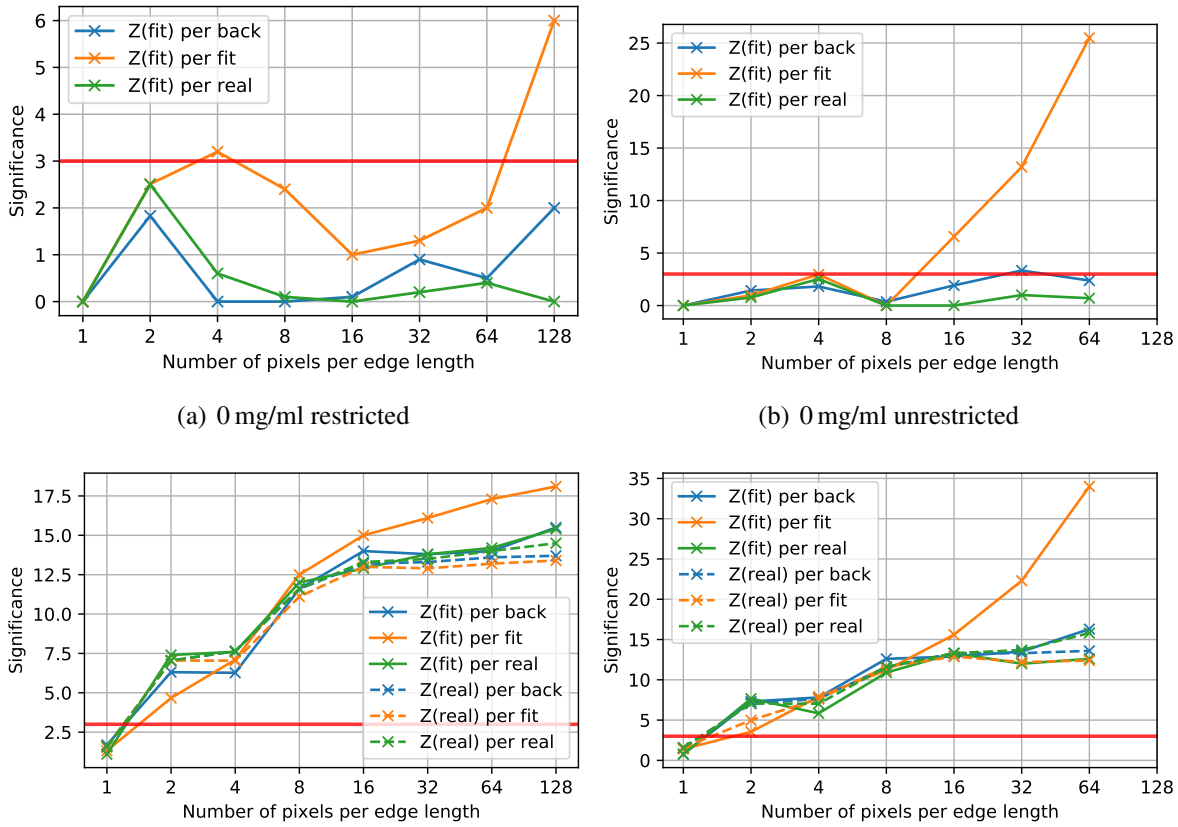

(a) 0 mg/ml restricted

(b) 0 mg/ml unrestricted

(c) 10 mg/ml restricted

(d) 10 mg/ml unrestricted

Figure 3.15 – For $1.3 \cdot 10^9$ incident photons, the pixel algorithm is applied to a different number of bins with and without gold present. For the restricted algorithm, besides the starting conditions, only pixels with at least 3 missing neighbors are allowed to be removed. Note that the fluctuations of the curves is based on the random spatial distribution of the counts and the calculated detector response using random numbers. The horizontal red line marks the detection limit of $Z = 3$.

then generally be removed if they are at the edge of the detector, which is in this case $\theta = \pm 1$ or at the openings for human phantoms to fit in. Furthermore, the pixels, where the maximum of single Compton scattering is expected due to the incident energy and the phantom position shall always be allowed to be removed.

In figure 3.15, the effect of such restrictions is shown. If too many pixels are used and no constraints are applied, even for no gold at all, the pixel selection would yield a supposedly significant signal, which is wrong. Similarly even if real fluorescence photons are present in the spectrum, the signal can be falsely increased by choosing adequate bins with background

looking more like signal. When imposing conditions on the removability of pixels and limiting the pixels to, e.g. 16x16, the error on the simulation containing gold is about 10% and the simulation without gold would be insignificant.

3.4 Reconstruction of Tracer Positions

For the spatial reconstruction of the Region Of Interest (ROI) containing the high-Z elements, several methods are possible. The scanning method used in this thesis using a pencil beam only yields a projection of the measured significances, but not the depth along the beam. Only with the knowledge of the 3D-position and the inner composition of the scanned object, the actual amount of fluorescent material can be reconstructed.

A very common method called X-ray Fluorescence Computed Tomography (XFCT) employs the reconstruction methods commonly used in CT [95]. The disadvantage of this method is clearly, that for every additional direction scanned, the sensitivity per scan decreases proportional to the square root of directions due to reduced statistics if the total applied dose should be constant and the phantom is scanned completely in each direction. Sometimes even up to 360 different directions are used for scanning [96]. Work performed in our group showed that up to 8 directions should be sufficient for most cases [97]. Furthermore, it is not necessary to scan each direction completely but only the ROI.

Another frequently used approach is the use of collimators in front of the detector that limit the FOV for different parts of the detector that have to be read out independently. The collimator types are described in more detail in the next chapter. A possible choice are parallel collimator sheets perpendicular to the beam. However, this method limits the detector area that can be used for the reconstruction of each point, but no further rotations of the phantom are necessary. The collimators could also be oriented in such a way, that the whole detector area only detects photons from one part of the beam axis. Some authors also use pinhole type collimators [98, 99], that use the *camera obscura effect* to project an inverted image of the phantom onto a pixelated detector.

A further approach is taken by Vernekohl et al. [100] by using a Compton camera. In this detector layout the target position is reconstructed by using two detector layers. The inner layer consists of a silicon detector in which the fluorescence photons only scatter once before

they are absorbed in the outer layer. By using the position of both energy depositions and calculating the scattering angle based on the deposited energy, a photon path is reconstructed.

If the amount of fluorescence photons can be detected in different directions and the inner geometry is known, their origin can also be calculated, which was also described by our group [101]. Although for small phantoms this approach seems promising, it poses problems for the large phantoms in this thesis because the required solid angle for the significant detection of a signal are larger. Besides the restrictions for the use of a pixel selection, a signal would need to be detectable in various parts of the detector despite the anisotropic background.

A completely different method that requires no additional dose but a detector system that can detect both energy and arrival time of photons is discussed in section 10.1. Although such detectors with the needed precision in both energy and time are not available (yet).

4 Variation of Collimator Parameters

Collimators can be immensely helpful for XFI because of the reduction of unwanted Compton background they provide. The already introduced collimator with leaves parallel to the beam axis, called *phi collimator*, allows the detector to measure photons from the whole beam axis without any prior knowledge. For such a collimator type, which is the basis of this work, some parameter variations are performed in this section. However, if the condition that the detector shall be able to measure fluorescence from the whole beam axis is dropped, some alternative basic collimator types are possible that are common in the SPECT community [102] and used throughout the XFI community.

All simulations in this chapter are performed for the 30 cm sphere made out of soft tissue with a 1 mm sized target in the middle containing 10 mg/ml of gold. The incident photons have a monoenergetic energy of 85 keV and the beam diameter is set to 1 mm without any divergence.

4.1 Overview of Collimator Geometries

The properties of four basic collimator types consisting of an array of sheets, which are called leaves here because they are not necessarily flat, are briefly summarized.

First, the collimator leaves could be orientated parallel to each other and perpendicular to the beam axis, this will be called *parallel collimator* here, which appears many times in the literature, e.g. [103–105]. Although it has to be stated, that they all apply it to a sheet beam geometry instead of a bin beam, which potential offers a faster scanning procedure. In figure 4.1(c) a sketch is shown. For the parallel collimator design, each detector segment measures a different part of the beam axis. So if a signal is measured, the complete coordinates are given instantaneously because the pencil beam already restricts two coordinate axes and the parallel

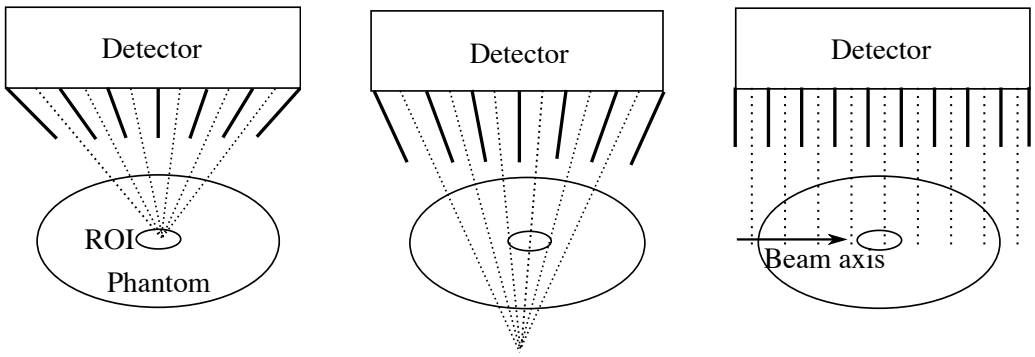

(a) Focusing Collimator (b) Converging Collimator (c) Parallel Collimator

Figure 4.1 – Sketches of the described collimator types. In (a) each detector element images the same part of the beam axis. If the beam axis is from left to right, this type is called theta collimator. For a beam axis perpendicular to the drawing, it is a phi collimator. In (b) the focus of the line of sights lies behind the beam axis. In (c) each detector element segmented by parallel collimator leaves images a different part on the beam axis.

detector leaves restrict the third. However, the big disadvantage of this system is the limited statistics since the detector area that could detect signal from a target is reduced strongly.

Second, the collimator leaves could be perpendicular to $\hat{e}_\theta$ in spherical coordinates, which will be called *theta collimator* and it is shown in figure 4.1(a). The theta collimator usually has the highest significance since all detector segments are aligned to the same position along the beam axis. This collimator type has already been used for XFI by our group and others [90, 91, 106]. If the alignment is perfect and there is no further target material outside the FOV, this collimator yields very high sensitivities because a high fraction of the background including single Compton scattering can be filtered while maintaining most of the signal photons. The clear disadvantage is, however, that for unknown target positions along the beam, the phantom has to be moved several times in the direction of the beam axis in order to scan the whole target area. To stay below a dose maximum, it has to be reduced for each individual spectrum taken which reduces the sensitivity and the scan itself becomes more complicated because the phantom now has to be moved in all three directions.

Third, a medium version between both is possible with the leaves tilted slightly inwards, this shall be called *converging collimator*, see figure 4.1(b). If a ROI smaller than the detector (otherwise the leaves would be diverging) is known inside a larger phantom, such as a specific organ, the leaves can be oriented in such a way, that they cover the whole ROI but not more. This is done by moving the focus point beyond the beam axis and place the outer leaves in

such a way, that their elongation touches the border of the ROI. The FOVs from the detector elements now overlap, but some spatial information can still be reconstructed.

Fourth, a *diverging collimator* is conceivable, if a ROI larger than the detector shall be mapped within a phantom. For this collimator type, the collimator leaves open towards the phantom instead of closing. However, this type will not be discussed further because small detectors are not sensitive enough for XFI with human-sized phantoms.

4.2 Phi Collimator

If the full solid angle is covered, the actual shape of the geometry does not have much influence on the resulting sensitivity. Here two very simple rotationally symmetric shapes, a sphere and a cylinder, are used and compared for different sizes. In figure 3.1 both shapes are shown with a reduced number of collimator shapes and a human phantom inside. In order for the human phantom to fit inside including head and feet, two extra openings with a radius of 30 cm are inserted into the detector as well as the collimator leaves in the middle of the detector perpendicular to the beam. For a detector with a radius of 600 mm, which is the standard radius used in this work, both openings reduce the detector surface and consequently reduce the solid angle by approximately 6%. Moreover, the collimation effect around the opening is impaired due to missing parts of the collimator leaves. Due to this issue, the significance deteriorates by 11% for an unpolarized incident beam with a spherical phantom. If polarization is available, the deterioration factor is between 7 and 21%, depending on whether the openings are in the polarization plane or perpendicular to it. However, considering the anatomy of a human phantom, for a detection in these parts of the detector, the attenuation of the fluorescence photons would be maximum anyway.

4.2.1 Variation of Detector Size

For the standard 30 cm phantom, there needs to be a free space of twice the phantom's diameter around the beam, otherwise it would not be possible to move the phantom arbitrarily in the beam. Therefore, initially the collimator leaves are built with a minimum radius of 300 mm and the detector radius is chosen as twice that size. The cylinder length is set to 1600 mm because then the cylinder jacket, for which the collimator works best, covers exactly 80% of

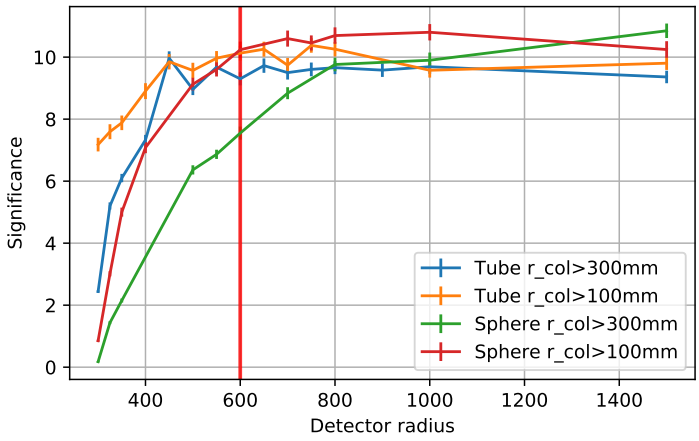

Figure 4.2 – Variation of the detector size for a cylinder and sphere detector with a phi collimator of 3600 leaves for 10^9 incident photons with 85 keV. For both detector shapes, the collimator and detector leaves start once at $r_{\text{col}} = 100\,\text{mm}$ and once at 300 mm distance from the beam axis. The chosen radius of 600 mm is marked with a vertical red line.

the solid angle and both cylinder covers at the beginning and end of the detector both make up the remaining 10% each.

In figure 4.2, the detector radius is varied for the 30 cm soft tissue phantom with a 1 mm target sphere in its center with 10 mg/ml of gold. For the cylinder detectors and the sphere detector with longer collimator leaves, larger detector radii than 60 cm yield no further improvement. It has to be kept in mind that the actual detector surface and therefore, the potential cost would scale with the radius squared. Concerning smaller detectors, the collimation effect decreases. Because the leaves are shorter, photons scattered farther away from the beam axis can still reach the detector without being collimated. Furthermore, the detector solid angle decreases due to the two openings for the human phantom which sizes are fixed. This is especially the case for the spherical detector, whose solid angle reaches zero at 30 cm detector radius. A smaller inner collimator radius does not change much for the cylinder detector apart from detector radii close to 30 cm because for that value the collimator with the same inner radius becomes quasi non-existent. Regarding the spherical detector, however, it is helpful to extend the collimator leaves closer to the beam axis because especially in forward and backwards direction, a larger share of the sphere is shielded by the collimator. In total, for the chosen standard radius of 60 cm in this thesis, the cylinder detector can be replaced by a sphere if the collimator leaves extend further to the beam axis without the loss in sensitivity. As long as the detector is shielded by the collimator, the actual shape of the detector is of

minor importance.

4.2.2 Variation of Number of Collimator Leaves

A crucial parameter for the detector layout is the number of collimator leaves, which is varied in this section for two different beam sizes with a fixed gap-to-collimator-segment ratio of 0.9. The phantom's material is water instead of soft tissue, but the attenuation coefficients are very similar as shown in figure 2.1(a) in the beginning. Besides the desired resolution of 1 mm, a larger beamsize of, e.g. 1 cm, could be used for different purposes. These include quick pre-scans with reduced dose to search for potential ROIs in the phantom that could subsequently be scanned with higher resolution. A larger beam could detect lower tracer densities for targets larger than 1 mm because incident photons can be used for the same dose per beam volume. Or for X-ray sources that do not intrinsically have a pencil beam, larger beam sizes can yield higher photon fluxes and therefore decrease the measurement time. However, it must be kept in mind that the spatial resolution is defined by the beamsize, therefore a 1 cm incident beam lowers the spatial resolution accordingly.

In figure 4.3 the number of collimator leaves is varied for both beamsizes. For the 1 mm beam, 3600 leaves are close to the optimum and for 1 cm 360 leaves are ideal. This can be well explained using the geometric eq. (3.1) for the FOV. For numbers of leaves below the optimum, the FOV is larger than the target in the beam and more photons scattered close to the beam axis are allowed into the detector. Once the FOV becomes smaller than the target, however, the fluorescence photons get blocked themselves. This is further shown in (c). At the optimal positions marked with the vertical red lines, both the numbers of fluorescence photons and of C1 photons begin to drop since both originate in the beam volume. For the 1 mm beam, the C1 share of the total detected counts increases from 60% for the uncollimated case to 99.7% for the collimator with 3600 leaves. It has to be noted, that the higher significance for the 1 cm case is misleading, because for this case there is 10^3 times more gold in the beam. Since the significance is proportional to the amount of gold per beam area, the significance values would need to be scaled down by a factor of 10 for direct comparison with the 1 mm beam. Therefore, for the same number of incident photons, the 1 mm beam is twice as significant because the filtering for higher Compton orders is more effective.

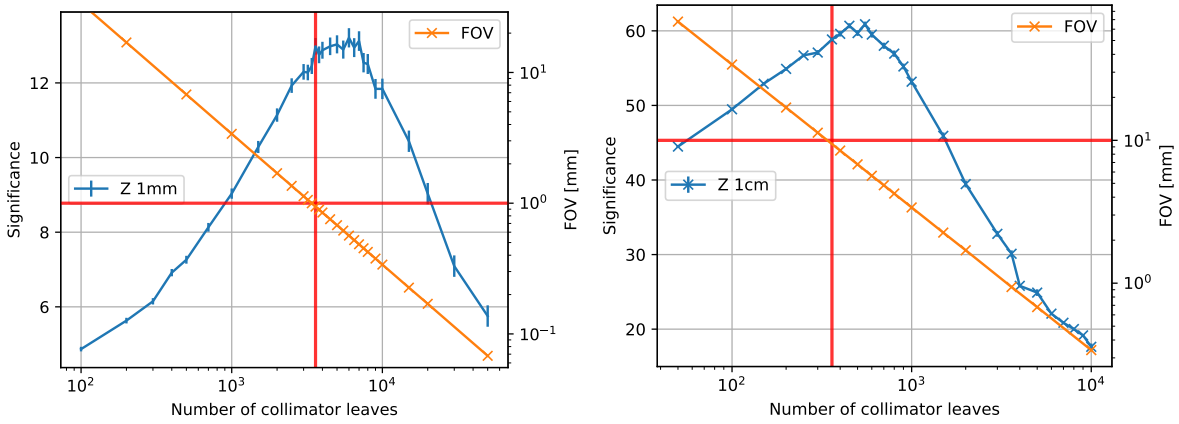

(a) 1 mm beam with 1 mm target with pixel selection (b) 1 cm beam with 1 cm target with pixel selection

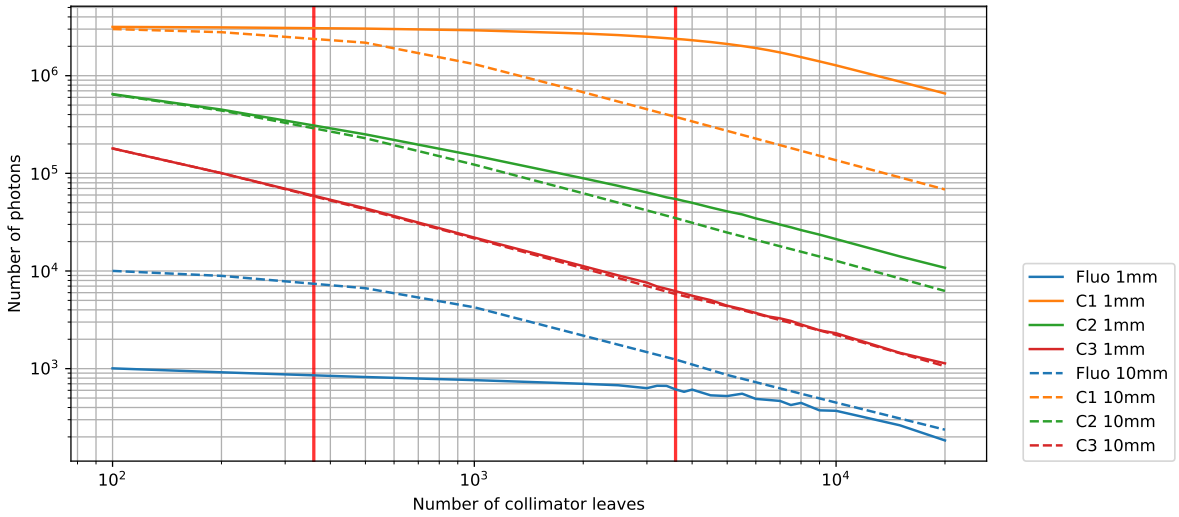

(c) Number of detected photons within $E_{K\alpha} \pm 600\,\text{eV}$ for 1e8 incident photons without pixel selection

Figure 4.3 – Variation of the number of collimator leaves for a spherical beam with 1 mm and 1 cm diameter with 10^9 incident photons and a gold solution target of the same size. The FOV is calculated using eq. (3.1) and the diameter of the target is marked with a horizontal red bar. The chosen optimum values of 360 and 3600 leaves are marked with vertical bars.

4.2.3 Variation of Collimator Leaf Thickness

The collimator's FOV in eq. (3.1) is not only determined by the number of leaves, but also by the collimator leaf thickness. The shape of the usual collimator leaves used in this thesis is defined as a part of the detector volume, which can be a sphere or a cylinder, with a minimal radius and the constraint to a phi-interval. Projecting its shape onto a plane perpendicular to

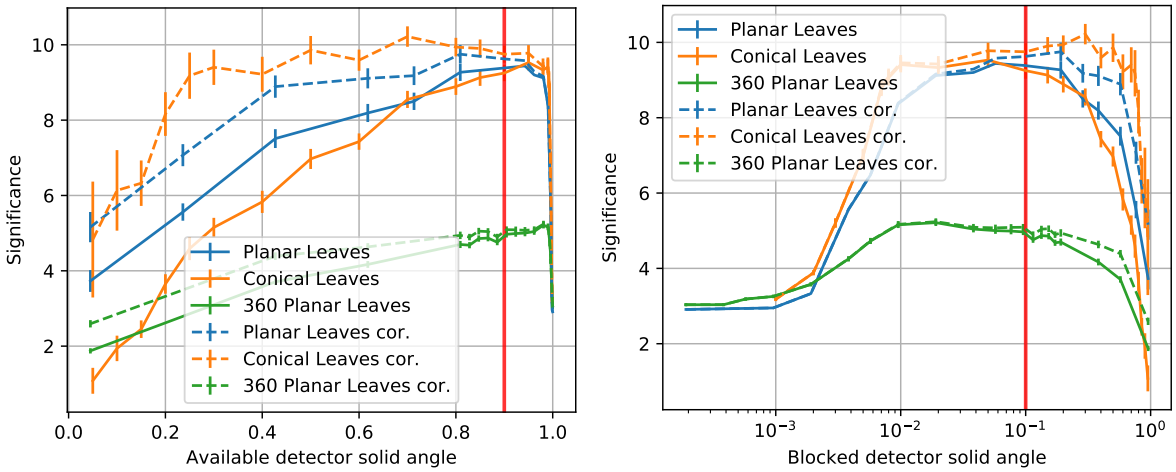

(a) (b)

Figure 4.4 – Variation of the collimator leaves' thickness for a planar collimator and a conical leaf shape for 10^9 incident photons. Both plots show the same data with a reversed x-axis. Blue and orange show 3600 leaves, whereas green shows only 360 leaves. The dashed plots are corrected for the solid angle blocked by the leaves. The chosen gap-to-segment ratio of 0.9 is marked by a vertical red line.

the beam axis the shape is therefore a circular sector with a minimal radius larger than zero. Initially, this conical shape was chosen for easier geometric estimations, but as shown here it can be replaced by planar sheets with the same thickness everywhere yielding the same significance. The planar shape is also used in the experiments in section 6.2.

In figure 4.4, the collimator leaf thickness is varied for both planar and conical leaves. For reasons of simplicity, issues of mechanical stability are not considered here. To compare both shapes, the planar leaf thickness is converted into the available detector solid angle using $1 - d \cdot N/(2\pi R_{\text{col}})$, which is the same as the gap-to-collimator-segment ratio. For the blocked detector solid angle, this value is simply subtracted from 1. As an example for the leaf thickness, a gap-to-segment ratio of 0.9 with 3600 leaves corresponds to a total thickness of 52 µm at the radius of 300 mm, where the collimator usually begins and extends until the detector radius of 600 mm. The conical leaf would then be twice as thick at its outer radius.

The gap-to-segment ratio of 0.9 seems to be a good choice since it yields maximum sensitivity for this simulation. The loss of 10% solid angle only decreases the significance to 95%, which can be neglected. Regarding smaller ratios, thus thicker leaves, the sensitivity decreases simply because the detector becomes more and more blocked. For a thickness of 523 µm,

the collimator leaves are then starting to overlap thus blocking the detector completely. For the dashed lines in figure 4.4, this loss of solid angle has been corrected, which shows a more constant progression of the curves. However, besides the decreasing solid angle for the detector, additionally the decreasing FOV plays a role for the loss of sensitivity by blocking fluorescence photons from the beam volume. At the opposite end of the plot, the collimator leaves become too thin, so that they simply do not absorb the scattered photons anymore. For gap-to-segment ratios larger than 99.8, for example, the leaves would be thinner than one micron. Besides the missing mechanical stability and producibility, the collimator becomes transparent and the significance turns into the same value as for the uncollimated detector.

4.3 Parallel Collimator

The parallel collimator design is used in some XFI literature for small phantoms, e.g. [103–105]. Although a spatial reconstruction along the beam axis would be possible and Compton scattering is decreased, the actual solid angle for the detector covering a possible target position along the beam axis is simply too small for large phantoms, if radiation dose is a limit. The spatial resolution along the z-axis can be estimated with $d_{\mathrm{col}} R_{\mathrm{det}} / (R_{\mathrm{det}} - R_{\mathrm{col}})$ with the variable detector radius R_{det}, the inner collimator radius $R_{\mathrm{col}} = 300\,\mathrm{mm}$, and the leaf distance $d_{\mathrm{col}} = 1\,\mathrm{mm}$. This yields 31 mm for $R = 310\,\mathrm{mm}$, 4 mm for $R = 400\,\mathrm{mm}$ or 2 mm for $R = 600\,\mathrm{mm}$. In figure 4.5, the resulting significances for different z-intervals along the beam axis are given. The calculated spatial resolutions fit the cut-off positions in (a) or the peak positions in (b). At detector positions outside these ranges, no further signal is expected. Consequently, for too large z-intervals, the significance has to decrease. Abiding by the dose limit of 10 mGy, a fluorescence signal from a 10 mg/ml gold sphere would not be significant, not even for spatial resolutions of a few centimeters. In figure 4.6 a spectrum is shown. Even for the depicted 10^{10} photons, which yield 80 mGy, only 138 fluorescence photons were detected which is the result of the effective detector solid angle of 0.2% for this case. Therefore, if the fluorescence target is not previously known to be close beneath the surface so that there are more fluorescence photons expected in the detector, this collimator is too insensitive for large phantoms and not used any further here.

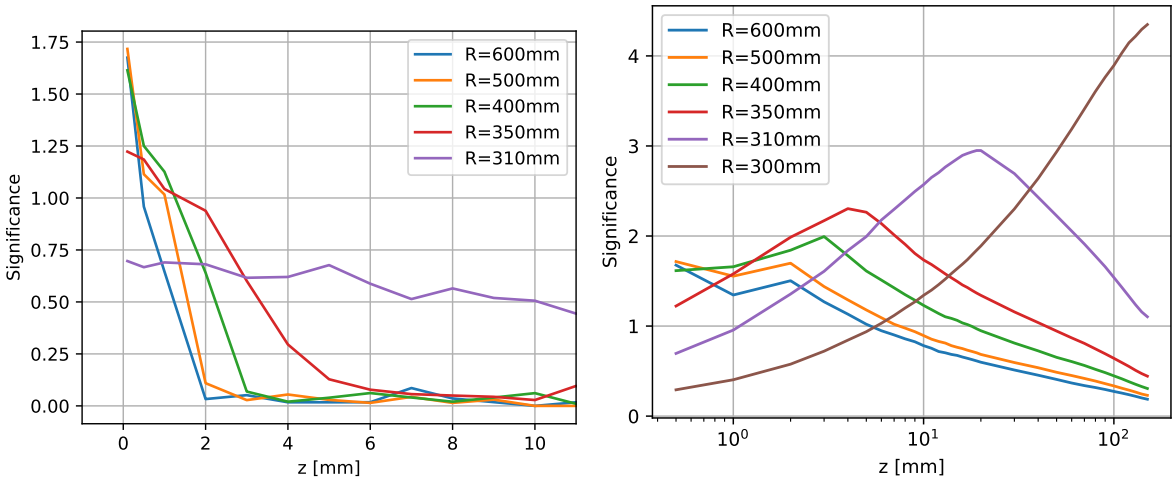

(a) Significance from $z-0.5\,\text{mm}$ to $z+0.5\,\text{mm}$

(b) Significance from $-z$ to $+z$

Figure 4.5 – A cylinder detector is equipped with parallel collimator leaves perpendicular to the beam axis for different detector radii (R). In (a) the significance for different detector elements between leaves is given and in (b) the data of detector elements is added up for different regions around the target. The data was simulated for 10^{10} photons and scaled down to 10 mGy.

4.4 Theta Collimator

A theta collimator allows the detector to only measure one part of the beam axis while blocking the rest. This expectedly yields the highest significance, since the detector solid angle is maximal apart from the blocking by the volumes of the leaves themselves and even single Compton scattering from the beam axis is mostly removed. In figure 4.6(b) such a spectrum yielding $Z = 28$ for 10^9 incident photons is shown. When combined with an additional phi collimator, which gives a combination of perpendicular leaves, the significance could even be increased to $Z = 67$. Despite these apparent high significances, this collimator has the disadvantage that the scanning has to be performed in a third dimension parallel to the beam, if the location of the fluorescence target is not known exactly before. First, this increases the complexity of the scanning, since even for a box of 10 cm length, already 10^6 different voxels of $1\,\text{mm}^3$ would need to be scanned for which the phantom has to be moved relative to the beam each time. Second, if dose is an issue, the number of incident photons for each scanning point has to be reduced such that the total dose adds up to the same value as if only one scan was performed using a phi collimator. Considering for example the 30 cm sphere with a scan through its center, 300 scanning positions would be necessary. If the dose is split

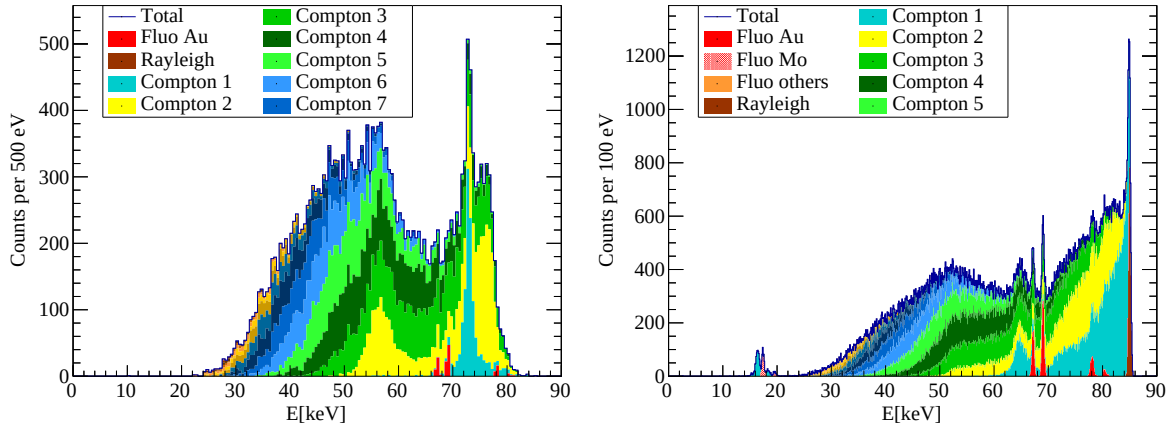

(a) Parallel collimator

(b) Theta collimator

Figure 4.6 – (a) shows a spectrum with the parallel leaves collimator and a detector radius of 600 mm yielding 2 mm resolution along the beam axis. For 10^{10} photons, the significance is $Z = 3.6$, which is only measurable under ideal conditions. (b) shows a spectrum with a theta collimator adjusted to the target position with 3600 leaves. For 10^9 photons, this results in a significance of $Z = 28$, which is almost three times more than for the phi collimator.

up evenly, the significance would be reduced by a factor $\sqrt{300} \approx 17$ resulting in an inferior method compared to the phi collimator. Consequently for large objects, this collimator type is not discussed further. If, however, a small ROI is determined previous to the scan, which could be a small organ, this type of collimator could be used to identify even smaller amount of tracer elements.

5 Simple Phantoms

In this chapter a very simple phantom is used: a homogeneous sphere consisting of soft tissue. Depending on the publication there are several soft tissue compositions available. Here the material refers to the definition by the International Commission on Radiological Protection (ICRP) [107] which is adapted by the Geant4 collaboration [67]. The 30 cm sphere used for many analyses in this thesis is also referred to as the International Commission on Radiation Units and Measurements (ICRU) standard sphere [108] in the literature, although the material composition differs slightly. Using the sphere as the most simple phantom shape possible, the effect of variation of size, energy, energy bandwidth or target located inside the phantom are studied in this section. If not explicitly mentioned otherwise, the cylinder detector layout described in section 3.1 is used throughout this chapter. The phantom is a 30 cm sphere with a 1 mm-sized gold target with a concentration of 10 mg/ml in its center which is placed centrally in a circular incident beam without divergence of the same size.

5.1 Variation of Phantom Size

A variation of the phantom radius immediately shows the difficulties for XFI with large objects. Besides the multiple Compton background, the important factor that cannot be prevented, unless with higher incident energies, is the attenuation of the incident beam until it reaches the target and the attenuation of the fluorescence photons afterwards. The product of both values yields an attenuation of over 99% for the 30 cm sphere. In figure 5.1(a) the significances are plotted against the phantom radius. The 4π plots are almost perfectly proportional to the product of ingoing and outgoing attenuation. At $r = 50\,\text{mm}$ the attenuation of the incident beam through the phantom is already over 80%. From there on until the considered maximum size of $r = 200\,\text{mm}$ the signal background stays practically the same because almost every incident photons has already scattered. So between these values the only thing

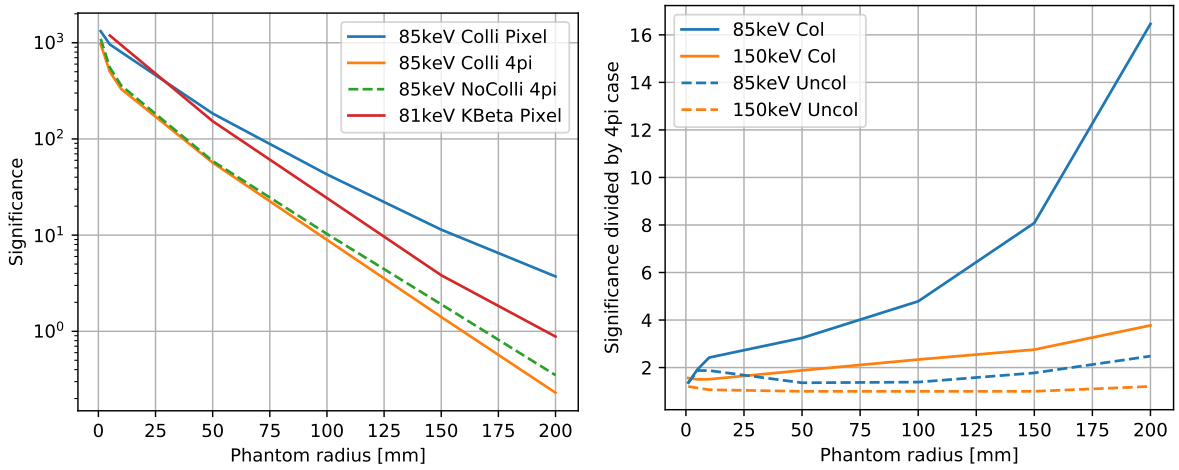

(a) Significance for various phantom radii

(b) Relative significance increase with pixel selection

Figure 5.1 – Variation of the phantom radius for 10^9 incident photons. In (a) the resulting significances for K_α using 85 keV and K_β analysis using 81 keV with a 4π detector or pixel selection are plotted against the phantom radius. For blue and orange, a collimator is used. In (b) the ratio of the significances using pixel selection versus 4π spectra is plotted for two different incident energies.

changing in the signal region is the amount of detected signal itself. The significance ratio between both radii is approx. 170 for the uncollimated 4π spectrum, which differs less than a factor of 2 from the simple product of both attenuation values. For smaller radii on the other hand, the background also plays a role because the amount of scattered photons from the incident beam decreases and thus the signal background becomes smaller.

The 4π spectra with a collimator are less significant than without. The reason is that the collimator eliminates approximately half of the fluorescence photons. In order for the significance to stay the same, the background would need to be reduced by a factor of four. Since the incident energy of 85 keV is close to the K-edge of gold, single scattered Compton photons can and do still reach the signal interval. For this incident energy, single scattered Compton photons are the dominant contribution to the signal background and they are not collimated better than signal photons because both arise in the beam volume. Therefore, a collimator alone does not increase the significance for low incident energies close to the K-edge of gold if no pixel selection is applied.

The significance using a pixel selection gains compared to the 4π spectra with increasing phantom radius. Whereas for a 10 cm phantom, the pixel selection increases the significance

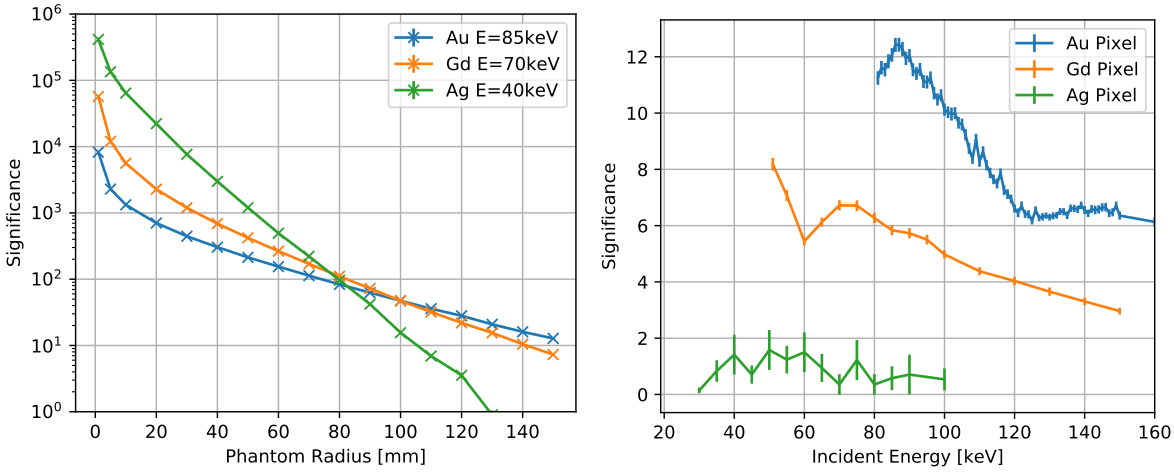

(a) (b)

Figure 5.2 – (a) shows the significance for a variation of the phantom radius for different elements. (b) shows an energy variation for the standard 30 cm sphere.

by a factor of 3, it already yields a factor of 16 for a phantom with 40 cm diameter. This can be attributed to the attenuation due to the phantom size because the forward direction with $\theta < 90°$ is chosen by the pixel selection for an incident energy of 85 keV. In contrast, the K_β-fluorescence is preferably measured in the backwards direction with an incident energy of 81 keV because the energy difference of only 3 keV towards the K_β fluorescence energy suppresses backwards scattering according to the Compton scattering angle formula (2.6). Consequently, an increasing phantom size does not shield the detector from the scattering background in the K_β signal energy interval as is does for K_α fluorescence measurements. This is the reason why K_α fluorescence can yield higher significances for larger phantoms than K_β fluorescence, which is shown in figure 5.1(a), where the blue curve surpasses the red curve more and more with increasing phantom radius, whereas the red curve is proportional to the 4π measurements.

5.2 Variation of Target Elements

The high attenuation in soft tissue for larger objects rules out almost all elements for suitable tracer materials. Although gold is probably the most frequently used material for XFI, others are possible. Sjölin et al. [91], for instance, compare iodine, gadolinium, gold and platinum

and note, that the signal to noise ratio and the optimal detector angle both are functions of the tracer element and the incident spectrum due to the angular dependency of the Compton background. In figure 5.2(a), for some exemplary elements, the phantom size is varied. It is evident, that the curves all have different slopes. To be specific, the slope can be very well reproduced by simply multiplying the Lambert-Beer law for the ingoing and outgoing radiation, whose product is directly proportional to the amount of signal created. Therefore, the lower the atomic number Z, the higher the slope. This causes different target elements to be optimal for different phantom sizes.

Regarding the relative differences between the elements, however, the relevant factor is not the difference in fluorescence signal, but the different background shape. For the medium-Z elements, the Compton plateaus are narrower, so that an increasing incident energy can quickly eliminate several Compton orders in the signal range, so that the signal becomes quasi background-free. Considering a phantom radius of, e.g., 5 cm, the product of attenuation and fluorescence cross section is six times larger for gold than for silver, nevertheless, simulations suggest silver to be 6 times more significant than gold. The only reason for that is the difference in background shape. Regarding larger objects, however, silver can definitely not be used because the attenuation of the fluorescence becomes too high. For $r = 15\,\text{cm}$, 1000 times more gold fluorescence leaves the phantom than silver due to the attenuation. Gadolinium is given here as a example of an element in between. After the phantoms become too large for the silver fluorescence to transmit sufficiently, gadolinium seems to be the optimal choice for $80\,\text{mm} < r < 100\,\text{mm}$ until heavier elements, such as gold listed here become more suitable.

For medium-Z elements and a perfect detector, incident energies closer to the K-edge already allow for the signal fluorescence to move below the Compton background peak so that the only photons in the signal background arise from the Doppler effect, which can cause photons to lose more energy than the Klein-Nishina equation would predict. To transfer these results to experiments, however, it has to be kept in mind, that for these background-free simulations, the real detector effects, such as electronic noise or escape events, play the dominant role for the background. To reliably predict the sensitivity in an experiment, the detector in the experiment has to be fully characterized and all its effects have to be added explicitly to the simulations used to prepare the experiments. Furthermore, for other materials, such as bone, silver has the disadvantage of being absorbed much stronger due to the high calcium content in bone. Whereas for soft tissue the product of mass attenuation coefficient and density is 4 times larger for silver fluorescence compared to gold fluorescence, it is already a factor of 12 for bone. Since this is the exponent in the attenuation law, measuring silver from, for instance,

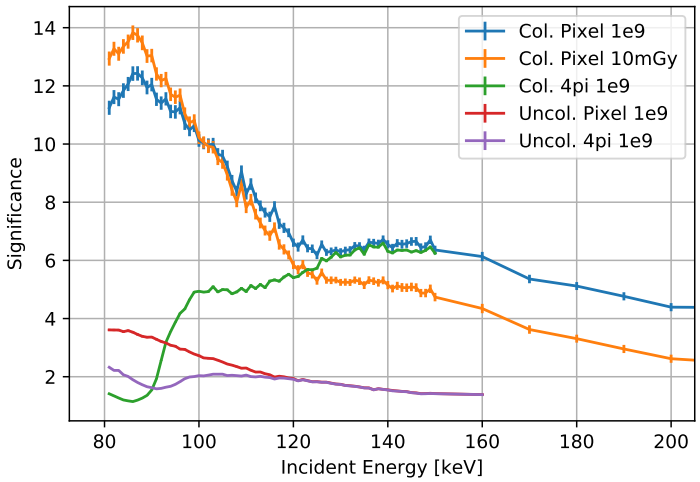

Figure 5.3 – For the 30 cm standard sphere, the resulting significances are plotted against different incident energies. The curves refer to a detector with (Col.) and without (Uncol.) a leaf collimator for 10^9 incident photons or a dose limit of 10 mGy with or without pixel selection.

inside a human skull is a difficult task.

5.3 Variation of Incident Energy

The choice of incident X-ray energy has a huge impact on the potential sensitivity of an XFI measurement. In figure 5.3, the significances for the 30 cm standard sphere are plotted against the incident energy. There are several reasons why an incident energy around 85 keV yields the best result. First, the fluorescence cross section drops with increasing energy. At 150 keV it is already at 20% compared to the value at the K-edge. This can be seen in figure 2.1 or 5.4(b). Second, the deposited dose per incident photon increases with the incident energy. For 150 keV, only $5.5 \cdot 10^8$ photons are allowed compared to 81 keV, where $1.3 \cdot 10^9$ photons result in a dose of 10 mGy. This loss in statistic results in a further sensitivity loss of $\sqrt{13/5.5} \approx 1.5$. Third, the angular dependence of the Compton background depends on the energy. In figure 5.4 the spatial background distribution in a collimated detector is illustrated. Starting at the bottom of the map, from $81 - 95$ keV the single Compton scattering maximum moves to the back of the detector until it is energetically not possible anymore to reach the gold K_α signal region around 68 keV. Then the red area moving to the right from 100 keV until

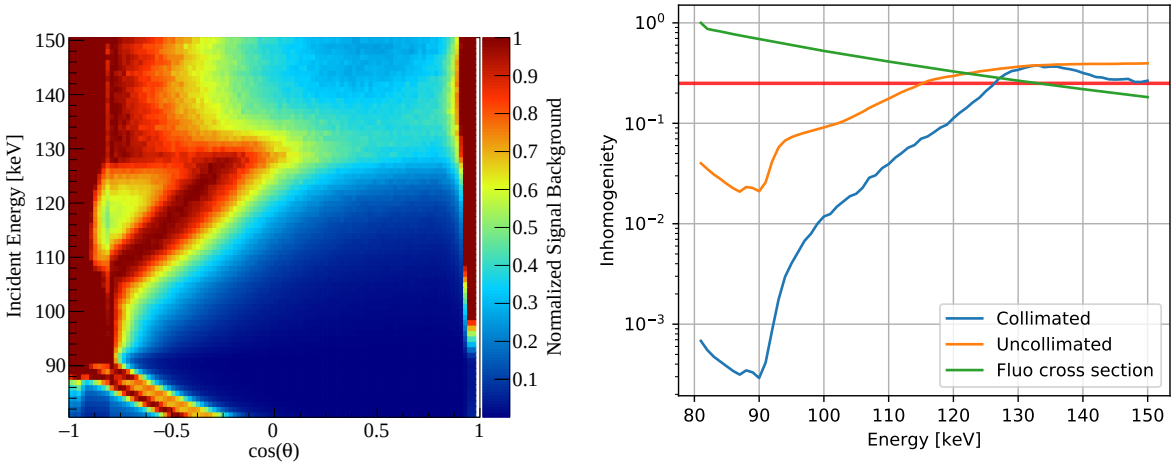

(a) Collimator background distribution

(b) Inhomogeneity per energy

Figure 5.4 – In (a) the collimated signal background distribution is plotted against the incident energy for 10^9 incident photons. The counts per line are normalized to a maximum of 1 on the cylinder jacket. In (b) the ratio of minimum and maximum value per incident energy from (a) is plotted together with the normalized fluorescence cross section. The red line marks the 0.25-level.

130 keV, where it stops at $\cos\theta = 0$, marks the double Compton exclusion edge. On the left of this region double scattering in the signal region is not possible anymore because the loss of energy is insufficient. Regarding smaller phantoms, this would continue until at 150 keV it reaches $\cos\theta = 1$, but due to the size of the phantom the scattering in forward direction is attenuated or rather replaced by higher scattering orders.

This map looks almost the same for an uncollimated detector. However, due to a higher amount of multiple scattered photons distributing themselves almost isotropically, the difference between minimum and maximum background decreases drastically. This can be seen in (b), where the actual ratios between minimum and maximum on the cylinder jacket is plotted. Below 90 keV there is a difference of two orders of magnitude between the collimated and uncollimated detector. For larger energies, the Compton2 maximum then moves to the middle of the detector. This effect and the increasing share of higher scattering orders decreases the background inhomogeneity until at 130 keV a pixel selection becomes useless, which is marked by the red line in the plot. A simplified calculation suggests, that when choosing the best half of pixels, also half of the fluorescence photons are lost. In order for the significance to increase by doing this, the background would need to drop to a value of 0.25. For energies larger than 130 keV, the lowest background pixel is already above that value.

The strength of a pixel selection comes into play below 100 keV. Considering this energy interval, the curve shape for a 4π detector and the pixel selection is almost flipped horizontally. With respect to a 4π detection, 81 keV is a better choice than 85, because the background level in the signal region is only half as high. This can be seen in the spectrum in figure 3.2 and derived from the relation of the Compton energy loss and the scattering angle. For an incident energy of 81 keV, a scattering angle of 90° would be necessary to reach the signal region, for which the cross section is smaller than for a backscattering occurring at higher energies. Note that in the plot of the background distribution the maximum is not exactly at $\cos\theta = 0$ because of the phantom's extension. A scattering before the coordinate's origin in the center of the detector shifts the position in the detector accordingly. The scattering angle is then the explanation of why a pixel selection at $85-90$ keV is more effective than at 81 keV, which is suggested by some authors, e.g. Ahmad et al. [109] as the optimum. The edges of the C1 maximum in figure 5.4(a) are not sharp as Klein-Nishina would suggest, which can be explained by Doppler scattering due to the electron movement broadening the maximum in both angular directions. Therefore, there are less single scattered photons in the forward direction for $85-90$ keV than for 81 keV and pixels in this part of the detector contain less background.

5.4 Variation of Energy Bandwidth

Besides the mean of the incident energy distribution, also the bandwidth determines the sensitivity of XFI. Concerning other X-ray sources besides a synchrotron, a certain bandwidth might be necessary in order to yield sufficient photon flux. Therefore, the incident energy bandwidth is varied for several incident energies to determine the requirements on the source. In figure 5.5 the significance is plotted against a variation of the energy bandwidth. The bandwidth's effect on the significance is twofold. First, for low incident energies with high bandwidths resulting in photons below the K-edge $E_0 - 3E_{\mathrm{rms}} < E_K$, a part of the incident spectrum cannot participate in the creation of the XFI signal anymore. Instead, these photons only create radiation dose and unwanted background. This is shown in figure 5.5(b), where the fluorescence cross section [50] is explicitly integrated over the incident spectrum as an analytic comparison to the reduction in fluorescence photons in the simulations. Especially for 81 keV there are some deviations between the simulated and calculated values that can be attributed to a different energy dependent behavior between Geant4 and xraylib. For example

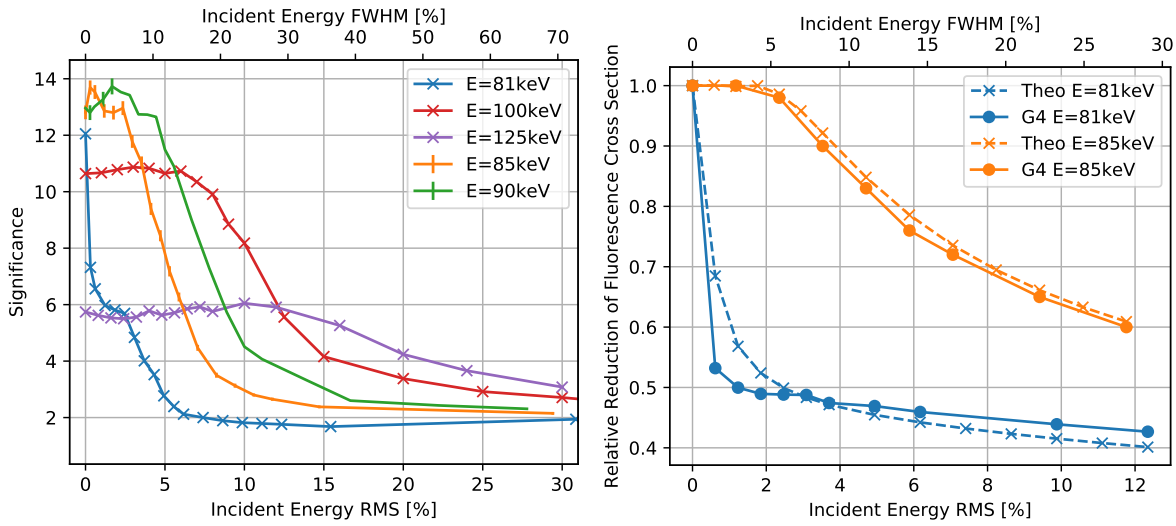

(a) (b)

Figure 5.5 – Figure (a) shows the effect of incident energy bandwidth on the significance with pixel selection for a dose of 10 mGy. In figure (b) the relative loss of fluorescence photons normalized to zero bandwidth is taken from simulations and compared to analytic calculations where the fluorescence cross section is integrated over the incident energy bandwidth.

the K-edge energy differs by 250 eV.

Furthermore, the spatial background distribution becomes more homogeneous for a larger bandwidth. This can be understood when taking the background distributions in figure 5.4 and integrating them over some energy interval. Taking for example 81 keV, an increasing bandwidth would cause the C1 peak to broaden, so that there is more background in the forward direction, where the pixels are preferably selected. For 81 keV, both these effects can be seen separately in figure 5.5a. The first drop below 1%RMS is caused by incident photons being below the K-edge reducing the amount of fluorescence photons. The second drop between 3 and 5%RMS is caused by broadening of the background and incident photons scattered elastically. For larger energies, such as 90 keV, where the C1 peak is at the backside of the detector, the necessary bandwidth is already a lot larger until it broadens into the forward direction. Concerning energies over 100 keV, the background for monoenergetic beams is already more homogeneous than for low energies, therefore a broadening has less effect there.

All in all, FWHMs of up to 10% have no negative effect when choosing 90 keV as a mean en-

ergy. A small bandwidth can even have a positive effect because fitting the signal background becomes easier since the Compton edges become smoothed. If the bandwidth is too large, e.g. over 30% FWHM, the pixel selection starts to become useless and higher incident energies are necessary, at least for homogeneous fluorescence distributions.

In fact, the spectral shape does not need to be Gaussian as long as it is narrow and the majority of the photons has an energy above the K-edge of the tracer material. To give a brief example, a spectrum of a conventional 140 kV X-ray tube was hardened by filtering it with 1 mm of uranium or 3 mm of bismuth. Not only do these high-Z filters absorb the unwanted low energy photons from the tube, but they also create a cut-off at their K-edge energy because their absorption coefficient increases abruptly. However, this happens at the cost of incident flux, which for uranium is reduced to 0.3% and for bismuth even to 0.01%. Nonetheless, the uranium filtered spectrum yields a significance in the same setup of $Z = 7.8$ with a mean energy of 105 ± 9 keV and the bismuth spectrum yields a smaller significance of $Z = 6$ because the mean energy of 87 ± 8 keV closer to the K-edge of gold, so that 13% are even below it. Note, that the bandwidths cannot be exactly compared to figure 5.5 because their shape is not Gaussian. The unfiltered spectrum is of course a bad choice yielding only $Z = 0.94$ because it is simply too broad.

5.5 Variation of Target Position

So far, the fluorescence distribution in the detector has been homogeneous, but for a more realistic phantom, such as an animal or human, the target's position is likely to be not in the center and of course the phantom is neither homogeneous nor symmetric. In figure 5.6 the minimum detectable gold density for target spheres with a radius of 0.5 mm is given. With respect to K_α-fluorescence, the worst case position inside the sphere with 20% less significance than in the center, is 6 cm behind it. For every target position along the central axis($x = 0$), the background is the same. The differences in the significance only relies on the attenuation of the fluorescence. Concerning photons reaching the detector close to $\cos\theta = 1$, the different target positions along the beam have no big influence on the amount of fluorescence photons. The difference in attenuation in, e.g., 10 cm soft tissue for 70 and 85 keV is only about 20%. Considering a detection at $\cos\theta = 0$, however, comparing a target in the beginning and in the end of the phantom, the incident beam distance is larger for a target in the end whereas the necessary path distance for the fluorescence photons afterwards is the same. Regarding

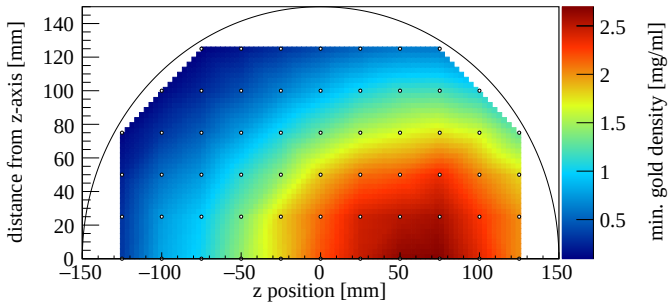

(a) K_α-fluorescence with $E = 85\,\text{keV}$

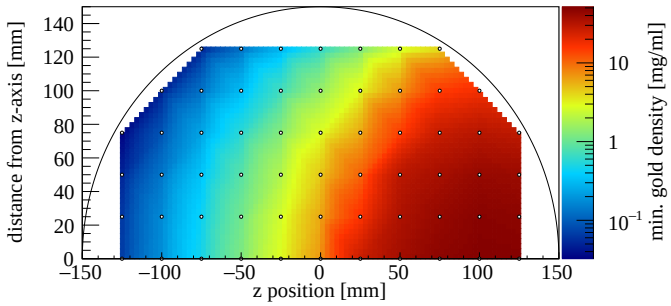

(b) K_β-fluorescence with $E = 81\,\text{keV}$

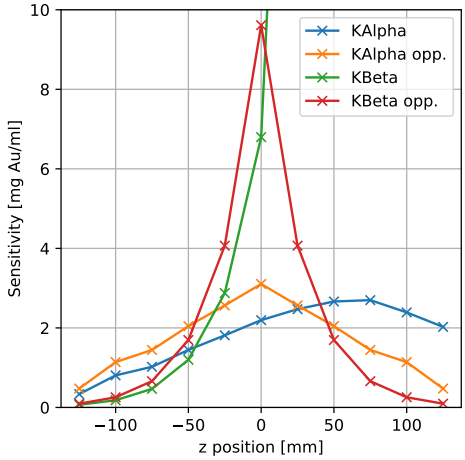

(c) Comparison with scans from opposite directions

Figure 5.6 – The minimum detectable gold density for 10 mGy is shown for different target positions inside a spherical phantom. The incident beam is parallel to $\hat{z}$. In (a) and (b) the black dots mark the simulated values for an incident beam parallel to $\hat{z}$. The black semicircle shows the border of the phantom. In (c) for target positions along a central axis through the phantom, a single scan from direction is compared to two scans from opposite directions sharing the total dose.

K_β-fluorescence, this is different. Here an incident energy of 81 keV is optimal. A collimator is not necessary and the location of the lowest signal background is in the backwards direction because for the energy difference from 81 keV to 78 keV K_β energy, Compton scattering is expected to be in forward direction. Therefore, the lengths of the mean photon paths increase a lot more for target positions moving along the beam because the fluorescence photons need to travel all the way back . So if K_β-fluorescence is used for an unknown target location, it is advisable to rotate the phantom relative to the source by 180° and scan twice. This is compared in figure 5.6(c). If the ROI for the fluorescence, such as a certain organ, is expected to be close to the phantom's surface, K_β-fluorescence is beneficial. However, if the target location is in the center of a 30 cm sphere, K_β-fluorescence measured from two directions is five times less sensitive than K_α fluorescence. Note that the $K_{\alpha 1}$ cross section is about 5 times larger than the $K_{\beta 1}$ cross section.

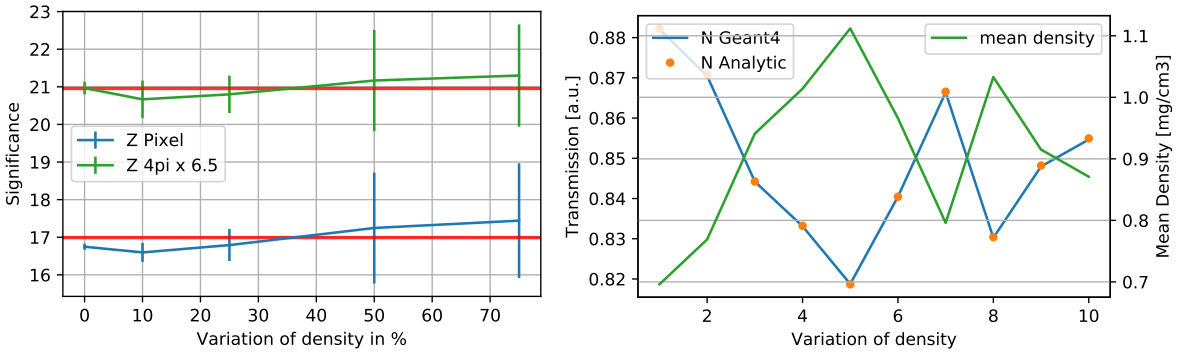

(a) (b)

Figure 5.7 – In (a) the resulting significances for a 30 cm sphere with a density fluctuating randomly with $\rho_{H2O} \pm X\%$ is averaged over three different combinations with the corresponding standard deviation. The red line marks the mean. In (b) the transmission through 10 voxels is simulated, calculated analytically and plotted together with the mean density for 10 different density distributions.

5.6 Impact of Phantom Inhomogeneity

One of the strengths of XFI is the insensitivity against anatomical noise or density fluctuations. Considering only the amount of signal photons, the significance is directly proportional to the product of the transmission of the incident beam to the target and the transmission of the fluorescence photons to the detector. Therefore, local inhomogeneities, such as bones for higher attenuation or the respiratory tract for lower attenuation, between the X-ray source and the irradiated fluorescence target, have a direct impact on the measured significance. However, compared to small solid angle detectors, for large solid angle detectors small local variations average out because of the diverse possibilities for photon tracks from the fluorescence target to the detector. In figure 5.7 the 30 cm(a) sphere was built using 1 mm^3 voxels. In each voxel a random density was chosen using a homogeneous probability distribution with different density intervals $\rho_{H2O} \pm X\%$. As expected, the mean significance over different density distributions stays the same. The standard deviation, however, increases with increasing density fluctuations because the possible transmission values for the path between the X-ray source and the target become more extreme. As a simple checkup, in figure 5.7(b) the simulated transmission values for only 10 voxels are compared to analytic calculations based on the mean density showing exact agreement.

5.7 Comparison with Transmission Imaging

As an alternative to the rather elaborate XFI procedure, the target material could also be measured by a difference in the incident's beam transmission. This approach is used for an imaging method called K-edge CT. If the precise geometry of the phantom is unknown, the transmission without tracer absorption could be approximated by either using incident energies slightly below and above the K-edge or by using transmissions for different beam positions close to each other. However, the latter is only reasonable for small fluorescence targets compared to fluctuations in the anatomy. The transmitted number of photons is calculated using

$$N_{\mathrm{Au}} = N_0 T(L) T_{\mathrm{Au}} \tag{5.1}$$

$$N_{!\mathrm{Au}} = N_0 T(L) \tag{5.2}$$

with the phantom length L, the number of incident photons N_0 and the transmission through the target T_{Au}. The signal is then the counting difference between the two cases with and without target material present. Using an equivalent to the $Z = 3$ condition with an error based on Poissonian statistics, the photons numbers must fulfill

$$\frac{N_{\mathrm{Au}} - N_{!\mathrm{Au}}}{\sqrt{N_{\mathrm{Au}} + N_{!\mathrm{Au}}}} \geq 3\,. \tag{5.3}$$

Inserting (5.1) and (5.2) in (5.3) and yields

$$T_{\mathrm{Au}} = \frac{9 - 3\sqrt{9 + 8N_0 T(L)} + 2N_0 T(L)}{2N_0 T(L)} \tag{5.4}$$

after some rearrangement. The minimal detectable gold density can then be calculated using the Lambert-Beer equation with T_{Au} calculated over eq. (5.4).

$$\rho = \frac{\ln(T_{\mathrm{Au}})}{-\frac{\mu}{\rho} L_{Target}}\,. \tag{5.5}$$

In figure 5.8, the actual simulated significances for XFI are shown normalized to the idealized values for transmission imaging based on eq (5.5) with $E = 81\,\mathrm{keV}$. It is interesting how close both values actually are, considering that for XFI the energy resolution of the detector, the ratio of Compton cross section to attenuation cross section and the actual shape of the spectrum are relevant factors that do not influence a transmission measurement. For the collimated XFI

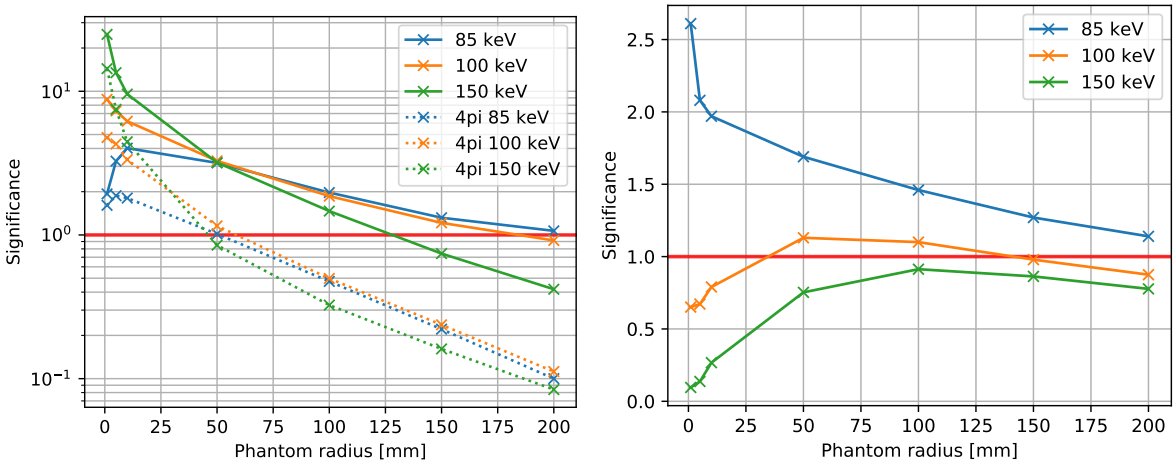

(a) XFI compared to ideal transmission imaging

(b) sim. XFI compared to analytic approximation

Figure 5.8 – (a) shows the simulated XFI sensitivity divided by an ideal transmission measurement. (b) shows the approximated XFI sensitivity divided by the simulated values for 4π detectors without a collimator.

value with pixel selection, then also the collimator layout, the beamsize limiting the collimation effect and the spatial background distributions become relevant, none of which plays a role for the transmission measurement. Here for large phantoms, XFI is only more sensitive if both a collimator and the pixel selection are used with a 4π detector. However, besides the difficulties of achieving a transmission without attenuation due to the agent present, the measurement can easily be misinterpreted. The theoretically lowest detectable gold density for the transmission imaging of 3.5 mg/ml corresponds to a mean length of 120 nm of pure gold. The same effect can also be reached by an additional 100 µm water, 47 µm bone or 9.2 cm of air, though. Therefore, small movements, deviating assumptions of the anatomy or slight misalignment might easily cause a false signal. XFI is a lot more stable since slight fluctuations in the background are less likely to produce signal like events at previously specified signal energies.

At least for the uncollimated 4π XFI measurement, this can be reasoned with an analytic approximation. As a simple approximation, the signal photons can be calculated as the product of the number of incident photons, ingoing transmission to the target, fluorescence yield and outgoing transmission. The total background in the whole spectrum is estimated as the number of attenuated photons which are approximated to be distributed homogeneously in the spectrum. Therefore, the signal background is only the ratio of the signal interval over the incident

energy. These simplifications then yield an approximation for the significance

$$Z(\mathrm{XFI}_{4\pi}) = \frac{N_0 \cdot T(E_0, L/2) \cdot R_{K\alpha} \cdot (1 - T_{\mathrm{Au}}) \cdot T(68\,\mathrm{keV}, L/2)}{\sqrt{N_0 \cdot R_{\mathrm{S}} \cdot R_{\mathrm{B}}(1 - T^2(E_0, L/2))}} \tag{5.6}$$

with the K_α-fluorescence yield $R_{K\alpha} = (2.81 + 1.65)/7.80 = 0.57$, the signal region ratio R_{S}, which is approximated as the signal interval divided by the incident energy for a homogeneous spectrum: $R_{\mathrm{S}} = 2 \cdot (6 \cdot 0.2\,\mathrm{keV})/85\,\mathrm{keV} = 0.028$ and the background detection ratio R_{B}, which is the ratio of background photons actually reaching the detector. In simulations with a 4π detector R_{B} actually is 67%, but for the approximation without further knowledge it is set to 1. In figure 5.8(b) it is shown that for large objects with $R > 100\,\mathrm{mm}$ this approximation works very well with less than 50% deviation from the actual simulations. For small objects, however, the approximation overestimates the sensitivity for incident energies close to the K-edge and underestimates it for larger energies because the assumption of a homogeneous spectrum does not hold true anymore. This is resulted from the fact that there are less higher Compton orders, so that for low incident energies the signal background is above average, since it is dominated by single Compton scattering, whereas for higher energies it is below average, since the single Compton scattered photons have energies higher than the K_α photons.

6 Experimental Validation

Since the proposed background reduction strategies for XFI simulations with human-sized phantoms in this work all rely on the validity of the anisotropy of the Compton background and the capabilities of leaf-based collimators, it is crucial to perform cross-checks of the performed Geant4 simulations. Although the physics models in Geant4 themselves are benchmarked regularly, the possibilities for mistakes are plenty. Besides analytic calculations, which are simple for the amount of fluorescence photons, a little more extensive for single Compton scattering and rather complex but possible for medium scattering orders, such as C2 and C3 [49], the effort for the analytic calculation of even higher scattering orders is too high without Monte Carlo simulations. Therefore, as a validation of the XFI simulations, some small scale experiments could be performed at the P07 [110] and P21 beamline at the PETRAIII synchrotron at DESY. As a substitute for the 30 cm soft tissue sphere used for simulations, a 30 cm cylinder was made of Polymethyl methacrylate (PMMA), also known as acrylic glass or plexiglass, whose mass attenuation coefficients are very similar to soft tissue. Without a 4π solid angle detector available, the Amptek XR-100CdTe was placed consecutively at different angular positions around the phantom to measure the angular dependence of the multiple Compton background. The X-ray source conditions, however, fully match the simulated ideal X-ray source conditions because of PETRA III being a high brilliance source. Considering the size of the phantom and the detector resolution, the incident photon beam is fully monochromatic and non-divergent. The available photon fluxes of $\mathcal{O}(10^{11}\mathrm{s}^{-1})$ at PETRA III allow for high statistics even with small detectors covering less than 0.01% of the solid angle due to the necessary distance to the beam when large phantoms have to fit in between.

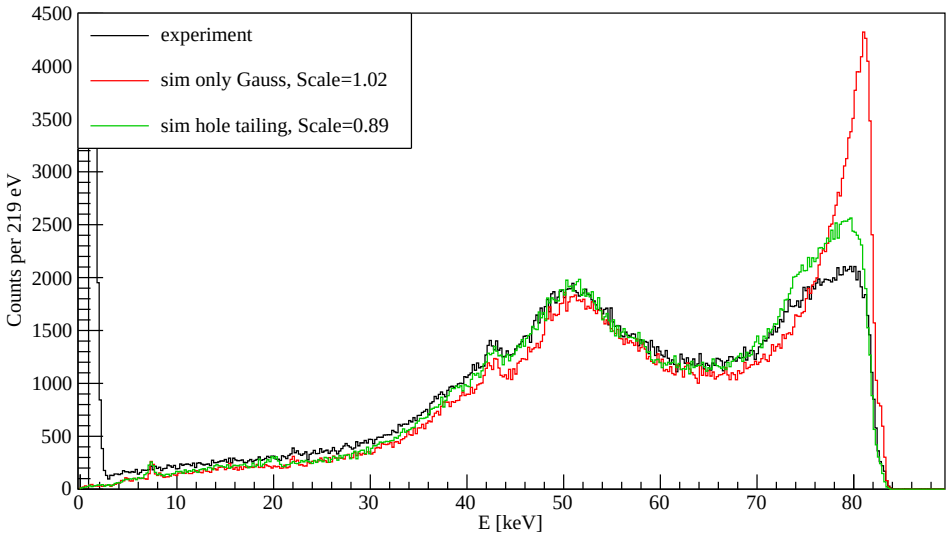

Figure 6.1 – Spectrum of the 30 cm PMMA phantom with an Amptek detector at $\theta = 45°$. Besides the experimental data, the simulation in red without hole tailing and rebuilt experimental setup, a newer green simulation is plotted including these effects. Note that the simulated spectra are scaled to the experimental counts above 10 keV. The black and red data have been published [44].

6.1 Angular Scans of PMMA Cylinder Phantoms

To validate the simulated background distributions, detector calibration experiments and angular variations with PMMA cylinder phantoms were performed at the P07 beamline[1]. With an incident energy of 82.84 keV, a 30 cm PMMA cylinder phantom with a height of 6 cm was placed centrally in the incident beam with its symmetry axis perpendicular to the beam axis. In its center an Eppendorf tube with a diameter of 6 mm containing 78 mg/ml of gadolinium was placed in a hole. A spectrum and a plot of the angular variation for the 30 cm phantom is already published [44].

More precise calculations of the detector response and the consideration of the experimental setup around the phantom allows for a reevaluation of the simulations. In figure 6.1 an experimental spectrum in forward direction at $\theta = 45°$ with the Amptek detector placed right at the surface of the phantom is compared to simulations. The newer version of the simulation in green shows an overall better agreement with the experiment, especially for the C1 peak at

[1] I acknowledge DESY (Hamburg, Germany), a member of the Helmholtz Association HGF, for the provision of experimental facilities. Parts of this research were carried out at PETRA III and we would like to thank Martin von Zimmermann, Olof Gutowski and Ann-Christin Dippel for assistance in using the P07 beamline.

80 keV. The depth dependent charge loss inside the chip, causes a broadening and thus flattening of the peak. At lower energies this is far less prominent because of the higher attenuation coefficients of 1 mm CdTe. At 80 keV the transmission rate is 17%, whereas for 60 keV it is only 2%, therefore high photon energies are necessary for this effect to occur. The inclusion of experimental setup, such as the aluminum plate on which the phantom was placed, adds to higher scattering orders mainly between 30 and 70 keV and yields a total count increase of 12%. Since the error on the incident beam flux measurement is considered to be larger than 10%, the total counts of the simulated spectra were scaled to the experimental spectrum for better comparison. The low energy peak below 10 keV in the experimental spectrum is attributed to internal detector electronics and is not considered any further. The remaining deviation for the single Compton scattering peak cannot be clearly assigned to a single reason without repeating the experiment. The most probable explanation is a mismatch in parameters, such as the exact positioning of the detector and the phantom relative to the beam, which was both placed by eye. Furthermore, the experimental setup around the phantom and detector was not measured precisely enough to exclude this as a possible source of error. Last but not least, deviations in the detector calibrations cannot be fully excluded, since it is possible to match both spectra when changing the detector response functions. On the other hand, later experiments show a far better agreement with the same detector response, especially in figure 6.7, therefore this seems unlikely to be the only reason.

In figure 6.2(a), the angular dependence of the measured counts in the gold K_α signal background interval is compared to simulations. Here also hole tailing yields a large improvement. For small detector angles, such as 45°, hole tailing increases the number of counts because the C1 peak is at higher energies than the signal interval at 68 keV. These counts are then shifted to lower energies and thus the counts in the signal region are increased. Regarding high detector angles, the effect is reversed, because there is no large peak above the signal region left which could be shifted there. Instead, the photons in the signal region are shifted to lower energies, thus reducing the overall amount. The experimental curve can be well explained with the simulations containing hole tailing, the loss of counts for large angles compared to simulations might be explained with the missing consideration of detector dead times. At these positions the count rates where higher and over $10^4\,\mathrm{s}^{-1}$, the detection becomes non-linear for the chosen peaking time[2] of 3 µs. The overall increase in counts for lower angles below 60° is caused by the position of the detector close to the phantom since the background distribu-

[2]The peaking time is the time necessary for a shaped pulse to reach its maximum. Both the maximum count rate as well as the energy resolution depend on the peaking time.

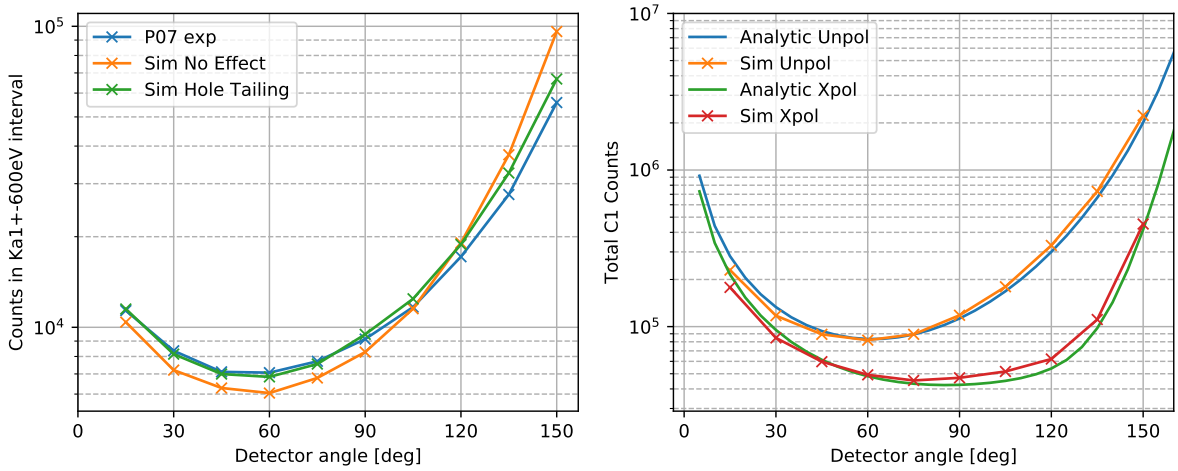

(a) C1 counts in Ka1 Signal interval

(b) Total C1 counts in spectrum

Figure 6.2 – In (a) the angular dependence of the background in the gold $K_{\alpha 1}$ signal interval is compared between experiment and scaled simulations. The data of the experimental values and the simulations without any calculated detector response are published [44]. In (b) the total number of C1 photons in the whole spectrum is compared to analytic calculations for polarized and unpolarized incident photons.

tions for large detectors, as, e.g., in figure 3.9, does not show this effect. However, it can be recreated when interchanging the cylinder detector with a spherical detector close to the 30 cm sphere's surface. The reason for this effect is, that the solid angle of one arbitrary detector element close to the phantom changes more for different positions along the beam axis, than for detector elements half a meter away. Therefore, for detector positions in forward direction, the detector covers a lot more different scattering angles for photons scattered in the forward part of the phantom compared to the detector far away. The overall integral of counts is of course the same, but the angular dependence changes.

As stated before, the single Compton scattering can be easily calculated quite precisely by just integrating the Klein-Nishina cross section for different possible scattering positions and multiplying this value with the transmission until this point and the transmission after this point until the detector is reached. In figure 6.3 for an ideal Amptek detector, the single Compton scattering of the spectrum is explicitly calculated for two different detector positions with polarized and unpolarized incident photons. Besides the missing Doppler effect in the analytic calculation, which causes the smoothing of the edges, the simulations can be reproduced well including the polarization based suppression at 71 keV, which corresponds to 90° scattering. When integrating the C1 counts per angle position, their angular dependency is shown in fig-

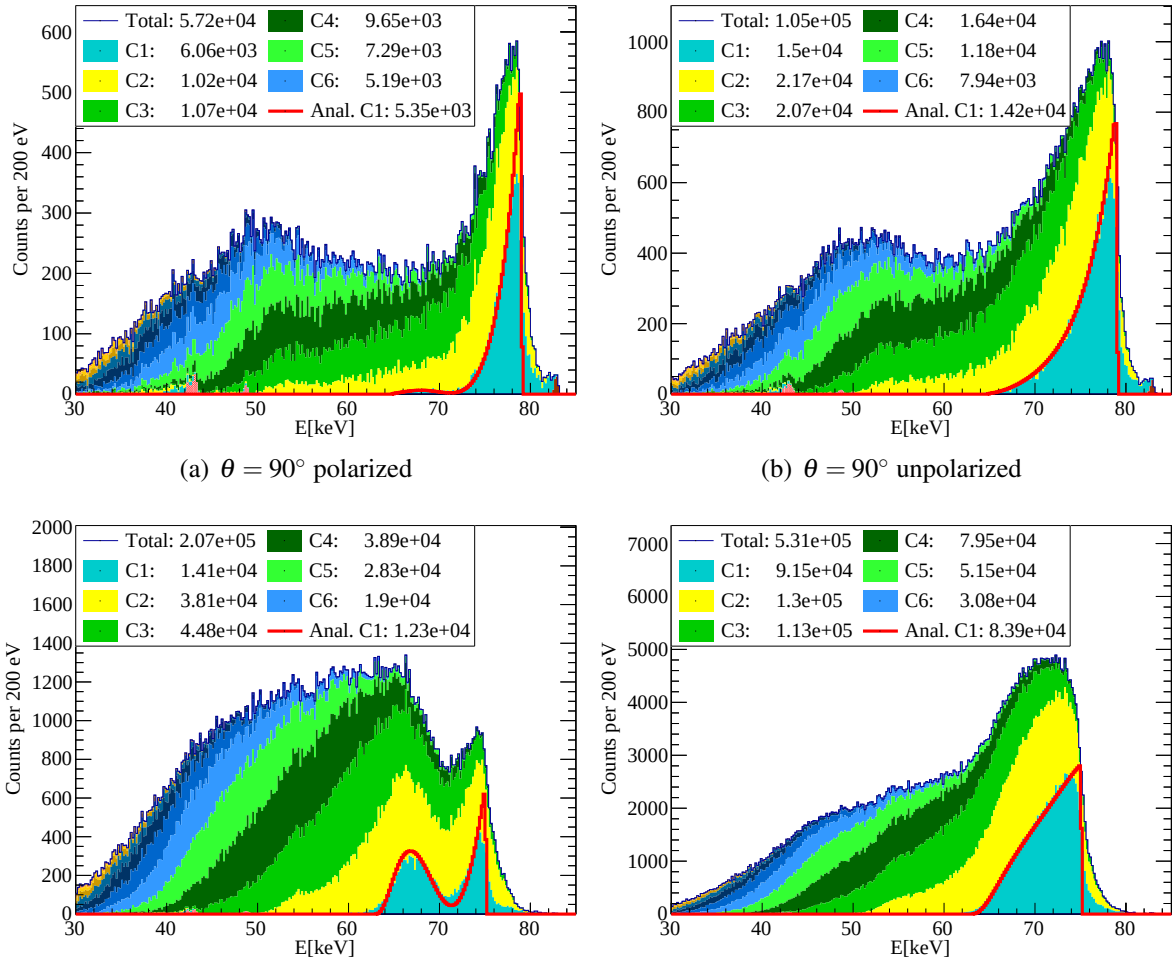

(a) $\theta = 90°$ polarized

(b) $\theta = 90°$ unpolarized

(c) $\theta = 135°$ polarized

(d) $\theta = 135°$ unpolarized

Figure 6.3 – Comparison of simulated and analytic C1 spectra for the 30 cm sphere for an Amptek detector without hole tailing and 100% efficiency. The analytic spectrum is overlaid as a thick red line.

ure 6.2(b) with a close match to the simulations. Here no scaling is applied. Comparing the plot of the unpolarized C1 integral with the counts in the fluorescence signal interval on the left, a similar shape becomes apparent. The reason for this is, that the ratio of the total C1 photons divided by all detected photons per solid angle is almost constant and because of the rather homogeneous flat shape of the spectrum, the counts in the signal interval are almost proportional to the total counts. For smaller phantoms or collimated spectra, this does not hold true anymore. In general the signal interval cannot be reliably calculated by simply calculating C1, since in this case for detector angles smaller than 90°, the share of C1 on the total

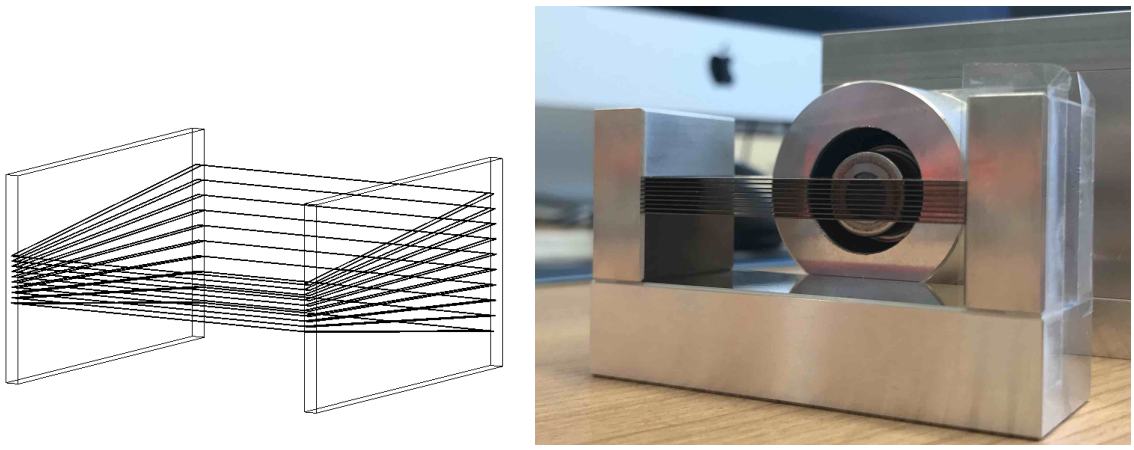

Figure 6.4 – Sketch and photo of the small scale molybdenum collimator in front of the Amptek detector. The actual collimator leaf separation angle of 0.75° is exaggerated in the sketch. The collimator is placed such that the extrapolated intersection of the leaves coincides with the beam axis.

signal background is below 4%. Instead, higher Compton scattering orders need to be taken into account, which becomes apparent when looking at the spectra in figure 6.3.

6.2 Molybdenum Collimator

A small scale version of the simulated phi collimator with 9 molybdenum leaves with a size of 0.2x25x50 mm^3 separated by 0.75° relative to a focus point 150 mm away was built and tested at the P07 beamline with $E_\gamma = 64\,\text{keV}$. With the leaf thickness being the smallest for which grooves could be cut into aluminum holders having adequate precision, the leaf separation angle and the collimator length parallel to the detector chip surface normal were optimized using simulations regarding the loss of detectable fluorescence photons. The width of 50 mm was chosen such that at the 90° position of the detector, fluorescence photons from anywhere along the beam could be detected within a 30 cm phantom. To avoid unnecessary sagging in the middle of the leaves, the width was not chosen any larger for the first experiment.

For the experiment, an incident energy of 64 keV was used. The phantoms and the detector were placed by eye on a 1.5 cm thick PMMA plate. It was not possible to move the setup in any way using motors. Therefore, the lack of precise positioning is assumed to be the largest source of error for this test series. To determine the photon flux, the detector was put directly in

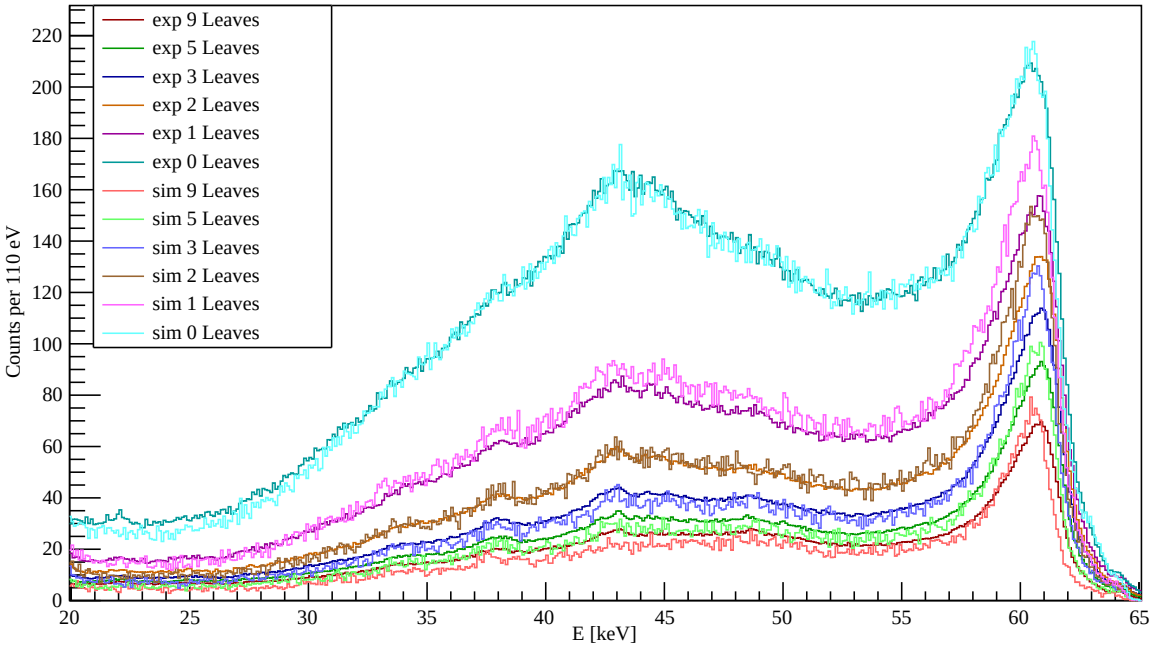

Figure 6.5 – Variation of the number of collimator leaves with experimental and simulated spectra. The simulated spectra are noisier due to less statistics and plotted in a brighter color. For each configuration, the leaves were placed symmetrically in the 9 available slots with the largest distance possible, whereas the single leaf was placed at the bottom.

the attenuated beam and an absorber variation was performed. This series resulted in a flux of $1.2 \cdot 10^{11}$ s^{-1}. However, a measurement by the beamline staff yielded $5 \cdot 10^{10}$ s^{-1}. To match the simulations, a value of $6.6 \cdot 10^{10}$ s^{-1} seems compatible. Self-performed measurement of the photon flux in any experiment fitting the simulations has not been possible until completion of this thesis.

In the experimental spectra, the Compton2 edge at 43 keV was more than two times higher than previously anticipated. This is explained with the disadvantageous properties of the PMMA plate combined with an insufficient number of collimator leaves. Compared to aluminum, the density of the PMMA is only 44% and its mass absorption coefficient is 10 times smaller. Therefore, for a path of 1 cm through the plate, photons become 22 times less absorbed at 60 keV and 9 times less absorbed at 40 keV. To reduce the negative influences of the experimental setup on the measured spectra, a shielding with high-Z material to absorb scattered photons would be beneficial. This effect is clearly seen in figure 6.5, when comparing zero with only one leaf. The one leaf was placed at the bottom so that mainly shields the detector

from scattering originating below the phantom itself, thus in the PMMA plate. The collimator leaves' thickness is chosen for angles of incidence close to zero, which is the case for origins of photons close to the beam axis. At an angle of 10°, the transmission is already below 1%. For a perpendicular hit, however, which would be possible for photons coming out of the PMMA plate below, the transmission is already at 44% for 60 keV photons. If it is not possible to shield the detector from below, more collimator leaves or a collimator bottom consisting of a higher-Z material than aluminum would be helpful. Further simulations showed, that with 30 leaves instead of the 9 leaves in the experiment, a maximum of the blocking is reached by a reduction of the C2 peak of a factor of two.

In figure 6.5 simulated and experimental spectra are plotted in comparison. Although the overall agreement is quite good when recreating the whole experimental setup in the simulations, there is a clear discrepancy at the C1 peak at 60 keV, which can be attributed to a vertical misplacement of the collimator. As soon as some detector segments in between are shielded from the beam axis itself, the single scattered photons and more important the fluorescence itself gets blocked. A vertical displacement of 1 mm would cause a loss in C1 peak height of 10%, see also figure 6.6. The slight variation in the C1 peak position can be explained with the manual placement of the detector on the plate without any mounting. After every removal of collimator leaves, the positions of the collimator and detector slightly differ. Therefore, the angle relative to the phantom's origin may vary a little. Furthermore, since the collimator's FOV relative to the beam axis is exactly the phantom's length, a slight misplacement of the collimator can block the scattering from the first part of the phantom, where the C1 peak originates and thus move the peak to lower energies.

For another experiment, a new improved version of the collimator was built. By increasing the number of leaves from 9 to 29, scattered photons from the experimental setup, especially the aluminum bottom, can be blocked more effectively. Simulations showed an additional reduction of higher Compton orders of a factor of two for the new collimator compared to the 9 leaves used before. Placing more than 30 leaves yields no further improvement because the detector is already fully covered. By also increasing the leaf width from 50 to 90 mm parallel to the detector surface the detector's FOV is increased, such that the whole path of the incident beam through the 30 cm phantom is uncovered for arbitrary angular positions. The smaller collimator before only enabled the detector to scan the whole beam axis through the 30 cm phantom if placed at the 90° position. For smaller angles, the last part of the beam axis was covered and for larger angles the first part respectively. The larger leaves, however, limit the positioning at very high or very low angles because of their size.

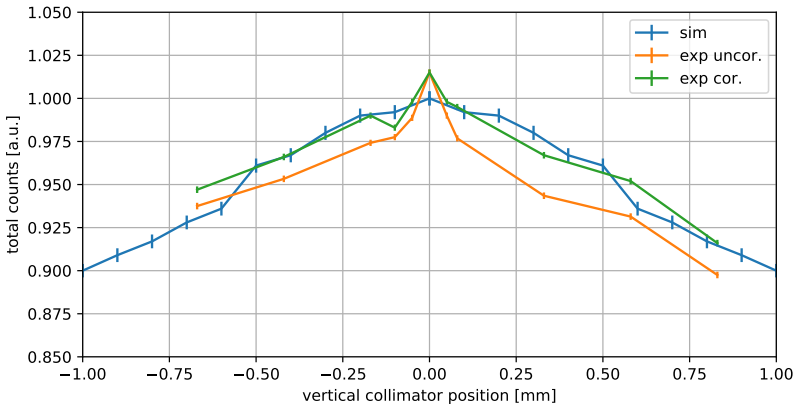

Figure 6.6 – The scaled number of total counts in a calibration measurement is plotted which were measured at different vertical positions of the collimator. For the experimental counts, the uncorrected version is given as well as the number corrected by the fluctuations of the incident beam in the experiment.

At the P07 beamline the new collimator was tested using the same 30 cm PMMA phantom as before. With an incident energy of 103.4 keV, a beamsize of 1x0.7 mm and an attenuated flux of $1.6 \cdot 10^{10} s^{-1}$, the new collimator was tested. For this and future beamtimes, an experimental mount was built, that allowed to place the detector at specific distances and angular positions with step sizes of 5°. In the past experiments, this was always an important source of error. In figure 6.8(a) there is a photo of the experimental mount together with the phantom and the Amptek detector the 90° position. During the beamtime, two problems occurred. First, the photon flux in the experimental hutch was not stable, which caused deviations between the different measurements if absolute flux numbers are used to scale simulated to the experimental spectra. Therefore, they are scaled to match the number of total counts instead. Second,

Table 6.1 – Relative reduction of Compton scattering orders and gold fluorescence counts. The fluorescence signal remains hidden in figure 6.7 because the significance is smaller than 3σ. The increase in significance with a collimator is approximately a factor of 2.

	θ	Fluo	C1	C2	C3	Z
[64,72] keV	45°	1.9 ± 0.2	1.4 ± 0.2	4.8 ± 0.1	12.7 ± 0.1	1.85 ± 0.09
	90°	1.9 ± 0.2	2.6 ± 0.6	6.4 ± 0.1	15.0 ± 0.1	2.02 ± 0.09
	135°	1.7 ± 0.1	1.8 ± 0.1	13.6 ± 0.1	28.3 ± 0.1	2.80 ± 0.09
[0,105] keV	45°	1.9 ± 0.1	1.8 ± 0.1	11.9 ± 0.1	18.4 ± 0.1	1.85 ± 0.09
	90°	2.0 ± 0.1	1.8 ± 0.1	16.0 ± 0.1	26.8 ± 0.1	2.02 ± 0.09
	135°	1.7 ± 0.1	2.0 ± 0.1	12.1 ± 0.1	21.0 ± 0.1	2.80 ± 0.09

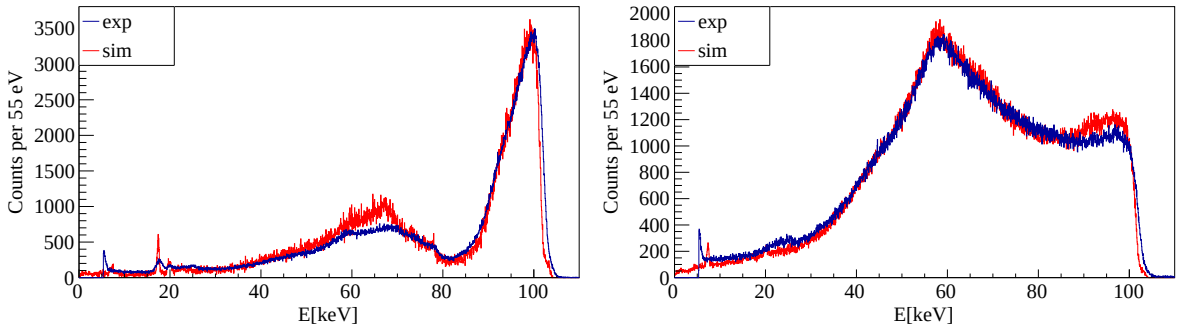

(a) 30 cm phantom, $\theta = 45°$ with collimator

(b) 30 cm phantom, $\theta = 45°$ without collimator

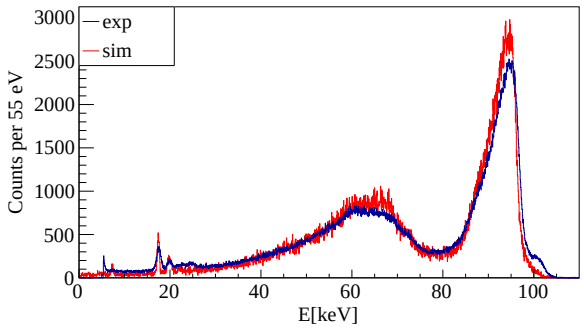

(c) 30 cm phantom, $\theta = 90°$ with collimator

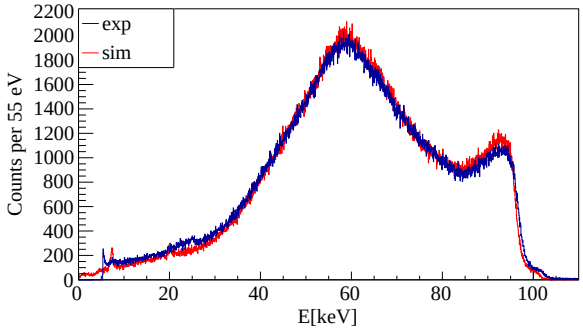

(d) 30 cm phantom, $\theta = 90°$ without collimator

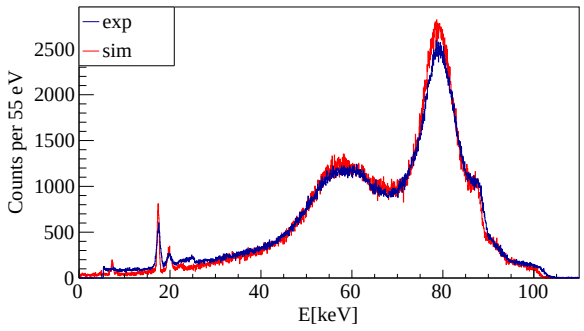

(e) 30 cm phantom, $\theta = 135°$ with collimator

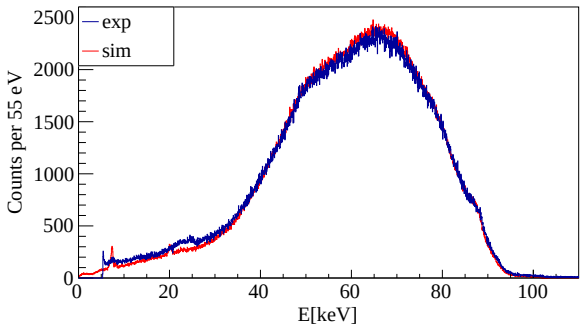

(f) 30 cm phantom, $\theta = 135°$ without collimator

Figure 6.7 – Simulated and experimental spectra for the 30 cm PMMA phantom for three different detector positions. The simulated spectra are scaled to the integral of the experimental spectra.

the detector showed a worse energy resolution than usual, which was repaired after the experiment by baking the detector for a few hours using the instructions of the manufacturer. The experiment started by carefully adjusting the vertical position of the collimator to the beam by maximizing the total counts in the spectrum. In figure 6.6, the counts are compared to the simulations. If the vertical position is not adjusted correctly, single Compton scattering and fluorescence photons from the beam volume would be blocked according to the shift in position. For quantitative fluorescence analysis, a careful adjustment is crucial.

In figure 6.7 the collimated and uncollimated spectra are shown for simulations and experiments. Overall the agreement is very good. The aforementioned decrease in detector resolution is clearly visible, when looking at the molybdenum fluorescence at 20 keV in the collimated spectra. In the experimental spectrum these peaks are clearly lower and broader. Around 23 keV there is a slight accumulation of counts in the experimental spectra, that might arise from internal materials inside the detector. Amptek for example uses indium as a contact material at the chip, whose fluorescence energy would fit. Furthermore, at $\theta = 45°$, the surplus counts in the simulation at 65 keV result amongst other things from scattering in the detector housing. Since the exact internal structure of the detector remains unknown, this is a cause for deviations between experiment and simulation. The entire reduction in Compton scattering and the resulting significances for this experimental setup are listed in table 6.1. Overall, the significance with a collimator is approximately a factor of two higher.

4 cm Phantom at the P21 Beamline The effect of a collimator on the background has already been demonstrated using the 30 cm phantom, however, no signal was detectable due to limits in the agent's concentration, the limited detector size and the available measurement time. Therefore, a smaller phantom with a radius of 2 cm was scanned with and without a collimator at the P21.1 beamline[3] at PETRA III with an incident energy of 102.7 keV. As sketched in figure 6.8(b) the phantom was orientated 45° relative to the beam and detector and it can be moved via a stepper motor along its axis. The phantom was moved 7 mm upwards from a centered position, so that the beam could pass through the center of the Eppendorf tubes with 6 mm diameter. Therefore, the beam's path through the phantom was $\sqrt{20^2 - 7^2}\text{mm}/\sin(45°) = 53\,\text{mm}$ long.

[3]I acknowledge DESY (Hamburg, Germany), a member of the Helmholtz Association HGF, for the provision of experimental facilities. Parts of this research were carried out at PETRA III and I would like to thank Oleh Ivashko and Olof Gutowski for assistance in using the P21.1 beamline.

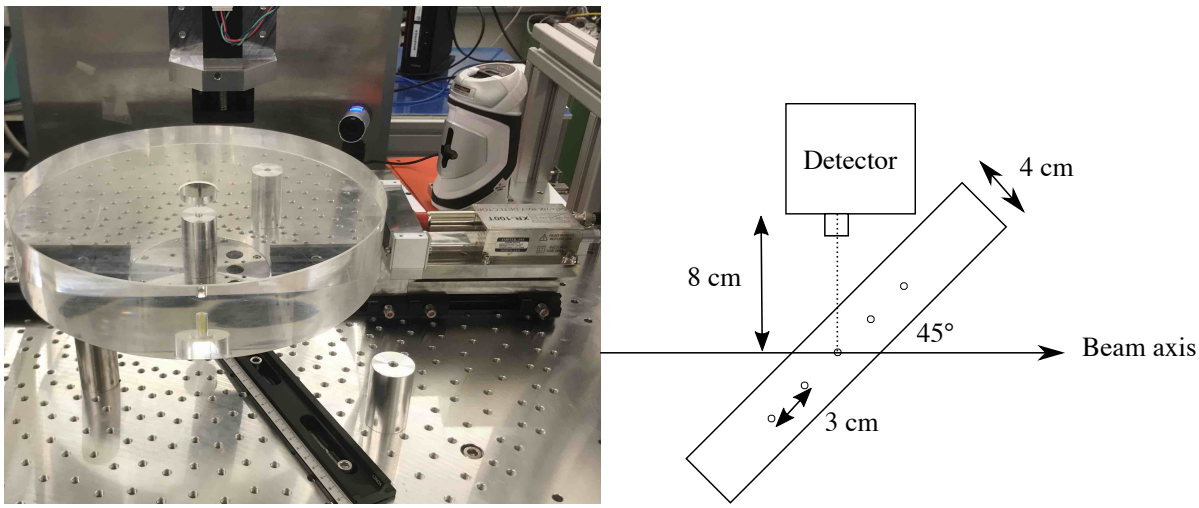

(a) P07 experiment with 30 cm phantom

(b) P21 experiment with 4 cm phantom

Figure 6.8 – In (a) there is a photo of the P07 setup with the 30 cm PMMA phantom placed on small metal cylinders on the stage with the Amptek detector and the collimator with 29 leaves in between. The beam direction is horizontal from top to bottom in the picture with the detector placed on the right at $\theta = 90°$. (b) shows a sketch of the experimental setup at the P21 beamline for the collimator test with the small cylinder phantom with $r = 2$ cm. The small circles along the cylinder axis refer to Eppendorf tubes filled with metal salt solutions.

In figure 6.9 two experimental spectra are compared to the simulated ones. The gold K_α-fluorescence is clearly visible around 68 keV and the K_β-fluorescence a little less prominently at 78 keV. At 40 keV the escape peaks from the gold fluorescence can be seen. The local maximum at 60 keV is the C2 edge, which is diminished relative to the C1 peaks as it is expected for a collimator. Double scattered photons are filtered three times more than single scattered photons in this geometry. For triple scattered photons, the filtering is five times stronger, which explains the lowering of the spectrum below 80 keV. Below 20 keV there is molybdenum fluorescence from the collimator and shielding for stray radiation. The most striking difference between the simulated and experimental spectra is the deviation of the C1 peak at 87 keV. With an incident photon energy of 102.7 keV, this corresponds to a scattering angle of 80° for photons from the beam axis before the Eppendorf tube. The 90° scattering at the target is suppressed because of the horizontal polarization, but for the 100° scattering occurring for photons in the beam behind the Eppendorf tube there is the second peak at 82 keV. In the collimated spectrum the dip between both maxima has vanished because the detector distance increased from 8 to 12 cm to fit the collimator in between. As the traveling

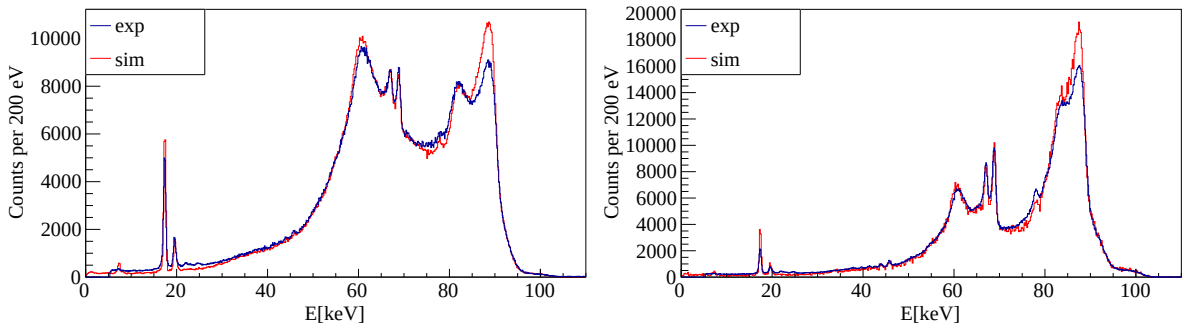

(a) Spectrum without collimator, $Z = 75$

(b) Spectrum with collimator, $Z = 248$

Figure 6.9 – Spectra showing the 5 mg/ml gold solution in the experiment and simulation. For the simulated spectra, $5 \cdot 10^{10}$ photons were simulated and scaled to the integral of the experimental spectra.

path and therefore the expected photon attenuation is larger for the 100° scattering, a peak ratio as in the simulations is expected. For a single experimental spectrum, those both peaks even have the same height, which can only be explained by misalignment of the phantom relative to the detector. In general this effect can be created by moving the phantom parallel to the direction of the incident photons. The photon attenuation does not really change of course, but the integrated yields for scattering before and after 90° do, simply because the path in the phantom behind the 90° position becomes longer. However, both peaks would be shifted to lower energies, which would then suggest a deviation in the incident energy between experiment and simulation. The detector energy calibration is assumed to be correct, since all fluorescence peaks visible in the spectrum match. For future experiments, the careful alignment of the phantom and especially of the collimator are of crucial importance, if the agreement between simulation and experiment shall improve further.

To determine the actual loss of fluorescence photons by using a collimator, five different targets were scanned in the phantom for which the phantom was only moved using the motors. For each target solution, a measurement with and without collimator was made and the amount of gold K_α-fluorescence photons was determined by applying a fit to the spectrum. In figure 6.10, such a fit for an experimental spectrum is exemplary shown for a 5 mg/ml gold solution. In this case, the reduction due to the collimator for the fluorescence photons is almost 50%. The exact values for both experiments and simulations are given in table 6.2. Generally, in the experiments the losses are a bit higher than in the simulations, which could be traced back to a vertical misalignment of the collimator of only 500 µm. Furthermore, slight differences in the experimental Compton background shape between the scan of different targets support that

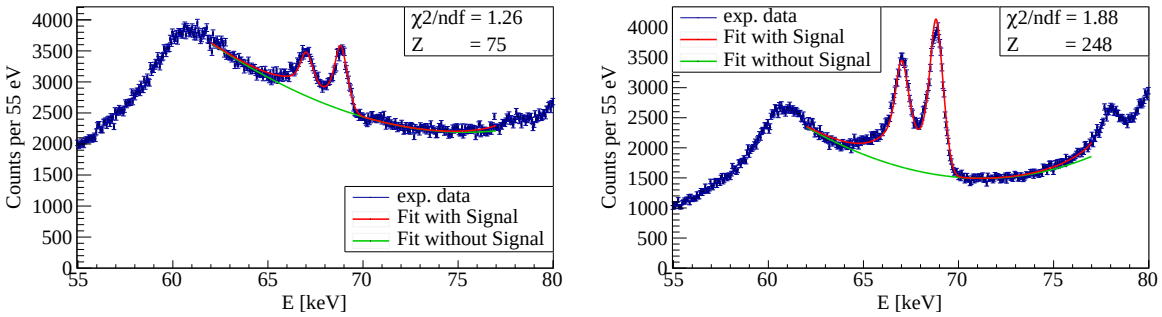

(a) Spectrum without collimator

(b) Spectrum with collimator

Figure 6.10 – This figure shows fits to experimental spectra of the 4 cm phantom containing 5 mg/ml of gold. The fits are made using the Hypermet equation (2.24) for the signals plus a third degree polynomial for the background.

the phantom was not exactly positioned as expected because this effect does not show in the simulations. Besides the placements in the experiment, deviations of the thin molybdenum leaves from being perfectly level and flat in the mounting can also cause a loss in the FOV and thus in the amount of detected signal photons. This results in $Z = 75$ for the uncollimated and $Z = 248$ for the collimated experimental spectra in figure 6.9. The amount of detected photons is approximately the same, which means that in case for PETRA III experiments with inanimate objects where detector overload usually limits the experiment and dose does not matter, the same sensitivity could be reached in a measurement time one order of magnitude smaller if a collimator is used. If, however, the dose is limited as it is the case in in vivo experiments, then the collimated spectrum only reaches 93% of the uncollimated, so there is no improvement. On the other hand, if the detector position is fixed for some reason and a collimator can be placed optionally between the detector and the phantom, then the collimated spectrum would be 40% more significant.

Table 6.2 – The relative amount of the fluorescence photons with a collimator normalized to the spectra without it is compared for simulation and experiment with different scanned gold solutions. The values are corrected for different values of photon flux and detector distance to the beam. In the last column no fluorescence signal was found in the experiment, possibly due to misalignment. The given errors are due to statistical uncertainties.

	5 mg/ml v.1	5 mg/ml v.2	2.5 mg/ml	1.25 mg/ml	0.625 mg/ml
sim	0.545 ± 0.013	0.542 ± 0.013	0.531 ± 0.017	0.519 ± 0.024	0.519 ± 0.034
exp	0.477 ± 0.006	0.458 ± 0.006	0.404 ± 0.008	0.463 ± 0.014	-

7 Human Voxel Model

Whereas simple geometric phantoms are very helpful to understand the basic concepts of XFI, a human or animal body for a real medical application is inhomogeneous and anisotropic. After the development of the MIRD phantom in 1967 by Fisher and Snyder [111], that used mathematical descriptions to describe human anatomy for dose calculations, it was replaced by voxelated phantoms in the 80s due to the higher capabilities and availabilities of computers. A new third generation model is being derived, called mesh models. Meshes offer the possibility to employ more details where needed and the possibility to deform the models, such as for different body postures [112]. For this work, they were not available yet.

In this thesis a human voxel model provided by the ICRP has been used to simulate several cases of different target sites in the human body. This model is available as a download [113] and discussed in detail in the ICRP-Publication 110 [114], a shorter version is offered by Maria Zankl [115]. All the information from this brief summary of the models come from these sources. A model for each, an adult male and an adult female, based on real medical image data taken from CT-scans is processed to be consistent with data already presented decades earlier [107, 116]. Furthermore, the CT greyscale values, called Hounsfield Unit (HU), is transformed into a specific material with a specific density. In total, 140 different body parts are distinguished consisting of 51 different material compositions. For some body parts, for example different cortical bones, the same material is used to build them. The starting point for the model was a whole-body CT scan of a 176 cm male weighing roughly 70 kg and a 168.5 cm female weighing 59 kg. Those values were similar to the design values presented in table 7.1. To reach the design values for the body height and skeleton mass, the voxel lengths have been scaled. After that several more manual changes were made of which a few shall be mentioned: the organs were scaled to the design values by adding or subtracting corresponding voxels, the body fat was adjusted by adding additional adipose tissue layers and lymph nodes were placed using anatomy textbooks since they were not identifiable in the CT images. The elemental compositions of the organs were modified to contain the right amount of blood

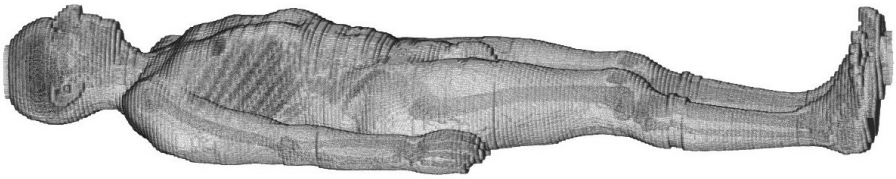

Figure 7.1 – This plot shows an Image of the International Commission on Radiological Protection - Anatomy Male (ICRP-AM) model used in this chapter with the available voxel sizes. Parts of the skeleton is visible because the tissue is semitransparent.

which was necessary because a large part of the blood vessels are missing and therefore the actual amount of blood voxels is way too small. Some changes in the posture were made, for example the arms were moved away from the body and the trunk shape remodeled to remove indentations.

Although these two models already offer quite a lot of details, there are some limitations due to the restriction to same-sized voxels. These restrictions comprise of missing boundaries for organs, such as the urinary bladder, stomach wall or even the skin, wrong thicknesses and shapes for small objects, such as the eye lens, missing blood vessels, missing cartilage, missing details in the respiratory system and missing cortical bone surrounding the inner parts because of space limitations and the wanted bone marrow to bone ratio. However, this not very important for the calculation of sensitivities, it can just pose some difficulties when manipulating the model to place artificial targets or performing dose calculations for very sensitive body parts. The two anatomical models are sometimes called ICRP-AM and International Commission on Radiological Protection - Anatomy Female (ICRP-AF) for the male and female body correspondingly, but the terms are not consistent throughout the literature. An image of the male model is shown in figure 7.1. In this chapter a few possible exemplary target positions in the body will be examined to assess the possible sensitivities and differences in diverse parts of the body. The coordinate axes to describe areas in the voxel phantom are used as follows: x

Table 7.1 – Human voxel model: Voxel edge length and number parallel to the coordinate axes

Sex	Height[m]	Mass[kg]	Voxel length [mm]			Number of voxels		
			x	y	z	x	y	z
Male	1.76	73.0	2.136	2.136	8	127	254	220
Female	1.63	60.0	1.775	1.775	4.84	137	299	436

starts at the belly and goes to the back, y starts from the patient's right side and goes to his left side and z starts at the feet and goes to the head. It has to be noted, that due to a sign error this has to be seen either a left-handed coordinate system or an existing medical condition called situs-inversus, where the organ positions are reversed.

It is obvious that real measurements with individuals or simulations with different models may deviate from the presented sensitivities here due to the individual anatomy and simplifications made for the detector setup.

7.1 Gold Target Located in the Kidneys and the Brain

A Swedish group around Jonson, Börjesson and Mattson wrote a series of papers starting in the 80s about performing in vivo XFI experiments on humans, e.g. [21–24]. Their setup was already quite sophisticated because they filtered a conventional X-ray source with uranium, polarized the beam, placed the detector at $\theta = 90^\circ$ and used ultrasound imaging to locate the ROI first. For the analysis they combined both K_α lines and used a $Z = 3$ significance limit, which is the same in this thesis. Although their detector had a diameter of 25 mm and therefore did not cover the whole solid angle, their results are recreated and extrapolated to the filtering methods presented here. The starting point here is a paper about measuring the retention of platinum in human kidneys published by Jonson et al. in 1988 /[23]. The probands had cisplatin administered as a treatment against cancer, which is known to be nephrotoxic. Non-invasive measurement of the actual amounts deposited in the tumors and kidneys might therefore be helpful in adjusting the necessary doses. Using scanning times of 30 min and a deposited dose of 0.3 mGy in the kidney, they report a detection limit of 8 µg/cm^3 for a tissue depth of 4 cm.

Target in the Kidneys To recreate their finding, a target sphere of 12.5 mm is placed in a kidney in the same depth of 4 cm at $(61.9, 90.1, 300.0)$ mm. The X-ray enters from the side and a detector of the same size is placed behind the back facing the target with a collimator of 2 cm diameter at a distance of 86 mm. Between the target and the detector there is also 4 cm of tissue.

In table 7.2, the resulting sensitivities are listed. For the mean dose of 10 mGy in the beam volume, the local dose in the kidney is actually 27 mGy, which is 90 times more than the

Swedish group used. Considering that the significance scales with $\sqrt{N}$, their detection limit was one order of magnitude better. Moreover, electronic noise etc. is not even considered in the simulations. The uranium filtered spectrum reduced the transmission to 3.5%, but creates a mean energy of 96 keV with an RMS of 16 keV. This can, however, not easily be transferred to the bandwidth variation from figure 5.5, because the spectrum is not Gaussian and no large solid angle detector is used.

To exclude problems with the voxel model, the phantom was simplified to a sphere with 40 mm radius containing the same target. For a chip distance of 53 mm, the significance for the same number of photons is 2 times higher, whereas the different solid angle would suggest a difference of 1.6. However, the spherical phantom is much smaller and less multiple Compton background is created. The difference between gold and platinum is only in the range of 10%, which is expected because their atomic number differs only by one, so that the cross sections and the fluorescence energy in the background spectrum are very similar. Increasing the distance between the collimator and detector can still increase the significance by 20% because the collimation effect improves despite the loss of statistics, however, none of that explains the large difference to Jonson's results. The number of fluorescence photons for the spherical phantom without a collimator using the monoenergetic beam is explicitly checked analytically. When multiplying the transmissions, that are approximately 50% each, the fluorescence cross section and the detector solid angle of 1.4%, $2.4 \cdot 10^4$-fluorescence photons are expected for a chip distance of 53 mm and $2.7 \cdot 10^4$ are detected in the simulation. Considering that photons scattered under a small angle can still excite fluorescence, which is ignored in the analytic calculation, the values seem to fit.

The reason why these simulations with ideal detectors are one order of magnitude worse than the 30 years old experimental finding is unclear. It is possible that either they made a mistake, for instance, by calculating a wrong photon flux, or that information about the experiment was misinterpreted. For example, the information about the collimator geometry and detector

Table 7.2 – For a 25 mm gold target in the kidney in 4 cm depth with 0.1 mg/ml 10^{10} photons were simulated. In the last column the minimal detectable densities for $Z = 3$ are extrapolated. The used incident spectra are a monoenergetic beam and the spectrum of a conventional X-ray source with 140 kV filtered with 0.35 mm of uranium.

Spectrum	$Z(10^{10}\gamma)$	$N_\gamma(10\,\mathrm{mGy})$	$Z(10\,\mathrm{mGy})$	$\rho_{\mathrm{Au}}(10\,\mathrm{mGy})$ [µg/ml]
85 ± 0 keV	5.75	7e11	48.1	6.2
140 kV + U 0.35 mm	4.49	6e11	35.0	8.6

distance was unclear. Nevertheless, their findings appear to be on the edge of possible sensitivity considering the used setup. It could only be improved using a source with a smaller bandwidth, which for them would mean less photon flux when increasing the filtering of their source, or using larger detector solid angles.

Gold Target Located in the Brain In 1991 Jonson reported depositions of platinum in the brain ranging from 14-40 µg [22]. As comparison in the XFI simulation gold is used, but since their atomic number only differs by one, the difference in sensitivity is very small. In total, four steps are made from the simulation with a 1 mm sized beam in the collimated 4π detector to the parameters described by Jonson.

First, a target of 1 mm diameter in the center of the brain at $(0, -2, 804)$ mm is scanned using a circular pencil beam of 1 mm diameter and a cylinder detector with a collimator. At this position, the path length to the top of the head and to the sides is 8 cm and the distance to the front and back of the head is 10.5 cm each. The resulting minimal detectable amounts of gold are listed in table 7.3 using three different incident spectra. Comparing the mass to the

Table 7.3 – Significances for a spherical gold target for different positions in the brain of the ICRP-AM phantom for different incident spectra. The simulation was performed using 10^9 incident photons for the 1 mm beam and 10^{10} for the 25 mm beam. The significances are subsequently scaled to a dose of 10 mGy. For a limit of $Z = 3$, the minimum detectable gold densities and masses are given.

Spectrum	$Z(10^9\gamma)$	Dose(1e7γ) [mGy]	$Z(10\,\text{mGy})$	ρ_{min} [mg/ml]	m_{min} [µg]
1 mm gold target in the center of the brain					
85 ± 0 keV	43.6	0.154	35.14	0.85	0.45
140 kV Unfiltered	3.28	0.134	2.83	10.58	5.5
140 kV U 1 mm	30.8	0.187	22.49	1.33	0.70
25 mm gold target in the center of the brain					
85 ± 0 keV	15	3.34E-04	82.05	0.0037	27
25 mm gold target in the brain within a depth of 4 cm					
85 ± 0 keV	35.8	3.80E-04	183.69	0.0016	13
140 kV U 0.35 mm	26.4	4.21E-04	128.71	0.0023	19
25 mm gold target in the brain within a depth of 4 cm using only a 25 mm detector					
85 ± 0 keV	6.69	3.90E-04	33.89	0.0089	72
140 kV Unfiltered	1.61	3.59E-04	8.48	0.0354	290
140 kV U 0.35 mm	5.28	4.31E-04	25.40	0.0118	97
140 kV U 1 mm	6.60	4.55E-04	30.94	0.0097	79

20 cm sphere, it is only 7% larger. If only the plane of the incident beam and the detector is considered, the mean radius is approximately 92.5 mm. Removing the attenuation of the different length and replacing 7 mm of soft tissue by bone, the already small difference in sensitivity is again halved. Then again, considering the approximations already made, this should be negligible. The more important difference to the sphere is that a part of the solid angle is simply blocked by the rest of the body. For the monoenergetic X-rays and the filtered X-ray tube the spectra are shown in figure 7.2. The target has also been moved along the beam in (a) with similar results to section 5.5. If the ROI is known to be close to the surface and an X-source with a narrow spectrum just above the K-edge is available, K_β-fluorescence is more sensitive than K_α-fluorescence because the attenuation to a measuring position in the back is simply smaller.

Second, as a first step to recreate Jonson's geometry, the target and the beam diameter are increased to 25 mm. The number of leaves is decreased to only 100 because the collimator's FOV needs to increase in order to not filter too much signal photons. However, such a collimator cannot filter effectively anymore. Actually, if comparing it to a simulation without collimator, for which the detector could be smaller while still covering the same solid angle by moving it closer to the beam, the sensitivity difference is only 10%, which should be negligible. As a consequence, the minimal detectable mass for the same amount of incident photons becomes 2.3 times larger compared to the 1 mm beam and normalizing both values to the beam cross section. This is exactly the factor lost by not using the collimator with 3600 leaves.

Third, the 25 mm target is moved out of the center to $(57, -24, 804)$ mm so that the path length of the incident beam to the target and the distance to the back of the head both are reduced to 40 mm. At this target position the sensitivity increases by a factor of two, which is explained by the path length reduction towards the target of 4 cm. The mean path distance to the detector in forward direction stays almost the same.

Fourth, the 4π detector is replaced by a small detector with a diameter of 25 mm as used by Jonson et al. Here the detector is placed at a distance of 61 mm to the target. If the detectable masses are scaled to the same detector distance as for the kidney scan, which means multiplying them with a factor of 1.4, they are almost exactly twice as high. As the path distances from the source towards the target and towards the detector are same, the main difference is the attenuation of the bone. The detectable masses also agree with the 4π detector because the solid angle is only 1% compared approximately 50% chosen by the pixel selection.

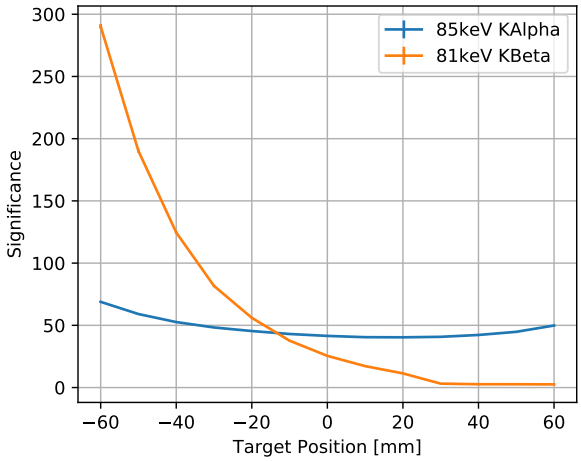

(a) Variation of the target position

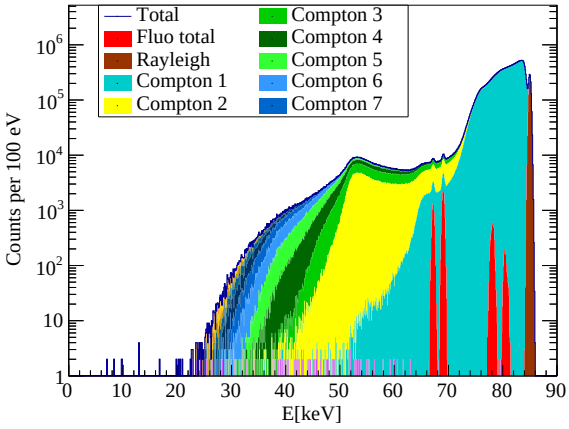

(b) Incident spectrum 85 ± 0 keV

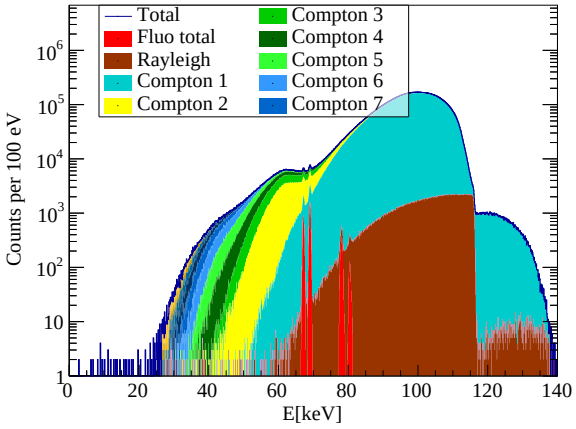

(c) Incident spectrum 140 kV with 1 mm uranium

Figure 7.2 – For XFI simulations from the side of the head, in (a) the target is moved along the beam for 10^9 photons. For K_β 81 keV and for K_α 85 keV are used. In (b) and (c) the resulting spectra after performing pixel selection are plotted for two different incident spectra.

Therefore, a difference of $\sqrt{50} \approx 7$ would be expected for a symmetric phantom. Since the small detector is placed at an ideal position whereas the large detector measures all around the head, the actual difference should be smaller than this factor.

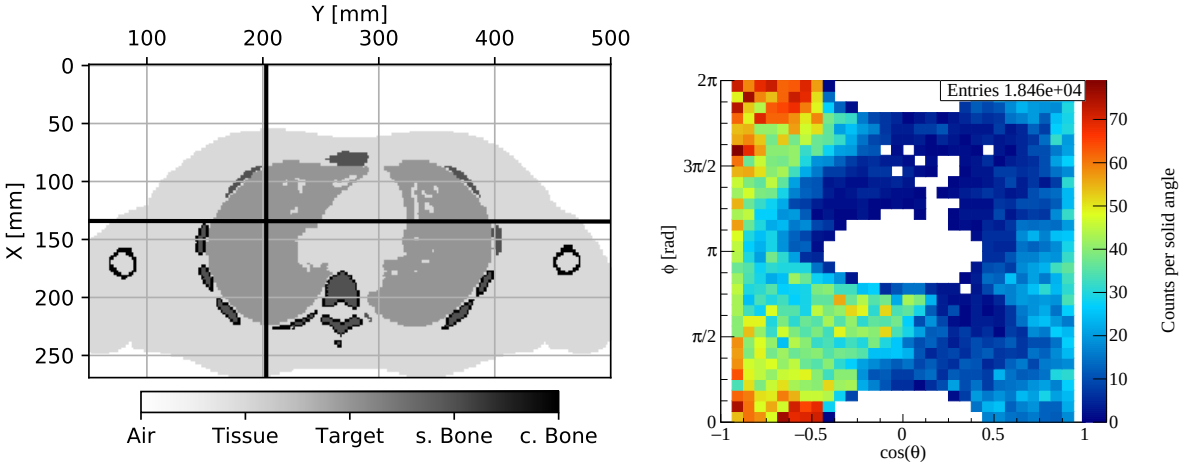

(a) Position of target in lung

(b) Fluorescence Distribution

Figure 7.3 – In (a) the target position in the lung is shown. In (b) the resulting fluorescence distribution per solid angle element in the detector based on the target position in (a) is shown for an XFI simulation with the incident beam coming from the chest. The white pixels in (b) contain zero counts with the two ellipses at $\cos(\theta) = 0$ corresponding to the openings in the detector for the human's legs and head.

7.2 Gold Target Located in the Lungs

A completely different reconstruction approach using a fluorescence target in the lungs is published by Vernekohl et al. [100]. They propose a detector layout using a two-layer detector of silicon inside and CdTe outside as a Compton camera to reconstruct the position of the target. For the gold fluorescence energy, Compton scattering in silicon is the most probable process. By detecting the energy deposition of the scattering event and the resulting energy loss, a scattering angle is reconstructed yielding a spatial resolution of the order of 1 cm. For a breathing human, higher resolutions will be difficult anyway. In addition, they use a sheet beam at the cost of sensitivity to increase data inquisition speed. With a monoenergetic beam of 82 keV and K_β analysis in backwards direction, they use four detector panels of 16x26 cm^2, which is close to an already existing 10x10 cm^2 array of Hexitec chips [89]. For a realistic CdTe resolution, they give a detection limit of $560\,\mathrm{pM/l} = 110\,\mu\mathrm{g/ml}$ gold for a cylinder target with a diameter of 5 mm in the lungs.

As comparison the same target is placed in the center of the left lung in the ICRP-AM model and scanned using the collimated cylinder detector. The exact target position is (0,-67,492)mm. Due to the asymmetry of the phantom, the K_β analysis actually is the best choice

for scanning a lung target as also done by Vernekohl. However, a pixel selection can still help to improve the significance. A collimator on the other hand is not needed for K_β, it even decreases the significance by 10% since the background is completely dominated by single scattered photons. For 81 keV, which is 20% more significant than the 82 keV chosen by Vernekohl, with a beam direction from the chest, 110 pM/l is the resulting detection limit if the cylinder target is scanned with a 1 mm beam and the spectra containing target fluorescence are added up. The resulting sensitivity is 5 times better than for Vernekohl's setup, but a reconstruction of the position along the beam is still missing. For an XFCT-like reconstruction method, at least 2 directions would be necessary for a single target decreasing the sensitivity by at least $\sqrt{2}$. Transferring that into a single scanning point with a circular beam, as in section 3.1 for the 30 cm sphere, the detectable mass of 0.18 µg is 7 times smaller than for the sphere.

Because of the anatomy and the position of the target in figure 7.3(a), the simulated fluorescence distribution in (b) is asymmetric. Here the coordinate system is oriented in such a way, that $\cos(\theta) = -1$ is at the front of the human model, its head is at $\cos(\theta) = 0$ and $\phi = 0$ and its back is at $\cos(\theta) = +1$. The longer path through the phantom, which is necessary for fluorescence photons to leave through its back side, and the attenuation of the rib cage and the spine are the main reasons for the higher amount of fluorescence photons detected at the front of the phantom. Optimizing the setup for K_β fluorescence is therefore a suitable choice because when the beam enters the phantom from its front side with an incident energy of 81 keV, the phantom's front side is also the position where the signal background is the smallest. The reason for that is that without the Doppler effect a Compton backscatter event would cause the photon to lose too much energy to be still detected within the signal interval around 78 keV. Consequently, a K_β scan from the back is five times less sensitive compared to the front. Half of the difference can be attributed to the attenuation of the straight path to the fluorescence target and the other half has to be attributed to the bones in the back attenuating the signal photons. Comparing this value to the K_β sensitivity for the sphere, the difference even is a factor of 20. Considering that the length of the phantom in the direction of the beam is 21 cm and the target is placed in a depth of 8 cm from the chest, the transmission towards the target back in soft tissue already is a factor of 11 higher for the phantom. When replacing half of that distance with lung material with a density of only 0.4 g/cm^3, the transmission for the lung target is 25 times higher. If in addition it is also considered, that the path out of the phantom is larger than the 8 cm for all scattering angles smaller than 180°, the K_β detection limit of 0.18 µg seems very plausible. The K_α-fluorescence for a scan from the front yields a

detection limit of 0.42 µg and almost half the mass (0.24 µg) with a scan from the back. The difference can be attributed to the bones in the back reducing the significance for a scan from the front. Comparing these values to a sphere of 20 cm diameter, both values are very close to the detection limit of 0.38 µg. The effect of the less dense lung material cancels the longer path lengths for photons scattered to the side.

7.3 Gold Target Located in the Thyroid

A scan of a target in the thyroid is made as an example for a very asymmetric target position. Furthermore, it has historic significance for the field of XFI since Paul Hoffer made the first in vivo measurements with iodine in the thyroid already in 1968 [20]. In figure 7.4(a), the target position right behind the trachea is shown. Strictly speaking it is outside of the thyroid, but moving the target a little to the left or to the right has little influence on the detectable masses. Not only is the difference through tissue to the front of the body only 18 mm compared to 115 to the back, the back is also shielded by the spine. Moreover, outside of the plane there are the shoulders, the arms, the trunk and the head. Here it is obvious that a detector placement close to the organ of interest might be a good decision. Therefore, K_α analysis with 85 keV, which is the ideal energy for many studied cases in this thesis, is not optimal here, the minimal detectable mass is 220 µg. For a detection in forward direction, the fluorescence photons would need to travel all the way through the neck. That is why a higher energy, like 120 keV is twice as sensitive yielding a detection limit of 100 µg because Compton1 is already excluded and Compton2 cannot be in the most backward part of the detector. But as expected, K_β-fluorescence is the best choice being twice as sensitive as the best K_α energy yielding a possible detection limit of 55 µg. In figure 7.4(c,d) the bandwidth is varied for different mean incident energies showing again, how sensitive K_β is to an increase in bandwidth. For a bandwidth of 7%, it becomes worse than K_α-fluorescence.

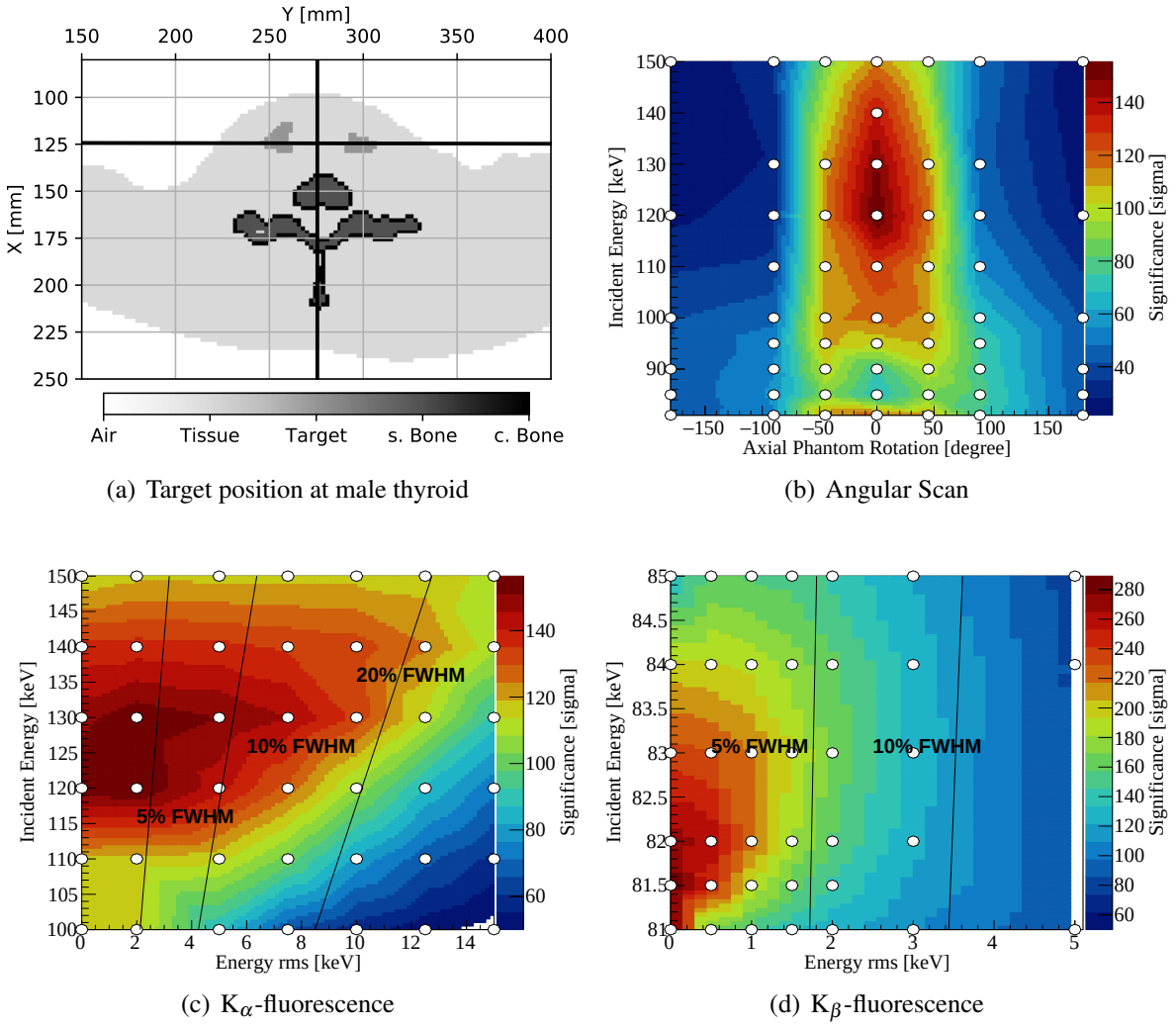

(a) Target position at male thyroid

(b) Angular Scan

(c) K_α-fluorescence

(d) K_β-fluorescence

Figure 7.4 – In (a) the target position at the thyroid marked by the black cross is shown together with the organ itself and the surrounding spongy and cortical bones. (b): For a dose of 10 mGy per scan, the thyroid is scanned from different angles with different incident energies. (c,d): The human thyroid is scanned with different energies and energy bandwidth from the front.

7.4 Gold Target Located in the Liver

The liver is chosen as an example target position that is not placed in the center of the body and surrounded by bones. A target sphere with 1 mm diameter is placed in the centroid of the liver in the ICRP-AM phantom at $x_S = \sum_i x_i \cdot V_i / \sum_i V_i$, as the midpoint of all coordinate intervals is outside the organ itself due to its non-convex shape. Due to the organ's role for the metabolism, in general a diffuse tracer distribution might be expected, which is not further considered here. As a consequence small increases in tracer depositions may not be detectable, which is also the case for the kidneys or the bladder.

In figure 7.5 the target position is shown together with an angular scan for both, K_α and K_β-fluorescence. For the angular scan the X-ray beam always stays in the axial plane shown in (a). This scan shows one of the flaws of the voxel models. Although five ribs are visible on the left in the anatomy image, only two of them are actually surrounded by cortical bone, which due to its density and calcium content is responsible for most of the attenuation. Starting at 0° only the second and third rib contain the cortical bone material which results in a decrease

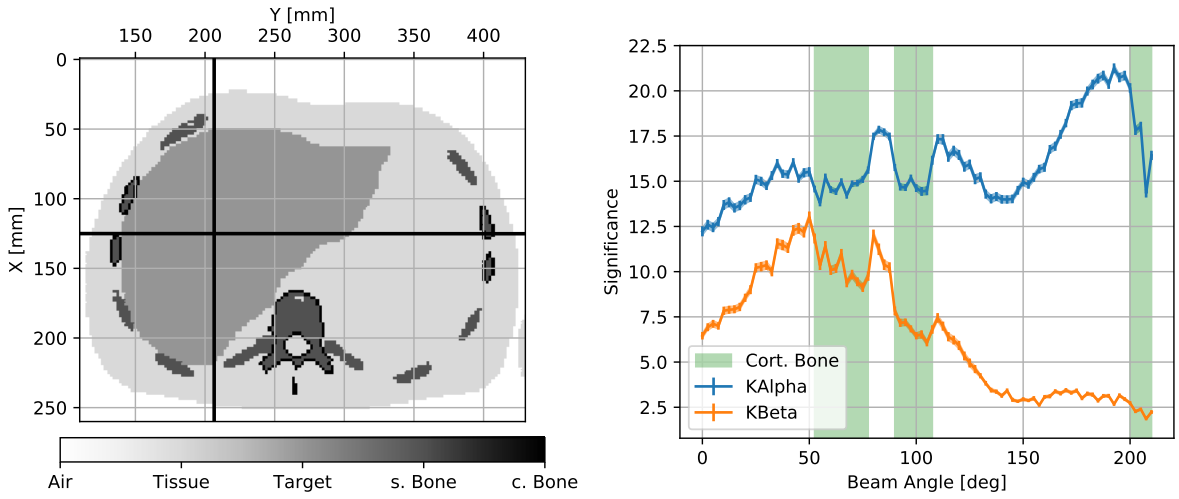

(a) Target position in male liver

(b) Angular scan of the target

Figure 7.5 – In (a) the target position in the liver marked by the black cross is shown together with the organ itself and the surrounding spongy and cortical bones. (b) shows an angular scan of the target in the liver with 85 keV. The green bars mark the angles, where the incident beam becomes diminished by cortical bone before reaching the target thus reducing the significance. At 0° the target is at the belly side and moves counterclockwise referring to (a).

of significance of 17%. 4 mm of that material absorb the same amount, which corresponds to two voxels of that material in the beam. At 200° the spine moves into the incident beam explaining the decrease here. When comparing the plots for both fluorescence lines, it has to be kept in mind, that K_β is analyzed in backwards direction. Therefore, a scan from the front has two advantages over a scan from the back. The distance to the target is shorter and the front part of the patient is less shielded because there are no spine and no ribs in the center. For the K_α-fluorescence the distance to the target is less important because it is preferably measured in the forward hemisphere. Therefore, the highest significance is reached from the back because of less shielding at the patient's front. The sensitivity limit is achieved here for a scan from the back with K_α-fluorescence, where the $Z = 21$ translates into a minimum detectable gold mass of 0.75 µg.

7.5 Gold Targets Located in the Abdomen

Three different target positions in the abdomen are summarized because the parameters are almost identical. Considering the depth inside the body, the pancreas, prostate and ovaries are very similar, which results in the same set of optimal parameters for an XFI scan and very similar minimum detectable gold masses. All these organs are relevant cancer sites [117]. For men, prostate cancer is the most probable variant of cancer with a share of 23% of newly diagnosed cases and it is responsible for 11.3% of male deaths by cancer. Pancreas cancer is fourth on the list of deaths by cancer and one of the most deadly with 5 year survival rates below 10%. Once there are symptoms, it is usually already too late. Ovary cancer for women is fifth on the list of deaths by cancer. Therefore, as a simple representation of a tumor, a sphere with a radius of $r = 0.5$ mm and 10 mg/ml of gold was placed in the center of these organs.

In table 7.4 the minimum detectable gold masses are listed for a spherical beam with $r = 0.5$ mm. For the target in the ovary, both paths to the front and towards the back are 95 mm long. The pelvic bones in that plane look a bit like a cone shielding the sites completely and the front more than the back. Therefore, the difference between scanning from the front to the back is not that large. Scanning K_α from the front is only 15% better than from the back.

Looking from the front, the prostate is shielded by 1 cm of pubic bone. The path distance to the front is 90 mm and 100 mm to the back. Both fluorescence lines are 25% more signifi-

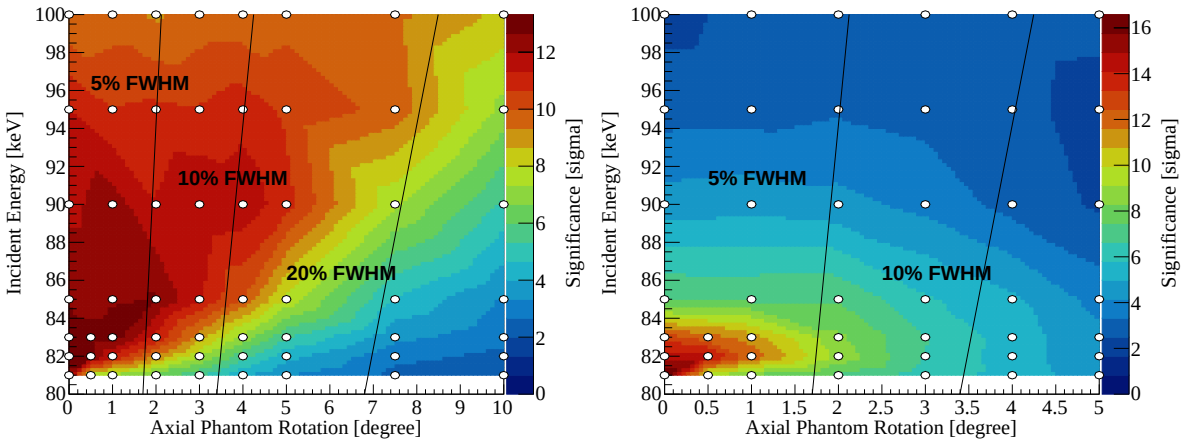

(a) K_α-fluorescence (b) K_β-fluorescence

Figure 7.6 – Simulated significances for a scan of the male pancreas from the front with different energies and energy bandwidths using 10 mGy. The space between the small circles is interpolated.

cant when scanned from the back. For K_α, the incident beam reaches the target with 25% higher intensity and the bone does not cover the full hemisphere towards the forward direction. Whereas for K_β, taking the longer path twice still yields a higher transmission than when going through the bone to the target. The two additional entries in the table again show, that the local inhomogeneities are of little importance, as already demonstrated in section 5.6. For XFI the material and path length towards the targets and from there on the outer shape of the

Table 7.4 – Minimum detectable masses for 10 mGy in different target locations with a circular beam with $r = 0.5$ mm entering the phantom from its front side. For Prostate[1] every phantom voxel was replaced by water and for Prostate[2] every voxel was replaced by the mean material along the beam. In the last two lines two homogeneous sphere phantoms are given as comparison.

Organ	position [mm]			K_α 85 keV		K_β 81 keV	
	x	y	z	m_{min} [µg]	N(10 mGy)	m_{min} [µg]	N(10 mGy)
Ovary	26	28	34	0.57	$8.1 \cdot 10^8$	1.1	$8.6 \cdot 10^8$
Pancreas	-12	1	320	1.3	$9.7 \cdot 10^8$	0.93	$1.0 \cdot 10^9$
Prostate	26	-9	12	0.77	$7.1 \cdot 10^8$	1.2	$7.4 \cdot 10^8$
Prostate[1]	26	-9	12	0.66	$7.9 \cdot 10^8$	X	X
Prostate[2]	26	-9	12	0.78	$7.6 \cdot 10^8$	X	X
20 cm Sphere	0	0	0	0.38	$8.6 \cdot 10^8$	0.61	$9.0 \cdot 10^8$
30 cm Sphere	0	0	0	1.1	$1.2 \cdot 10^9$	3.6	$1.3 \cdot 10^9$

phantom are the dominant factors for the resulting sensitivity. The phantom, whose material is completely homogenized based on the material in the incident beam, yields the same result as the phantom actually containing localized bones.

The target in the pancreas is located a little more asymmetric. To the front the path length is also 95 mm and in the middle there are no ribs, but towards the back it is 125 mm and there is also the spine. Therefore, the K_β scan from the front yields very similar values as the other targets. The K_α photons, however, need to travel 30 mm further, resulting in 80% higher attenuation. Comparing the minimum detectable masses to the two spheres listed, all cases are close to the sphere with 20 cm diameter, which is plausible when considering the distances to the phantom's surface. Regarding the difference between the two listed spheres, K_β scales as it is expected from the two additional attenuation factors for 5 cm. Both yield a factor of 6. Since most of the background is created close to the phantom's surface, the actual depth is of minor importance for the signal background. For K_α, the difference is smaller because also the signal background becomes attenuated in the forward detector hemisphere.

For the target in the pancreas, in figure 7.6 the energy bandwidth is varied for different incident energies. Very similar to the bandwidth variation for the 30 cm sphere in figure 5.5, energies close to the K-edge, that are favorable for K_β analysis are very sensitive to an increase in bandwidth. If the X-ray available has, e.g. 10% FWHM of bandwidth, using energies around 95 keV allow for the detection of two times smaller tracer masses.

8 Gadolinium Retention from MRI Contrast Agents

Since 1988 it is estimated that over 450 million doses of Gadolinium Based Contrast Agent (GBCA)s have been used for MRI procedures [118]. Due to its paramagnetic properties, gadolinium shortens the T1 and T2 relaxation times of nearby nuclei [119]. Although the medical compatibility of GBCAs has been assumed to be very good, in 2013 Kanda et al. [120] showed an abnormal T1 shortening in some parts of the brain (globus pallidus and dentate nucleus) during unenhanced MRI with patients who had repeated MRIs previously. This has been explained with gadolinium retention in the body after the procedure. Since then several studies where performed to determine the amount of retained gadolinium and its toxicity to the human body, e.g. [121–123]. The amount of gadolinium found depends strongly on the type of GBCA and the amount of injected dose [121]. Finally, in 2017 the European Medicines Agency recommended the suspension and restriction of several GBCAs [124].

XFI offers a non-destructive and non-invasive possibility to find and quantify gadolinium retention inside the body compared to tissue extraction or laser tissue ablation [122]. For the latter methods, the extracted tissue can then be analyzed using, for instance, Inductively Coupled Plasma - Mass Spectrometry (ICPMS). In this work the proposed detector design and scan procedure for large phantoms is used to explore its sensitivity in determining the amount of gadolinium in this context. As an example a human finger from the ICRP voxel model is used in the Geant4 simulations. The sensitivity is then compared with exemplary values found in the literature. After hip replacement, the extracted hip bones were analyzed using ICPMS and showed 1.770(704) µg Gd/g bone for Omniscan and 0.477(271) µg Gd/g bone for the more stable macrocyclic Prohance [123]. Another study concerning retention in the brain with only five patients showed values from 0.1 µg Gd/g bone to 19.4 µg Gd/g bone after receiving Omniscan.

For XFI, simulations and phantom experiments with human bones are already done by two groups by Lord et al. [40] and Mostafaei et al. [41] using an almost identical setup with a radioactive ^{109}Cd source emitting 88 keV gamma photons in the GBq regime and germanium detectors placed in the backwards direction directly besides the radioactive source. Both use phantoms to simulate measurements in the human tibia and present very similar sensitivities of 1.64 µg/g to 1.72 µg/g bone [40] and 1.81 µg/g to 3.47 µg/g bone [41]. However, both analysis methods do not recover spatial information but only the existence and amount of gadolinium. Michelle Lord, furthermore, already performed and published results for in vivo measurements of volunteers who were exposed to the macrocyclic Gadovist produced by Bayer 5 years before and showed a mean deposition of 1.19(73) µg Gd/g bone mineral, which was a significant increase compared to the control group [125]. For a 30 min measurement, the calculated doses are given as 357 µSv organ dose to the tibia and 0.13 µSv full body dose.

8.1 Human Finger

The scan of a finger offers a high potential to assess the amount of gadolinium retention in bones due to its high bone to tissue ratio, meaning less absorption of the created signal, and its small size which offers the possibility to build a rather small detector that covers a large solid angle. The tibia scans used by Lord et al. [125] are not as sensitive as finger scans when using a pencil beam and large detectors. Using the cylinder detector with a collimator, the minimum detectable gadolinium density in the tibia bone is estimated as 1.6 µg Gd/g bone using simulations, which is 2-3 times worse than in the finger. The used dose of 10 mGy in the beam volume corresponds to 24 nSv full body dose, which is 5 times less than the source measurement by Lord. A finger seems to be the better choice because the calf absorbs fluorescence photons and creates scattering background because of a higher attenuation of the incident beam. However, if the source is isotropic as used by Lord, then the larger bone is probably an advantage.

The male phantom had the disadvantage of flexed fingers which prevents scanning several aligned phalanges (bones in fingers) with the beam parallel to the finger and simulations with small cylinder detectors covering the whole finger. Therefore, the left index finger of the female phantom was chosen which is in straight posture and cut out to separate it from the rest of the hand. The finger bone is filled homogeneously with 1 mg/ml gadolinium to ensure the simulated statistics are high enough to avoid misinterpretations. This includes both the cortical

and cancellous part of the bone. The voxel model does not have explicit bone marrow voxels in the finger bones. It is made sure by a variation of the concentration over several orders of magnitude, that the significance still scales linear with decreasing gadolinium density.

4π Detector As a starting point the human-sized cylinder detector with the phi collimator as described in section 3.1 is used to scan the isolated left index finger. The cylinder surface is closed apart from two spherical openings of 300 mm around the beam entry and exit. The rest of the voxel model is not built to increase simulation speed. But since only the arm would be needed to reach into the detector, the error by this simplification should be negligible. Nonetheless only the arm would need to reach into the detector, consequently the error caused by this simplification should be negligible.

The finger is scanned using two orientations relative to the beam using an incident energy of $E_\gamma = 70\,\text{keV}$. The first orientation of the finger is parallel to the beam. Due to the X-ray beam entering through the finger tip, the amount of bone inside the beam volume is at maximum. The sensitivity is therefore the highest achievable, but the spatial information of the gadolinium deposition is very limited because using this orientation the projection of the finger bone is very small. The maximum point at $x = 2\,\text{mm}$ and $y = 0\,\text{mm}$ is chosen for further analysis. Here the significance is $Z = 4900$ for 10 mGy which is $5.5 \cdot 10^8$ photons within a box beam with side length of 1 mm. The box-shaped beam is used in order to allow for a continuous scan of an area without overlap, which would not be possible using a circular beam. For these values, there is 63 µg of gadolinium in the beam which means that the bone in the beam volume is 63 mm long. For a detection limit of $Z = 3$, this transfers to 0.44 µg Gd/g bone with an actual bone mass of 86 µg. The minimum gadolinium density is calculated using $\rho_{\text{min}} = 3\sigma/Z \cdot m_{\text{Gd}}/m_{\text{bone}}$ with the actual gadolinium and bone masses depending on the position of the finger in the beam. The effective body dose for one scan point with 10 mGy in the beam volume is 25 nSv for the female voxel phantom weighing 59 kg.

For a scan with the finger orientation perpendicular to the beam, the incident beam moves from the side of the fingernail to the palm. A rotation of 180° yields the approximately same result, since the finger is quite symmetric and the transmission through the surrounding tissue is high. The significances and the minimum gadolinium density are again shown in figure 8.1. Here the local sensitivity maximum at $x = 4\,\text{mm}$ and $y = -2\,\text{mm}$ is chosen because there is the finger joint between the second and third phalanx, where the bone is actually the thickest. The part on the right-hand side already belongs to the palm. Because of the smaller mass in the

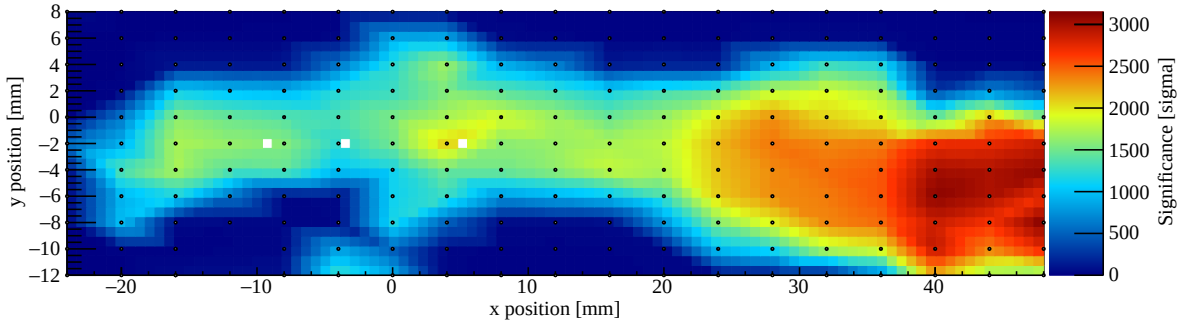

(a) Significances for 1 mg/ml of Gd homogeneously in the bone

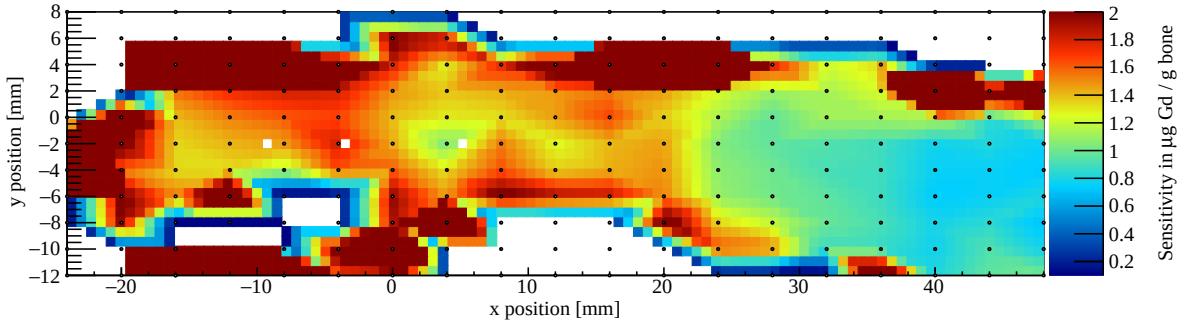

(b) Minimum Gd concentration in units of µg Gd/g bone

Figure 8.1 – This figure shows a position scan with 10 mGy of the female left index finger perpendicular to the beam. The small circles mark the actual data points, the space in between is interpolated.

beam volume, here only $2.3 \cdot 10^8$ incident photons with 70 keV may be used for the dose of 10 mGy. At this position there are 10.2 µg gadolinium in the beam volume and the minimum detectable density would be 1.04 µg Gd/g. Calculating the whole body dose with a single scan at this local maximum yields 4 nSv, which is 32 times less than the dose Lord et al. use for a sensitivity of 2.3 µg/g bone at the time of the experiment [125].

In figure 8.2(a), the energy dependence of the significance is given for both finger orientations with and without a collimator. Unlike for gold, the significance increases with higher energies until at 120 keV the Compton background is almost zero so that from there on only the fluorescence cross section becomes smaller, thus the significance becomes lower again. Furthermore, the dose per incident photon increases. However, this is only valid for perfect detectors with 100% efficiency, no electronic noise and no incomplete energy depositions in this regime. The energy variation with the Amptek detector shows that these effects actually diminish the sensitivity for higher energies.

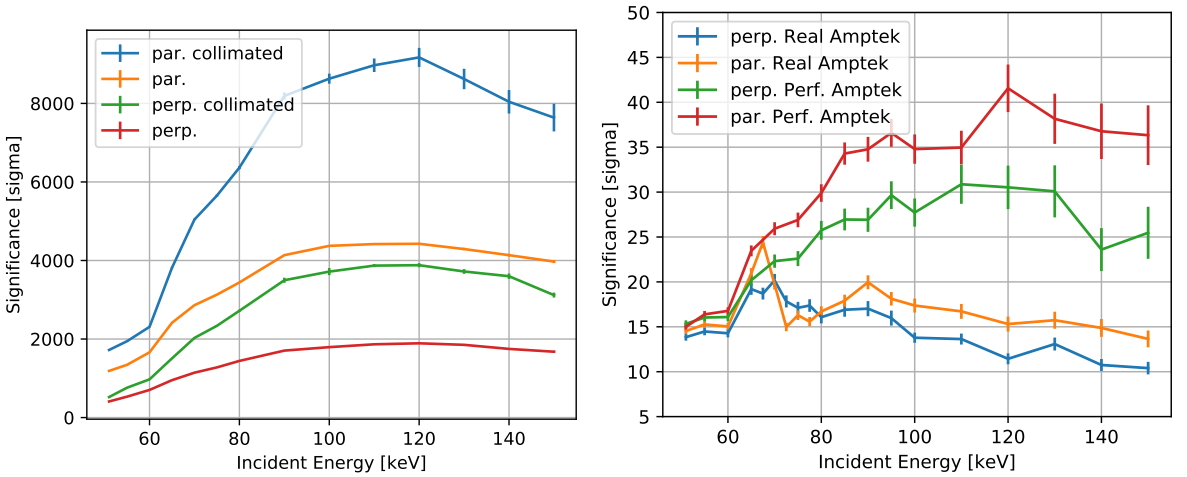

(a) 4π detector with 1 mg/ml and 10 mGy

(b) Amptek detector with 0.1 mg/ml and 10^{10} incident photons

Figure 8.2 – For two orientations of the finger, parallel and perpendicular to the beam, the incident energy is varied. In (b) the Amptek is placed at $\theta = 90°$. For the perfect detector, every photon is completely absorbed. The error bars result from statistic uncertainty alone.

The pixel selection algorithm is not really needed for gadolinium measurements because it only improves the sensitivity by a factor of 2-3 for energies below 55 keV where the sensitivity is not optimal anyway. For higher energies, the background distribution is almost isotropic because the background consists of higher Compton orders. Moreover, the fluorescence photons are not attenuated very much because of the small size of a finger so that apart from some pixels around the beam axis and openings for the phantom, where the collimation is not optimal, there are no pixels to be discarded. The collimator itself yields an improvement of approximately a factor of 2, however, in the current layout, where it fills half the detector radius, the necessary detector surface quadruples if a collimator is implemented. Compared to the use with small detectors, here the solid angle does not become smaller because the detector is enlarged accordingly to always cover the full solid angle.

If the only purpose of an XFI scanner is investigating small objects, such as fingers, the size of the standard detector in this work is of course a lot bigger than what is actually needed. A smaller cylinder detector with a radius of 2.5 cm and a length of 10 cm could be put over the finger like a ring with two openings on the side for the beam. It yields the same results as the large meter-sized detector without a collimator. If a collimator shall be used, a size reduction down to a radius of 5 cm can be made without loosing sensitivity. For smaller

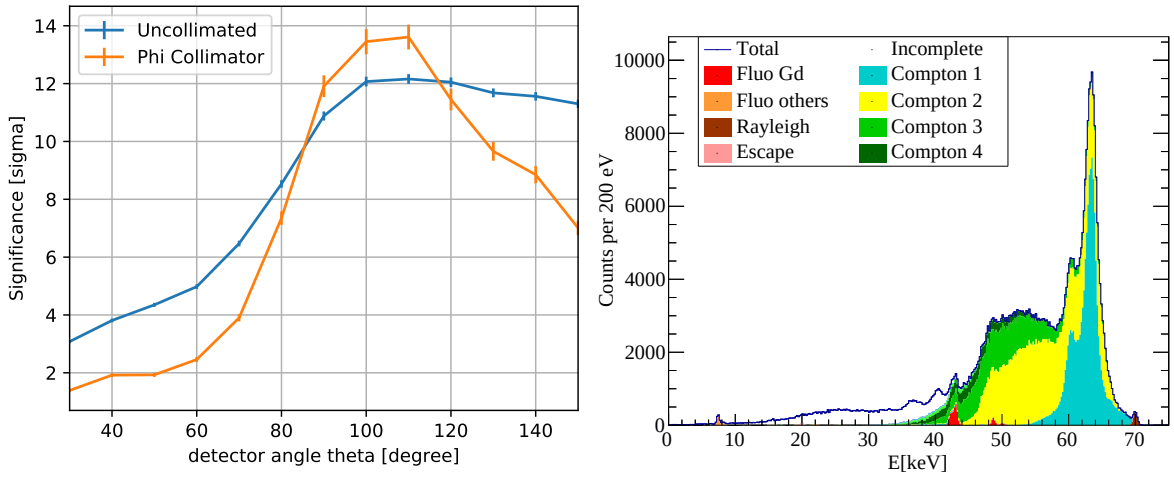

(a) Hexitec angular variation

(b) Amptek spectrum at $\theta = 90°$

Figure 8.3 – (a): Variation of the detector angle θ for 70 keV and 10^{10} photons with and without a phi leaves collimator for a Hexitec detector. Without a collimator the detector is placed at a distance of 5 cm, with a collimator it is placed at 7.5 cm. The spectrum in (b) was simulated with the finger perpendicular to the beam with an Amptek detector at a distance of 5 cm at $\theta = 90°$. 10^{10} incident photons with 70 keV yield a significance of $Z = 30$ for 100 µg/ml. The *Incomplete* counts in the legend summarize all photons that deposited only a part of their energy without forming an identifiable escape peak.

detector radii, the number of collimator leaves needs to increase in order to keep the small FOV. Otherwise more Compton scattering can reach the detector. But even with a higher number of thinner leaves at some point they become transparent and therefore useless. If spatial information about the gadolinium distribution is irrelevant and the only goal is to find the average concentration, spectra from neighboring beams could be added up or a larger incident beam could be used, which at PETRA III is not possible. Depending on the desired sensitivity, the dose could also be reduced, which, however, is already quite low if projected to the full body mass. If the whole index finger with a mass of 54 g is exposed to 10 mGy, the full body dose would thus be 9 µSv. For a significance limit of $Z = 3$, the minimum detectable concentration would then be 30 ng Gd/g bone.

Small Detectors To simulate a measurement of the gadolinium finger of a dead person without concern about dose, the Amptek and Hexitec detectors are used with a setup suitable for the P07 or P21 beamline at PETRA. Compared to the fully calibrated Amptek, which was used for the experimental data in chapter 6, the Hexitec is expected to yield a four times better

sensitivity due to its 16 times larger chip. In figure 8.2(b) the incident energy is varied for the same two orientations: once parallel and once perpendicular to the incident beam. To explain the sensitivity drop after 70 keV the Amptek is additionally simulated as a perfect detector in comparison, which means every photon reaching the chip is fully absorbed. In figure 8.3(b), a spectrum for 70 keV is shown with CdTe detector effects. At 40 keV in this spectrum the escape peak from the C1 peak at 63 keV is clearly visible. Therefore, for higher incident photon energies the signal background becomes dominated by incomplete absorbed energies. It has to be noted that this depends on the detector material. If instead for example a germanium detector is used, this effect changes accordingly.

The minimum detectable gadolinium concentration for an Amptek distance of 5 cm at $\theta = 90°$ and 10^{10} incident photons is 6.6 µg/g for the finger perpendicular and 5.5 µg Gd/g bone for the finger parallel. The dose for the first case is 470 mGy and 180 mGy for the second case because of more mass in the beam. The Hexitec detector with the perpendicular finger orientation the minimum concentration is 1.84 µg/g Gd/g bone, which is about a factor of four better than the Amptek. A quarter would be expected because of the 16-times larger chip area. If the Hexitec value is scaled to 10 mGy and a 4π detector, the value is 80% better than an actual 4π simulation without collimator from the large chapter. Since the position of the Hexitec is almost ideal, it is expected to be better than a real 4π scan, since there also unfavorable angle positions, e.g. from the finger tip, are covered with the detector.

In figure 8.3(a) an angular variation for the detector position at $E = 70\,\text{keV}$ is given. It can be seen that $\theta = 90°$ is very close to the maximum value. Furthermore, at 90°, the detector could be moved closest to the phantom before a part of the detector or collimator moves into the beam axis. Smaller angles are less sensitive because the Compton peak moves to higher energies and so does the Compton escape peak. The collimator offers only an increase of 10% for angles around 100°. The reasons why a collimator for such small objects is not helpful, are explained in the next chapter for a rat voxel model. Additionally an assumed homogeneous distribution of gadolinium distribution in the bone and a higher incident energy compared to the K-edge energy of the agent, allows for Compton scattered photons to excite fluorescence outside of the beam volume. Thus the loss of signal due to collimation here is over 50%, whereas for the rat it was 30%.

Differences towards Imaging Gold XFI Both energy variations in this section in figure 8.2 showed a continuous increase in sensitivity with increasing incident energies for perfect de-

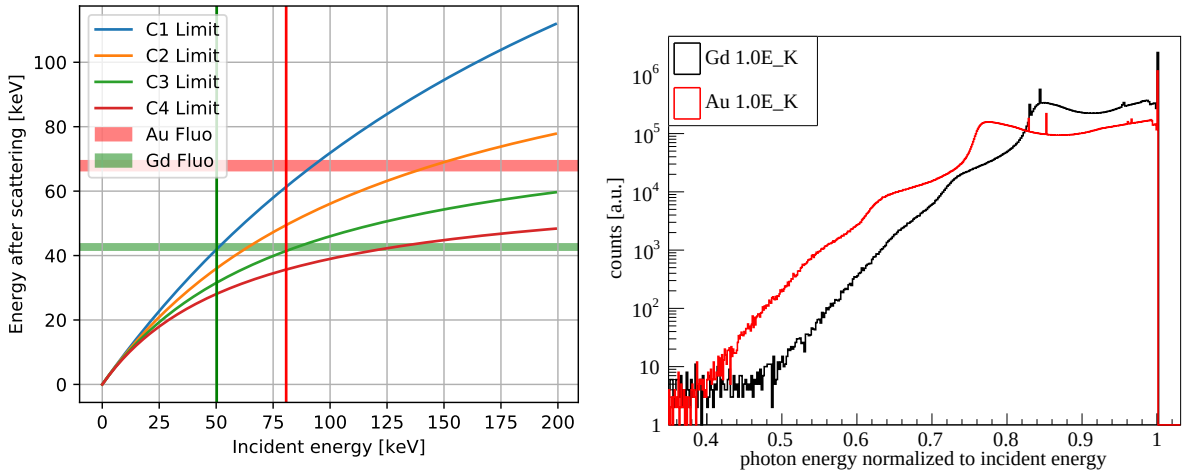

(a) Compton exclusion energies for Au and Gd

(b) Incident energy equals K-edge energy

Figure 8.4 – In (a) the Compton exclusion energies are illustrated for gold and gadolinium. The four curves give the possible minimum energy with 1 to 4 consecutive 180° scatterings. The vertical red lines marks the K-edge, the horizontal bars the K-fluorescence energies. In (b) two energy spectra normalized to the K-edge energy for gold and gadolinium inside a sphere with a radius of 1 cm without any detector effects are given.

tectors. This is completely different for gold agents. The reason lies in the shape of the Compton background, which becomes narrower with decreasing energy because less energy is lost per scattering event. This actually follows directly from eq. (2.6) which is nonlinear in energy. In figure 8.4(a) it is shown for gold and gadolinium at which incident energies Compton scattering orders can be energetically excluded to reach the signal interval without Doppler effect. For gadolinium, the maximum incident energy for a single scattered Compton photon to reach the signal energy is $1.03E_K = 52\,keV$ with E_K being the K-edge energy. The exclusion energy for double scattering is $1.3E_K = 65\,\text{keV}$ and $1.7E_K = 85\,\text{keV}$ for triple scattering. For gold, however, the C1 exclusion energy is $1.17E_K = 85\,\text{keV}$, the C2 exclusion energy $1.85E_K = 150\,\text{keV}$ and for C3 it is already $4.4E_K = 360\,\text{keV}$. Therefore, for gadolinium K-fluorescence, it is possible for the signal photons to move down the Compton background for energies a lot closer to the K-edge than for gold. If as an example, C1 and C2 shall be excluded from the signal background, the fluorescence cross section for gold drops to 18% compared to the K-edge, but it is still at 49% for gadolinium. To yield the same significance as for incident energies at the K-edge, the gadolinium background needs to be reduced by a factor of 4 and for gold it is already 31. On top of that, the dose deposition increases for energies over 60 keV, as it was shown in figure 2.4. In figure 8.4(b) this can additionally directly be seen in simulated energy spectra.

9 Rat Voxel Model

Considering the smaller detector sizes needed and the higher dose which can be applied, rodents are attractive subjects to, for instance, preclinical pharmacological studies. XFI experiments with rodents are already performed in vivo by several groups [38, 39]. In the context of possible future experiments, inflammatory bowel disease called ulcerative colitis disease [126] shall be examined. An in vivo experiment has already been performed using labeled T-cell antibodies and PET imaging [127]. A mass of 22 pg ^{89}Zr was injected in mice suffering from the bowel disease and a control group. In vivo PET images, ex vivo PET images with extracted colons and chemical analysis were performed confirming an increased uptake of the antibodie in the colon, cecum and lymph nodes. However, the concentration was not significantly increased but these organs were enlarged resulting in a higher amount of T-cells. PET is highly sensitive and shows very tiny amounts of the tracer down to 1% injected dose/gram. However, the spatial resolution is limited. XFI on the other hand has an almost arbitrary resolution, especially for ex-vivo scans without dose limitations. Furthermore, the handling of the slowly decaying ^{89}Zr with a half-life time of 78 h and subsequent 900 keV gamma emission acquires more and longer shielding than the frequently used ^{18}F [34, 128]. Therefore, XFI is explored as an alternative.

To assess the future feasibility, a voxelated rat phantom by Zaidi et al. [129] based on a 156 g Sprague-Dawley rat is used for Geant4 simulations. The available data for the phantom was obtained by cryosection and distinguishing 17 organs with a resolution of $0.2\,\text{mm} \times 0.2\,\text{mm} \times 0.4\,\text{mm}$ [130]. The organ material compositions are assumed to be human-like and taken from the ICRP [116, 131]. The material densities are obtained by dividing the organ masses [129] by the number of voxels per organ times the voxel volume. To simulate the disease in a simplified manner, the whole intestine is enriched homogeneously with gold and scanned using simulations for different detector geometries.

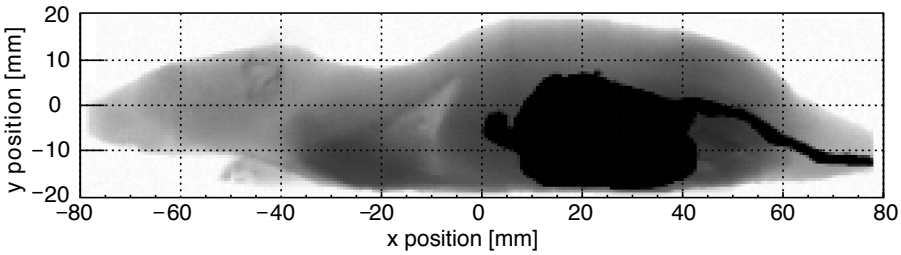

(a) Transmission image to locate the colon

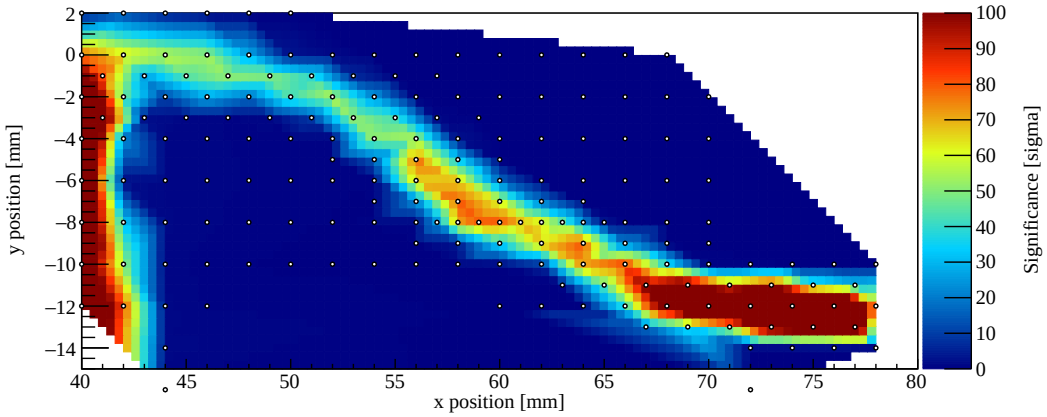

(b) Lateral XFI scan of the rat

Figure 9.1 – Lateral X-ray transmission image to show the position and shape of the colon with artificially increased attenuation inside the rat. (b) shows an XFI position scan where the rat is moved relative to the beam-detector-combination. The data points taken are marked by small dots, the space in between is extrapolated.

9.1 XFI with Full Solid Angle Detectors

For scanning smaller phantoms, such as rodents for pharmaceutical studies, it would be suitable to shrink the detector for humans. Since the rat studied in this chapter has a maximum diameter of roughly 5 cm, the detector size can be reduced by a factor of 6 while still keeping all the flexibility. This results in a detector cylinder with a radius of 10 cm and a length of 26.7 cm, resulting in an effective detector area of 1678 cm^2. The detector is filled with 570 collimator leaves starting at a minimum radius of 5 cm and ending at the detector radius. The rat was positioned in this cylinder detector with the collimator shrunk to rodent-size and moved around in the beam, whose position has to be fixed relative to the collimator. The photon energy is chosen as 85 keV and the beam is a box-shaped beam with 1 mm edge length. In figure 9.1(b), the part of the colon isolated from the rest of the intestines is shown for 10^8

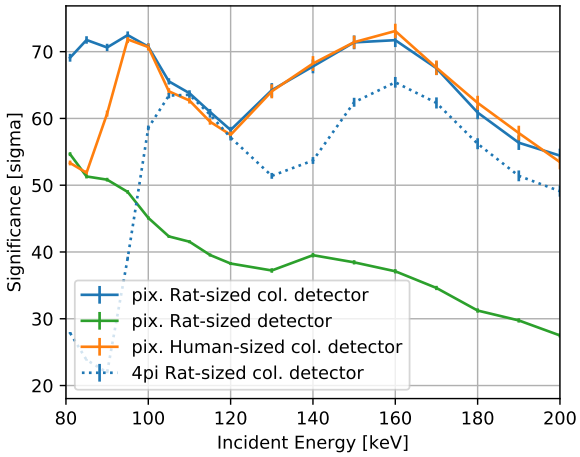

Figure 9.2 – Variation of incident photon energy for 4π-detectors for a dose of 15 mGy and a gold mass of 1 µg in the beam volume. Besides the standard detector, a smaller rat-sized version of 10 cm diameter is simulated with and without collimator. For the solid lines, the pixel selection is used.. The energy scan in figure 9.1(b) was performed at an arbitrary local maximum at $x = 60$ and $y = -8$.

incident photons per beam position. This corresponds to 2.5 mGy but differs depending on the phantom mass in the beam. The local maximum at $(x = 60, y = -8)$ was then chosen for further variation of the energy.

In figure 9.2, the significance scaled to a dose of 15 mGy and a gold mass of 1 µg in the beam volume is presented. The only difference between the two detector sizes with a collimator occurs for incident energies $E \leq 90\,\mathrm{keV}$. The reason for that is single Compton scattering happening in the air surrounding the phantom in the simulation. Although of course due to the low air density of $1.2\,\mu\mathrm{g/cm}^3$ at room temperature, even for the long beam path of 1.6 m in the large detector, the total amount of Compton scattered photons caused by air is less than 10% of the amount caused by the rat phantom. More importantly the anisotropy of the background is strongly reduced. At for example $\cos(\theta) = 0.6$, the amount of background in the K_α signal region triples because without air, it would be energetically impossible for single Compton scattered photons to reach this angle. The spectrum shown in figure 9.3 shall aid to explain the energy dependent behavior in figure 9.2. As a simplification it will be assumed here, that for different incident energy the spectrum just scales in its energy, so that the Rayleigh peak and the Compton edges change their energy, but the overall shape remains the same. The capital letters correspond to incident energy depending positions of the signal interval in the spectrum.

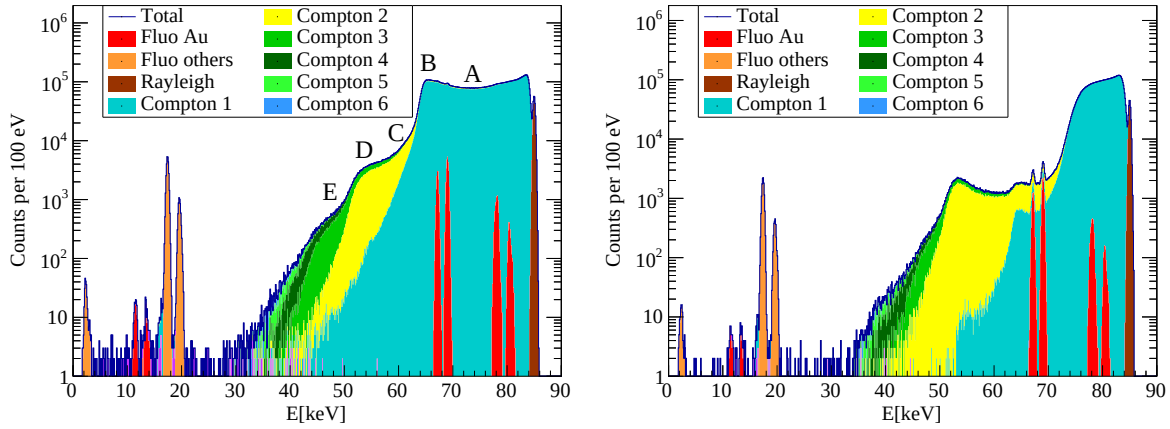

(a) 4π detector (b) optimal pixel selection

Figure 9.3 – This figure shows the 4π energy spectrum with and without pixel selection for the shrunk cylinder detector with a collimator for 10^8 photons. The capital letters are used as reference points to explain the energy-dependence of the significance.

A At 81 keV, the C1 maximum is in the backwards half of the detector, but still close to the middle. It can be eliminated by cutting away 70% of the pixels but the fluorescence cross section is at its maximum, the significance is high.

B At 90 keV, the C1 maximum is fully at the backwards side. The increase of sensitivity by pixel selection is maximum here because by cutting away a rather small part almost all C1 photons can be eliminated.

C At this inflection point of the spectrum at 110 keV, there is local maximum for the 4π significance graph. The background is C2 dominated, but mostly isotropic, so that no pixel optimization can be made.

D This refers to 130 keV to 140 keV. The signal interval lies on the C2 edge, where the 4π spectrum has a local background maximum. Thus the significance is at a local minimum. Here two almost 180° scatterings are energetically necessary to lose sufficient energy so that the background maximum is now at the front of the detector and can be cut away by pixel selection.

E At 160 keV the background is dominated by C3. Both significances, the 4π and the pixel selected case are at a maximum because the signal interval is at an inflection point

of the spectrum. Although for higher energies the background level lowers itself further, the decrease in fluorescence cross section happens faster.

The fluorescence distribution is of no importance for the pixel selection because it is almost isotropic in the detector apart from the direction of the rat's upper body, but there is an opening in the detector anyway. The attenuation in water for 70 keV is only 18% per centimeter and since the colon is almost in the middle of the back part of the phantom, it is quasi isotropic for more than a hemisphere in the solid angle. Comparing the collimated and uncollimated detector, the advantage of a collimator here at 85 keV offers only an increase in sensitivity of 40% while requiring a four times larger detector. When staying at photon energies around 85 keV, it might be sufficient to use a hemisphere detector with a radius of 5 cm, such as the 10x10 cm Hexitec [89], in forward direction covering 30% of the solid angle if placed 2 cm away, resulting in a detector size 10 times smaller.

For a monoenergetic beam of 81 keV, also K_β-fluorescence can be chosen as the signal. Without a collimator $Z = 84$ would be possible for the 10 cm detector. A collimator impairs the significance to $Z = 74$ because in the backward direction for an energy loss of 3 keV there are almost no multiple scattered photons. For that case, the collimator just filters disproportionately much fluorescence to be of any help. However, as soon as the beam energy has a non-zero bandwidth, the K_β sensitivity drops.

9.2 XFI with Small Detectors

For an experiment at PETRA III, first the Amptek detector is considered that has been used for several experiments in this thesis. The rat is placed lying down in a 45° angle with its back between the beam direction and the detector. This angle is chosen because like this the rat can be moved to scan the whole colon and the distance from the colon where the gold signal is created to the detector stays more or less the same, if the phantom is moved. The translation vector for the phantom is $(-50, 12, -50)$ mm. In figure 9.4 the incident photon energy is varied for a simulated measurement with the Amptek detector with and without a collimator. The energy dependent behavior is straightforward to explain. In figure 9.5 the corresponding spectrum is shown. The detector is placed at $\theta = 90°$ for which Compton scattering is strongly suppressed because of the polarization of the incident beam. That is the reason why in the spectrum there are as many double scattered as single scattered photons

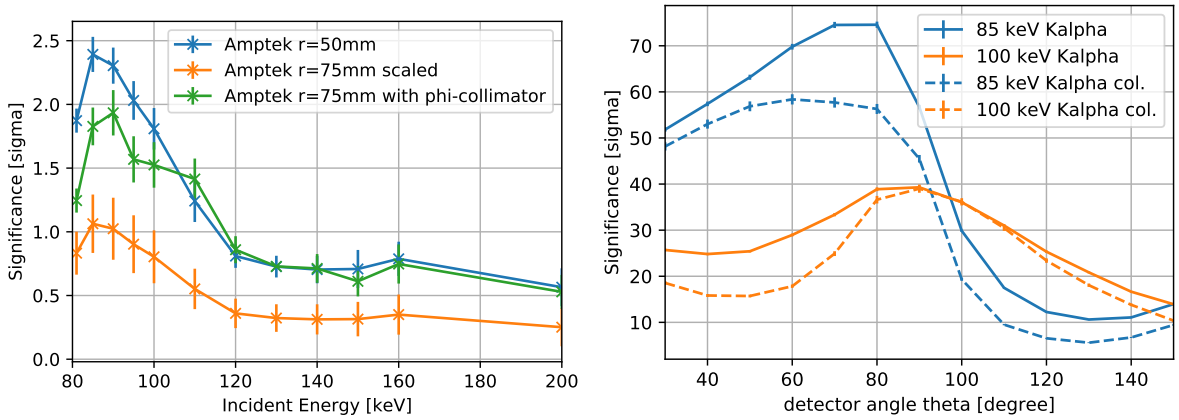

Figure 9.4 – For the Amptek detector, significances with the statistical uncertainties for different incident energies are given scaled to 15 mGy and 1 µg gold in the beam volume. (b) shows a variation of the detector angle of a Hexitec for two different incident energies once with ($r = 75$ mm) and once without collimator ($r = 50$ mm).

although the mean free path of 5 cm would suggest that the phantom is too small for this. Having a radius of approximately 1 cm from the beamline towards the detector until the border of the phantom, one would expect five times more single scattered photons. In a 4π detector this is the case. This results in two peaks in the spectrum of similar height. For 85 keV to 90 keV, the situation is ideal because the signal region is in the local minimum between the C1 and C2 peak. For increasing incident energies, the signal region moves up the C2-shoulder and thus the significance decreases strongly until 120 keV from here on the background becomes smaller, but so does the fluorescence cross section. Of course it is obvious, that the Amptek's chip size of 25 mm^2 is just too small to consider in vivo experiments. Therefore, for the rest of this section, the Hexitec detector with a 16-times larger detector chip is used.

In figure 9.4(b) the Hexitec detector is placed at various angles for two representative energies. For the best case of 85 keV, the optimum is achieved at 80° because here it is energetically and geometrically not possible for C1 photons to reach the signal area anymore. Higher incident energies do not yield a better best case position, but the best case angle changes of course. The collimator will be dealt with in the next section. For 30° and 90°, the signal regions of the energy spectra are shown in figure 9.5. Since for 30° the spectrum is dominated by double Compton scattering, it will be tried to reduce this background by using a collimator.

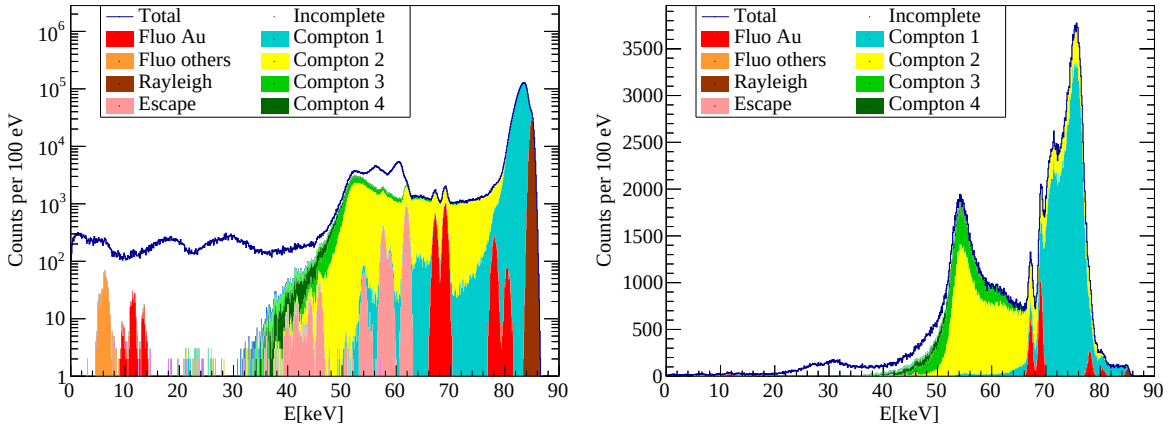

(a) Hexitec detector at $\theta = 30°$

(b) Hexitec detector at $\theta = 90°$

Figure 9.5 – This figure shows the energy spectrum for 10^9 incident photons with 85 keV and an uncollimated Hexitec detector at a distance of 50 mm. The statistical significances are $Z(30°) = 73$ and $Z(90°) = 78$ for 1 mg/ml or 5.2 µg of gold.

9.2.1 Assessment of Collimators for Small Detectors

A phi collimator with leaves oriented perpendicular to $\hat{e}_\varphi$, i.e. in plane with the z-axis, was of great help for the simulations with human-sized phantoms. Therefore, its potential for small objects with small detectors such as a rat shall be examined here. To calculate how many leaves are necessary for a Hexitec detector, a simple geometric calculation is made. For a segmentation angle of $\beta = 0.75°$, the distance on the chip is $75\,\text{mm} \cdot \tan(0.75°/2) \cdot 2 = 0.98\,\text{mm}$. This is three times the angle from the collimator used in the experimental validation, but due to the three times closer beam axis, the vertical distance would be the same. To cover the 2 cm chip diameter 20 spaces in between or 21 leaves are necessary. Although for an experiment more leaves should be used to avoid scattering from above or below the beam axis, for the understanding of the collimation effect, the collimator acceptance value ξ in eq. (3.12) is added up for 21 leaves. Experience from past experiments showed that molybdenum leaves with 0.2 mm diameter are useful because the necessary drillings can be made with sufficient precision, the absorption is high enough for low angles to the surface and they are thin enough to cover only 30% of the solid angle. Using eq. (3.1) the focus diameter is 2.6 mm which of course is too large but reducing it would only be possible using a smaller segmentation angle or longer leaves, which both reduces the solid angle of the detector surface. A variation of the collimator leaf thickness and separation angle in simulations showed that these values are

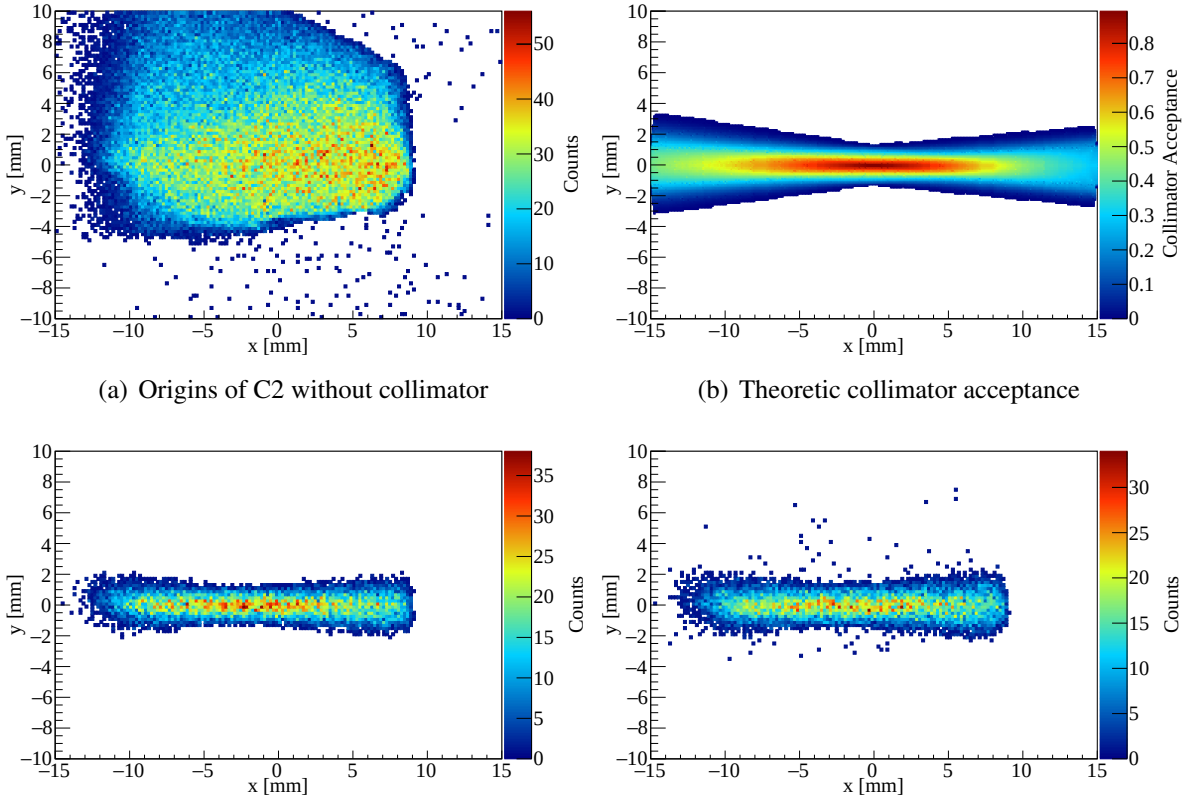

(a) Origins of C2 without collimator

(b) Theoretic collimator acceptance

(c) Resampling of (a) using (b)

(d) Simulation of C2 with collimator

Figure 9.6 – This plot illustrates the reduction by a collimator for second order Compton scattering comparing analytic calculations of the collimator with actual simulations. The Hexitec detector is placed at $\theta = 30^\circ$ at a distance of 75 mm.

very close to the optimum.

As an example, the detector position at $\theta = 30^\circ$ is discussed. The uncollimated spectrum shown in figure 9.5 is clearly dominated by double Compton scattering because the phantom is too small to make higher orders more probable and the detector position prohibits single scattering to reach this energy interval. The plane on which all photon origins are projected is perpendicular to the plane of the detector chip by simply rotating the coordinate system with $\hat{x}_{\text{rot}} = \cos 30^\circ \hat{x} - \sin 30^\circ \hat{z}$, so that $\hat{x}_{\text{rot}} \times \hat{y} \parallel \hat{n}_{\text{det}}$ with $\hat{n}_{\text{det}}$ as the normal vector for the detector chip. In figure 9.6 the origins of the last scattering position for exactly twice scattered photons that reach the detector afterwards are shown from simulation. Using the calculated collimator acceptance values, a distribution is resampled by using the collimator acceptance as a probability distribution. It can be seen that the actual simulated collimation effect agrees very

well both in shape as well as in absolute counts with the simple geometric considerations.

There are, however, two disadvantages of the collimator, first the leaves eliminate also approximately half of the fluorescence photons and the detector has to be placed further away from the phantom simply because the collimator has to fit in between. Considering the length of the collimator of 25 mm and the detector distance without collimator of 50 mm, this necessary increase reduces the covered solid angle by half. For large phantoms, a leaf-type collimator can filter a lot of the higher Compton orders, but because of the small size of the phantom compared to the beam size, there is not a lot to filter since the filtering should be minimal in the whole beam volume. If the same dose is applied, the results using a collimator do not yield an improvement for the experiment. A collimator only further complicates the setup because it has to be carefully aligned with its focus, otherwise it might filter all the fluorescence photons away. It would, however, be possible to collect the data faster at high flux facilities like a synchrotron because here often the detector is the slowest part. Though if the radiation dose is fixed and not the measurement time, this does not help for the sensitivity.

In table 9.1 the actual reduction values for the first three Compton scattering orders are given. Although there is some discrepancy shown for the first scattering order, possibly due to a lack of numeric precision in the calculations, the second and third order reduction using simulations agree very well with the calculations. The lower relative reduction for the 90° case can be explained by two effects. First, because of the energy constraints that the photons need to reach (68 ± 2) keV, the scattering position cannot be too far in the vertical direction otherwise the scattering angles would be too large and thus the energy loss too high. That restricts the vertical spread. Second, the focus line of the collimator is exactly at the beam axis for the 90° case, so that photons scattering close to the axis still have a higher acceptance probability. As an example for a larger phantom, a water box with 5 mm edge length is also presented to show

Table 9.1 – In this table some exemplary values are given to show the relative reduction of the first three Compton orders for two different detector angles and relative background reduction by the use of a collimator. Besides the rat, here also a box phantom is listed as an example for larger objects.

detector angle	Phantom	Analytic			Geant4		
		C1	C2	C3	C1	C2	C3
30°	Rat	2.4	7.9	9.2	2.4	8.4	10.3
90°	Rat	1.5	4.1	6.6	1.8	4.2	6.8
90°	50 mm Box	1.4	13.1	30.4	1.9	14.2	32.7

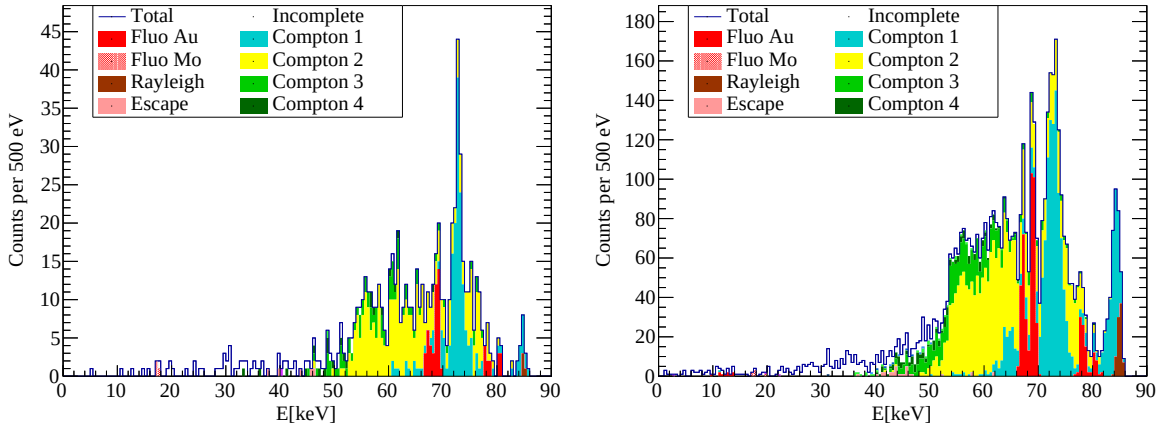

(a) Parallel collimator

(b) Theta collimator

Figure 9.7 – For $5 \cdot 10^8$ photons with 85 keV and a mass of 1 µg gold in the beam volume contained in a 1 mm sphere in the middle of the colon, the spectra are given in ascending order of sensitivity.

that the collimation effect works a lot better for larger phantoms.

Collimators restricting the field of view of the beam axis If the condition that the detector shall be able to measure fluorescence from the whole beam axis is dropped, some alternative basic collimator types are possible, that are introduced in section 4. The different collimator types are simulated with a sphere of 1 mm diameter in the colon containing 1 µg of gold with aligned collimators. For all compared simulations, the detector is placed at $\theta = 90°$. The resulting spectra are shown in figure 9.7 with the calculated significances given in table 9.2. All collimator leaves are 25 mm long, 0.2 mm thick and consist of molybdenum. For the parallel collimator, the distance is set to 1 mm. Regarding the phi and theta collimator, the angular difference between the leaves is 0.75° with the focus on the beam axis. Concerning the

Table 9.2 – Resulting significances, number of fluorescence photons and background photons in the gold K_α regime for 15 mGy in the beam volume and a gold mass of 1 µg in the beam volume in the colon. The detector distance for the uncollimated case if 50 mm, for all other cases 75 mm.

	uncollimated	phi	parallel	converging	theta	theta + phi
Z	11.7	9.3	7.4	12.2	20.25	23.9
N_{Fluo}	1595	415	52	154	365	228
N_{Back}	18707	1963	49	160	325	91

converging detector, the focus is moved 25 mm beyond the beam axis and the angle difference between adjacent leaves is reduced to 0.57°.

As a result only the theta collimator, the combination of theta and phi and the converged collimator can increase the significance, while all other types lower it. The first reason is the necessary unavoidable increase of the detector distance which halves the statistics for the assumed values. Whereas the second reason is that the collimator leaves themselves cover fluorescence both due to their own volume and due to their orientation. Furthermore, both these collimator types containing theta leaves have to be carefully adjusted. In fact by moving the target 1 mm out of the collimator focus, the significance decreases to 39% and even below 1% for a 2 mm shift. The sensitivity increase of 2 for the combined detector and 1.73 for the theta collimator allow for a division into 4 and 3 scanning positions with a total dose of the same as one scan without the collimator. The simulated spectrum for the parallel collimator, however, is extremely sensitive to any kind of electronic noise that results in additional photons in the spectrum. In this case only 52 signal photons were detected divided into two peaks. This low statistic makes fitting very unstable.

9.3 Medium-Z Target Elements for Rats

For small phantoms, such as rodents, medium-Z elements, as for example silver (Ag), might be advantageous over the frequently used gold nanoparticles because of several reasons. The lower incident energies makes the whole experimental setup easier because multilayer mirrors for monochromatization of conventional X-ray sources are available, less radiation shielding is necessary and detectors with better energy resolution that have a low efficiency at higher energies, such as silicon detectors, can be used for the experiment. The feasibility has, for instance, been demonstrated by Larsson et al. [132] with an experiment about scanning molybdenum nanoparticles in mice.

Despite the advantages for the experimental setup, the most important advantage of medium Z-elements is the sensitivity in small objects. If the back part of the rat is approximated as a sphere with a radius of 1 cm, the amount of fluorescence photons for Y at 25 keV, Mo at 24 keV, Ag at 40 keV, Gd at 70 keV or Au at 85 keV all lie within the range of a factor of 2 for the same agent mass. The fluorescence values can be calculated by simply using the Lambert-Beer equation for attenuation and tabulated mass attenuation coefficients. Due to

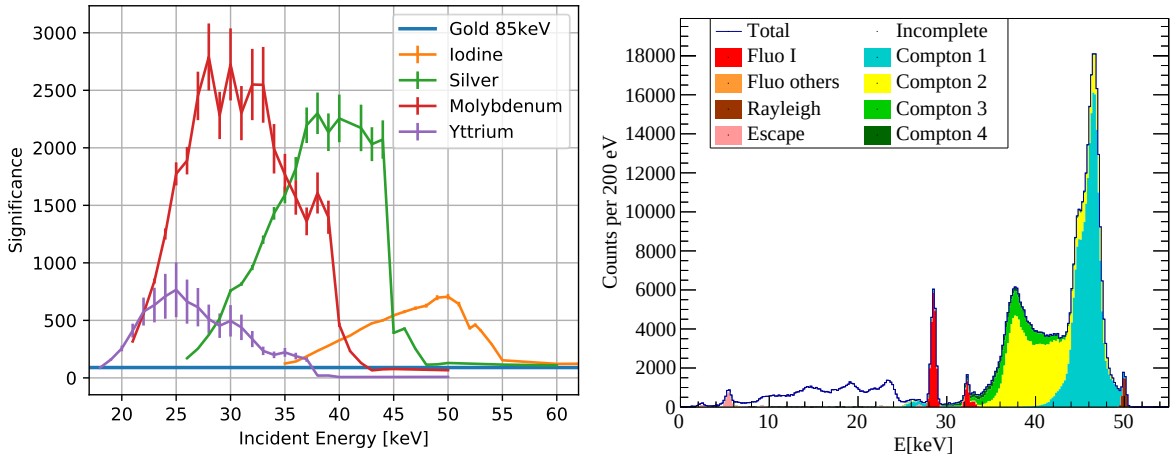

(a) Variation of Target Elements

(b) Spectrum with iodine and 50 keV

Figure 9.8 – In (a) different target elements inside the rat's colon are compared using a Hexitec detector with 10^9 photons. In (b) a spectrum with 50 keV using iodine is given to demonstrate the quasi background-free measurement.

the small size of the phantom, the higher photoabsorption and therefore higher fluorescence cross section for lower-Z elements compensates the higher attenuations of both incident and fluorescence photons. Considering, for instance, yttrium, the fluorescence cross section at 25 keV is 4.6 times higher than for gold at 85 keV, but the transmission is 6 times smaller. However, for human-sized phantoms the attenuation dominates and these medium-Z elements become unsuitable, as shown in section 5.2.

Since the amount of signal photons is very similar, the Compton background is the main reason for the medium-Z elements to be so sensitive. As the relative energy loss per Compton scattering decreases with lower photon energies, the Compton spectra become narrower. This can be seen in figure 9.8(b) in a spectrum with iodine, where there is almost no background left in the signal range. To be specific, for iodine at 50 keV there are at least for Compton scatterings necessary to reach the fluorescence energy, for silver at 40 keV its already five and for molybdenum at 28 keV even 6. As a comparison, for gold it is almost impossible to lose all the Compton background because to remove the fourth order Compton scattering from the signal background, the incident energy already needs to be in the MeV range. Of course, the simulated scan of the back part of a rat is not large enough to produce lots of higher Compton scattering orders, therefore for these medium-Z elements, the simulated signal is quasi background-free. To give an example, within 1 cm the Compton scatter probability is only about 20% and the signal background of silver is only 20% of the iodine background, which matches

since one additional Compton scattering is necessary to lose enough energy. However, for even lower-Z, this does not continue because the signal background is already almost at zero: silver has only 32 background counts left for 10^9 incident photons. Hence, in a real measurement the intrinsic detector effects, such as electronic noise, escape events or hole tailing will be the dominant part of the signal background. These have to be well characterized in order to predict the sensitivity limits for such experiments. Therefore, the Compton background reduction methods for larger phantoms, like collimators or pixel selection, are not necessary here. The collimators might even deteriorate the sensitivity because of the accompanying signal loss.

In figure 9.8(a), there is an overview over some examples of target elements in the colon scenario. Regarding the size of a rat, molybdenum or silver yield 30 times more sensitivity in the simulations than gold, which could be used to detect smaller amounts of target material, or to reduce the dose and thus the necessary scanning time. The maximum significance for each element is reached, once the signal has left the Compton background and the background slope becomes almost constant. From this point, the decrease in fluorescence cross section with increasing incident energy stops a further increase in significance. However, the abrupt decrease in sensitivity for molybdenum at 40 keV, silver at 50 keV or iodine at 52 keV is caused by the Cd escape peaks of the detector chip. Therefore, for different detector materials, the progression of the plots change inevitably. Regarding the example scan position in the rat chosen in this chapter, molybdenum seems to be the ideal choice. Lower elements, such as yttrium already become attenuated a lot stronger, which is why, they are less significant. Altogether, the choice an ideal element for an experiment is not trivial and depends strongly on the geometry of the phantom and the effects of the detector used for the measurement.

10 Additional Filtering Possibilities

10.1 Time Filters

An alternative detection method using time information instead or complementary to energy shall be briefly discussed in this section. The concept of including time-of-flight information to XFI has been published in the meantime by Vernekohl et al. [133]. For the K_β analysis in backwards direction for phantoms with diameters up to 36 cm diameter, he reports an increase in sensitivity especially for targets deep inside the phantom since most detected scattered photons come from the surface thus at a different arrival time.

To combine the time information with the XFI analyses including pixel selection, first, a detector using only time information without any energy resolution will be used and finally, a detector using both, which until today has not been developed yet with the necessary resolution. The exact knowledge of the creation time of the primary photon is a mandatory requirement for this analysis method. If it is unknown, as it would be the case for conventional X-ray tubes, this method could not be applied. Also for a synchrotron, the time information is already limited even if ignoring the bunch positions because of the bunch lengths, which for PETRA III is 44 ps or 13 mm [134]. However, when using a pulsed X-ray source, such as an all laser-driven Thomson source, the starting time for the X-ray photon would be well known because it fully depends on the laser interaction points.

Semiconductor detectors, which are commonly used for XFI because of their great energy resolution, usually have a time resolution larger than 1 ns, which corresponds to a travel distance of $c \cdot t = 30\,\text{cm}$ at the speed of light. This does not help to reduce Compton background in phantoms of the same size. Scintillation detectors, which are commonly used for PET detectors, might have a time resolution of the order of 10 ps [135, 136]. Unfortunately the energy resolution is rather at a level of 10%, which is a lot worse than for semiconductors. If a possible future detector is able to detect both energy and time with a high resolution, the sensitivity

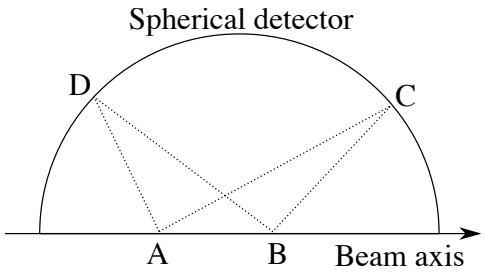

Figure 10.1 – Sketch of the time reconstruction for two different scattering positions A and B. For a detection in forward direction at position C, the two photon paths are $\overline{ABC}$ and $\overline{AC}$. For a detection in backward direction at position D on the detector, the two photon paths are $\overline{ABD}$ and $\overline{AD}$. In the backwards direction the path difference is larger thus resulting in better filtering possibilities.

of XFI could be pushed by an order of magnitude, which will be demonstrated here. At the necessary time scales in the picosecond range not only the detector crystal, but also the electronic would need to allow for that. In this chapter it will be assumed, that such technology exists.

If every detector element detects the arrival time of a photon and the timing of the X-ray source is known, a total travel length d can easily be calculated by $d = c \cdot t$. The basic filtering idea is simply that every photon that takes either a shorter or a longer path compared to a fluorescence target, will be eliminated. The individual detector elements could now assign a specific time to every position z along the beam axis, which a photon would need to reach this detector element if it only scatters once or it is created as a secondary fluorescence photon at that position. If elastic scattering is neglected, for a fluorescence photon to reach the detector, two paths need to be traveled. First, an incident photon needs to reach the target at position z along the beam from the position of the X-ray source z_{source}. From there the new fluorescence photon travels a straight line until it reaches a detector element at the position z_{Det} and R_{Det}. For rotational symmetry, φ will be neglected. The complete path d is therefore calculated using

$$d = (z - z_{\text{source}}) + \sqrt{R_{\text{Det}}^2 + (z_{\text{Det}} - z)^2}\,. \tag{10.1}$$

Substituting $\tilde{d} = d + z_{\text{source}}$ for easier reading, this equation can be solved for the supposed

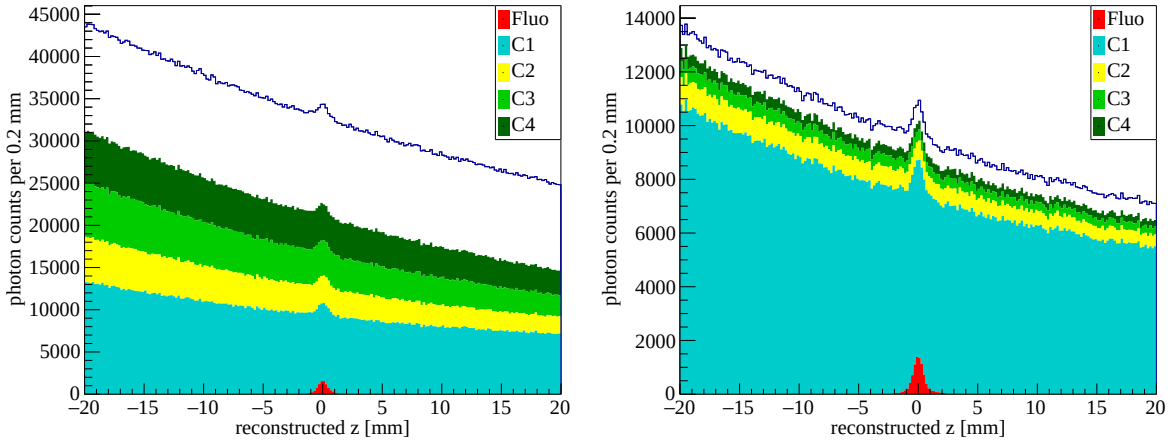

(a) 4π detector (b) pixel selection

Figure 10.2 – These z-spectra are created with an ideal time resolution of $\pm 3 \cdot 1\,\mathrm{ps}$ without any information about photon energy with $E = 85\,\mathrm{keV}$. On the right, an ideal pixel selection has been performed resulting in a significance increase from $Z = 15$ to 26.

target position z along the beam axis

$$z = \frac{\tilde{d}^2 - R_{\mathrm{Det}}^2 - z_{\mathrm{Det}}^2}{2(\tilde{d} - z_{\mathrm{Det}})}\,. \tag{10.2}$$

This target or scattering position z along the beam axis could be used to draw an alternative spectrum, where the counts are not plotted against the energy but against the z-position along the beam axis from which they come, if multiple scattering is ignored. In this spectrum the target containing the high-Z element may then appear as a peak whose width is determined by the target size and time resolution of the detector. In figure 10.1 it is illustrated, that such a position reconstruction based on time information depends on the angle position of the detector. For a forward detection position, the travel distance for two different scattering positions along the beam axis is less than for a detection in backward direction. For the example cases $\theta = 0°, 90°, 180°$, a path difference of $\Delta z = 1\,\mathrm{mm}$ corresponds to a difference in photon travel length of $0, 1$ and $2\,\mathrm{mm}$. This means that for very small scattering angles, time resolution filtering would be useless. If eq. (10.2) is used to plot $z(d) - z(d - 1\,\mathrm{mm})$ against $\cos(\theta)$, which is a function of z_{Det}, the result is very close to a linear function.

For a z-spectrum, there are several differences compared to an energy spectrum that is normally used for XFI analysis. Without energy resolution, such a method, however, has several disadvantages. First, different fluorescent elements cannot be distinguished anymore. Sec-

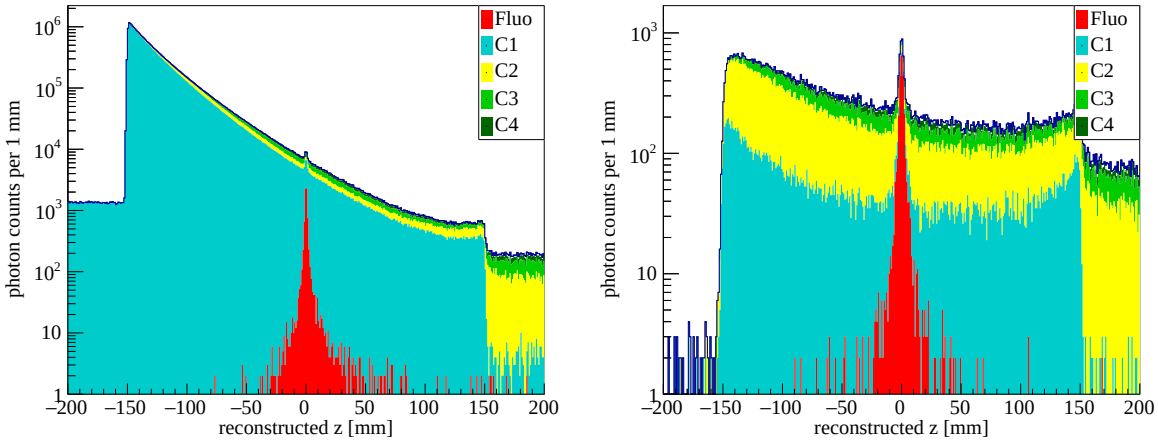

(a) 4π detector (b) pixel selection

Figure 10.3 – These z-spectra are created with an ideal time resolution of $t_{\mathrm{rms}} = 3\,\mathrm{ps}$ and an energy resolution of $E_{\mathrm{rms}} = 200\,\mathrm{eV}$. For an incident energy of 85 keV and 10^9 photons, the resulting significances are $Z = 33$ and $Z = 76$. The colors refer to the same Compton scattering orders as in the energy spectra, see for example figure 10.4.

ond, the problem of the *Look-elsewhere Effect* arises since the number and actual position of the target along the beam is unknown, therefore one or more peaks may be found anywhere along the beam. The size of the parameter space for all possible target positions increases the probability that at some position a peak arises by chance. Third, inhomogeneities, such as bones, might create peaks in the z-spectrum, that could be misinterpreted as a target. On the plus side, however, a full 3D information limited only by the beam size and time resolution would be acquired for each beam position without need for rotations. If the alternative spatial reconstruction method requires additional scans from more directions, like XFCT, a further sensitivity increase can be added to this method because more dose could be applied for a single scan. In addition, all fluorescence energy lines may contribute to the same signal.

To assess the effect on polarization filtering on XFI, the same setup as in section 3.1 will be used consisting of the 30 cm soft tissue sphere in the cylinder collimator with a phi leaves collimator. In the middle of the phantom, there is a target sphere of 0.5 mm radius with 10 mg/ml of gold. The photon statistics is 10^9 for each spectrum.

If no energy resolution is available, the time resolution needs to be better than 10 ps in order to yield better significances than the classical energy spectra. For 10 ps even with an ideal pixel selection, only $Z = 9$ would be available, whereas $Z = 11$ is possible with energy resolution alone. In figure 10.2 the target region for an ideal time resolution of 1 ps is plotted with a

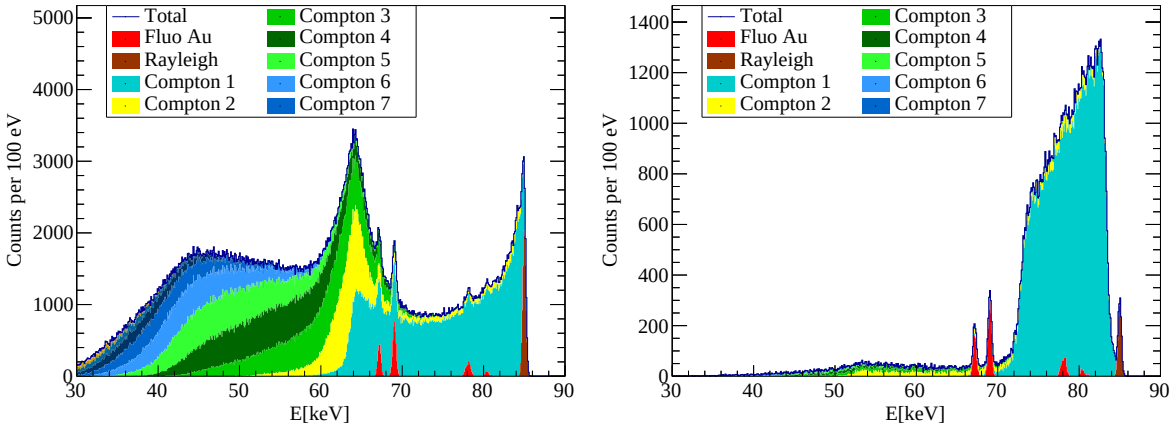

(a) 4π detector

(b) 4π with pixel selection

Figure 10.4 – As a comparison to figure 10.3, for the same parameters two energy spectra for the 4π and the pixel selected case are presented. The significances are $Z = 35$ and $Z = 75$. This agrees with the z-spectra and it is expected, because in the signal interval for both consists of the same energy and z- interval.

significance approximately $\sqrt{10}$ times better. If both, energy and time resolution are available, a sensitivity increase of over an order of magnitude is possible. In figure 10.3 such a z-spectrum is plotted. The single Compton scattering for $z < 150\,\text{mm}$ is caused by scattering in air, whereas the higher scattering orders for $z > 150\,\text{mm}$ are caused by path lengths created inside the phantom because the assumption of a single scattering event is wrong. Using the pixel selection, as usual the single Compton scattering can be mostly eliminated, the remains are only caused by Doppler effect and combinations of Rayleigh and Compton scattering. The same data is plotted as an energy spectrum in figure 10.4 for comparison. The significance in these plots is almost the same as in the z-spectra, which is expected because the signal range is defined by the same energy and time conditions for both methods. Compared to the spectra without any time resolution in figure 3.2, the shape changes completely.

In figure 10.5 the time resolution is varied for a fixed energy resolution. For this case, the optimum time resolution would be $0.4 - 0.5\,\text{mm}$ because of the target size of $r = 0.5\,\text{mm}$. For smaller cuts, signal photons are lost, which can be clearly seen in the red curve. If the fluorescence target is larger, then of course the time cut has to be set accordingly, otherwise signal gets lost. For time resolutions better than 100 ps, the background is reduced inversely proportional to the time cut. This is expected, if the z-spectrum is approximated to be linear. For larger time cuts, the background slope increases because here on the back plate on the

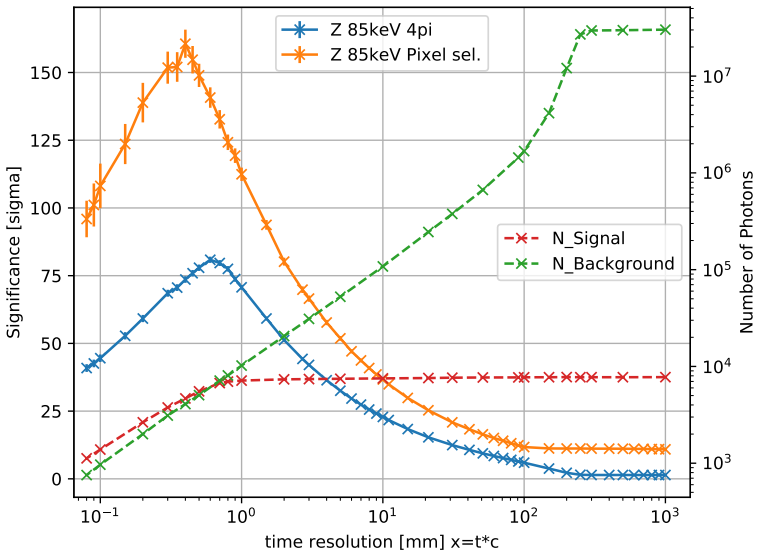

Figure 10.5 – For an energy resolution of $E_{\mathrm{rms}} = 200\,\mathrm{eV}$, the significances are calculated for different time resolutions. A time resolution of x corresponds to a signal interval of $\pm(x = ct)$. To help understand the significance curve progression, in addition the photon numbers in the signal range in the 4π detector are given.

cylinder back scattered photons are cut away. Because of the limited collimation on the back plate, in the unfiltered case here is the maximum of the background photons. Their reduction decreases the absolute background photon number the fastest. This continues until 300 mm because in the backward direction 300 mm difference in photon travel path means 150 mm difference along the scattering position at the beam axis. Since this is the phantom radius, larger time cuts do not improve the significance any further. Small changes in energy or time resolution for $E_{\mathrm{rms}} < 10\,\mathrm{keV}$ and $1\,\mathrm{ps} < t_{\mathrm{rms}} < 300\,\mathrm{ps}$ can be approximated by $Z \propto 1/\sqrt{t_{\mathrm{rms}} \cdot E_{\mathrm{rms}}}$ quite well. For more precise values, the actual spectra need to be calculated.

As already explained, the time cut works best in backward direction. Therefore, K_β-fluorescence analysis profits even more than K_α-fluorescence because the favorable detector area is in the backward direction. Even for rather low time resolutions of 100 mm, there is already a factor of 4 improvement to $Z = 17$ compared to no time resolution at all. For an ideal time resolution around 1 mm$\hat{=}$3 ps, the significance even reaches $Z = 180$, which is a factor of 40 better than without time resolution and 50% better than K_α-fluorescence analysis because the latter only increases by a factor of 15 since it prefers the forward direction where the time cut is less effective.

10.2 Polarization Filters

The effect of a linear polarized incident photon beam on the spatial distribution of the Compton background has already been used by many groups (e.g. [21, 37, 38]) to reduce the signal background by placing a detector in the plane of polarization at an angle of $\theta = 90^\circ$ to the incident beam. It follows directly from the polarized Klein-Nishina cross section (2.7) that Compton scattering is suppressed into this direction. This has also been used in this thesis for the pixel selection where the background maps are clearly asymmetric in φ due to the polarization and for the optimization of detector placement at the PETRA III synchrotron experiments. Instead, in this section the possibility to use the direction of the photon polarization $\vec{P}$ itself in every detector pixel for filtering purposes shall be investigated. This could be achieved by using either polarimeters in front of the pixels to measure the polarization of a photon before its energy is measured and use this information for the analysis to filter the spectrum afterwards or by using a filter that simply eliminates certain polarization directions before reaching the detector. In theory an improvement in sensitivity is possible, if a high degree of polarization is kept after Compton scattering, i.e. a low variation of the polarization angle.

To filter or determine the polarization, to the best of my knowledge, there is no ideal solution for the energy signal region around 70 keV that offer a high efficiency and a high degree of polarity. Here a few possibilities for polarization filtering shall be mentioned. Elastic scattering at high-Z targets suffers from low efficiency due to photoabsorption and photons scattered into different angles [137]. Inelastic scattering in low-Z targets suffers from low efficiency due to photons scattering into different angles, deterioration of energy resolution due to different possible scattering angles and Doppler broadening and a limited degree of polarity due to multiple scattering events. Bragg reflection offers a high degree of polarity and efficiency, but the energy bandwidth is very low [138], although this can be improved using multilayers or polycrystals [139]. Another concept is the detection of the direction of the photoelectron in the detector which happens preferably into the direction of the photon's electric field [140]. However, due to the very short mean free paths, gas detectors would probably be necessary. Transmission devices such as perfect crystals using the Borrmann effect were reported with efficiencies in the order of 10^{-4} [141]. Highly ordered materials can be used as transmission filters for very narrow energy intervals around K-edges. Because of the preferred direction of the photoelectron and a different electronic structure in perpendicular axes, these materials can be used to filter polarization [142]. Collins even reported a polarization filtering using ordinary Polaroid H-sheets for optical wavelengths for 33 keV photons [143].

Unfortunately for gold K_α-fluorescence, the nearest K-edges of tungsten ($E_K = 67.4\,\text{keV}$) and tantalum ($E_K = 69.525\,\text{keV}$), do not match.

To assess the possible use for XFI, the resulting polarization of the Compton photons is simulated first for a small phantom and second for the 30 cm phantom used throughout this thesis. To verify and better understand the simulated data, a few analytical calculations will be performed. The following three formulas are all taken from an overview about polarized Compton scattering by Matt et al. [58]. Since the direction of polarization is perpendicular to the plane created by the incident photon direction and the scattering direction, for $\theta = 90^\circ$ even for primarily unpolarized radiation a polarization is achieved with $\vec{P} \parallel \hat{e}_\varphi$ where $\hat{e}_\varphi$ is a unit vector from the spherical coordinate system. The degree of polarization for unpolarized radiation can be calculated using

$$\Pi_u = \frac{1 - \sin^2\theta}{\frac{E}{E'} + \frac{E'}{E} - \sin^2\theta} \tag{10.3}$$

and for polarized incident photons

$$\Pi_p = 2\frac{1 - \sin^2\theta\cos^2\Phi}{\frac{E}{E'} + \frac{E'}{E} - 2\sin^2\theta\cos^2\Phi} \tag{10.4}$$

where E' is the energy after Compton scattering given by eq. (2.6). When averaging over all polarization angles Φ, the term $\cos^2\Phi$ turns to $1/2$ and thus the equation for unpolarized photons is obtained. The degrees of polarization are plotted in figure 10.6.

The polarization vector after Compton scattering can be calculated using

$$\vec{P} = \frac{1}{\left|\vec{P}\right|}\left(\vec{P}_0 \times \vec{v}\right) \times \vec{v} \tag{10.5}$$

with the polarization before scattering $\vec{P}_0$ and the direction of the photon momentum $\vec{v}$ after scattering. This is only valid for the polarized fraction calculated with the degree of polarization, the rest is assumed to be arbitrary.

For the investigation of the filtering potential, the Malus law

$$I = I_0 \cdot \cos^2(\alpha) \tag{10.6}$$

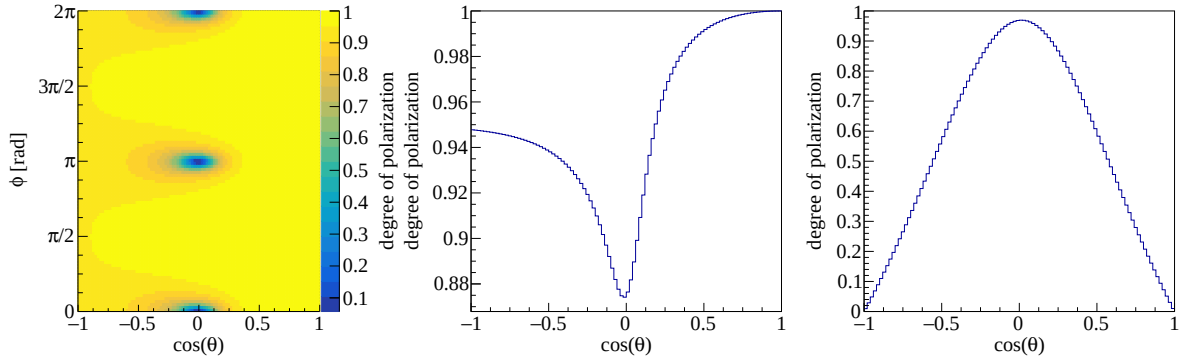

(a) polarized photons (b) polarized photons (c) unpolarized photons

Figure 10.6 – On the left and in the middle the degree of polarization for completely polarized primary photons is plotted according to eq. (10.4). On the right the degree of polarization for unpolarized photons is plotted. The polarized fraction at 90° is polarized parallel to φ.

will be used. The former intensity I_0 is lowered depending on the angle α between the plane of polarization and the axis of the polarizer. For reasons of simplicity, a possible change in frequency, as described by Volobuev et al. [144], is not considered here. To define an angle β for the polarization at different elements of a large solid angle detector, spherical coordinates will be used. The three-dimensional polarization vector obtained in the Geant4 simulations is projected onto the unit vectors of φ and θ for each detector pixel using

$$\beta\left(\vec{P},\varphi,\theta\right) = \arctan\left(\frac{\vec{P}\cdot\hat{e}_{\varphi}}{\vec{P}\cdot\hat{e}_{\theta}}\right). \tag{10.7}$$

This angle is then averaged over all photons reaching this detector pixel and using the Malus law an optimal axis is calculated for the polarizer that blocks as many photons as possible. It is taken into account that half of the fluorescence photons will be filtered too due to their arbitrary polarization. So in order to increase the sensitivity with a polarization filter assuming 100% efficiency, the background has to be reduced by at least a factor of four due to equation (2.19).

Small Spherical Phantom with 5mm Radius First, a small spherical phantom made of water with a radius of 5 mm using a linear polarized pin beam in vacuum inside a 4π detector without a collimator with a photon energy of 85 keV will be used for verification purposes. Because of the small size of the phantom, first order Compton scattering will be dominant to

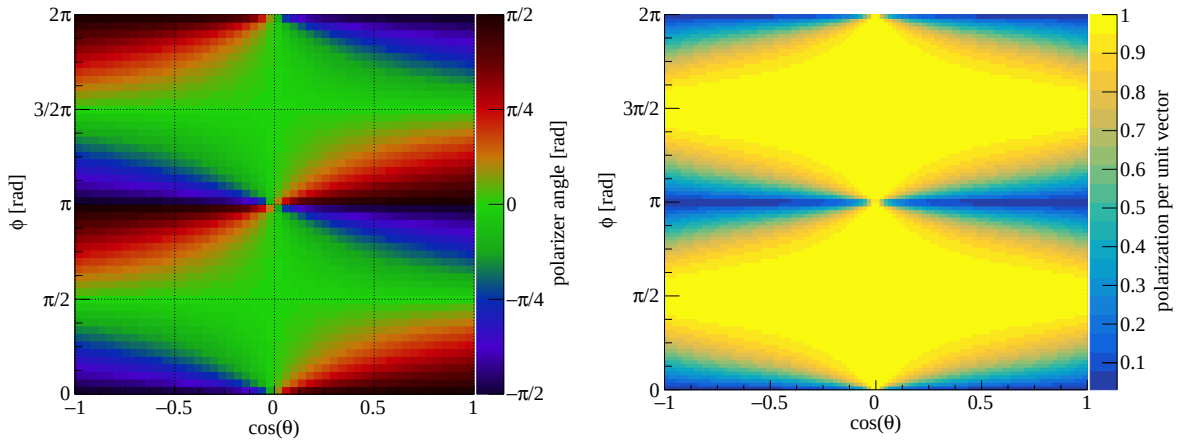

(a) sim. optimal polarizer angle

(b) calc. φ component of C1 polarization angle

Figure 10.7 – For a 1 cm phantom, the optimal polarizer angle in (a) is compared to the φ component of the C1 polarization angle in (b) calculated using only equation (10.5). In (a) a cyclic color map is used, because for the polarization angle β is the same as $\beta + \pi$.

the background and compared to the size of the detector which is described in section 3.1, the scattering positions are all approximately at the same place in the center of the detector. To verify the simulations the polarizations for all photons regardless of their energy are considered. For the sensitivity of XFI, of course only the energy interval around the K-fluorescence is relevant, but there the situation becomes a little more complicated due to Klein-Nishina (2.6). It is not possible for single scattered photons to reach all positions in the detector without Doppler effect or additional elastic scattering. This means that the forward direction in the detector is dominated by photons of higher Compton orders. The optimal polarizer angle for each detector pixel, meaning minimizing the number of detected photons, are presented in figure 10.7 and agree quite well with the calculated direction of polarization. A polarization parallel to φ, reduced in a polarization angle of $\pi/2$ which leads to an optimal polarizer angle of 0.

The actual photon reduction values are given in table 10.1. It is important to notice, that the relative reduction of Compton scattered photons decreases with their scattering order. The reason is that the degree of polarity decreases with each scattering order because the polarization angle of a photon may change if scattered not perpendicular to its former polarization direction thus resulting in a rotated coordinate system for the scattering event. The resulting effect on the polarity is illustrated in figure 10.8 where the RMS for the first and second order of Compton scattering is given. It is apparent that the mean degree of polarity decreases with

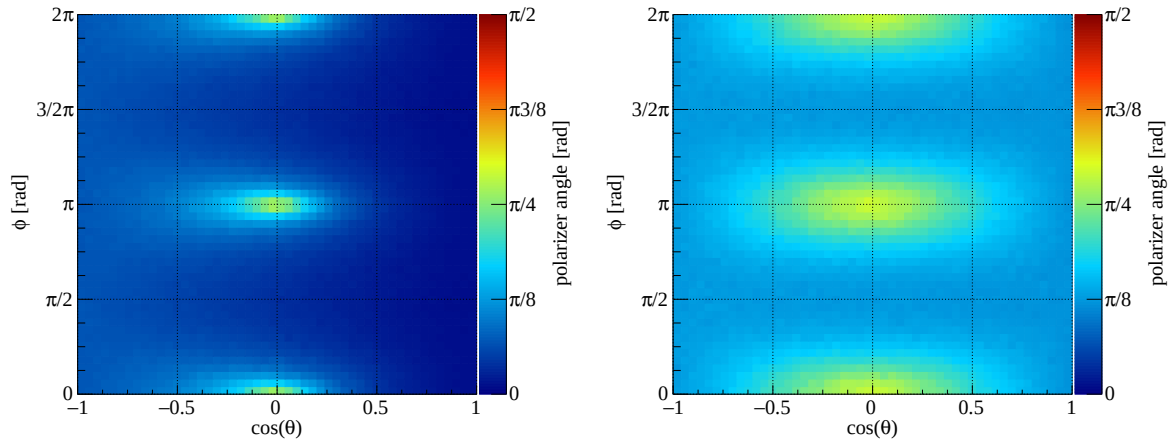

(a) RMS of polarization angle for C1

(b) RMS of polarization angle for C2

Figure 10.8 – The RMS values for the angle of polarization are shown for photons that scattered once (a) and for photons that scattered twice (b). These plots are in good agreement with the theoretically predicted degree of polarization in figure 10.6.

a second scattering event and the suppressed angles at $\theta = 90°$ are not as sharp any more. The reduction of photons projected on the $\cos\theta$-axis is also shown in figure 10.9, where it can be seen that the relative amount of photon reduction for single Compton scattering agrees quite well with the theory. Furthermore, for $\theta = 90°$, where the degree of polarity is at its minimum, the photon reduction is also at its minimum. Moreover, the reduction values for higher orders become less with each additional scattering event.

To calculate the sensitivity it has to be kept in mind that not only the background decreases, but also half of the fluorescence photons are lost. This means that in order to keep the same sensitivity after polarization filtering, the background has to be reduced by at least 75% because of the significance being inversely proportional to the square root of the background: $Z = s/\sqrt{b}$. The amount of background reduction in table 10.1 would yield a sensitivity improvement of a factor of 3.4, if all these photons were in the energy signal region. If the background only consisted of third order Compton scattering, there would already be no improvement.

If only the signal energy range for gold K_α photons is considered, the increase in sensitivity is reduced to a factor of 2.8. There are two reasons for that. First, the relative reduction in the number of photons in the forward direction decreases because single scattered photons are not expected in this energy interval. Instead, the forward region is dominated with double scattered photons with a lower degree of polarity. Nevertheless, since the absolute number

of photons in the forward direction is one order of magnitude smaller than in the backward direction, this is not so important. Second, the photon distribution has its maxima around $\cos\theta = -0.6$ and $\cos\theta = -0.4$ because certain scattering angles need to be fulfilled in order to reach the fluorescence signal region due to Klein-Nishina. However, at these positions the mean degree of polarity is lower than for very high or very low scattering angles where the distribution for all photon energies was at maximum.

All the information given so far is valid for a 4π detector and helpful to understand the underlying principles involved, but since a pixel selection is performed in the rest of the thesis, the same algorithm shall be applied for polarization filtered pixels. Regarding the analysis of gold K_α photons, with photon energies below 100 keV, when for single Compton scattering it is energetically possible to reach the energy signal region, those pixels containing a lot of C1 will usually be deleted first. For the optimal pixel selection, single Compton scattered photons are therefore mostly eliminated, left are higher scatter orders which cannot be filtered as efficiently using a polarizer. This is the reason why the increase of sensitivity for the optimal pixel selection using a polarizer is only better by a factor of 1.2. A special case is the analysis of K_β-fluorescence with an incident energy of 81 keV. In this case the energy difference between the signal region and the incident energy is only 3 keV. Because of that, single scattered photons are primarily scattered in the forward direction. In fact, they make up 98.6% of the total background photons in the 4π detector. For the K_α-fluorescence with 85 keV in table 10.1, the amount of higher scattering orders was higher by a factor of 3.8. That is why the increase in sensitivity for K_β-fluorescence is a factor of 5 for the 4π case and a factor of 2.3 for each optimized pixel selection. Considering higher photon energies, the positive effect of the polarization filtering reduces because the number of higher scattering orders increases. For unpolarized incident photons, there is no sensitivity improvement at all since the overall degree of polarity is just too low.

Table 10.1 – The actual numbers for the Compton background reduction of 10^9 incident photons using polarization filtering for a 1 cm phantom for the first three scattering orders are given. In this table all photon energies are considered. Note that also the fluorescence photons are halved.

	Total	C1	C2	C3
absolute number before filter	1.60e8	1.42e8	1.03e7	6.93e5
absolute number after filter	3.42e6	1.55e6	1.66e6	1.83e5
relative reduction	97.8%	98.9%	83.8%	73.6%

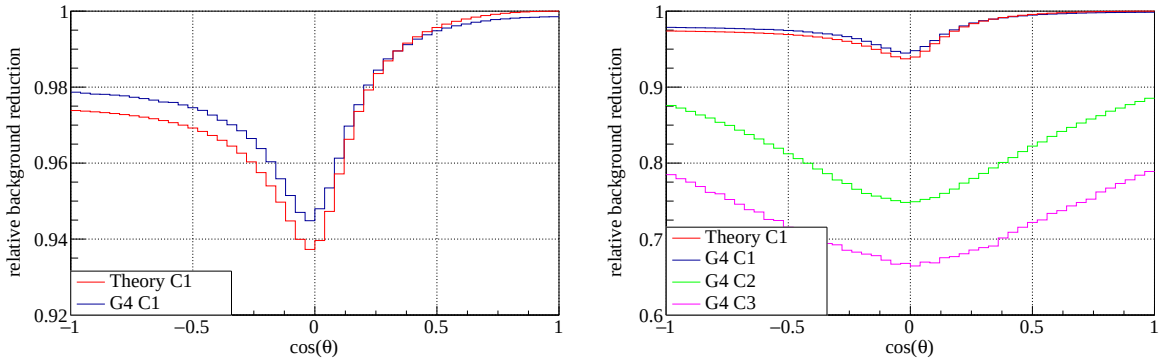

Figure 10.9 – This figure shows the relative reduction of the Compton background per scatter order in the 1 cm phantom. (a) and (b) differ only in the axis range. In red the calculated degree of polarization for single scattering is shown in comparison to the simulated values.

30 cm phantom To examine the effect of polarization filters on large phantoms, a sphere phantom with 30 cm diameter made of water with a 1 mm spherical gold target containing 10 mg/ml is used. The phantom is placed in the center of the tube detector with a leaves collimator as described in section 3.1. In comparison to the small phantom, the origin of scattering is not as localized anymore. To be specific, the scattering in the phantom now extends from $z = -150\,\text{mm}$ to $z = 150\,\text{mm}$ due to its size. The distribution of polarization angles, as shown in figure 10.7 for an almost point-like phantom, broadens for first order scattering along the $\cos(\theta)$-axis which results in a higher RMS for the mean polarization angle compared to figure 10.8. For higher orders, the blurring also occurs along φ since the photons can scatter farther away from the beam axis. Therefore, the singularity-like $\theta = 90^\circ$ scattering position in the polarization planes spreads between $\cos\theta = \pm 0.24$. Of course the spread is not homogeneous but modulated due to attenuation along the beam axis. This is why the maximum scattering occurs at the beginning of the phantom. Due to the size of the phantom, single pixels cannot be assigned a certain scattering angle needed to reach this pixel as it is possible for small phantoms. Because of this it is plausible that the RMS of the polarization angle increases and thus the relative reduction of the background photons decreases. Although 97.6% of Compton1 may still be filtered, the remaining amount of unfiltered Compton1 photons doubles.

Although because of the collimator, the C1-share of the signal background is still above 90%, Compton scattering of the order of three or higher increases by over a magnitude compared to the 1 cm phantom discussed before. Without the collimator the share of C1-photons would

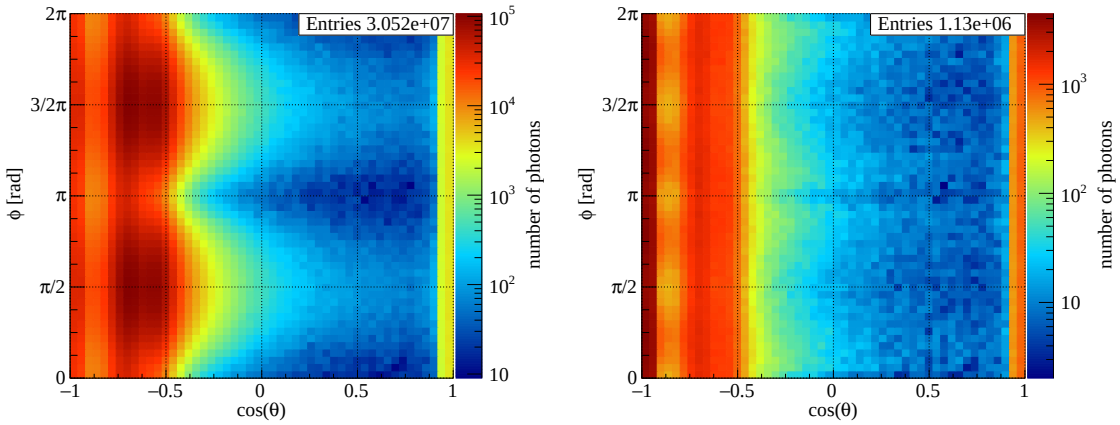

(a) K_α background map without polarizer

(b) K_α background map with polarizer

Figure 10.10 – This figure shows the K_α background maps without a polarizer(a) and with an optimal polarizer (b). The phantom is a 30 cm water sphere with 10^9 85 keV photons using the tube detector with collimator described in section 3.1.

be below 60%, for which polarization filters could not increase the sensitivity. Using a collimator, the increase in sensitivity for a 4π detector results in a factor of 2.6 and for an optimal pixel selection the improvement reduces to a factor of 1.37. Both values are quite similar to the small phantom described before. The improvement by polarization filters for simultaneous pixel selection is not very high because the single scattered photons are mostly eliminated by the pixel selection anyway. The remaining higher Compton orders are more isotropic both in position in the detector and in the orientation of their polarization vectors. Therefore, the polarizers cannot improve the sensitivity very much. In figure 10.10 both background maps are presented: the background map without polarizers as described before and the background map after application of optimized polarizers for each individual pixel. The corresponding spectra are shown in figure 10.11. Although these spectra appear to be very similar to the spectra without filters in section 3.1, the total amount of K_α signal background in 4π is reduced by a factor of 27. Comparing the background maps the polarization filters do not work very well for $\cos\theta \approx \pm 1$. The reason for that is that this part is not covered by the collimator therefore it is dominated with higher Compton scattering orders. However, when using a pixel selection, these pixels would be removed early on. It is furthermore interesting to see that the former background maxima at $\varphi = \pi/2$ and $\varphi = 3/2\pi$ are no maxima anymore after applying the polarizers but rather a slight minimum. This can be understood with the theoretically expected degree of polarity which is maximum for the plane perpendicular to the former polarization plane. Similar to the small phantom discussed before, polarizers are not

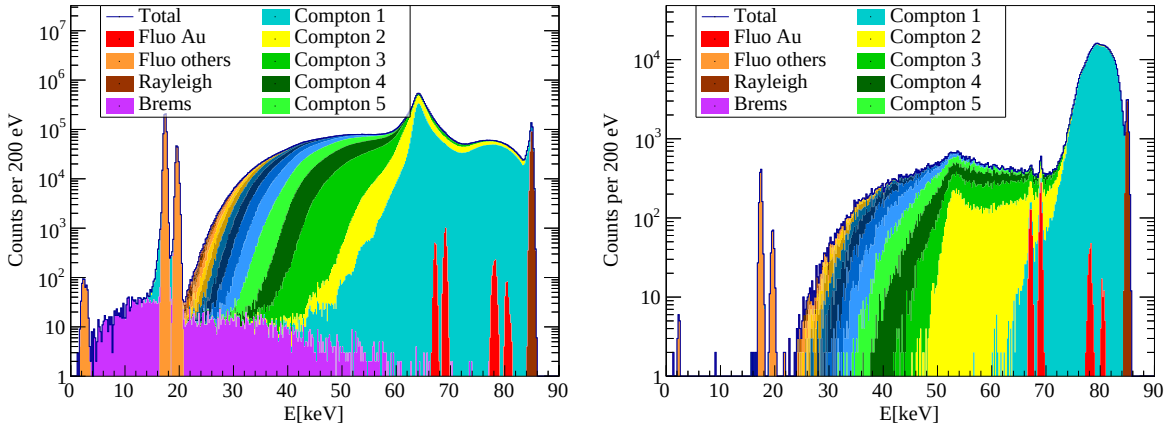

(a) 4π detector with polarization filters

(b) 4π detector with polarization filters with pixel selection

Figure 10.11 – Spectra of the 30 cm sphere using polarization filters for 85 keV with 10^9 photons. The signal background in (a) corresponds to the background map in figure 10.10(b). In (b) the spectrum for the optimal pixel selection is given.

helpful when using higher incident photon energies. Considering, for instance, 150 keV, even perfect polarizers can only decrease the sensitivity because of the unavoidable signal loss of 50%. Instead, the polarizers help a lot more for low photon energies of 81 keV, especially for K_β analysis. Using the optimal pixel selection, the polarizers still offer an improvement in sensitivity by a factor of 3.8 compared to a factor of 6.1 for the 4π detector. With respect to the K_β energy region, higher orders of Compton scattering are highly anisotropic, if they occur at all. It is simply unlikely for a photon to scatter several times, lose only 3 keV of energy and be detected in the backwards direction. For the first quarter of the detector, i.e. $\cos\theta < -0.5$, they only make up 4% of the background photons instead of 9.6% for the full solid angle. This is completely different compared to the K_α analysis, where the share of higher Compton scattering orders increase with each pixel removed on the way to the optimum choice. Furthermore, for 81 keV the detection limit could be improved because both K-fluorescence regions can be analyzed independently if the detector covers both forward and backward direction. Of course this can always be done, but using polarizers both significances are very close to each other. Therefore, there are two regions in the spectrum that both offer the possibility of detecting and quantifying the tracer in the beam volume. For the standard case in this thesis described in section 3.1, the K_β analysis does not add much since it only becomes detectable after K_α is already clearly significant. In figure 10.12 the resulting significances for gold K_α and K_β-fluorescence in the 30 cm phantom are plotted against the detector solid angle used

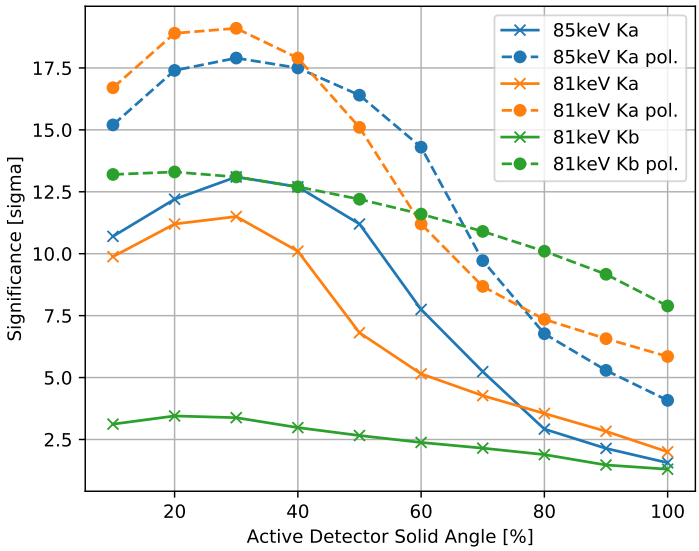

Figure 10.12 – The effect of optimized polarization filters for each pixel is plotted for different stages of the pixel selection with 10^9 photons. For blue and green, the K_α-fluorescence is chosen as the evaluated signal for two different incident energies and for red $K_{\beta 1,3}$ is chosen.

for the analyses. The 4π detector is therefore at 100%, from where the pixel selection starts to remove pixels. The resulting maximum significances for the optimal pixel configuration are $Z(K_\beta, 81\,\text{keV}) = 13.3$, $Z(K_\alpha, 81\,\text{keV}) = 19.1$ and $Z(K_\alpha, 85\,\text{keV}) = 17.9$.

In total, for K_α-fluorescence the effect of polarization filters is limited because the pixel selection filters C1 anyway. Regarding K_β-fluorescence, the sensitivity could be increased by a factor of 4 with 100% efficient polarizers because there single Compton scattering is the main background for monoenergetic incident photons close to the K-edge. The polarization filtering might also be interesting if a smaller detector has to be placed in an angle strongly dominated by single Compton scattering. Background reductions of two orders of magnitude are possible, which could not only increase the sensitivity but also increase the measurement speed, if the detector is the limiting part.

11 Conclusion

The presented setup including a leaf-based collimator and data analysis method by the use of pixel selection was attempted to maximize the sensitivity for high-Z element detection in human-sized objects using a 1 mm resolution without any previous knowledge about the target's location. Using the combination of both a collimator and a pixel selection with incident energies close to the K-edge in the range of 85 to 90 keV, gold concentrations of 2.3 mg/ml corresponding to 1.2 µg are detectable in a simulation for a chosen significance detection limit of $Z = 3$ in the center of a 30 cm sphere. Similar values are also obtained for various tested positions inside a human voxel model depending of course on the position and depth underneath the surface, for example 0.45 µg in the brain, 0.75 µg in the liver or 1.2 µg in the prostate. The actual amount of deposited tracer material in the body is still subject to many studies and it is not trivial to be determined as is depends not only on the size and shape of the nanoparticles but also on the method of functionalization. A comparative value used in this thesis was reported by Manohar et al. [39] in an experiment with unfunctionalized gold nanoparticles in a mouse tumor. Their XFI analysis yielded a concentration of 4.6 mg/ml, which was supported by chemical analysis with the value of 3.9 mg/ml. If these values are also biologically feasible for human beings, the discussed methods in this thesis might offer the possibility to find 1 mm sized targets at arbitrary positions in the average body if irradiated by an external X-ray beam, which, for instance, would allow for the detection of still very small tumors. Without the right choice of the solid angle used for the XFI analysis, these amounts would be undetectable. Using a full solid angle detector instead decreases the sensitivity by a factor of 8, which would make the application of XFI to human-sized scales unrealistic. In fact, it would be completely sufficient to cover 30-40% of the solid angle to reach the optimum for K_α, whereas for K_β analysis suitable for scanning targets close to the surface 10-20% are already sufficient. Everything on top would be discarded by the pixel selection algorithm. However, these numbers are only valid for gold fluorescence and only if an X-ray source with a narrow bandwidth close to the K-edge is available. For scanning other elements, such as gadolinium,

it was shown that the background is more isotropic because the signal background is not dominated by single Compton scattering anymore. Therefore, the significance is best for a full solid angle detector.

The simulations in this thesis are validated not only by using analytic calculations for the single Compton scattered background and the amount of fluorescence photons, but also by using experiments. At the PETRA III synchrotron background spectra of 30 cm PMMA cylinder phantoms with and without molybdenum leaf collimators were measured and compared to simulations resulting in good agreement. To improve the agreement even further, however, the positioning of detector and phantom relative to the beam has to be very precise since even differences of a few millimeters result in visible differences of the background spectra. Considering experiments in the near future, two scenarios with a human finger scan and a rat model are prepared by the optimization of parameters for simulations using available small pixel detectors and extrapolations on the possible improvements, if large solid angle detector would be used. If a spatial resolution of millimeters is not important, smaller concentrations could be detected with an increase of the statistics by adding up adjacent scan positions. Moreover, if a region of interest is defined before the measurement, the use of SPECT-like collimators focusing on that target range can also offer an increase in sensitivity. Apart from that, possible further development of technology might increase the sensitivity limits. A better energy resolution might increase the sensitivity up to a factor of $\sqrt{25\,\mathrm{eV}/200\,\mathrm{eV}} \approx 3$ compared to the ideal detectors used in the simulations. Further improvement would be physically impossible due to the natural linewidth. Thermal Calorimeters offer this energy resolution [145], however, they are still very slow and need special helium cooling. However, if it was possible to detect both energy and time resolution simultaneously with adequate precision, that might increase the sensitivity of XFI by an order of magnitude. The concept of filtering photons based on their polarization angle is less promising because it mainly filters single scattered photons, which also does a pixel selection.

Nevertheless, before XFI is fit for clinical practice, there are still some problems to overcome. First, an adequate X-ray source would need to be developed that delivers a high flux within a small bandwidth. Of course synchrotrons do that already, but the limited access would restrict the use of medical XFI to few very special cases. Thomson sources might provide what is needed, but so far they do not fulfill the necessary beam parameters. Second, large pixelated detector areas in the order of a square meter would need to be developed and to be affordable. Third, 3D-reconstruction is not considered here. Of course, different methods are already developed and used frequently in the XFI community, but reconstruction methods

like XFCT require scans from different directions, so that the dose per direction has to be lowered accordingly and thus the sensitivity decreases. Further research, for example, in lowering the necessary amount of directions, might be very helpful. Fourth, the scanning speed is a potential problem because using a pencil beam, as it is done in this thesis, might cause long measurement times that are not feasible with the use for living patients. Even an area of 10x10 cm already needs 10^4 individual spectra to be taken and analyzed to create a simple projection of the tracer yet without 3D-knowledge. For a measurement time of one second per line scan, this would take 3 hours for the total scan. Without anesthesia it will be almost impossible to remain still for such a long time, especially for ill patients. Fan beams geometries offer a lot faster scanning time, but at the cost of sensitivity. Fifth, a dose of 10 mGy might be too high to use this method without appropriate suspicion just as a tool for the general cancer screening. Sixth, the large collimator leaves used in the detector layout in this thesis would need to be mechanically stable without sagging. The implementation of supports or the use of thicker and thus more stable leaves would decrease the sensitivity.

As for today, the proposed methods might as a first step be applied for the development of a small animal scanner for pharmacological studies. For rodents, a lot higher radiation doses are used, usually between 0.1 Gy and 1 Gy [38, 39], the signal photons are less attenuated and overall less scattering occurs thus leading to less signal background. Moreover, the advantage of XFI having a theoretically arbitrary spatial resolution may be even more important for a rodent than for humans because the limits of, e.g., PET of approximately 1 mm [31] compared to the organ size is a lot larger than for humans. Furthermore, lower-Z elements, such as silver or molybdenum, are additionally possible tracers yielding even higher sensitivities than gold in small objects. Different types of collimators can be helpful to increase the measurement speed, if detector overload is a problem, or to increase the significance depending on the actual experiment, although due to the smaller size, higher order Compton scattering is less of a problem. In addition, the pixel selection algorithm can be used independently of a collimator if either the background or the signal is anisotropic not based on statistical fluctuations within a pixelated detector of arbitrary size.

List of Abbreviations

AMR	Adaptive Mesh Refinement 37
CdTe	Cadmium Telluride 16
CT	Computed Tomography 1
DESY	Deutsches Elektronen-Synchrotron
FDAs	Functionalized Diagnostic Agents 1
FOV	Field of view 27
FWHM	Full Width at Half Maximum 20
GBCA	Gadolinium Based Contrast Agent 101
Geant4	**Ge**ometry **an**d **T**racking 4
HOPG	Highly oriented pyrolytic graphite 24
HU	Hounsfield Unit 85
ICPMS	Inductively Coupled Plasma - Mass Spectrometry 101
ICRP	International Commission on Radiological Protection 10
ICRP-AM	International Commission on Radiological Protection - Anatomy Male 86
ICRP-AF	International Commission on Radiological Protection - Anatomy Female . . 86
ICRU	International Commission on Radiation Units and Measurements 57
IUPAC	International Union of Pure and Applied Chemistry 7
MPI	Magnetic Particle Imaging 1
MRI	Magnetic Resonance Imaging 1
PET	Positron Emission Tomography 1
PETRA	Positron Elektron Tandem Ring Anlage
PMMA	Polymethyl methacrylate 71
RMS	Root Mean Square 15
ROI	Region Of Interest 45
SPECT	Single Photon Emission Computed Tomography 1
XFI	X-ray Fluorescence Imaging I
XFCT	X-ray Fluorescence Computed Tomography 45

Bibliography

[1] W. C. Röntgen. Über eine neue Art von Strahlen. *Annalen der Physik*, 300(1):12–17, 1898.

[2] Gabor T. Herman. *Fundamentals of Computerized Tomography*. Springer, 2009.

[3] Girish Katti, Syeda Ara, and Ayesha Shireen. Magnetic Resonance Imaging (MRI) – A Review. *International Journal of Dental Clinics*, 3(1), 2011.

[4] M .S. Chaitra, Bindu Sudarshan, Balaganur Sathyanarayana, and Prasanna Kumar. Ultrasound imaging system : A review. *International Journal of Pharmacology and Pharmaceutical Technology*, 1:103–108, 2017.

[5] Patrick Cras, M. Kawai, D. Lowery, Patricia Gonzalez-DeWhitt, Barry Greenberg, and George Perry. Senile plaque neurites in Alzheimer disease accumulate amyloid precursor protein. *Proceedings of the National Academy of Sciences of the United States of America*, 88:7552–6, 10 1991.

[6] Magdy Khalil, Jordi L. Tremoleda, Tamer Bayomy, and Willy Gsell. Molecular SPECT imaging: an overview. *International journal of molecular imaging*, 2011:796025, 04 2011.

[7] Johannes G. Czernin, Martin S. Allen-Auerbach, David Allan Nathanson, and Constantin Lapa. PET/CT in oncology: Current status and perspectives. In *Current radiology reports*, 2013.

[8] Bernhard Gleich and Jürgen Weizenecker. Tomographic imaging using the nonlinear response of magnetic particles. *Nature*, 435:1214–7, 07 2005.

[9] Hongyu Chen, Melissa M. Rogalski, and Jeffrey Anker. Advances in functional x-ray imaging techniques and contrast agents. *Physical chemistry chemical physics : PCCP*, 14:13469–86, 09 2012.

[10] Cynthia H. McCollough, Shuai Leng, Lifeng Yu, and Joel G. Fletcher. Dual- and multi-energy CT: Principles, technical approaches, and clinical applications. *Radiology*, 276(3):637–653, 2015. PMID: 26302388.

[11] Scott A. Huettel, Allen W. Song, and Gregory McCarthy. *Functional Magnetic Resonance Imaging*. Sinauer Associates, 2nd edition, 2008.

[12] Stefaan Vandenberghe and Paul K. Marsden. PET-MRI: a review of challenges and solutions in the development of integrated multimodality imaging. *Physics in Medicine and Biology*, 60(4):R115–R154, 02 2015.

[13] Alexandre Albanese, Peter S. Tang, and Warren C. W. Chan. The effect of nanoparticle size, shape, and surface chemistry on biological systems. *Annual review of biomedical engineering*, 14:1–16, 04 2012.

[14] Jay F. Dorsey, Lova Sun, Daniel Y. Joh, Alon Witztum, Ajlan Al Zaki, Gary D. Kao, Michelle Alonso-Basanta, Stephen Avery, Andrew Tsourkas, and Stephen M. Hahn. Gold nanoparticles in radiation research: potential applications for imaging and radiosensitization. *Translational Cancer Research*, 2(4), 2013.

[15] Hadi Rezaei, Mansour Zabihzadeh, Mahdi Ghorbani, Foad Goli Ahmadabad, and Hesameddin Mostaghimi. Evaluation of dose enhancement in presence of gold nanoparticles in eye brachytherapy by (103)Pd source. *Australasian physical & engineering sciences in medicine*, 40, 05 2017.

[16] R. Glocker and H. Schreiber. Quantitative Röntgenspektralanalyse mit Kalterregung des Spektrums. *Annalen der Physik*, 390(8):1089–1102, 1928.

[17] Michael Mantler and Manfred Schreiner. X-ray fluorescence spectrometry in art and archaeology. *X-Ray Spectrometry*, 29(1):3–17, 2000.

[18] Temitope D. Timothy Oyedotun. X-ray fluorescence (XRF) in the investigation of the composition of earth materials: a review and an overview. *Geology, Ecology, and Landscapes*, 2(2):148–154, 2018.

[19] F. Pax C. Blamey, David J. Paterson, Adam Walsh, Nader Afshar, Brigid A. McKenna, Miaomiao Cheng, Caixan Tang, Walter J. Horst, Neal W. Menzies, and Peter M. Kopittke. Time-resolved analyses of elemental distribution and concentration in living plants: An example using manganese toxicity in cowpea leaves. *bioRxiv 228577*, 2017.

[20] Paul B. Hoffer. Fluorescent thyroid scanning. *Am. Jo. Roentgenol. Radium. Titer*, 105(4):721–727, 1969.

[21] J. O. Christoffersson and S. Mattsson. Polarised x-rays in XRF-analysis for improved in vivo detectability of cadmium in man. *Physics in Medicine and Biology*, 28(10):1135–1144, 10 1983.

[22] R. Jonson, Jimmy Börjesson, Sören Mattsson, B. Unsgaard, and A. Wallgren. Uptake and retention of platinum in patients undergoing cisplatin therapy. *Acta oncologica (Stockholm, Sweden)*, 30:315–9, 02 1991.

[23] R. Jonson, S. Mattsson, and B. Unsgaard. A method for in vivo analysis of platinum after chemotherapy: with cisplatin. *Physics in Medicine and Biology*, 33(7):847–857, 07 1988.

[24] Jimmy Börjesson, Magne Alpsten, Shibin Huang, Ragnar Jonson, Sören Mattsson, and Charlotte Thornberg. In vivo x-ray fluorescence analysis with applications to platinum, gold and mercury in man — experiments, improvements, and patient measurements. In *Human Body Composition: In Vivo Methods, Models, and Assessment*, pages 275–280. Springer US, Boston, MA, 1993.

[25] John Shakeshaft, Anthony K. Clarke, Martyn J. Evans, and Stephen C. Lillicrap. X-ray fluorescence determination of gold in vivo. In *Human Body Composition: In Vivo Methods, Models, and Assessment*, pages 307–310. Springer US, Boston, MA, 1993.

[26] Maria Fernanda Hornos Carneiro and Fernando Barbosa Jr. Gold nanoparticles: A critical review of therapeutic applications and toxicological aspects. *Journal of Toxicology and Environmental Health, Part B*, 19(3-4):129–148, 2016. PMID: 27282429.

[27] Jimmy Börjesson and Sören Mattsson. Medical applications of x-ray fluorescence for trace element research. *Powder Diffraction*, 22(2):130–137, 2007.

[28] David Chettle. In vivo applications of x-ray fluorescence in human subjects. *Pramana-journal of Physics - PRAMANA-J PHYS*, 76:249–259, 02 2011.

[29] Stephen Derenzo, Thomas Budinger, Ron Huesman, and J. L. Cahoon. Dynamic positron emission tomography in man using small bismuth germanate crystals. In *Sixth International Conference on Positron Annihilation, Ft. Worth, TX*, 04 1982.

[30] William W. Moses. Fundamental limits of spatial resolution in PET. *Nuclear instruments & methods in physics research. Section A, Accelerators, spectrometers, detectors and associated equipment*, 648 Supplement 1:S236–S240, 08 2011.

[31] Matthew Walker, Marlies Goorden, Katherine Dinelle, Ruud Ramakers, Stephan Blinder, Maryam Shirmohammad, Frans van der Have, Freek Beekman, and Vesna Sossi. Performance assessment of a preclinical PET scanner with pinhole collimation by comparison to a coincidence-based small-animal PET scanner. *Journal of nuclear medicine : official publication, Society of Nuclear Medicine*, 55, 06 2014.

[32] Oleksandra Ivashchenko, Frans van der Have, Jose L. Villena, Harald C. Groen, Ruud M. Ramakers, Harrie H. Weinans, and Freek J. Beekman. Quarter-millimeter-resolution molecular mouse imaging with U-SPECT+. *Molecular Imaging*, 14(1):7290.2014.00053, 2015.

[33] Pontus K. E. Börjesson, Yvonne W. S. Jauw, Remco Bree, Jan C. Roos, Jonas Castelijns, C. Leemans, Guus A. M. S. van Dongen, and Ronald Boellaard. Radiation dosimetry of Zr-89-labeled chimeric monoclonal antibody U36 as used for immuno-PET in head and neck cancer patients. *Journal of nuclear medicine : official publication, Society of Nuclear Medicine*, 50:1828–36, 11 2009.

[34] Melissa A. Deri, Brian Zeglis, Lynn Francesconi, and Jason S. Lewis. PET imaging with 89Zr: From radiochemistry to the clinic. *Nuclear Medicine and Biology*, 40:3–14, 01 2013.

[35] H. von Busch, G. Harding, G. Martens, J.-P. Schlomka, and B. Schweizer. Investigation of externally activated x-ray fluorescence tomography for use in medical diagnostics, 2005.

[36] Bernhard H Müller, Christoph Hoeschen, Florian Grüner, Vladimir A. Arkadiev, and Thorsten R. C. Johnson. Molecular imaging based on x-ray fluorescent high-Z tracers. *Physics in Medicine and Biology*, 58(22):8063–8076, 10 2013.

[37] Kate Ricketts, Andrea Castoldi, Chiara Guazzoni, Cigdem Ozkan, Christiana Christodoulou, Adam Gibson, and G.J. Royle. A quantitative x-ray detection system for gold nanoparticle tumour biomarkers. *Physics in medicine and biology*, 57:5543–55, 08 2012.

[38] Tohoru Takeda, Jin Wu, Qingkai Huo, Tetsuya Yuasa, Kazuyuki Hyodo, Avraham Dilmanian, and Takao Akatsuka. X-ray fluorescent CT imaging of cerebral uptake of stable-iodine perfusion agent iodoamphetamine analog IMP in mice. *Journal of synchrotron radiation*, 16:57–62, 02 2009.

[39] Nivedh Manohar, Francisco Reynoso, Parmeswaran Diagaradjane, Sunil Krishnan, and Sang Hyun Cho. Quantitative imaging of gold nanoparticle distribution in a tumor-bearing mouse using benchtop x-ray fluorescence computed tomography. *Scientific Reports*, 6:22079, 02 2016.

[40] Michelle Lord, F.E. McNeill, J.L. Gräfe, A.L. Galusha, P.J. Parsons, Michael Noseworthy, L Howard, and David Chettle. Confirming improved detection of gadolinium in bone using in vivo XRF. *Applied Radiation and Isotopes*, 120, 12 2016.

[41] Farshad Mostafaei and L.H. Nie. The study of in vivo x-ray fluorescence (XRF) technique for gadolinium (Gd) measurements in human bone. *Journal of Instrumentation*, 11:T08001–T08001, 08 2016.

[42] Theresa Brümmer. *Design Study of a Laser-Driven X-ray Source for Medical Fluorescence Imaging*. PhD thesis, Universität Hamburg, Von-Melle-Park 3, 20146 Hamburg, 2017.

[43] Tong Xu, Min Chen, Feiyu Li, Lu-Le Yu, Zheng-Ming Sheng, and Jie Zhang. Spectrum bandwidth narrowing of thomson scattering x-rays with energy chirped electron beams from laser wakefield acceleration. *Applied Physics Letters*, 104:013903, 01 2014.

[44] Florian Grüner, Florian Blumendorf, Oliver Schmutzler, Theresa Staufer, Michelle Bradbury, Ulrich Wiesner, Tanja Rosentreter, Gabriele Loers, David Lutz, Bernadette Richter, Markus Fischer, Florian Schulz, Swantje Steiner, Martin Warmer, Anja

Burkhardt, Alke Meents, Matthew Kupinski, and Christoph Hoeschen. Localising functionalised gold-nanoparticles in murine spinal cords by x-ray fluorescence imaging and background-reduction through spatial filtering for human-sized objects. *Scientific Reports*, 8(1):16561, 2018.

[45] Florian Grüner, Christoph Hoeschen, and Florian Blumendorf. Verfahren und Messvorrichtung zur Röntgenfluoreszenz-Messung, 4 2017. Applicant: University of Hamburg, International application No. PCT/EP2018/058859.

[46] Beer. Bestimmung der Absorption des rothen Lichts in farbigen Flüssigkeiten. *Annalen der Physik*, 162(5):78–88, 1852.

[47] M.J. Berger, Hubbell, J.H., S.M. Seltzer, J. Chang, J.S. Coursey, R. Sukumar, D.S. Zucker, and K. Olsen. XCOM: Photon Cross Section Database (version 1.5). https://physics.nist.gov/PhysRefData/Xcom/html/xcom1.html, 2010. [Online; accessed 2016-2019].

[48] Hubbell, J.H., and S.M. Seltzer. Tables of x-ray mass attenuation coefficients and mass energy-absorption coefficients, NIST standard reference database 126. http://www.nist.gov/pml/data/xraycoef/index.cfml, 2004. [Online; accessed 2016-2019].

[49] Florian Blumendorf. Signal analysis for medical imaging with x-ray fluorescence. Master's thesis, University of Hamburg, 2016.

[50] Tom Schoonjans, Antonio Brunetti, Bruno Golosio, Manuel Sanchez del Rio, Vicente Armando Solé, Claudio Ferrero, and Laszlo Vincze. The xraylib library for x-ray–matter interactions. recent developments. *Spectrochimica Acta Part B: Atomic Spectroscopy*, 66(11):776 – 784, 2011.

[51] R. Jenkins, R. Manne, R. Robin, and C. Senemaud. IUPAC—nomenclature system for x-ray spectroscopy. *X-Ray Spectrometry*, 20(3):149–155, 6 1991.

[52] Manne Siegbahn. Relations between the K and L series of the high-frequency spectra. *Nature*, 96:676–676, 1916.

[53] H.G.J. Moseley M.A. Xciii. the high-frequency spectra of the elements. *The London, Edinburgh, and Dublin Philosophical Magazine and Journal of Science*, 26(156):1024–1034, 1913.

[54] Tomas Soltis, Lorcan M. Folan, and Waleed Eltareb. One hundred years of Moseley's law: An undergraduate experiment with relativistic effects. *American Journal of Physics*, 85(5):352–358, 2017.

[55] O. Klein and Y. Nishina. Über die Streuung von Strahlung durch freie Elektronen nach der neuen relativistischen Quantendynamik von Dirac. *Zeitschrift für Physik*, 52(11):853–868, 11 1929.

[56] Steven Weinberg. *The Quantum Theory of Fields*, volume 1. Cambridge University Press, 1995.

[57] K. A. Olive et al. Review of Particle Physics. *Chin. Phys.*, C38:090001, 2014. 1. PHYSICAL CONSTANTS.

[58] Giorgio Matt, Marco Feroci, Massimo Rapisarda, and Enrico Costa. Treatment of Compton scattering of linearly polarized photons in monte carlo codes. *Radiation Physics and Chemistry*, 48(4):403 – 411, 1996.

[59] J. H. Hubbell, Wm. J. Veigele, E. A. Briggs, R. T. Brown, D. T. Cromer, and R. J. Howerton. Atomic form factors, incoherent scattering functions, and photon scattering cross sections. *Journal of Physical and Chemical Reference Data*, 4(3):471–538, 1975.

[60] Arthur H. Compton. A quantum theory of the scattering of x-rays by light elements. *Phys. Rev.*, 21:483–502, May 1923.

[61] Francesco Longo, Luciano Pandola, and Maria Grazia Pia. New Geant4 developments for doppler broadening simulation in Compton scattering - development of charge transfer simulation models in Geant4. *IEEE Nuclear Science Symposium Conference Record*, pages 2865 – 2868, 11 2008.

[62] ICRP. Recommendations of the international commission on radiological protection. in: ICRP publication 103 (valentin j, eds.). *Ann ICRP*, 37:12, 01 2007.

[63] Christoph Lee, Andrew H. Haims, Edward P. Monico, James A. Brink, and Howard Forman. Diagnostic CT scans: Assessment of patient, physician, and radiologist awareness of radiation dose and possible risks. *Radiology*, 231:393–8, 05 2004.

[64] David J Brenner and Eric J Hall. Computed tomography–an increasing source of radiation exposure. *The New England journal of medicine*, 357(22):2277—2284, November 2007.

[65] Aruna Kaushik, Abhinav Jaimini, Madhavi Tripathi, Maria D'Souza, Rajnish Sharma, Anupam Mondal, AnilK Mishra, and Bilikere Dwarakanath. Estimation of radiation dose to patients from [18] FDG whole body PET/CT investigations using dynamic PET scan protocol. *Indian Journal of Medical Research*, 142:721, 12 2015.

[66] B.N. Taylor. *International System of Units (SI) (rev. , 2008 Ed.)*. DIANE Publishing Company, 2009.

[67] Geant4 Collaboration. Geant4 book for application developers, 3 2019.

[68] Wolfgang A. Rolke and Angel M. López. Estimating a signal in the presence of an unknown background. *Nuclear Instruments and Methods in Physics Research A*, 685:16–21, 09 2012.

[69] Serguei Chatrchyan et al. Observation of a new boson at a mass of 125 GeV with the CMS experiment at the LHC. *Phys. Lett.*, B716:30–61, 2012.

[70] Pekka K. Sinervo. Signal significance in particle physics. In *Advanced Statistical Techniques in Particle Physics. Proceedings, Conference, Durham, UK, March 18-22, 2002*, pages 64–76, 2002.

[71] Georges Aad et al. Observation of a new particle in the search for the Standard Model Higgs boson with the ATLAS detector at the LHC. *Phys. Lett.*, B716:1–29, 2012.

[72] Matthew Chalmers. Physicists find new particle, but is it the Higgs? *Nature*, 07 2012.

[73] Ton J. Cleophas. Clinical trials and p-values, beware of the extremes. *Clinical Chemistry and Laboratory Medicine (CCLM)*, 42, 2005.

[74] Harvey Motulsky. *Intuitive Biostatistics: A Nonmathematical Guide to Statistical Thinking*. Oxford University Press, third edition, 2013.

[75] Rene Andrae, Tim Schulze-Hartung, and Peter Melchior. Dos and don'ts of reduced chi-squared. *arXiv e-prints*, page arXiv:1408.5899, 12 2010.

[76] S. Agostinelli et al. Geant4—a simulation toolkit. *Nuclear Instruments and Methods in Physics Research Section A: Accelerators, Spectrometers, Detectors and Associated Equipment*, 506(3):250 – 303, 2003.

[77] Geant4 Collaboration. Physics reference manual, 3 2019.

[78] Rene Brun and Fons Rademakers. ROOT - An Object Oriented Data Analysis Framework. Proceedings AIHENP'96 Workshop, Lausanne, Sep. 1996, Nucl. Inst. & Meth. in Phys. Res. A 389 (1997) 81-86.

[79] Guido van Rossum. Python tutorial. Report CS-R9526, pub-CWI, 4 1995.

[80] AMPTEK Inc. Manufacturerer Homepage of XR-100CdTe detector. http://amptek.com/products/xr-100cdte-x-ray-and-gamma-ray-detector/#8. [Online; accessed 2019-05-08].

[81] R. H. Redus, J. A. Pantazis, T. J. Pantazis, A. C. Huber, and B. J. Cross. Characterization of CdTe detectors for quantitative X-ray spectroscopy. *IEEE Transactions on Nuclear Science*, 56(4):2524–2532, 08 2009.

[82] Robert Redus. Application note ANCZT-2 rev. 3 charge trapping in XR-100T-CdTe and -CZT detectors, 11 2007.

[83] Karl Hecht. Zum Mechanismus des lichtelektrischen Primärstromes in isolierenden Kristallen. *Zeitschrift für Physik*, 77(3):235–245, 03 1932.

[84] U. Fano. On the theory of ionization yield of radiations in different substances. *Phys. Rev.*, 70:44–52, 07 1946.

[85] Adriano Cola, Isabella Farella, A.M. Mancini, and A. Donati. Electric field properties of CdTe nuclear detectors. *Nuclear Science, IEEE Transactions on*, 54:868 – 872, 09 2007.

[86] Akram Mohammadi, Mamoru BABA, and Hideo HIRAYAMA. Simulation of the carrier trapping effect in a Schottky CdTe detector by considering a nonuniform electric field. *Journal of Nuclear Science and Technology - J NUCL SCI TECHNOL*, 46:1032–1037, 11 2009.

[87] Gary W. Phillips and Keith W. Marlow. Automatic analysis of gamma-ray spectra from germanium detectors. *Nuclear Instruments and Methods*, 137(3):525 – 536, 1976.

[88] J. W. Scuffham, M. D. Wilson, P. Seller, M. C. Veale, P. J. Sellin, S. D. M. Jacques, and R. J. Cernik. A CdTe detector for hyperspectral SPECT imaging. *Journal of Instrumentation*, 7(08):P08027–P08027, 08 2012.

[89] Matthew Wilson, Louise Dummot, Diana D. Duarte, Faith Green, Silvia Pani, Andreas Schneider, James Scuffham, Paul Seller, and Matthew Veale. A 10 cm x 10 cm CdTe spectroscopic imaging detector based on the HEXITEC ASIC. *Journal of Instrumentation*, 10:P10011, 10 2015.

[90] Martin Stieben. Design studies on gold nanoparticle x-ray fluorescence imaging. Master's thesis, University of Hamburg, 2013.

[91] Martin Sjölin and Mats Danielsson. Improved signal-to-noise ratio for non-perpendicular detection angles in x-ray fluorescence computed tomography (XFCT). *Physics in Medicine and Biology*, 59:6507, 10 2014.

[92] Moiz Ahmad, Magdalena Bazalova, Liangzhong Xiang, and Lei Xing. Order of magnitude sensitivity increase in x-ray fluorescence computed tomography (XFCT) imaging with an optimized spectro-spatial detector configuration: Theory and simulation. *IEEE transactions on medical imaging*, 33:1119–28, 05 2014.

[93] Tomasz Plewa, Timur Linde, and V. Gregory Weirs. *Adaptive Mesh Refinement - Theory and Applications*. Springer, 2005.

[94] J. Herman, K. Dilcher, R. Kucera, and J. Simsa. *Counting and Configurations: Problems in Combinatorics, Arithmetic, and Geometry*. CMS Books in Mathematics. Springer New York, 2013.

[95] John P. Hogan, Robert A. Gonsalves, and Allen S. Krieger. Fluorescent computer tomography: A model for correction of x-ray absorption. *Nuclear Science, IEEE Transactions on*, 38:1721 – 1727, 01 1992.

[96] M. Bazalova, Y. Kuang, G. Pratx, and L. Xing. Investigation of x-ray fluorescence computed tomography (XFCT) and K-edge imaging. *IEEE Transactions on Medical Imaging*, 31(8):1620–1627, 08 2012.

[97] Simon Reichert. Reconstruction and dose minimization for CT-based x-ray fluorescence imaging. Master's thesis, University of Hamburg, 2019.

[98] Seongmoon Jung, Wonmo Sung, and Sung-Joon Ye. Pinhole x-ray fluorescence imaging of gadolinium and gold nanoparticles using polychromatic x-rays: A monte carlo study. *International Journal of Nanomedicine*, Volume 12:5805–5817, 08 2017.

[99] Tenta Sasaya, Naoki Sunaguchi, Kazuyuki Hyodo, Tsutomu Zeniya, and Tetsuya Yuasa. Multi-pinhole fluorescent x-ray computed tomography for molecular imaging. *Scientific Reports*, 7, 12 2017.

[100] Don Vernekohl, Moiz Ahmad, Garry Chinn, and Lei Xing. Feasibility study of Compton cameras for x-ray fluorescence computed tomography with humans. *Physics in medicine and biology*, 61:8521–8540, 11 2016.

[101] Christian Körnig. Spatial reconstruction of small objects for medical x-ray fluorescence imaging using multiple detectors. Master's thesis, University of Hamburg, 2019.

[102] Karen Van Audenhaege, Roel Van Holen, Stefaan Vandenberghe, Christian Vanhove, Scott D. Metzler, and Stephen C. Moore. Review of SPECT collimator selection, optimization, and fabrication for clinical and preclinical imaging. *Medical physics*, 42:4796, 08 2015.

[103] Qingkai Huo, Hidenori Sato, Tetsuya Yuasa, Takao Akatsuka, Jin Wu, Thet-Thet Lwin, Tohoru Takeda, and Kazuyuki Hyodo. First experimental result with fluorescent x-ray CT based on sheet-beam geometry. *X-Ray Spectrometry*, 38:439 – 445, 05 2009.

[104] Shanghai Jiang, Peng He, Luzhen Deng, Mianyi Chen, and Biao Wei. Monte carlo simulation for polychromatic x-ray fluorescence computed tomography with sheet-beam geometry. *International Journal of Biomedical Imaging*, 2017, 03 2017.

[105] Bernard Jones and Sang Cho. The feasibility of polychromatic cone-beam x-ray fluorescence computed tomography (xfct) imaging of gold nanoparticle-loaded objects: A monte carlo study. *Physics in medicine and biology*, 56:3719–30, 06 2011.

[106] Jakob C. Larsson, Kian Shaker, and Hans M. Hertz. Focused anti-scatter grid for background reduction in x-ray fluorescence tomography. *Opt. Lett.*, 43(11):2591–2594, 06 2018.

[107] W.S. Snyder. Report of the task group on reference man. *ICRP Publication*, 23, 1975.

[108] K. Kawashima. Radiation quantities and units, ICRU report 33, 1980. *Journal of the Atomic Energy Society of Japan / Atomic Energy Society of Japan*, 25:445–452, 01 1983.

[109] Moiz Ahmad, Magdalena Bazalova, Rebecca Fahrig, and Lei Xing. Optimized detector angular configuration increases the sensitivity of x-ray fluorescence computed tomography (xfct). *IEEE transactions on medical imaging*, 34, 12 2014.

[110] Norbert Schell, Andrew King, Felix Beckmann, Torben Fischer, Martin Müller, and Andreas Schreyer. The high energy materials science beamline (HEMS) at PETRA III. In *Mechanical Stress Evaluation by Neutrons and Synchrotron Radiation VI*, volume 772 of *Materials Science Forum*, pages 57–61. Trans Tech Publications, 2 2014.

[111] H.L. Jr. Fisher and W.S. Snyder. Distribution of dose in the body from a source of gamma rays distributed uniformly in an organ. *Proceedings of the First International Congress of Radiation Protection*, pages 1473–1486, 10 1967.

[112] C.H. Kim, Y.S. Yeom, T.T. Nguyen, Z.J. Wang, H.S. Kim, M.C. Han, J.K. Lee, M. Zankl, N. Petoussi-Henss, W.E. Bolch, C. Lee, and B.S. Chung. The reference phantoms: voxel vs polygon. *Annals of the ICRP*, 45(1_suppl):188–201, 2016. PMID: 26969297.

[113] ICRP. ICRP voxel model data. http://www.icrp.org/docs/V1.2.zip, 09 2009.

[114] Bernd Grosswendt. ICRP Publication 110. *Radiation Protection Dosimetry*, 150(1), 01 2012.

[115] Maria Zankl. Adult male and female reference computational phantoms (ICRP publication 110). *Japanese Journal of Health Physics*, 45:357–369, 01 2010.

[116] J. Valentin. Basic anatomical and physiological data for use in radiological protection: reference values: ICRP publication 89. *Annals of the ICRP*, 32(3):1 – 277,244–245, 2002.

[117] Robert Koch-Institut. Krebs in Deutschland für 2013/2014, 2017. doi:10.17886.

[118] Thomas Balzer. Presence of gadolinium (Gd) in the brain and body, 09 2017. Bayer.

[119] M. Helena Mendonça-Dias, Elena Gaggelli, and Paul C. Lauterbur. Paramagnetic contrast agents in nuclear magnetic resonance medical imaging. *Seminars in Nuclear Medicine*, 13(4):364 – 376, 1983.

[120] Tomonori Kanda, Kazunari Ishii, Hiroki Kawaguchi, Kazuhiro Kitajima, and Daisuke Takenaka. High signal intensity in the dentate nucleus and globus pallidus on unenhanced t1-weighted MR images: Relationship with increasing cumulative dose of a gadolinium-based contrast material. *Radiology*, 270(3):834–841, 2014. PMID: 24475844.

[121] Robert J. McDonald, Jennifer S. McDonald, David F. Kallmes, Mark E. Jentoft, Michael Paolini, David L. Murray, Eric Williamson, and Laurence Eckel. Gadolinium deposition in human brain tissues after contrast-enhanced MR Imaging in adult patients without intracranial abnormalities. *Radiology*, 285:161595, 06 2017.

[122] Robert McDonald, Deborah Levine, Jeffrey Weinreb, Emanuel Kanal, Matthew S. Davenport, James H. Ellis, Paula M. Jacobs, Robert E. Lenkinski, Kenneth R. Maravilla, Martin R. Prince, Howard A. Rowley, Michael F. Tweedle, and Herbert Y. Kressel. Gadolinium retention: A research roadmap from the 2018 NIH/ACR/RSNA workshop on gadolinium chelates. *Radiology*, 289(2):517–534, 11 2018.

[123] Gregory W. White, Wendell Gibby, and Michael Tweedle. Comparison of Gd(DTPA-BMA) (Omniscan) versus Gd(HP-DO3A) (ProHance) relative to gadolinium retention in human bone tissue by inductively coupled plasma mass spectroscopy. *Investigative radiology*, 41:272–8, 04 2006.

[124] European Medicines Agency. Gadolinium-containing contrast agents, 12 2017.

[125] Michelle Lord, David Chettle, J.L. Gräfe, Michael Noseworthy, and Fiona E. McNeill. Observed deposition of gadolinium in bone using a new noninvasive in vivo biomedical device: Results of a small pilot feasibility study. *Radiology*, 287:171161, 12 2017.

[126] Daniel C. Baumgart and Simon R. Carding. Inflammatory bowel disease: cause and immunobiology. *The Lancet*, 369(9573):1627 – 1640, 2007.

[127] Amanda Freise, Kirstin Zettlitz, Felix Salazar, Richard Tavaré, Wen-Ting Tsai, Arion Hadjioannou, Nora Rozengurt, Jonathan Braun, and Anna M. Wu. ImmunoPET in inflammatory bowel disease: Imaging CD4+ T cells in a murine model of colitis. *Journal of Nuclear Medicine*, 59:jnumed.117.199075, 01 2018.

[128] Orit Jacobson, Dale O. Kiesewetter, and Xiaoyuan Chen. Fluorine-18 radiochemistry, labeling strategies and synthetic routes. In *Bioconjugate chemistry*, 2015.

[129] Tianwu Xie and Habib Zaidi. Assessment of S values in stylized and voxel-based rat models for positron-emitting radionuclides. *Molecular Imaging and Biology*, 15:542–551, 2013.

[130] Li Wu, Guozhi Zhang, Qingming Luo, and Qian Liu. An image-based rat model for monte carlo organ dose calculations. *Medical physics*, 35:3759–64, 09 2008.

[131] Tianwu Xie, Dao Han, Yang Liu, Wenjuan Sun, and Qian Liu. Skeletal dosimetry in a voxel-based rat phantom for internal exposures to photons and electrons. *Medical Physics*, 37(5):2167–2178, 2010.

[132] Jakob C. Larsson, Carmen Vogt, William Vågberg, Muhammet S. Toprak, Johanna Dzieran, Marie Arsenian-Henriksson, and Hans M Hertz. High-spatial-resolution x-ray fluorescence tomography with spectrally matched nanoparticles. *Physics in Medicine & Biology*, 63(16):164001, 08 2018.

[133] D. Vernekohl and L. Xing. Enhanced molecular sensitivity of cisplatin imaging by time-of-flight x-ray fluorescence CT for simultaneous chemoradiation therapy. *International Journal of Radiation Oncology - Biology - Physics*, 99(2, Supplement):E732, 2017. Proceedings of the American Society for Radiation Oncology.

[134] H. Ch. Schröder, A. Affeldt, H. P. Gausepohl, G. Kube, and G. Priebe. Bunch Length Measurement for PETRA III Light Source Storage Ring. pages 113–115, Geneva, 05 2011. 10th European Workshop on Beam Diagnostics and Instrumentation for Particle Accelerators, Hamburg (Germany), 16 May 2011 - 18 May 2011, JACoW.

[135] Stefan Seifert, Herman T. van Dam, and Dennis R. Schaart. The lower bound on the timing resolution of scintillation detectors. *Physics in Medicine and Biology*, 57(7):1797–1814, 03 2012.

[136] P. Lecoq. Pushing the limits in time-of-flight PET imaging. *IEEE Transactions on Radiation and Plasma Medical Sciences*, 1(6):473–485, 11 2017.

[137] Stanislav Tashenov, A. Khaplanov, Bo Cederwall, and K.-U Schässburger. Hard x-ray polarimetry by means of Rayleigh scattering. *Nuclear Instruments and Methods in Physics Research Section A: Accelerators, Spectrometers, Detectors and Associated Equipment*, 600:599–603, 03 2009.

[138] Poen S. Ong and John N. Randall. A focusing x-ray polarizer for energy-dispersive analysis. *X-Ray Spectrometry*, 7(4):241–248, 1978.

[139] Philip Kaaret. X-Ray Polarimetry. *arXiv e-prints*, page arXiv:1408.5899, 08 2014.

[140] Fabio Muleri, Ronaldo Bellazzini, Enrico Costa, Paolo Soffitta, Francesco Lazzarotto, Marco Feroci, L. Pacciani, Alda Rubini, Ennio Morelli, Luca Baldini, Francesco Bitti, Alessandro Brez, Francesco Cavalca, Luca Latronico, M.M. Massai, Nicola Omodei, M Pinchera, Carmelo Sgro, Gloria Spandre, and Rodolfo Canestrari. An x-ray polarimeter for hard x-ray optics. *Proc SPIE*, 6266:62662X, 06 2006.

[141] R.H. Howell and W.L. Pickles. Possible sources of polarized x-rays for x-ray fluorescence spectra with reduced backgrounds. *Nuclear Instruments and Methods*, 120(1):187 – 188, 1974.

[142] A. Martindale, N. Bannister, K.D.M. Harris, Gregory Solan, S.P. Collins, Yohan Champouret, V.K. Muppidi, G.W. Fraser, and Mervyn Roy. Narrow-band x-ray polarizing filters. *Proceedings of SPIE - The International Society for Optical Engineering*, 6686, 09 2007.

[143] S.P. Collins. Polaroid H-sheet as a polarizer for 33 kev x-rays. *Nuclear Instruments and Methods in Physics Research Section B: Beam Interactions with Materials and Atoms*, 129(2):289 – 296, 1997.

[144] Andrey N. Volobuev, Eugene S. Petrov, and Eugene L. Ovchinnikov. Features of malus law in the region of x-ray radiation. *Journal of Modern Physics*, 03:585–596, 01 2012.

[145] D. McCammon, W. Cui, M. Juda, J. Morgenthaler, J. Zhang, R.L. Kelley, S.S. Holt, G.M. Madejski, S.H. Moseley, and A.E. Szymkowiak. Thermal calorimeters for high resolution x-ray spectroscopy. *Nuclear Instruments and Methods in Physics Research Section A: Accelerators, Spectrometers, Detectors and Associated Equipment*, 326(1):157 – 165, 1993.

List of Figures

2.1 Theory: Mass attenuation coefficients 6
2.2 Theory: Simplified illustration of a fluorescence process 7
2.3 Theory: Compton scattering cross section 9
2.4 Absorbed dose: Photon numbers for 10 mGy and dose outside the beam . . . 11
2.5 Amptek detector: Spectra showing detector response 19
2.6 Amptek detector: Signal intervals 21

3.1 Detector layout with collimator 24
3.2 30 cm sphere: Spectrum with collimator 4π and pixel selection 25
3.3 30 cm sphere: Uncollimated spectrum and positions for Compton scattering . 27
3.4 30 cm sphere: Comparison with analytic models 28
3.5 Collimator: Geometry sketches for analytic calculations 29
3.6 Collimator: Analytic field of view 31
3.7 Collimator: Compton reduction compared with analytic comparison 33
3.8 Pixel selection: Background anisotropy and solid angle effects 35
3.9 Pixel selection: Background maps for 4π and pixel selection 36
3.10 Pixel selection: Flow chart 38
3.11 Pixel selection: Significance and χ^2 for different progress stages 39
3.12 Pixel selection: Spectra with fits for different progress stages 40
3.13 Pixel selection: Spectrum with wrong signal 41
3.14 Pixel selection: Upper limit for the number of pixels 42
3.15 Pixel selection: Significance dependence of number of pixels and restraints . 44

4.1 Collimator variation: Sketches of diff. collimator types 48
4.2 Detector size variation 50
4.3 Variation of the number of collimator leaves 52
4.4 Variation of the collimator leaves' thickness 53
4.5 Parallel sheet collimator: Spatial resolution 55
4.6 Parallel and theta collimator: Spectrum 56

5.1 R150mmSphere: Variation of phantom size 58
5.2 R150mmSphere: Variation of target elements 59
5.3 R150mmSphere: Variation of incident energy 61
5.4 R150mmSphere: Energy-background inhomogeneity map 62

5.5 R150mmSphere: Variation of energy bandwidth 64
5.6 R150mmSphere: Variation of target position for K_α and K_β-fluorescence . . 66
5.7 Variation of phantom density 67
5.8 Comparison of XFI with transmission imaging 69

6.1 P07 experiment: Spectrum comparison for 30 cm phantom 72
6.2 P07 experiment: Angular dependence of photon counts 74
6.3 P07 experiment: Analytic Compton1 spectra 75
6.4 P07 experiment: Sketch and picture of the collimator 76
6.5 P07 experiment: Variation of the number of collimator leaves 77
6.6 P07 experiment: Variation of the vertical collimator position 79
6.7 P07 experiment: Spectra with 30 cm phantom and collimator 80
6.8 P21 experiment: Sketch of 20 mm phantom and collimator 82
6.9 P21 experiment: 20 mm phantom spectra from experiment and simulation . . 83
6.10 P21 experiment: 20 mm phantom spectrum with fit 84

7.1 Human voxel model: Picture of male voxel model 86
7.2 Human voxel model: Brain position scan and spectra 91
7.3 Human voxel model: Gold target in lung 92
7.4 Human voxel model: Thyroid energy RMS variation 95
7.5 Human voxel model: Liver angle scan 96
7.6 Human voxel model: Pancreas energy RMS variation 98

8.1 Voxel finger model: Area Scan with 4π detector 104
8.2 Voxel finger model: EnergyScan with 4π detector 105
8.3 Voxel finger model: Energy and angular variation 106
8.4 Voxel finger model: Compton exclusion energies for Au and Gd 108

9.1 Rat voxel phantom: X-ray transmission image 110
9.2 Rat voxel phantom: Energy variation with 4π detector 111
9.3 Rat voxel phantom: 4π spectrum at 85 keV 112
9.4 Rat voxel phantom: Energy variation with Amptek detector 114
9.5 Rat voxel phantom: Uncollimated Hexitec spectrum at $= 30^\circ$ 115
9.6 Rat voxel phantom: Background reduction for small leaves collimator 116
9.7 Rat voxel phantom: Spectra for collimators restricting view of beam axis . . . 118
9.8 Rat voxel phantom: Variation of target elements 120

10.1 Time resolution: Sketch of spatial reconstruction 124
10.2 Time resolution: Spatial spectrum without energy information 125
10.3 Time resolution: Spatial spectrum with energy information 126
10.4 Time resolution: Energy spectrum for 3 ps time resolution 127
10.5 Time resolution: Significance plotted against time resolution 128
10.6 Polarization filters: Degree of polarization after Compton scattering 131

10.7 Polarization filters: Optimal polarization filter angles 132
10.8 Polarization filters: RMS of polarization after Compton scattering 133
10.9 Polarization filters: Degree of polarization after Compton scattering 135
10.10 Polarization filters: Background maps for 30 cm phantom 136
10.11 Polarization filters: Spectra for 30 cm phantom 137
10.12 Polarization filters: Significance increase with pixel selection 138

List of Tables

2.1 Au and Gd fluorescence energies used in this thesis 7
2.2 Theory: Statistical Significances and p-values 15
2.3 Amptek Detector: Significances for different possible signal range definitions 20

3.1 Relative reduction of Compton scattering orders for 30 cm phantom 31

6.1 Experiment: Compton reduction values with collimator 79
6.2 Experiment: Reduction of fluorescence by the use of a collimator 84

7.1 Human voxel model: Voxel numbers and edge lengths 86
7.2 Human voxel model: Sensitivity for target in kidney 88
7.3 Human voxel model: Sensitivity for target in center of brain 89
7.4 Human voxel model: Overview on sensitivities 98

9.1 Rat phantom: Possible background reduction for Hexitec detector 117
9.2 Rat phantom: Significances for different collimator types 118

10.1 Polarization filters: Compton background reduction 134

Acknowledgements

Ich danke zunächst meinem Doktorvater Prof. Dr. Florian Grüner dafür, dass er sich für das gesamte Thema der medizinischen Bildgebung durch Röntgenfluoreszenz so stark engagiert hat. Er hat diese Arbeit immer sehr unterstützt und sie mit umfangreicher Betreuung und konstruktiver Kritik stets vorangetrieben. Außerdem danke ich Prof. Dr. Wolfgang Hillert dafür, für sein Interesse und die Bereitschaft sich als Zweitgutachter zur Verfügung zu stellen.

Insbesondere danke ich dem gesamten Medical-Imaging-Team in unserer Arbeitsgruppe für die langjährige tolle Zusammenarbeit und die vielen anregenden Unterhaltungen. Wenn ich mal nicht weiter wusste, war stets jemand zu finden, durch den ich wieder die richtigen Ansätze bekommen habe. Trotz stetigem Wechsel der Mitglieder war die Atmosphäre immer sehr angenehm und ich hoffe, dass das noch weiterhin so bleiben wird. Hier zu nennen sind insbesondere die Doktoranden, die mich über Jahre begleitet haben: Martin Stieben, Theresa Brümmer, Oliver Schmutzler, Theresa Staufer und Christian Körnig. Ein herzlicher Dank auch an Fenna Reinholdt und Heike Kaminski, die immer hilfsbereit waren und stets ein offenes Ohr hatten für die vielen kleinen Probleme auf dem Weg. Ohne euch wäre die Gruppe nicht das gleiche.

Mein Dank gilt darüber hinaus dem P07/P21-Teams bestehend aus Olof Gutowski, Dr. Martin von Zimmermann, Dr. Ann-Christin Dippel und Dr. Oleh Ivashko , da ohne ihre Hilfestellungen und kreativen Lösungsansätze, um Dinge passend zu machen, die Experimente für diese Arbeit nicht möglich gewesen wäre.

Declaration on oath/Eidesstattliche Erklärung

Hiermit versichere ich an Eides statt, die vorliegende Dissertationsschrift selbst verfasst und keine anderen als die angegebenen Hilfsmittel und Quellen benutzt zu haben.

Die eingereichte schriftliche Fassung entspricht der auf dem elektronischen Speichermedium.

Die Dissertation wurde in der vorgelegten oder einer ähnlichen Form nicht schon einmal in einem früheren Promotionsverfahren angenommen oder als ungenügend beurteilt

Florian Blumendorf – Hamburg, 13.09.2019